Journal of Fluids Engineering

Published Monthly by ASME

VOLUME 131 • NUMBER 5 • MAY 2009

FLUIDS ENGINEERING DIVISION

Editor
J. KATZ (2009)

Assistant to the Editor
L. MURPHY (2009)

Associate Editors
M. J. ANDREWS (2009)
E. M. BENNETT (2012)
S. L. CECCIO (2009)
D. DRIKAKIS (2012)
P. DURBIN (2012)
I. EAMES (2010)
C. HAH (2010)
T. J. HEINDEL (2011)
J. KOMPENHANS (2009)
YU-TAI LEE (2009)
J. A. LIBURDY (2011)
R. MITTAL (2010)
T. J. O'HERN (2009)
N. A. PATANKAR (2011)
H. PEERHOSSAINI (2011)
U. PIOMELLI (2010)
Z. RUSAK (2010)
D. SIGINER (2009)
M. STREMLER (2012)
M. WANG (2011)
St. T. WERELEY (2011)
Y. ZHOU (2009)

PUBLICATIONS COMMITTEE
Chair, **B. RAVANI**

OFFICERS OF THE ASME
President, **THOMAS M. BARLOW**
Executive Director, **THOMAS G. LOUGHLIN**
Treasurer, **T. D. PESTORIUS**

PUBLISHING STAFF

Managing Director, Publishing
P. DI VIETRO

Manager, Journals
C. MCATEER

Production Coordinator
A. HEWITT

RESEARCH PAPERS

Flows in Complex Systems

Fundamental Issues and Canonical Flows

Multiphase Flows

Techniques and Procedures

(Contents continued on inside back cover)

Transactions of the ASME, Journal of Fluids Engineering (ISSN 0098-2202) is published monthly by The American Society of Mechanical Engineers, Three Park Avenue, New York, NY 10016. Periodicals postage paid at New York, NY and additional mailing offices.
POSTMASTER: Send address changes to Transactions of the ASME, Journal of Fluids Engineering, c/o THE AMERICAN SOCIETY OF MECHANICAL ENGINEERS, 22 Law Drive, Box 2300, Fairfield, NJ 07007-2300.
CHANGES OF ADDRESS must be received at Society headquarters seven weeks before they are to be effective. Please send old label and new address.
STATEMENT from By-Laws. The Society shall not be responsible for statements or opinions advanced in papers or ... printed in its publications (B7.1, Par. 3).
COPYRIGHT © 2009 by the American Society of Mechanical Engineers. Authorization to photocopy material for internal or personal use under those circumstances not falling within the fair use provisions of the Copyright Act, contact the Copyright Clearance Center (CCC), 222 Rosewood Drive, Danvers, MA 01923, tel: 978-750-8400, www.copyright.com. Request for special permission or bulk copying should be addressed to Reprints/Permission Department.
Canadian Goods & Services Tax Registration #126148048.

This journal is printed on acid-free paper, which exceeds the ANSI Z39.48-1992 specification for permanence of paper and library materials. ♾™
♲ 85% recycled content, including 10% post-consumer fibers.

Downloaded 03 Jun 2010 to 171.66.16.159. Redistribution subject to ASME license or copyright; see http://www.asme.org/terms/Terms_Use.cfm

Journal of Fluids Engineering Volume 131, Number 5 MAY 2009

TECHNICAL BRIEFS

The ASME Journal of Fluids Engineering is abstracted and indexed in the following:

Applied Science & Technology Index, Chemical Abstracts, Chemical Engineering and Biotechnology Abstracts (Electronic equivalent of Process and Chemical Engineering), Civil Engineering Abstracts, Computer & Information Systems Abstracts, Corrosion Abstracts, Current Contents, Ei EncompassLit, Electronics & Communications Abstracts, Engineered Materials Abstracts, Engineering Index, Environmental Engineering Abstracts, Environmental Science and Pollution Management, Excerpta Medica, Fluidex, Index to Scientific Reviews, INSPEC, International Building Services Abstracts, Mechanical & Transportation Engineering Abstracts, Mechanical Engineering Abstracts, METADEX (The electronic equivalent of Metals Abstracts and Alloys Index), Petroleum Abstracts, Process and Chemical Engineering, Referativnyi Zhurnal, Science Citation Index, SciSearch (The electronic equivalent of Science Citation Index), Shock and Vibration Digest, Solid State and Superconductivity Abstracts, Theoretical Chemical Engineering

Performance and Radial Loading of a Mixed-Flow Pump Under Non-Uniform Suction Flow

B. P. M. van Esch
Technische Universiteit Eindhoven,
P.O. Box 513,
5600MB Eindhoven, The Netherlands
e-mail: b.p.m.v.esch@tue.nl

Many centrifugal pumps have a suction velocity profile, which is nonuniform, either by design like in double-suction pumps, sump pumps, and in-line pumps, or as a result of an installation close to an upstream disturbance like a pipe bend. This paper presents an experimental study on the effect of a nonuniform suction velocity profile on performance of a mixed-flow pump and hydrodynamic forces on the impeller. In the experiments, a newly designed dynamometer is used, equipped with six full Wheatstone bridges of strain gauges to measure the six generalized force components. It is placed in between the shaft of the pump and the impeller and corotates with the rotor system. A high accuracy is obtained due to the orthogonality of bridge positioning and the signal conditioning electronics embedded within the dynamometer. The suction flow distribution to the pump is adapted using a pipe bundle situated in the suction pipe. Results of measurements show the influence of the suction flow profile and blade interaction on pump performance and forces. Among the most important observations are a backward whirling motion of the rotor system and a considerable steady radial force. [DOI: 10.1115/1.3089539]

Keywords: fluid-induced forces, hydrodynamics, mixed-flow pump, nonuniform suction flow

1 Introduction

Forces on pump shafts may have several causes. The origin can be mechanical, such as mass unbalance or misalignment, or induced by the working fluid. Generally, a nonuniform pressure distribution at the periphery of the impeller is regarded as a cause for a steady lateral force, like the one encountered in pumps equipped with a volute type of casing. Hydrodynamic excitation forces result from a variety of unsteady flow phenomena such as stall, flow recirculation, cavitation, and blade interaction, while hydrodynamic reaction forces on the other hand may result from rotor whirl or precessing motion relative to the casing.[1].

Agostinelli et al. [2] and Iversen et al. [3] were the first to measure the steady lateral force on an impeller in a vaneless volute. Domm and Hergt [4] did similar experiments in which they demonstrated that impeller forces are dependent on rotor eccentricity. Hergt and Krieger [5] extended these measurements for an impeller, which was placed eccentrically in a vaned diffuser. Uchida et al. [6] measured the unsteady lateral forces on an impeller in a volute type of casing. In all of these experiments, force sensing devices of different designs were used to measure reaction forces in the bearing support structures. Chamieh et al. [7] used an external balance to measure the hydrodynamic stiffness matrix for a centrifugal impeller in a volute, whirling at a very low speed.

Internal balances, or so-called dynamometers, were used by subsequent investigations to assess the fluid-induced rotordynamic behavior of centrifugal pumps. These force sensing devices are located between the impeller and the shaft so as to directly measure forces acting on the impeller. Jerry et al. [8] constructed a dynamometer with four square posts parallel to the shaft, onto which were mounted nine full Wheatstone bridges of strain gauges to measure six generalized force components. Rotordynamic forces were measured for a radial-type centrifugal impeller in a vaneless volute forced into a whirling motion. Further research focused on the effect of leakage flow on rotordynamic forces (e.g., Refs. [9–11]). Ohashi et al. [12] designed a dynamometer consisting of two pairs of parallel plates with four strain gauges each, to measure the two lateral forces and associated force moments. Rotordynamic behavior was assessed for a centrifugal impeller in a vaneless diffuser, set into precessing motion. The same device was subsequently used in a series of experiments studying the rotordynamic behavior of several pumps of different designs and specific speeds, as well as the influence of seal geometry (e.g., Refs. [13–16]).

A nonuniform suction flow to a pump has an influence on pump performance (e.g., Refs. [17–19]). This type of flow is encountered in many different pump designs, e.g., double-suction pumps, in-line radial pumps, sump pumps, the suction stage of a boiler feed pump, and in pumps positioned closely to an upstream flow disturbance like a pipe bend. Yet, the effect on hydrodynamic forces has hardly been addressed in literature. Bolleter et al. [20] measured lateral forces on the shaft of a radial pump with different inlet chamber designs. Fujii et al. [21] investigated the blade loading of an inducer under cavitating conditions, with and without inlet flow distortion.

This paper presents an experimental assessment of the effect of a nonuniform suction flow on pump performance and radial loading. The pump is a scale model of a waterjet pump, introduced in Sec. 2. In practice, the suction flow to this pump is highly nonuniform. Even at normal operating conditions, variations in axial velocity can be as high as 50% of its average value. A general description of the experimental setup is given in Sec. 3, while the details of the dynamometer and the flow redistribution device are given in Secs. 4 and 5. Finally, results of measurements are given in Sec. 6. Both general performance of the pump and radial loading of the impeller are addressed. Results with and without suction flow distortion are compared.

2 Waterjet Pumps

Figure 1 shows a frequently used design of a waterjet system, a mixed-flow pump with an intake duct flush-mounted to the hull of the ship. Water is taken from below the ship and flows through the

---

Contributed by the Fluids Engineering Division of ASME for publication in the Journal of Fluids Engineering. Manuscript received June 26, 2008; final manuscript received January 19, 2009; published online April 1, 2009. Assoc. Editor: Chunill Hah.

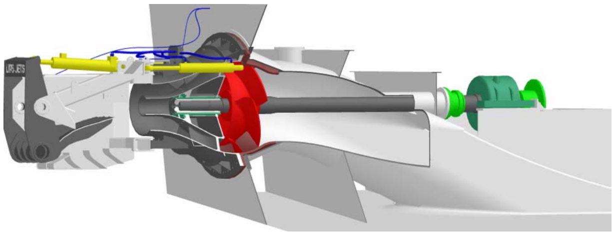

Fig. 1 Waterjet propulsion system employing a mixed-flow pump with stator bowl and nozzle

duct to the pump, is subsequently pressurized, and accelerated in the nozzle. The inlet flow distribution in systems like these is inevitably nonuniform, caused by the following:

- suction from the boundary layer
- diffusion and/or acceleration in the inlet duct, depending on operating conditions
- the double bend in the inlet duct
- the rotating pump shaft protruding into the inlet duct

The nonuniform inflow velocity distribution at normal operating condition is a phenomenon, which is widely recognized [22–24].

As an example, measured axial velocity distributions are shown in Fig. 2 [25]. Two operating conditions are given, representing a fully loaded and an unloaded vessel at maximum power. Operating conditions of waterjet propelled ships are customarily classified according to the inlet velocity ratio (IVR), which is defined as

$$\mathrm{IVR} = v_s / v_p$$

with v_s the ship speed and v_p the average axial velocity entering the pump. Thus, a fully loaded ship at maximum velocity has a medium IVR value while an unloaded ship at maximum velocity is characterized by a high value of IVR. Operating conditions during the start-up phase are characterized by low values of IVR.

3 Experimental Setup

A scale-model version of a waterjet pump manufactured by Wärtsilä Propulsion Netherlands (Drunen, The Netherlands) is built into the test facility at the Technische Universiteit Eindhoven (Eindhoven University of Technology) (Fig. 3). The main characteristics of this setup are a closed-loop circuit of 18 m, a pipe diameter of 315 mm, an electromagnetic flow meter, a discharge butterfly valve, air release valves, and a pressure tank. The pump is of mixed-flow type with a six-bladed impeller and a stator bowl with seven vanes. The impeller outer diameter is 335 mm. A key component is the dynamometer. A detailed description of this force sensing device is given in Sec. 4.

In a normal waterjet pumping unit, the shaft is mounted at the suction side of the pump (Fig. 1). However, in this setup, the shaft construction is changed and installed at the discharge. The reason for this alteration is that it enables a comparison between results obtained at nonuniform suction flow and equivalent results with uniform inlet flow. This is why the straight suction pipe is equipped with a flow redistribution device. Further discussion of this device is postponed until Sec. 5.

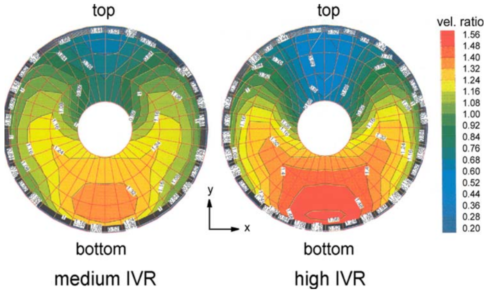

Fig. 2 Examples of measured axial velocity distribution in a plane just upstream of the impeller. Velocities are normalized with the average axial velocity.

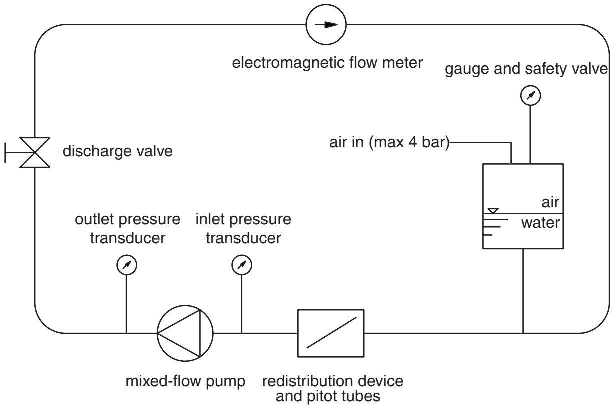

Fig. 3 Experimental facility

Another adaptation to the pump, which is currently not in use, however, is the dual shaft system by means of which the rotor can be set into a whirling or precessing motion. This feature is included in the design to allow for future measurements of hydrodynamic reaction forces.

Signals of the dynamometer are transmitted by cables, which lead to a set of slip rings through a hole in the central shaft. The shaft of the pump is equipped with an optical encoder providing a once-per-revolution pulse from which the impeller orientation is determined for synchronization with the data acquisition system.

4 Dynamometer

The dynamometer is a force sensing device, which is placed between the shaft of the pump and the impeller (Fig. 4). Forces on the impeller are measured directly, as opposed to using external balances in bearings or pump support structures for which measurements are often hampered by unknown properties of dynamically loaded bearings and seals, or suffer from inaccuracies due to bearing play. The dynamometer has four square posts (Fig. 5) onto which 24 strain gauges are mounted, grouped into six full Wheatstone bridges to enhance temperature compensation. This way, six generalized force components (radial forces, bending moments, axial force, and torque) can be measured. The capability of the dynamometer to measure radial force as well as its associated bending moment is essential to this investigation, since the point of action of the radial force is not known a priori. The design resembles that of Jerry et al. [8] although positions of strain gauges are different.

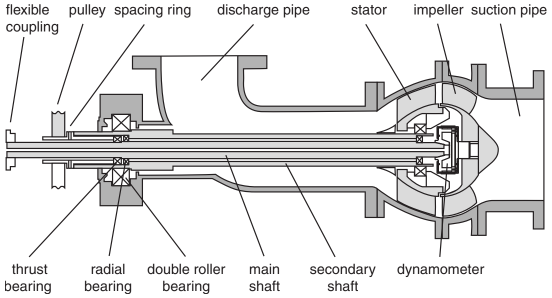

Fig. 4 Cross section of the mixed-flow pump indicating the position of the dynamometer

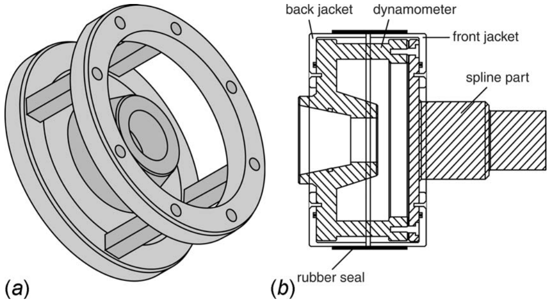

Fig. 5 Drawing of dynamometer showing four posts (left) and cross section of dynamometer with spline part and sealing jackets

To minimize noise and prevent loss of signals, electronics for stabilized bridge power supply and signal amplification are built into the dynamometer (Fig. 6). Eight wires carrying the supply voltage and the bridge output signals are connected to a slip ring assembly with 24 channels. Three channels are used for each wire connection to minimize the effect of noise in the transmission.

Calibration of the dynamometer is done both statically and dynamically. Static radial loading consists of a series of measurements with different weights applied at different axial distances from the dynamometer. The accuracy of the calibration is increased further by a dynamic calibration procedure in situ. A disk of known mass is mounted on the shaft at two different axial positions. Bridge signals are sampled while the system is running at the intended shaft speed. From these two measurements and the known mass and axial distances, the response of all six bridges to radial force and associated bending moment can be assessed. Additional runs with a disk of different weight at different positions revealed that the weight and the axial location of its center of mass are determined with accuracies of 0.1% and 0.2%, respectively. The error in phase angle was less than 1.5 deg. The error in instantaneous forces, determined from the standard deviation in the ensemble-averaged signal, was 3%.

5 Flow Redistribution Device

Since the axial velocity profile in the straight suction pipe of the setup is approximately uniform, a flow redistribution device of some sort is required. Its purpose is to modify the velocity distribution into a nonuniform profile as given in Fig. 2. A bundle of small diameter tubes was shaped according to the method of Kotansky [26], extended to three dimensions. However, measurements showed that the resulting velocity distribution, though stable and nonuniform, did not resemble the intended shear profile. Velocity measurements were performed with Pitot tubes in a plane located approximately one pipe diameter upstream of the impeller and at a distance of three pipe diameters downstream of the redistribution device. Measured velocity profiles are given in Fig. 7. Velocity profile *B* was obtained after rotation of the pipe bundle over 180 deg.

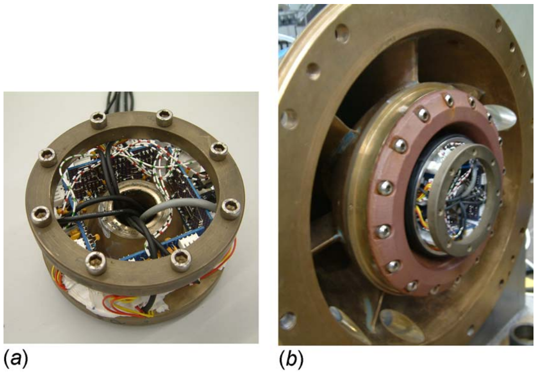

Fig. 6 Dynamometer with electronics for bridge power supply and signal conditioning (left) and dynamometer mounted on the shaft

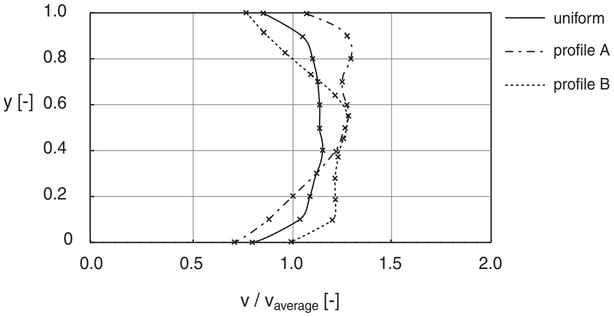

Fig. 7 Axial velocity profiles along a vertical traverse, with and without a pipe bundle installed

Although velocity profile *B* does not closely resemble the situation encountered in waterjet pump installations, the main characteristic of a changing axial velocity in vertical direction is obtained. The resulting variation in velocity is almost in the range of what is normally encountered at medium values of IVR (Fig. 8). Therefore, it is concluded that many of the phenomena in waterjet installations, related to the nonuniform entrance flow, can be studied in the current setup.

6 Results

Experiments are performed with and without velocity redistribution device for different shaft speeds ranging from 450 rpm to 900 rpm. Reynolds numbers are in the range $\mathrm{Re}_\Omega = (5-11)\times 10^6$, and $\mathrm{Re}_v = (6-12)\times 10^5$, based on BEP operation. Flow rates are varied between 10% Q_{BEP} and the maximum flow rate of 120% Q_{BEP} (110% Q_{BEP} with pipe bundle installed). For each run, bridge signals are sampled during ~500 shaft revolutions and ensemble averaged. No additional filtering is performed apart from the 50 Hz line frequency.

In Sec. 6.1 global characteristics of the pump are given for both uniform and nonuniform suction flows. Results of force measurements are given in Sec. 6.2, for a shaft speed of 700 rpm at BEP flow rate. The influence of the nonuniform suction flow distribution, as well as blade interaction on radial forces, is shown. A detailed study of the influence of flow rate on the steady fluid-induced force is presented in Sec. 6.3.

6.1 Global Performance Characteristics. Figures 9–11 present characteristic curves for manometric head, torque, and axial force, at different shaft speeds. No suction flow redistribution device was installed. The manometric head was calculated

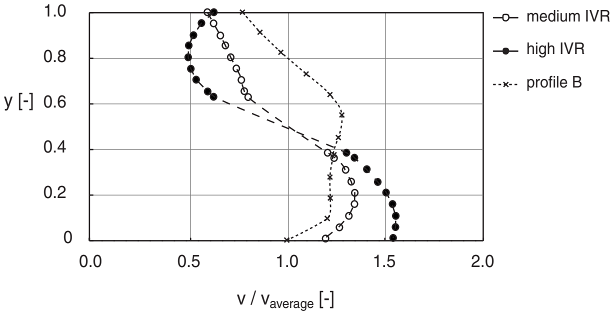

Fig. 8 Comparison of velocity profile *B* with measured profiles in a waterjet intake duct (Fig. 3)

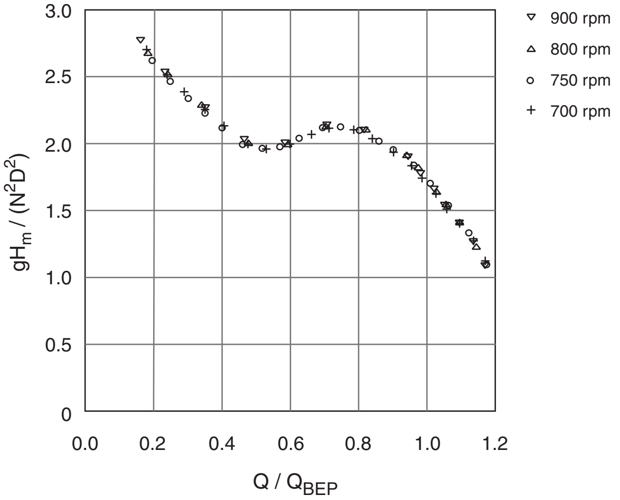

Fig. 9 Manometric head for uniform suction flow, at different shaft speeds

from measured (and averaged) static pressure and average axial velocity. Four pressure taps along the circumference of the pipes were used to measure static pressure at stations approximately one diameter up- and downstream of the pump. Torque and axial force were measured by the dynamometer and thus represent the forces on the impeller only. Axial force was corrected for shaft force by adding the suction gauge pressure multiplied by the cross sectional area of the shaft. Results scale appropriately, although Reynolds effects are present for these fairly low shaft speeds. Characteristic curves show a trend typical for pumps of mixed-flow type.

For a nonuniform suction velocity profile, the manometric head is difficult to determine, since an accurate mass-average of total pressure should be measured. Therefore, the static head, based on a difference in average static pressure, is used in stead. Figures 12–15 present the results of this comparison, where use is made of profile *B* (see Fig. 7). It appears that a nonuniform suction flow reduces pump performance in the sense that both head and torque are reduced over a large part of the pump curve. For this mild nonuniformity the decrease in head and torque is limited to ~2.5% at most. However, (static) efficiency is not affected, as illustrated in Fig. 14. It means that a nonuniform suction flow does not lead to an increase in power consumption; the reduction in pump head can be compensated by a slight increase in shaft speed. This is different from, for example, the effect of tip clearance. Figures 12–15 also present results for a (small) clearance of 1 mm and a (large) clearance of 2 mm. Clearly, the effect of an increase in tip clearance on performance is much larger. But, more important in this respect, it leads to a true reduction in perfor-

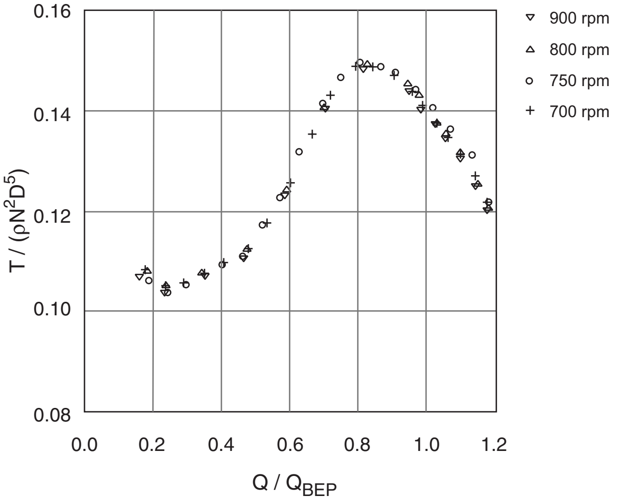

Fig. 10 Impeller torque for uniform suction flow, at different shaft speeds

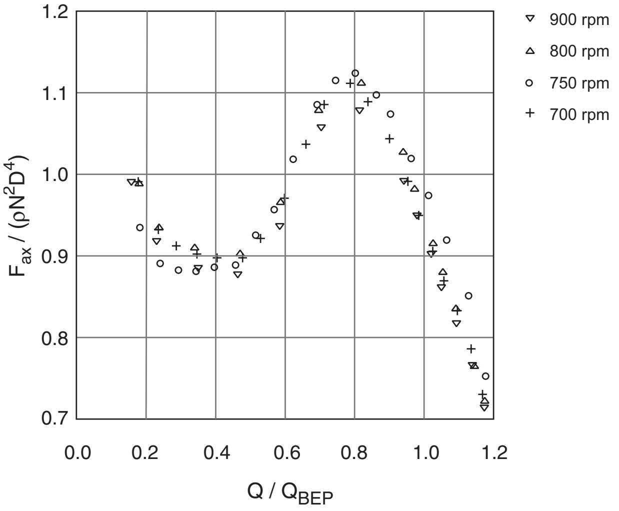

Fig. 11 Axial force on the impeller for uniform suction flow, at different shaft speeds

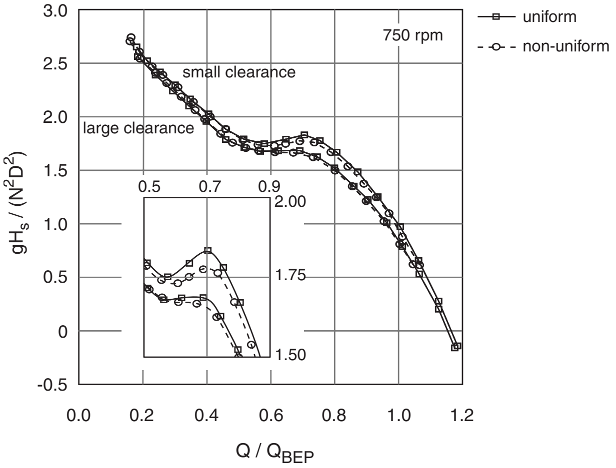

Fig. 12 Static head for uniform and nonuniform suction flows, at small and large tip clearances

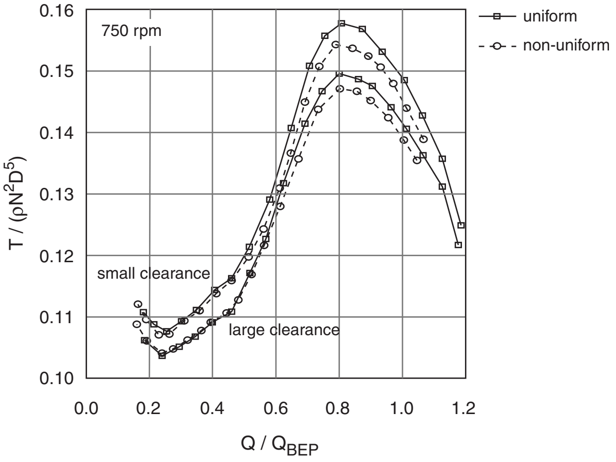

Fig. 13 Impeller torque for uniform and nonuniform suction flows, at small and large tip clearances

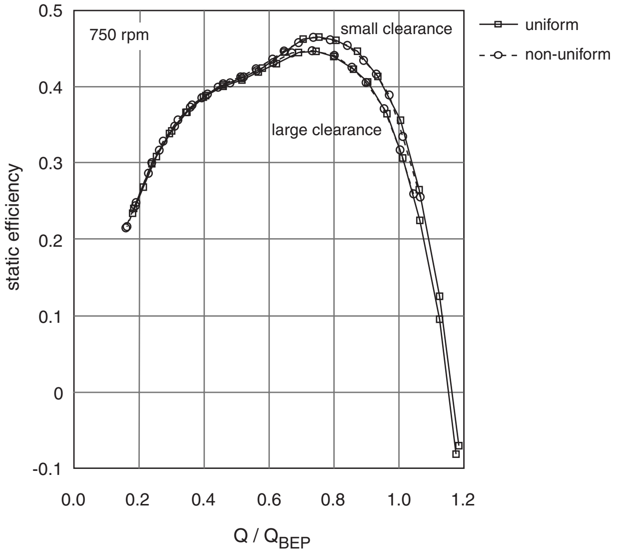

Fig. 14 Pump efficiency based on static head for uniform and nonuniform suction flows, at small and large tip clearances

mance since also efficiency is reduced. Figure 15 shows results for axial force on the impeller, which are consistent with the results for head and torque.

6.2 Hydrodynamic Forces. From the ensemble-averaged bridge signals, one can calculate instantaneous radial force components F_X and F_Y in the inertial frame of reference, during one impeller revolution. A typical result is given in Fig. 16 for a shaft speed of 700 rpm, at 100% Q_{BEP}, and uniform suction flow profile. Since the geometry is axisymmetric and the suction flow is almost uniform, the time-averaged radial force is approximately equal to the weight of the impeller in water. This means that the net fluid-induced force on the impeller is small.

The dynamometer bridge signals show spectral content with main contributions at frequencies equal to the shaft frequency and higher harmonics. Of these higher frequencies, the seventh harmonic is dominant. This is clearly observed in Figs. 17 and 18, where forces at different ranges in frequency are shown. In Fig. 17, the influence of impeller weight and centrifugal force is apparent. The latter is caused by mass imbalance and, to a larger extent, hydraulic imbalance. The centrifugal force component rotates in the direction of shaft revolution. Time-averaged hydrodynamic force is small. Rotor-stator blade interaction force is shown in Fig. 18, in the inertial frame of reference. Note that this blade passing excitation force induces a backward whirling motion of the impeller at a frequency of six times shaft frequency.

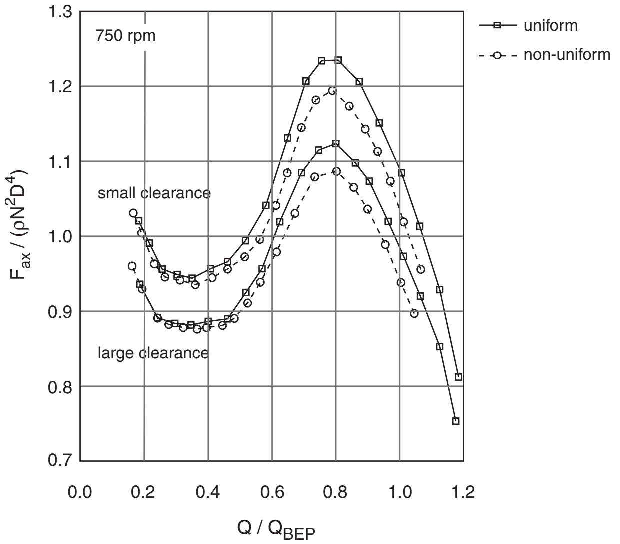

Fig. 15 Axial force for uniform and nonuniform suction flows, at small and large tip clearances

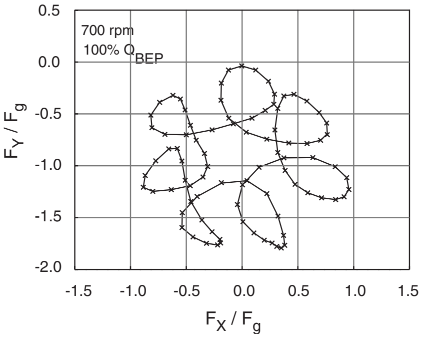

Fig. 16 Force vector plot in the inertial frame of reference, normalized with impeller weight F_g in water, for uniform suction flow profile

In case of a nonuniform suction flow distribution, similar force plots are obtained. However, an additional steady fluid-induced force is observed in a direction, which depends on the suction flow profile. A detailed analysis is given in Sec. 6.3.

6.3 Steady Fluid-Induced Forces. Hydrodynamic forces were measured for different combinations of shaft speed and flow rate, and for different suction flow profiles. In case of nonuniform suction flow, a steady fluid-induced force emerges, which results from an unbalanced torque loading of the impeller blades [27]. The magnitude and direction of this steady force are given in Fig. 19, for different flow rates. It is apparent that the force magnitude increases with flow rate, which confirms the findings of Bolleter et

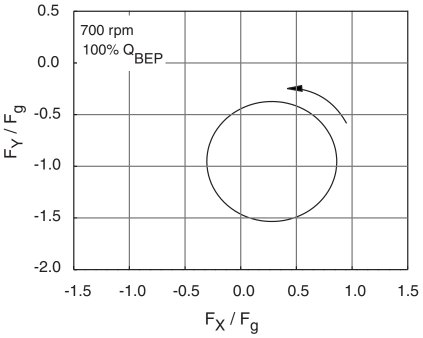

Fig. 17 Force vector plot for frequencies up to and including shaft frequency, for uniform suction flow profile

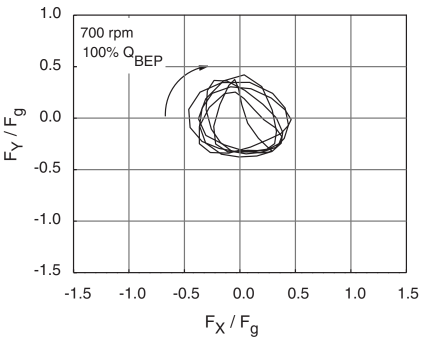

Fig. 18 Force vector plot for frequencies above shaft frequency showing rotor-stator blade interaction and backward whirl of the impeller

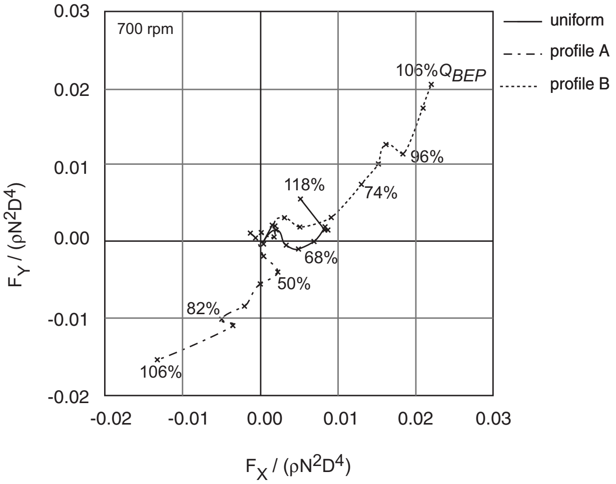

Fig. 19 Normalized steady fluid-induced force, for different flow rates and suction flow profiles

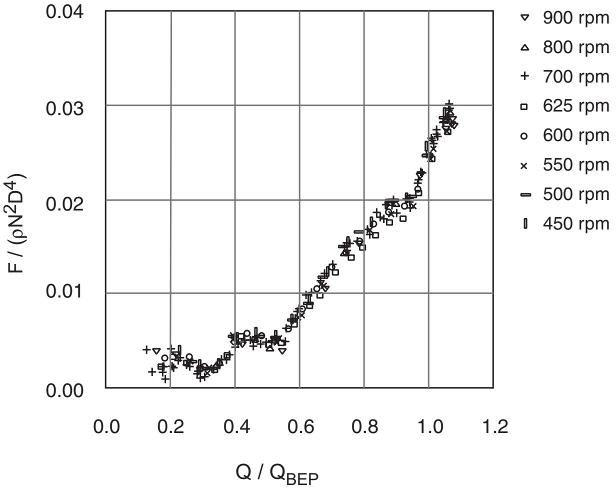

Fig. 21 Magnitude of normalized steady fluid-induced force for different shaft speeds and suction velocity profile *B*

al. [20]. The direction of the force is opposite for the two nonuniform suction flow profiles *A* and *B*, consistent with the two profiles being approximately inversed in vertical direction.

Further measurements for suction profile *B* (indicative of the suction flow profile in practical waterjet applications) are presented in Figs. 20–22, for different shaft speeds. Note that the steady fluid-induced force scales with the square of the shaft speed. The direction of the force vector with respect to the horizontal axis is ~35–45 deg, for flow rates above 50% Q_{BEP}. For lower flow rate the direction deviates, presumably due to inlet recirculation, which influences the suction velocity profile.

7 Discussion and Conclusion

An important observation in this study is that the global performance of a pump is influenced by the type of inflow velocity profile. For the relatively mild nonuniformity in the experiments, the head, torque, and axial force were reduced by a few percent. And although the efficiency of the pump was not reduced, it still has an important practical implication. Many pumping systems that face nonuniform inflow conditions during service are selected based on performance under uniform inflow, e.g., sump pumps or cooling water pumps. The reason is that most pump manufacturers use standard closed-loop test-rigs with straight suction piping. Selection of the drive train components should then allow for adjustment of the intended shaft speed in order to compensate for the reduced head.

A second phenomenon related to nonuniform suction flow is the radial loading of the impeller. It is of interest to compare the magnitude of the forces measured in this investigation to forces mentioned in literature for pumps of the same type. An overview of force measurements on pump shafts can be found in, e.g., Ref. [28]. The magnitude of forces is customarily divided into steady and unsteady components (in the inertial frame of reference). Figure 23 presents a comparison of the steady force components, as a function of flow rate. Clearly, at a larger flow rate, the measured force is much higher than the values normally anticipated in these pumps. A high radial loading not accounted for will lead to excessive wear of bearings and seals and even rubbing of the impeller at the casing wall. Moreover, the force being steady in the inertial frame of reference is potentially harmful to the shaft, since it may lead to damage through fatigue failure.

A second remark on the radial loading of the impeller concerns the direction of the force vector. From the measurements it was concluded that the impeller undergoes a radial force with an upward component. Depending on the type of suction velocity profile this force may be in upward direction entirely. For example, consider a double-suction pump with its suction nozzle in an unfavorable direction, or a waterjet system in a ship during maneu-

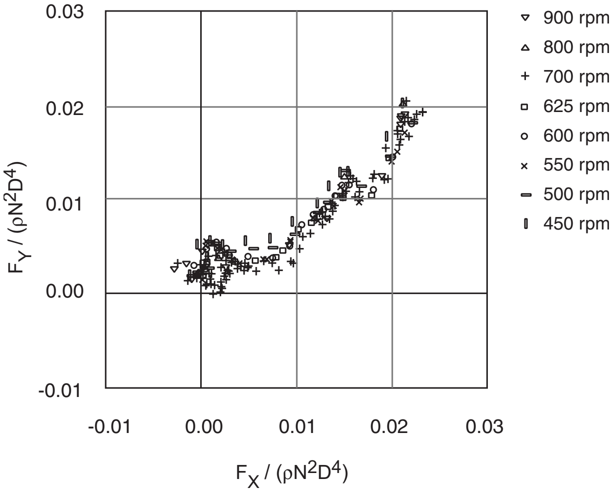

Fig. 20 Vector plot of normalized steady fluid-induced force for different flow rates and shaft speeds, and suction velocity profile *B*

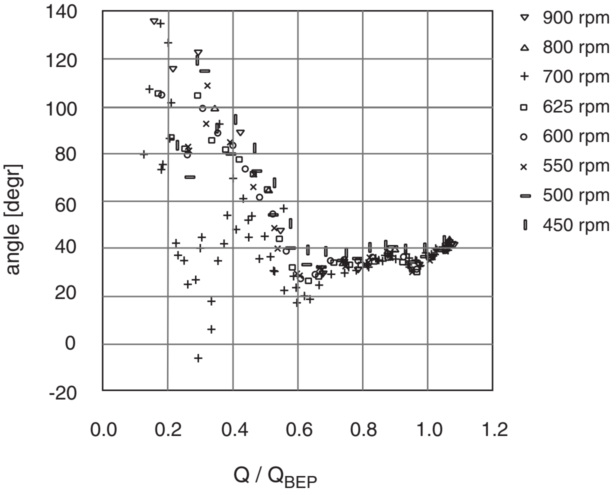

Fig. 22 Direction of steady fluid-induced force vector for different shaft speeds and suction velocity profile *B*

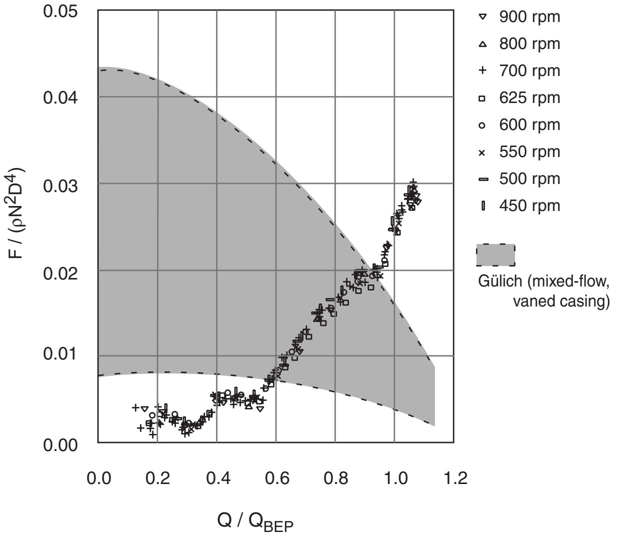

Fig. 23 Comparison of radial forces as given in literature with measured values of Fig. 21

vering. If not properly accounted for in the design phase of these pumps, the effect may lead to the bearings being unloaded at times, and thus to high levels of vibration and noise.

The measurement of hydrodynamic forces led to the conclusion that the rotor-stator blade passing excitation force induces a backward whirling motion of the impeller at a frequency of six times shaft frequency. It is anticipated by several authors that, from a theoretical analysis, it is to be expected that rotor-stator systems with a number of stator vanes exceeding the number of rotor blades by one may exhibit perturbations propagating in the reverse direction at blade passing frequency [29,30]. However, the resulting backward rotor whirl was never confirmed experimentally up to now. A detailed account of hydrodynamic force measurements will be presented in a future paper.

Acknowledgment

The author would like to thank Wärtsilä Propulsion Netherlands for providing the scale-model pump and supporting the publication of this paper.

Nomenclature

g = gravitational acceleration ($\mathrm{m/s^2}$)
D = impeller outer diameter (m)
F = force (N)
H_m = manometric pump head (m)
H_s = static pump head (m)
N = shaft speed (rps)
Q = flow rate ($\mathrm{m^3/s}$)
T = torque (N m)
Re_Ω = Reynolds number based on impeller tip speed, $\mathrm{Re}_\Omega = \Omega D^2/\upsilon$
Re_v = Reynolds number based on pipe velocity and diameter
ν = kinematic viscosity ($\mathrm{m^2/s}$)
ρ = mass density ($\mathrm{kg/m^3}$)

Subscripts and Superscripts

ax = axial direction
r = radial direction
X, Y = x-and y-components in lateral direction, in the steady frame of reference

References

[1] Ehrich, F. F., and Childs, D. W., 1984, "Self-Excited Vibrations in High Performance Turbomachinery," Mech. Eng. (Am. Soc. Mech. Eng.), **106**, pp. 66–79.

[2] Agostinelli, A., Nobles, D., and Mockridge, C. R., 1960, "An Experimental Investigation of Radial Thrust in Centrifugal Pumps," ASME J. Eng. Power, **82**, pp. 120–126.

[3] Iversen, H. W., Rolling, R. E., and Carlson, J. J., 1960, "Volute Pressure Distribution, Radial Force on the Impeller and Volute Mixing Losses of a Radial Flow Centrifugal Pump," ASME J. Eng. Power, **82**, pp. 136–144.

[4] Domm, U., and Hergt, P., 1970, *Radial Forces on Impeller of Volute Casing Pumps, Flow Research on Blading*, L. S. Dzung, ed., Elsevier, Netherlands, pp. 305–321.

[5] Hergt, P., and Krieger, P., 1969, "Radial Forces in Centrifugal Pumps With Guide Vanes," Proc. Inst. Mech. Eng., **184**, pp. 101–107.

[6] Uchida, N., Imaichi, K., and Shirai, T., 1971, "Radial Force on the Impeller of a Centrifugal Pump," Bull. JSME, **14**, pp. 1106–1117.

[7] Chamieh, D., Acosta, D. S., Brennen, C. E., and Caughey, T. K., 1985, "Experimental Measurements of Hydrodynamic Radial Forces and Stiffness Matrices for Centrifugal Pump Impeller," ASME J. Fluids Eng., **107**(3), pp. 307–315.

[8] Jerry, B., Acosta, A. J., Brennen, C. E., and Caughey, T. K., 1985, "Forces on Centrifugal Pump Impellers," *Proceedings of the second International Pump Symposium*, Houston, TX, Apr. 30–May 2.

[9] Guinzburg, A., Brennen, C. E., Acosta, A. J., and Caughey, T., 1993, "The Effect of Inlet Swirl on the Rotordynamic Shroud Forces in a Centrifugal Pump," ASME J. Eng. Gas Turbines Power, **115**, pp. 287–293.

[10] Uy, R. V., and Brennen, C. E., 1999, "Experimental Measurements of Rotordynamic Forces Caused by Front Shroud Pump Leakage," ASME J. Fluids Eng., **121**, pp. 633–637.

[11] Hsu, Y., and Brennen, C. E., 2002, "Effect of Swirl on Rotordynamic Forces Caused by Front Shroud Pump Leakage," ASME J. Fluids Eng., **124**, pp. 1005–1010.

[12] Ohashi, H., Imai, H., and Tsuchihashi, T., 1991, "Fluid Force and Moment on Centrifugal Impellers in Precessing Motion," ASME FED Fluid Machinery Forum, Vol. **119**(3), Portland, OR, pp. 57–60.

[13] Yoshida, Y., Tsujimoto, Y., Ohashi, H., and Kano, F., 1999, "The Rotordynamic Forces on an Open-Type Centrifugal Compressor Impeller in Whirling Motion," ASME J. Fluids Eng., **121**, pp. 259–265.

[14] Yoshida, Y., Tsujimoto, Y., Yokoyama, D., Ohashi, H., and Kano, F., 2001, "Rotordynamic Fluid Force Moments on an Open-Type Centrifugal Compressor Impeller in Precessing Motion," Int. J. Rotating Mach., **7**, pp. 237–251.

[15] Yoshida, Y., Tsujimoto, Y., Morimoto, G., Nishida, H., and Morii, S., 2003, "Effects of Seal Geometry on Dynamic Impeller Fluid Forces and Moments," ASME J. Fluids Eng., **125**, pp. 786–795.

[16] Suzuki, T., Prunières, R., Horiguchi, H., Tsukiya, T., Taenaka, Y., and Tsujimoto, Y., 2007, "Measurements of Rotordynamic Forces on an Artificial Heart Pump Impeller," ASME J. Fluids Eng., **129**, pp. 1422–1427.

[17] Toyokura, T., 1961, "Studies on the Characteristics of Axial-Flow Pumps," Bull. JSME, **4**, pp. 287–340.

[18] Badowski, H. R., 1970, "Inducers for Centrifugal Pumps," Worthington Canada, Ltd., Internal Report.

[19] Del Valle, D., Braisted, D. M., and Brennen, C. E., 1992, "The Effects of Inlet Flow Modification on Cavitating Inducer Performance," ASME J. Fluids Eng., **114**, pp. 360–365.

[20] Bolleter, U., Leibundgut, E., Sturchler, R., and McCloskey, T., 1989, "Hydraulic Interaction and Excitation Forces of High Head Pump Impellers," *Joint ASCE/ASME Pumping Machinery Symposium*, San Diego, CA, pp. 187–193.

[21] Fujii, A., Azuma, S., Yoshida, Y., Tsujimoto, Y., and Laffite, S., 2002, "Unsteady Stress of 4-Bladed Inducer Blades and the Effect of Inlet Flow Distortion," JSME Int. J., Ser. B, **45**, pp. 47–54.

[22] Seil, G. J., Fletcher, C. A., and Doctors, L. J., 1995, "The Application of Computational Fluid Dynamics to Practical Waterjet Propulsion System Design and Analysis," *Proceedings FAST'95*, pp. 1379–1389.

[23] Verbeek, R., and Bulten, N. W. H., 1998, "Recent Developments in Waterjet Design," *Proceedings Rina Waterjet Propulsion Conference*, Amsterdam.

[24] Brandner, P., and Walker, G. J., 2001, "A Waterjet Test Loop for the Tom Fink Cavitation Tunnel," *Proceedings Waterjet Propulsion III Conference*, Gothernburg.

[25] Bulten, N. W. H., Verbeek, R., and van Esch, B. P. M., 2006, "CFD Simulations of the Flow Through a Waterjet Installation," Int. J. Marit. Eng., **148**, pp. 23–33.

[26] Kotansky, D. R., 1966, "The Use of Honeycomb for Shear Flow Generation," AIAA J., **4**, pp. 1490–1491.

[27] Bulten, N. W. H., and van Esch, B. P. M., 2007, "Fully Transient CFD Analyses of Waterjet Pumps," Marine Technology, Vol. **44**(3), pp. 185–193, Society of Naval Architects and Marine Engineers (SNAME).

[28] Gülich, J. F., 1999, *Kreiselpumpen—Ein Handbuch für Entwicklung, Anlageplanung und Betrieb*, Springer-Verlag, Berlin.

[29] Dubas, M., 1984, "Über die Erregung infolge der Periodizität von Turbomachinen," Ing.-Arch., **54**, pp. 413–426.

[30] Brennen, C. E., 1994, *Hydrodynamics of Pumps*, Oxford University Press, Oxford.

Experimental and Computational Study of Oscillating Turbine Cascade and Influence of Part-Span Shrouds

X. Q. Huang[1]
L. He[2]
University of Durham,
Durham DH1 3LE, UK

David L. Bell
Alstom Power Ltd.,
Rugby CV21 2NH, UK

This paper presents a combined experimental and computational study of unsteady flows in a linear turbine cascade oscillating in a three-dimensional bending/flapping mode. Detailed experimental data are obtained on a seven-bladed turbine cascade rig. The middle blade is driven to oscillate and oscillating cascade data are obtained using an influence coefficient method. The numerical simulations are performed by using a 3D nonlinear time-marching Navier–Stokes flow solver. Single-passage domain computations for arbitrary interblade phase angles are achieved by using the Fourier shape correction method. Both measurements and predictions demonstrate a fully 3D behavior of the unsteady flows. The influence of the aerodynamic blockage introduced by part-span shrouds on turbine flutter has been investigated by introducing flat plate shaped shrouds at 75% span. In contrast to practical applications, in the present test configuration, the mode of vibration of the blades remains unchanged by the introduction of the part-span shroud. This allows the influence of the aerodynamic blockage introduced by the part-span shroud to be assessed in isolation from the change in mode shape. A simple shroud model has been developed in the computational solver. The computed unsteady pressures around the shrouds are in good agreement with the experimental data, demonstrating the validity of the simple shroud model. Despite of notable variations in local unsteady pressures around the shrouds, the present results show that the blade aerodynamic damping is largely unaffected by the aerodynamic blockage introduced by part-span shrouds.
[DOI: 10.1115/1.3111254]

1 Introduction

In modern blading designs, there has been an increasing need to adequately predict blade flutter stability, particularly for low pressure compressors and turbines with long blades. In recent years, 3D computational modeling tools for blade flutter predictions have been actively developed, for example, Gerolymos [1], Hall and Clark [2], He and Denton [3], and Vahdati and Imregun [4]. There has been some considerable effort in experimental work to produce test data (e.g., Bölcs and Fransson [5], Buffum et al. [6], and Lepicovsky et al. [7]) for both code validation and advancing our physical understanding of flutter mechanisms, but most of the tests were confined to 2D cascades with data taken at midspans. Given the significant progress in development in advanced 3D computational methods, it is, however, recognized that there has been notable lack of detailed 3D experimental data for method validations.

Bell and He [8] experimentally illustrated the importance of 3D effects in aeroelastic applications from test data, which were obtained on a single turbine blade oscillating in a profiled channel. Yang and He [9] conducted a flutter experiment on a linear compressor cascade oscillating in a 3D bending mode. They pursued a one oscillating blade strategy and the tuned cascade data were constructed using a linear superposition based on the influence coefficient method [10]. Their results showed strong effects from both the 3D unsteady flow behavior and the aerodynamic coupling between blades. Vogt [11] (also Vogt and Fransson [12]) carried out a test using the influence coefficient method on an annular sector cascade featuring a 3D background flow. From the observations on influence coefficients on the middle blade (3D tuned cascade data are not available for their studies), they attributed the 3D behavior of increasing response magnitude from hub to tip observed at bending modes to the respective blade mode shape. The locally varying response magnitude observed at a torsion mode was suggested to be due to the 3D effects of the mean flow field. To further clarify the main source of 3D unsteady effects, it would be useful to investigate a case where the baseline mean flow would be largely of 2D nature. Prismatic blading profiles have been previously used for a single turbine blade [8] and for a compressor cascade [9], where the 3D unsteady effects have been identified to be due to the instantaneous spanwise interactions. But no such work has been carried out for a turbine cascade. It should be mentioned that the nominal setting of the present experiment is similar to that of Yang and He [9]. However, high quality of data and a first of its kind effort on a turbine cascade make it a useful complement to test cases currently available in the turbomachinery aeroelastic community.

Regarding turbine flutter prediction, another issue of interest is the modeling requirement for part-span shrouds. To prevent flutter from occurring, passive measures are often introduced at the final blade design stage. Of them, using part-span shrouds ("dampers" or "snubbers") is one typical option. The presence of part-span shrouds would introduce blockage to the radial propagation of unsteady flow disturbances. It is, however, not clear, how a part-span shroud would behave and affect the blade aerodynamic damping. To the authors' knowledge, none of previously published unsteady CFD analyses has included modeling the shrouds in blade flutter predictions.

The objectives of the present work are twofold. First, the de-

---

[1] Present address: Northwestern Polytechnical University, China.

[2] Corresponding author. Present address: Dept. of Engineering Science, Oxford University, Oxford OX1 3PJ, UK.

Contributed by the Fluids Engineering Division of ASME for publication in the JOURNAL OF FLUIDS ENGINEERING. Manuscript received September 10, 2006; final manuscript received December 8, 2008; published online April 10, 2009. Assoc. Editor: Yu-Tai Lee.

Fig. 1 Low-speed turbine cascade rig

tailed 3D experimental data are obtained on a low-speed linear turbine cascade through applying the influence coefficient method. The experimental cases are numerically simulated by a 3D time-marching Navier–Stokes method for validation purposes. Second, the modeling issue regarding part-span shrouds is addressed also experimentally and computationally. In Secs. 2.1–2.3, the experimental rig, instrumentation, the data acquisition/processing, and the results for the nominal condition will be first described. This will be followed by the computational methods, results, and discussions for the nominal condition. Finally, the study on part-span shrouds will be presented.

2 Experimental Study

2.1 Low-Speed Test Rig. A low-speed test facility, shown in Fig. 1, is commissioned in the present experimental study. In this rig, air flow is driven by a centrifugal fan (powered by an 11 kW ac motor; speed of 0–1500 rpm) through a two-stage slatted diffuser and into a large settling chamber. The flow, under a propelling force generated by the high pressure in the settling chamber, accelerates through a shaped contraction (a contraction ratio of 7.5:1) and discharges into the working section. In this setup, uniform flow is developed at inlet to the working section, through appropriate design of the contraction profile, and the deployment of screens and honeycomb before and after the contraction, respectively. The wind tunnel is of a variable speed, with the mass flow being accurately controlled by a digital three-phrase inverter.

The working section is a self-contained linear turbine cascade. It consists of seven prismatic turbine blades, Perspex sidewalls, and a wooden frame. The blade profile (Table 1) is a bespoke low-speed design, which is developed within the framework of the present investigation. The cascade data and operational conditions are summarized in Table 2. The top and bottom walls of the cascade are profiled to simulate the two adjacent blades in cascade; therefore, eight blade passages are formed, with four passages on each side of the middle reference blade. Bleed slots are applied upstream of blades to break down the boundary layer development on the sidewalls whereas no such effort is made to remove the boundary layer on the profiled top and bottom walls. Two adjustable tailboards, acting as the extension of top and bottom walls, are used to help establish blade-to-blade periodicity. To achieve a 3D bending condition, the reference blade is hinged at the hub and driven at the tip end. This allows a linear variation in bending amplitude along the span, corresponding to the first bending mode. A sinusoidal oscillation rate is enforced by using a single bar crank connection between a dc motor shaft and a rod protruding from the blade tip. Since the hinge at the hub is mounted outside the working section, it should be noted that a small displacement is introduced to the hub of the oscillating blade. Indeed, the amplitude at the hub is a tenth of that at the tip. To allow the small blade translational movement through the wall

Table 1 Blade profile

X (mm)	Y (mm)
0.00	92.26
0.11	92.91
0.48	93.46
0.74	93.67
2.25	94.46
6.16	96.28
9.91	97.69
13.53	98.76
16.16	99.37
19.58	99.93
22.89	100.26
26.14	100.41
29.32	100.38
32.44	100.20
35.49	99.87
38.49	99.38
41.43	98.76
44.32	98.00
47.15	97.11
49.93	96.08
52.65	94.91
55.32	93.62
57.94	92.19
60.50	90.62
63.01	88.91
65.46	87.05
67.85	85.04
70.17	82.87
72.43	80.53
74.61	78.00
76.73	75.34
78.82	72.56
80.85	69.67
82.85	66.67
84.81	63.59
86.73	60.42
88.62	57.16
90.48	53.82
92.29	50.37
94.95	45.02
97.50	39.44
99.56	34.60
101.55	29.58
103.45	24.37
105.28	18.96
106.69	14.48
108.03	9.85
109.32	5.08
110.28	1.20
110.30	1.02
110.29	0.85
110.18	0.52
109.96	0.25
109.66	0.07
109.32	0.00
108.98	0.05
108.68	0.22
108.45	0.48
108.37	0.64
107.99	1.74
106.46	5.93
104.48	10.94
102.40	15.73
100.25	20.32
98.04	24.79
95.80	29.18
93.54	33.49
91.23	37.70
88.86	41.76
86.43	45.67
83.94	49.42

Table 1 (***Continued.***)

X (mm)	Y (mm)
81.41	53.07
78.88	56.72
76.34	60.34
73.70	63.73
70.96	66.85
68.12	69.73
65.20	72.39
62.19	74.85
59.10	77.10
55.94	79.16
52.70	81.04
49.39	82.73
46.69	83.96
43.25	85.33
39.75	86.56
36.21	87.68
33.33	88.44
30.39	89.08
27.41	89.58
24.37	89.96
20.49	90.24
16.55	90.35
12.60	90.45
8.66	90.55
4.71	90.65
1.49	90.73
0.85	90.91
0.34	91.33
0.05	91.93

and the hub displacement, profiled slots were located on the hub wall. It should be mentioned that sealing measure was taken to prevent flow leakage though these slots.

2.2 Instrumentation, Data Acquisition and Reduction. The oscillating blade and one nonoscillating blade are instrumented with pressure tappings at six spanwise sections (10%, 30%, 50%, 70%, 80%, and 95% span sections). At each section, 14 pressure tappings are located on the suction surface (SS) and 10 on the pressure surface (PS), as indicated in Fig. 2. In total, there are 144 tappings on each blade surface. These pressure tappings are used for both steady and unsteady pressure measurements. The instrumented nonoscillating blade is interchangeable with all other stationary blades, thereby enabling both steady and unsteady pressure measurements at all blade positions in the cascade.

In this low-speed test facility, realistic reduced frequencies can be achieved at low frequencies of blade vibration. For example, a nominal frequency of 10.3 Hz here is equivalent to a reduced frequency of 0.4, which is based on the blade chord and exit isentropic velocity. This makes it possible for the unsteady pressure signals to be recorded with off-board pressure transducers. The rig is equipped with five off-board pressure transducers (Sensym 142C01D, 0–1 psi range), so a total of 30 sets of measurements are required for each blade in one test. Unsteady signals from the transducers are recorded on a personal computer (PC) through an Amplicon PC30G data-logging card. The unsteady pressure acquisition procedure is synchronized by a signal from an optical Schmitt trigger.

Table 2 Cascade data and operation conditions

Blade chord, *C*	0.143 m
Blade span, *h*	0.180 m
Pitch length, *S*	0.100 m
Stagger angle	40.0 deg
Inlet flow angle	0.0 deg
Vibration mode	First bending normal to absolute chord
Bending amplitude	3%C at tip, 0.3%C at hub
Reynolds number, Re	2.2×10^5
Reduced frequency, *k*	0.2, 0.4, 0.6
Nominal frequency, *f*	5.2 Hz, 10.3 Hz, 15.5 Hz

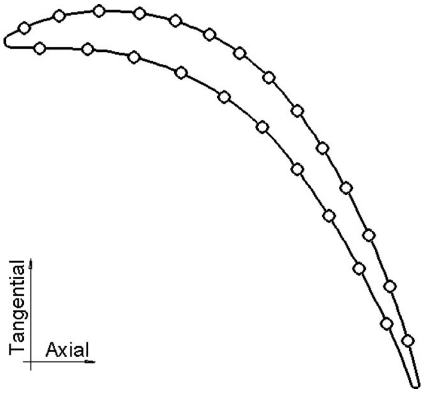

Fig. 2 Pressure tappings

The unsteady pressure signals are ensemble-averaged over 150 periods. The ensemble-averaged unsteady pressure signals are reduced into their harmonic components using a Fourier series. To correct the unsteady pressure signal for phase shift and attenuation, along the tubing lengths, a tubing transfer function (TTF) scheme, proposed by Irwin et al. [13], is applied. The present application of the TTF method follows the procedures of Sims-Williams [14] and Yang and He [9].

Once the unsteady pressure measurements are obtained, on each individual blade, they are superposed to construct the tuned cascade data by utilizing the influence coefficient method. The validity of the method for this case has been validated by examining the convergence of influence coefficients on those blades away from the central oscillating blade and the linearity of the unsteady pressures at different oscillation amplitudes. As described earlier, all influence coefficients have been reduced into their harmonic components. Accordingly, the first harmonic component Cp_1 for a tuned cascade can be expressed as a sum of the first harmonic components $Cp_1(n)$ of influence coefficients from all seven blades:

$$Cp_1 = \sum_{n=-3}^{3} Cp_1(n) e^{-in\sigma} \qquad (1)$$

where n is the blade index number, and σ is the inter blade phase angle. The direction of blade indexing is the same as that of a forward traveling wave (i.e., that of the rotation if the cascade was taken from a turbine rotor) with index 0 denoting the middle reference blade. Consequently, the sign convention for the interblade phase angle (IBPA) is such that a negative IBPA corresponds to a backward traveling wave mode.

2.3 Experimental Results

2.3.1 Steady Flow. The steady flow results are discussed aiming at identifying the main steady flow features. Since the major unsteady pressure response happens on the central three blades, which will be verified later, the steady flow results are, therefore, presented only on the central three blades.

Shown in Figs. 3(*a*)–3(*c*) are the steady flow blade surface pressure distributions for the three middle blades at the flow conditions described in Table 2. The steady flow blade surface pressure measurements were obtained at six spanwise sections from 10% to 95% span. For each blade, the blade surface pressure distributions are almost identical for different spanwise sections, although slight deviations in pressure distribution are observed toward

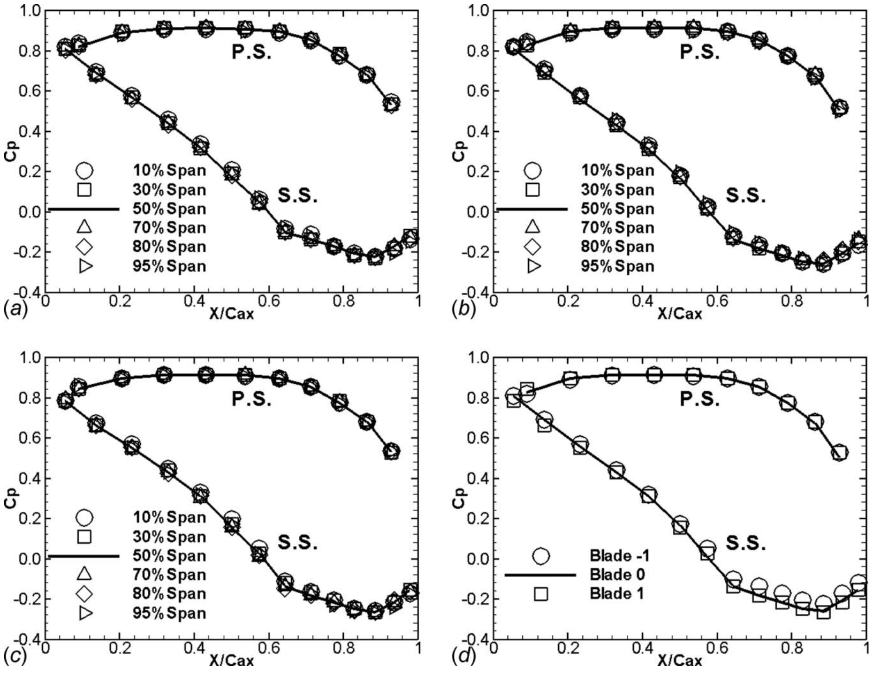

Fig. 3 Steady pressure distributions at six spanwise sections on three central blades. (*a*) Blade −1, (*b*) blade 0, (*c*) blade 1, and (*d*) midspan section

blade ends over the suction surface. These deviations are believed to be associated with the endwall effects with slight unloading present on the suction surface. These slight endwall effects are attributable to the favorable pressure gradient present in the cascade and the relatively small blade deflection angle. Overall, the results indicate that the steady flow blade surface pressure response is predominantly two dimensional.

Figure 3(*d*) shows the comparison of the steady flow blade surface pressure distributions at the midspan section on the three central blades. Because of the predominant two-dimensional feature of the steady flow, this comparison at the midspan section is sufficient to verify the blade-blade periodicity in the cascade. The plot demonstrates an excellent comparison on the pressure surface, while a good comparison is achieved on the suction surface despite some deviation present on the rear half chord of blade −1. Good blade-blade periodicity achieved in the steady flow surely forms a sound basis for the unsteady flows presented hereafter.

2.3.2 Unsteady Flow. To assess the uncertainty of unsteady flow measurements, a series of tests was performed to evaluate the experimental errors and repeatability. In these tests, five tappings were chosen from the 70% span of the oscillating blade to provide a representative range of unsteady pressure response. For each tapping, 40 sets of measurements were obtained, through the experimental procedure described in Sec. 2.2. The results showed that the deviation from mean values fell within a range of ±0.08 for the nondimensional amplitude of the first harmonic pressure and ±5° for the phase angle. The corresponding overall standard deviation is below 0.029 in amplitude and 1.95 deg in phase angle of unsteady pressure coefficients, indicating an excellent level of repeatability.

Pitchwise finiteness is an inherent nature of linear cascade. Therefore, the basic requirement of a linear cascade experiment when using the influence coefficient method is that the unsteady pressure response is to attenuate quickly away from the oscillating blade in the pitchwise direction. This pitchwise convergence in the present linear cascade is to be evaluated herein.

Figure 4 shows the amplitude (normalized by the blade tip bending amplitude) of the first harmonic pressure coefficient at the midspan section on the five middle blades with blade 0 oscillating at a reduced frequency of 0.4 and a tip bending amplitude of 3%*C*. Clearly, the unsteady aerodynamic response converges quickly away from the reference oscillating blade. On the suction surface, the amplitude of the first harmonic pressure on the blade −1 (the immediate neighbor on the pressure surface side of the reference blade) shows the same order of magnitude as that on blade 0, while those on blades +1 and ±2 have an order of mag-

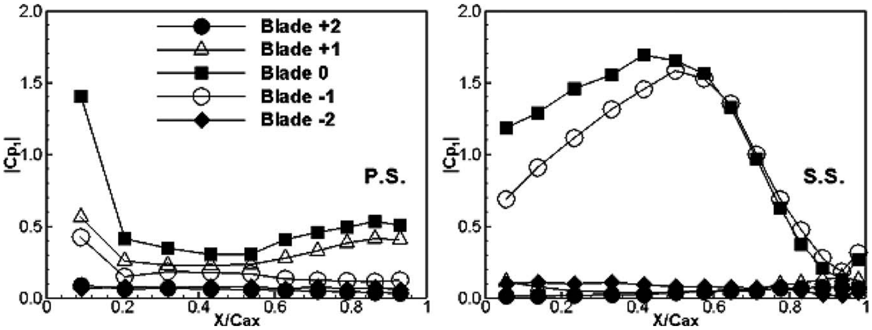

Fig. 4 Unsteady pressure amplitudes on five central blades

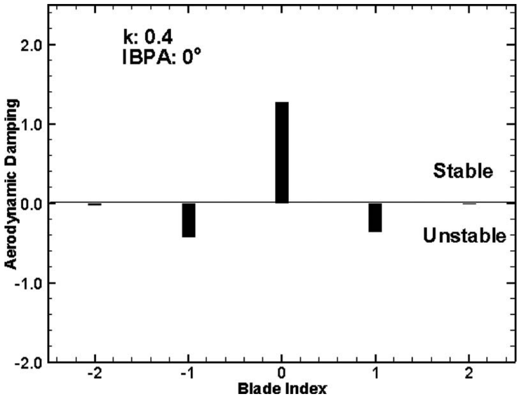

Fig. 5 Experimental test for pitchwise convergence: aerodamping contribution from five central blades ($k=0.4$, IBPA=0 deg)

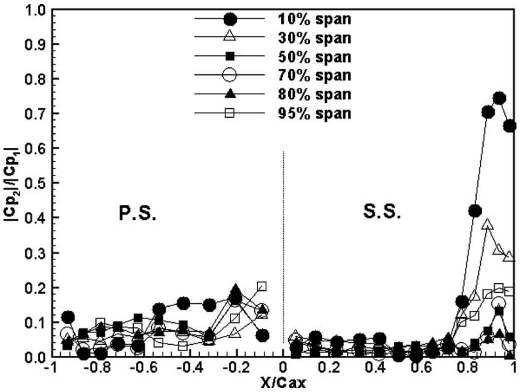

Fig. 7 Experimental test for linearity: relative amplitudes of the second harmonic pressure coefficient at different spanwise sections

nitude lower. On the pressure surface, the main unsteady pressure response happens on blades 0 and ±1 and blades ±2 sense much smaller unsteady disturbance. Figure 5 shows the global aerodynamic damping contributions from the middle five blades to the tuned cascade at a reduced frequency of 0.4 and an IBPA of 0 deg. The oscillating blade exerts the stabilizing contribution (direct term). At this IBPA, the coupling terms do have the destabilizing contributions. For different values of IBPA, the direct term would remain unchanged whereas coupling terms vary as indicated by Eq. (1). From Fig. 5, it is found that aerodynamic coupling effects are mainly from the immediate neighbors (blades ±1) while the contributions from blade ±2 are of negligible magnitudes.

The linearity assumption is the fundamental premise of the application of the influence coefficient method. Moreover, it is a general interest in the unsteady aerodynamic modeling of oscillating blade flows. Two sets of measurements of unsteady pressure response at different oscillating amplitudes were performed, in order to evaluate the linearity assumption of the superposition employed to reconstruct the tuned cascade data. The values of two bending oscillation amplitudes at the blade tip were arbitrarily chosen to be 3% and 5% chord. Figure 6 compares the amplitudes and phase angles of the first harmonic pressure coefficients on the reference blade at these two oscillating amplitudes. The results presented in this figure shows a predominantly linear behavior of the unsteady pressure response with very good agreement in the first harmonic pressure coefficients in terms of both amplitude and phase angle between the two different oscillating amplitudes.

Another measure of linearity of the oscillating blade flows is the relative amplitude of the second harmonic pressure response. Figure 7 presents the amplitudes of the second harmonic pressure coefficients relative to the first on the reference blade for reduced frequency 0.4. At most locations on the suction surface, the amplitudes of the second harmonic pressure reveal to be an order of magnitude lower than those of the first, which indicates a predominant linear behavior of the unsteady pressure response. On the suction surface, high relative amplitudes of the second harmonic pressure aft of 80%*Cax* at the 10% span section, to a less extent at the 30% span section, are evident, while on other spanwise sections, which have much higher bending amplitudes, do not reveal similar behavior. Considering this, the high relative second harmonic pressure response at spanwise sections located near the hub is believed to be most likely arising from a leakage flow through the imperfect hub sealing as well as the relative low pressure response (locally near the hub), rather than indicating a nonlinear unsteady aerodynamic response to the blade oscillation. In addition, low signal-to-noise ratio is expected toward the trailing edge on the suction surface where the amplitude of unsteady pressure is small. On the pressure surface, the amplitudes of the second harmonic pressure are relatively bigger, which certainly is attributable to the smaller amplitude of the unsteady pressure response and accordingly the lower signal-to-noise ratio. Overall, the unsteady pressure response to the blade oscillation is largely linear on both surfaces.

The amplitudes and phase angles of the first harmonic pressure, presented in Figs. 8 and 9, are for an IBPA of −60 deg. This particular IBPA is chosen because it is identified to be the least stable IBPA. The effects of IBPA on the blade stability are shown in Fig. 10.

Figure 8(*a*) shows the amplitudes of the first harmonic pressure on the suction surface. Along the blade span, the amplitude of the first harmonic pressure consistently increases away from the hub except for the area toward the leading edge. However, the increase in the amplitude of the first harmonic pressure is not proportional to the increase in the local vibration amplitude along the span. In

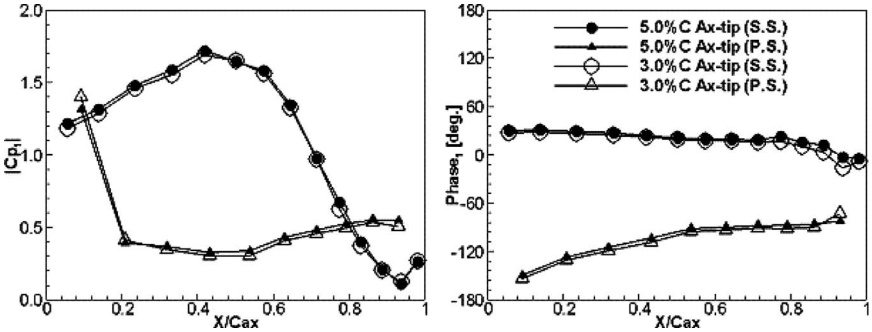

Fig. 6 Experimental test for linearity: first harmonic pressure coefficient at 50% span section on blade 0 at two bending amplitudes ($k=0.4$)

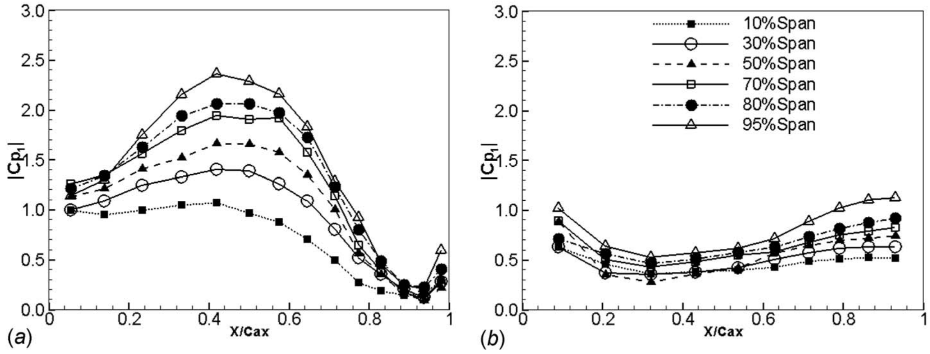

Fig. 8 Amplitudes of first harmonic pressure at IBPA=−60 deg: (*a*) suction surface and (*b*) pressure surface

fact, the amplitude of the first harmonic pressure at 95% span is only about 2.5 times that at 10% span, while the local vibration amplitude at 95% span appears to be five times that at 10% span. This nonproportional unsteady response to the local vibration amplitude, at different blade spans, certainly indicates that the unsteady flow response is of a strong three-dimensional nature. On the pressure surface, displayed in Fig. 8(*b*), a consistent increase in the amplitude along the span height is noticed for a range from 55% chord to the trailing edge. Toward the leading edge, the change of the first harmonic pressure amplitude is not in a clear trend along the span on both surfaces. This behavior may be associated with a high sensitivity to the local incidence. Overall, the presence of unsteady pressure peak around midchord of the suction surface and toward the trailing edge of the pressure surface suggests that the unsteady response is largely driven by the variation of the passage flow area.

In Fig. 9(*a*), the phase angle distributions of the first harmonic pressure along the chord are plotted at six spanwise sections on the suction surface. Apart from the 95% span section, the phase angle shows consistent shift along the chord from 10% to 80% span. The phase angle becomes more diverse near the trailing edge, particularly at 10% and 95% span sections, which may suggest some 3D end wall effects. Also, the influence of the imperfection of endwall sealing should be recognized. The phase angles on the pressure surface (Fig. 9(*b*)) are on the whole insensitive to the local span height.

Figure 10 shows the global aerodynamic damping for three reduced frequencies tested. The global aerodynamic damping, which gives a direct indication of aeroelastic stability, is an overall assessment of the unsteady aerodynamic response to the blade oscillation. It allows easy comparison of the influence of reduced frequency on the unsteady pressure response and direct examination of the variation in aeroelastic stability with regard to the IBPA for each reduced frequency.

Apparently, the variation in the global aerodynamic damping with regard to the IBPA reveals an S-curve shape as expected of a summation of sinusoidal functions for each reduced frequency. The vertical position of the damping S-curve depends on the value of reduced frequency. Generally, it shifts consistently upward as well as rightward as reduced frequency increases. For a reduced frequency 0.2, the present cascade is unstable based on the aerodynamic damping for a range of IBPA from −150 deg to −10 deg. As the reduced frequency increases to 0.4, the cascade is unstable at a small range of IBPA values around −60 deg, whereas the cascade is stable at the whole range of IBPA for a reduced frequency of 0.6.

The damping variation with IBPA is the direct reflection of the aerodynamic coupling between blades. The consequence of the aerodynamic coupling is such that blade flutter only picks up the least stable IBPA, which has the lowest aerodynamic damping. Upon examining the least stable IBPA for different reduced frequencies, it shows a consistent shift as indicated by the bold line in the plot. Indeed, the least stable IBPA is identified to be around −80 deg, −60 deg, and −45 deg for the reduced frequencies of 0.2, 0.4, and 0.6, respectively. This is consistent with a quasi-steady consideration, in which the least stable IBPA should be −90° [15].

3 Computational Study

3.1 Method Description. The computational fluid dynamics (CFD) code used in this study, TF3D, has been developed at University of Durham [16]. It solves the 3D Reynolds averaged unsteady Navier–Stokes equations in time domain. The governing equations are discretized in space using the cell-centered finite volume scheme, together with the blend second- and fourth-order

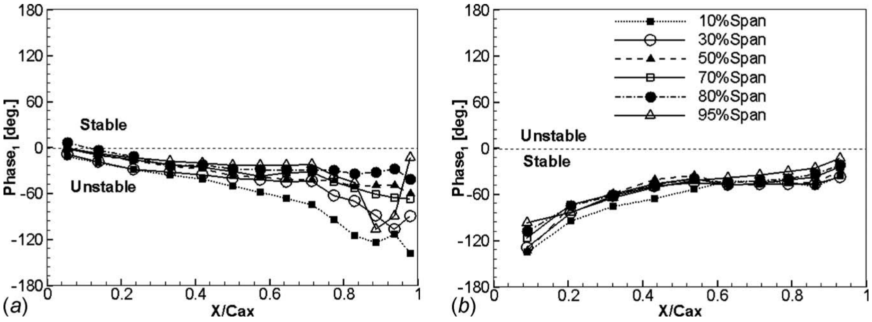

Fig. 9 Phase angles of first harmonic pressure at IBPA=−60 deg: (*a*) suction surface (*b*) and pressure surface

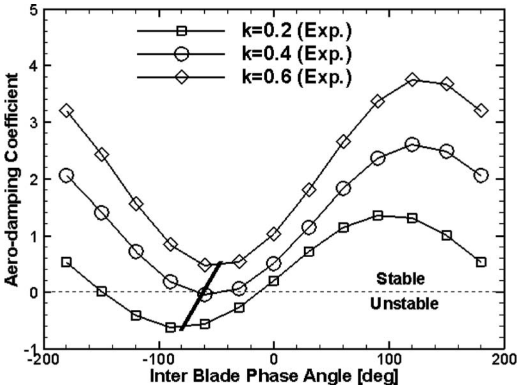

Fig. 10 Global aerodynamic damping at three reduced frequencies (bold line: trend of the least stable IBPA with regard to reduced frequency)

artificial dissipations [17]. Temporal integration of the discretized equations is carried out using the second-order four-step Runge–Kutta approach. The convergence is speeded up by a time-consistent multigrid technique [16,18].

The computational domain consists of a single passage with the blade positioned at the middle of the passage, as shown in Fig. 11. The present single-passage method employs a Fourier decomposition based shape-correction scheme [19] to deal with phase-shifted periodic boundary conditions. The unsteadiness concerned here is induced by the blade harmonic vibration and satisfies a temporal and circumferentially spatial periodicity. Being periodic in time, any flow variable U can be decomposed into a time-averaged part $\bar{U}$ and an unsteady part $\tilde{U}$, which can be approximated by a set of Fourier series in time.

$$U(x,\theta,r,t) = \bar{U}(x,\theta,r) + \tilde{U}(x,\theta,r,t) \tag{2}$$

$$\tilde{U}(x,\theta,r,t) = \sum_{n=1}^{N_{\mathrm{Fou}}} [A_n(x,\theta,r)\sin(n\omega t) + B_n(x,\theta,r)\cos(n\omega t)] \tag{3}$$

where A_n and B_n are the nth order Fourier coefficients; N_{Fou} is the order of the Fourier series; x, θ, and r are the axial, circumferential, and radial coordinates, respectively, and t is the physical time. The phase-shifted periodic conditions are then defined as

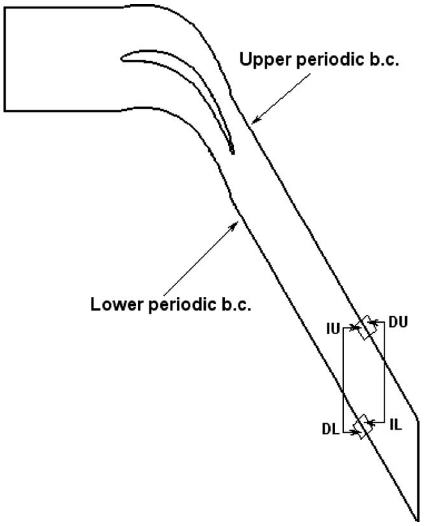

Fig. 11 Single-passage computational domain

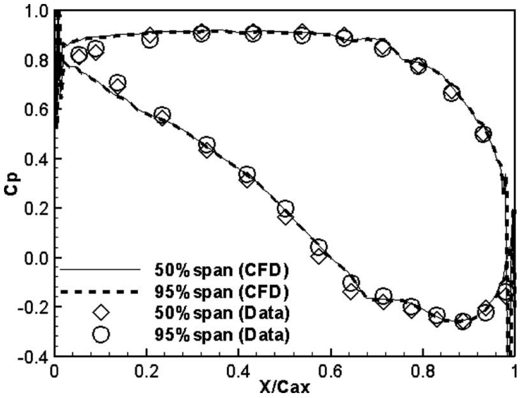

Fig. 12 Steady pressure distributions

$$\tilde{U}(x,\theta \pm G,r,t) = \sum_{n=1}^{N_{\mathrm{Fou}}} [A_n(x,\theta,r)\sin(n(\omega t \pm \sigma)) + B_n(x,\theta,r)\cos(n(\omega t \pm \sigma))] \tag{4}$$

where G is the circumferential angular spacing between two neighboring blades and σ is the IBPA of the unsteadiness.

During the computation, the Fourier coefficients, which are used to approximate the flow variables (Eq. (3)), are stored and updated at the periodic boundary inner cells (IL and IU). To apply periodic boundary conditions, flow variables at the dummy cells (DL and DU) need to be determined at every time step. According to Eq. (4), the flow variables at dummy cells DL and DU are obtained from the stored Fourier coefficients at inner cells IU and IL, respectively.

The shape-correction method is able to deal with multiple disturbances [20] and its applications in multirow configurations can be found in Refs. [21–23]. The computational mesh is of a simple-H type with a density of $107\times41\times51$ nodes in the streamwise, pitchwise, and spanwise directions, respectively. The numerical tests on mesh dependence show that this mesh density is adequate [24].

At the inlet, stagnation parameters and flow angles are specified. At the exit, back pressure is set at a fixed value. It is well known that the density based compressible flow solver is unsuitable to calculate flows of very low Mach number. The flow velocity is therefore elevated to avoid the difficulty. The exit Mach number, prescribed in the calculations, is around 0.3, at which the flow compressibility influence is still negligible. On blade and endwall surfaces, the tangential velocity is allowed to slip but restricted by the wall shear stress, which is determined from an approximation of the logarithmic law [25]. For unsteady computations, the tested reduced frequency is matched and the experimental Reynolds number of 2.2×10^5 retained. The blade oscillating amplitude is, however, reset to 1% chord for a better convergence of solution.

3.2 Comparison of Results. Figure 12 presents the predicted and measured steady flow blade pressure distributions at 50% and 95% span sections. These results are representative of the whole blade surface, at least from 10% to 95% span, and demonstrate good correlation between the measurements and the predictions.

Figures 13 and 14 show the measurements and numerical predictions of the first harmonic pressure obtained at a reduced frequency of 0.4 for the least and the most stable IBPAs, respectively. The results are shown at three spanwise sections. For each section, the left plot is the amplitude and the right is the phase angle of first harmonic pressure. For both the least and most stable IBPAs, the predicted amplitudes of the first harmonic pressure demonstrate very good correlation to the experimental measurements at most locations on both pressure and suction surfaces (see

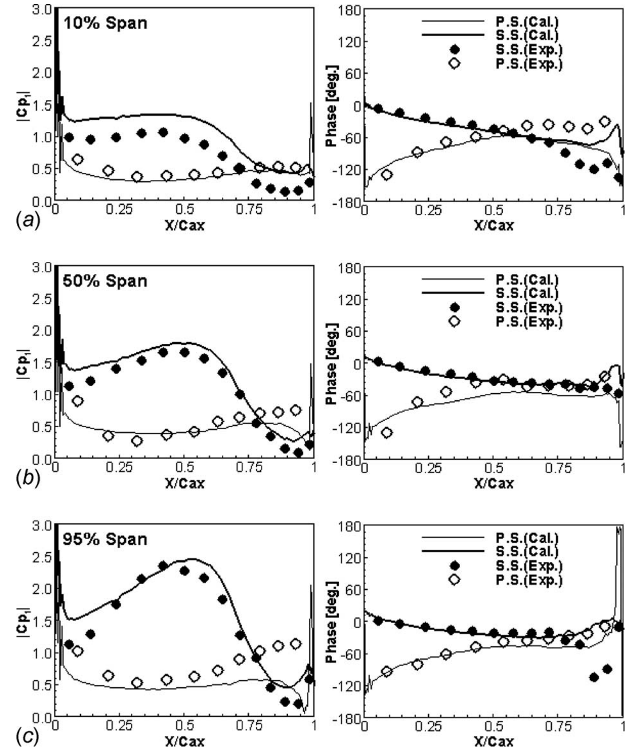

Fig. 13 Amplitude and phase of unsteady pressure at $k=0.4$ and the least stable IBPA ($\sigma=-60$ deg): (*a*) 10% span section, (*b*) 50% span section, and (*c*) 95% span section

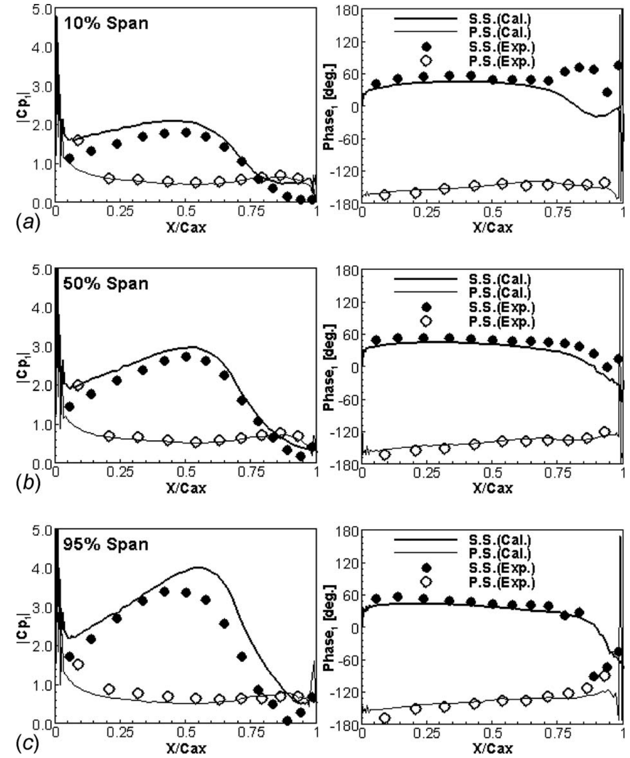

Fig. 14 Amplitude and phase of unsteady pressure at $k=0.4$ and the most stable IBPA ($\sigma=120$ deg): (*a*) 10% span section, (*b*) 50% span section, and (*c*) 95% span section

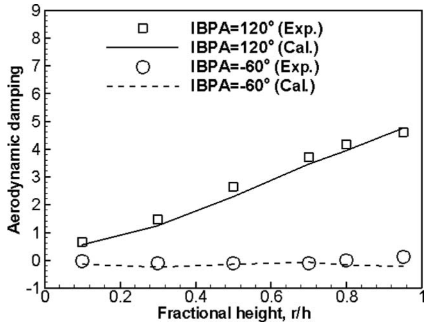

Fig. 15 Aerodamping variation along blade span ($k=0.4$)

Figs. 13 and 14). Discrepancy between the predicted and measured amplitudes of the first harmonic pressure is observed at sections near the cascade endwalls. The predicted phase angles of the first harmonic pressure are in good agreement with the test data over most locations on both pressure and suction surfaces except the area toward the trailing edge.

The predicted and measured variations in local aerodynamic damping along the blade span are presented in Fig. 15 for the least and most stable IBPAs. The local damping gives an aggregate indication of the quality of the amplitude and phase angle prediction of the first harmonic pressure at different spanwise sections. Clearly, this plot shows excellent local damping prediction. The overall aerodynamic damping prediction is shown in Fig. 16 and a good agreement with the data is achieved over the whole range of IBPA, although the predicted damping S-curve has a slight shift from the measured.

4 Effects of Part-Span Shrouds

The cascade has been modified to include 75% span shrouds in blade passages, as shown in Fig. 17. The shroud profile is chosen to be of flat plate for simplicity of application. The specifications of the part-span shrouds are summarized in Table 3. To accommodate the movement of the oscillating blade, small gaps (2 mm) are allowed in the two immediate neighboring passages of the oscillating blade. At the gap location, a thin flexible sliding card is applied to minimize the flow leakage through the gap. It should be noted that, in a real machine, the configuration of part-span shrouds is more complex and the presence of part-span shrouds would cause distortion to the steady flow field and result in aerodynamic loss. With respect to the negative impact of part-span shrouds on the aerothermal performance, it is beyond the scope of the present study. Also, the potential influence of the baseline steady loading change resulting from the presence of part-span shrouds on the unsteady flow response is not included. The simplification made herein is to highlight the interference effects of part-span shrouds on the unsteady pressure propagation in an oscillating cascade with a 3D bending mode.

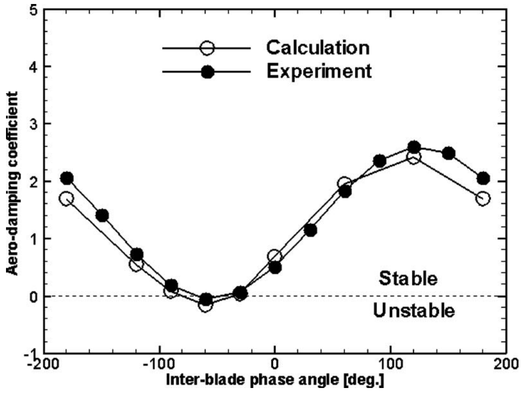

Fig. 16 Overall aerodynamic damping prediction ($k=0.4$)

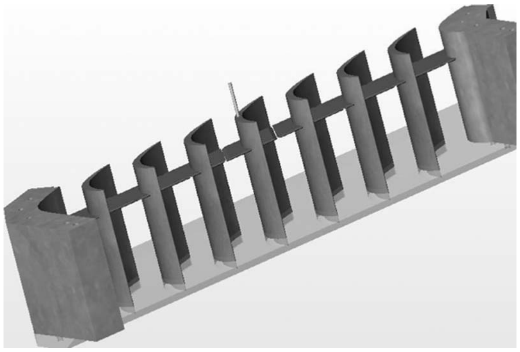

Fig. 17 Part-span shrouded linear turbine cascade (endwall on the blade tip side is removed for clarity)

The shroud modeling is achieved by applying solid wall boundary conditions at shroud surface locations. Figure 18 shows the computational mesh used for the study of effects of part-span shrouds. It consists of 132 nodes in the axial direction, 41 in the pitchwise direction and 51 in the spanwise direction. The mesh clustering is applied toward the shroud location in the spanwise direction and finer mesh spacing is also used around the shroud leading and trailing edges. For the comparison purpose, the same mesh density is utilized in both calculations with and without shrouds to eliminate the influence of mesh dependency on the results. During blade oscillation, the shrouds are assumed to stretch in a plane of constant span height. In other words, the analyzed shroud configuration is otherwise identical to the tested one except that the radial movement of shrouds is neglected. The part-span shroud plates are thin and do not induce noticeable steady pressure loading change on the blade surface. The results presented are, therefore, confined to those for the unsteady flow.

Figure 19 shows the amplitudes of the first harmonic pressure at 50%, 70%, 80%, and 95% span sections for settings with and without part-span shrouds. For each section, the left plot shows the experimental results and the right shows the predictions. Upon inspection of the set of the first harmonic pressure, it is found that the influence of part-span shrouds manifests itself mainly in terms of the change in the pressure amplitude on the suction surface. The presence of the part-span shrouds results in reduced amplitudes for the sections below 75% span and increased amplitudes for those sections above 75% span. It is evident that the computational predictions for settings with and without part-span shrouds reveal exactly the same behavior as that observed in the measurement. This demonstrates the overall validity of the present simple shroud model.

The opposite trends in the amplitude change of the first harmonic pressure for spanwise sections below and above the part-span shrouds reflect a 3D behavior of the unsteady pressure propagation. Recall the observation on the results in Fig. 8 that the amplitude of the first harmonic pressure is nonproportional to the local blade vibration amplitude along the blade span. The basic mechanism is that the spanwise unsteady interaction results in an instantaneous redistribution of the unsteady pressure. The unsteady loading is alleviated toward the tip and enhanced toward the hub, which can be simply regarded as an unsteady "3D relief." The presence of part-span shrouds, on the other hand, blocks a radial propagation of unsteady pressures and hence reduces the 3D unsteady relief effects. Consequently, the amplitude of the first harmonic pressure with part-span shrouds is larger than that of the nominal case for sections above 75% span, whereas the trend in the amplitude change is reversed for sections below 75% span.

Figure 20 shows the phase angles of first harmonic pressure for settings with and without part-span shrouds. Regardless the spanwise locations, the phase angles of the unsteady pressure are largely unaffected.

The overall influence of the part-span shrouds on the blade flutter is indicated by the integrated aerodynamic damping. The experimental data show that the part-span shroud has a small stabilizing effect, and this behavior has been also correctly captured by the CFD results. The differences in the aerodynamic damping as caused the stabilizing effects are, however, comparable to or smaller than the discrepancies between the experimental data and the CFD predictions for the nominal case (as shown in Fig. 16). Hence, the overall influence of the part-span shroud can be regarded as insignificantly small for the present case studied. This is largely due to the fact that the part-span shrouds have predominantly local effects on unsteady pressures and hence the aerodynamic damping.

Table 3 Part-span shroud specification

Thickness	3 mm
Length in axial direction	60 mm
Spanwise location	75% span
Axial location	18–78%*Cax*

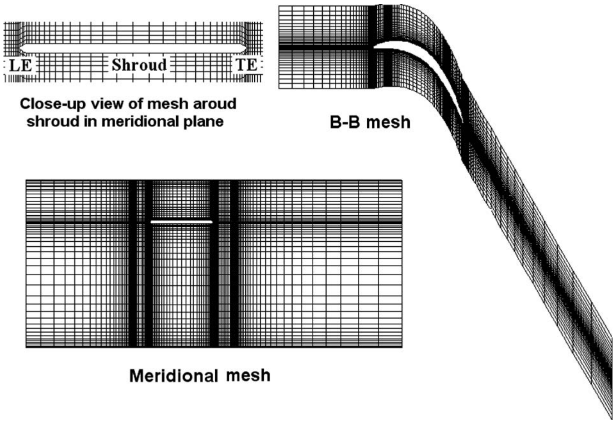

Fig. 18 Mesh used for computation with part-span shrouds

5 Concluding Remarks

A linear oscillating turbine cascade is investigated experimentally and computationally. Detailed unsteady pressure measurements are made at six spanwise sections from 10% to 95% blade height. The steady pressure coefficient distributions reveal a predominant 2D steady background flow, while the unsteady pressure results demonstrate a strong 3D behavior of unsteady pressure response to a three-dimensional blade flapping oscillation. The computational solutions are obtained from a 3D unsteady time-marching Navier–Stokes flow solver using a single-passage domain. The computational results are in good agreement with experimental data.

A further study is performed to investigate the influence of the aerodynamic blockage that is introduced by the application of part-span shrouds, on the blade flutter characteristics in the linear turbine cascade with the same blade oscillation mode shape. The part-span shrouds are positioned at 75% span height. Notable variations in local unsteady pressure at spanwise sections near the shroud location, as shown in the experimental data, are well captured by the computational method with a simple part-shroud model. The influence of the aerodynamic blockage associated with the part-span shrouds on the overall aerodynamic damping, however, seems insignificant for the present cascade.

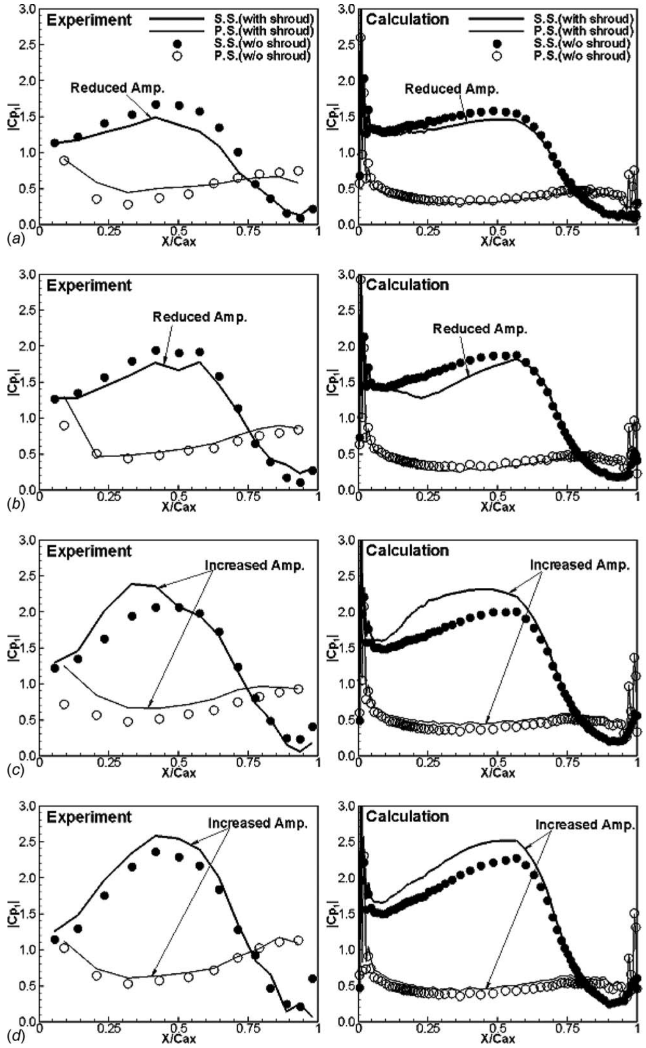

Fig. 19 Effects of part-span shrouds on amplitude of the unsteady pressure response. Left: experiment. Right: calculation ($k=0.4$, $\sigma=-60$ deg): (*a*) 50% span section, (*b*) 70% span section, (*c*) 80% span section, and (*d*) 95% span section.

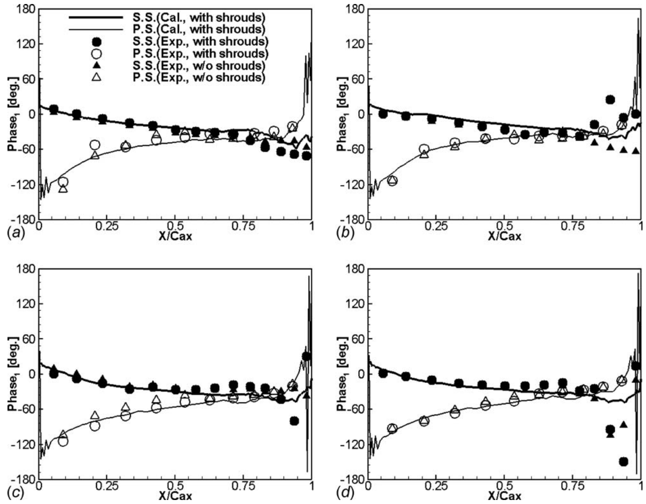

Fig. 20 Phase angle of first harmonic pressure for settings with and without part-span shrouds: (*a*) 50% span section, (*b*) 70% span section, (*c*) 80% span section, and (*d*) 95% span section

Acknowledgment

This work was carried out at University of Durham, Durham UK, sponsored partially by ALSTOM Power Ltd, which is gratefully acknowledged. The authors would also like to thank Dr. Peter Walker (ALSTOM) for continued interest and technical discussions

Nomenclature

Ax = bending amplitude, nondimensionalized with chord
Ax_{tip} = bending amplitude at blade tip, nondimensionalized with chord
Ap_1 = amplitude of the first harmonic pressure, Pa
C = blade chord length
Cax = axial blade chord length
Cp = blade surface pressure coefficient, $Cp=(P-P_2)/(P_{01}-P_2)$
$|Cp_1|$ = amplitude of the first harmonic pressure coefficient, $|Cp_1|=Ap_1/(P_{01}-P_2)Ax_{\text{tip}}$
h = blade span, m
k = reduced frequency, $k=\omega C/V_{\text{ref}}$
P_2 = exit static pressure
P_{01} = inlet stagnation pressure
Re = Reynolds number
S = pitch length
V_{ref} = reference (isentropic exit) velocity, m/s, $V_{\text{ref}}=\sqrt{2(P_{01}-P_2)/\rho}$
x = axial coordinate, m
θ = circumferential coordinate, deg
ϕ = phase angle, deg
σ = IBPA, deg
ω = angular frequency, rad/s
ξ = aerodynamic damping coefficient, $\xi=1/h\int_0^h \xi_l dr$
ξ_l = local aerodynamic damping coefficient, $\xi_l=\int_C(-\pi\cdot Ax_l|Cp_1|\sin(\phi_1))/C\cdot Ax_{\text{tip}}ds$

Subscript

1 = inlet parameter; first harmonic
2 = exit parameter; second harmonic

References

[1] Gerolymos, G. A., 1993, “Advances in the Numerical Integration of the Three-Dimensional Euler Equations in Vibrating Cascades,” ASME J. Turbomach., **115**, pp. 781–790.
[2] Hall, K. C., and Clark, W. S., 1993, “Linearized Euler Predictions of Unsteady Aerodynamic Loads in Cascades,” AIAA J., **31**, pp. 540–550.
[3] He, L., and Denton, J. D., 1994, “Three-Dimensional Time-Marching Inviscid and Viscous Solutions for Unsteady Flows Around Vibrating Blades,” ASME J. Turbomach., **116**, pp. 469–475.
[4] Vahdati, M., and Imregum, M., 1994, “Nonlinear Aeroelasticity Analysis Using Unstructured Dynamic Meshes,” Symposium on Unsteady Aerodynamics and Aeroelasticity of Turbomachines, Fukuoka, Japan, Sept.
[5] Bölcs, A., and Fransson, T. H., 1986, “Aeroelasticity in Turbomachines Comparison of Theoretical and Experimental Cascade Results,” Communication du Laboratoire de Thermique Applique et de Turbomachines, Ecole Polytechnique Federale de Lausanne, Report No. 13.
[6] Buffum, D. H., Capece, V. R., King, A. J., and El-Aini, Y. M., 1998, “Oscillating Cascade Aerodynamics at Large Mean Incidence,” ASME J. Turbomach., **120**, pp. 122–130.
[7] Lepicovsky, J. and McFarland, E. R. and Capece, V. R. and Hayden, J., 2002, “Unsteady Pressures in a Transonic Fan Cascade Due to a Single Oscillating Airfoil,” ASME Paper No. GT2002-30312.
[8] Bell, D. L., and He, L., 2000, “Three-Dimensional Unsteady Flow for an Oscillating Turbine Blade and the Influence of Tip Leakage,” ASME J. Turbomach., **122**, pp. 93–101.
[9] Yang, H., and He, L., 2004, “Experimental Study on Linear Compressor Cascade With Three-Dimensional Blade Oscillation,” J. Propul. Power, **20**(1), pp. 180–188.
[10] Vogt, D. M., 2005, “Experimental Investigation of Three-Dimensional Mechanisms in Low-Pressure Turbine Flutter,” Ph.D. thesis, Royal Institute of Technology, Sweden.
[11] Vogt, D. M., and Fransson, T. H., 2004, “Effect of Blade Mode Shape on the Aeroelastic Stability of a LPT Cascade,” presented at the Ninth National Turbine Engine High Cycle Fatigue (HCF) Conference, Pinehurst, NC, Mar.
[12] Hanamura, Y., Tanaka, H., and Yamaguchi, Y., 1980, “A Simplified Method to Measure Unsteady Forces Acting on the Vibrating Blades in a Cascade,” Bull. JSME, **23**(180), pp. 880–887.
[13] Irwin, H. P. A. H., Cooper, K. R., and Girard, R., 1979, “Correction of Distortion Effects Caused by Tubing Systems in Measurements of Fluctuation Pressures,” J. Wind. Eng. Ind. Aerodyn., **5**, pp. 93–107.
[14] Sims-Williams, D. R., 2001, “Self-Excited Aerodynamic Unsteadiness Associated With Passenger Cars,” Ph.D. thesis, School of Engineering, University of Durham, Durham.
[15] Huang, X. Q., He, L., and Bell, D. L., 2008, “Effects of Tip Clearance on Aerodynamic Damping in a Linear Turbine Cascade,” J. Propul. Power, **24**, pp. 26–33.
[16] He, L., 2000, “Three-Dimensional Unsteady Navier–Stokes Analysis of Stator-Rotor Interactions in Axial-Flow Turbines,” Proc. Inst. Mech. Eng., Part A, **214**, pp. 13–22.
[17] Jameson, A., 1983, “Numerical Solution of the Euler Solution for Compressible Inviscid Fluids,” Princeton University, Report No. MAE 1643.
[18] He, L., 1993, “New Two-Grid Acceleration Method For Unsteady Navier–Stokes Calculations,” J. Propul. Power, **9**(2), pp. 272–280.
[19] He, L., 1990, “An Euler Solution for Unsteady Flows Around Oscillating Blades,” ASME J. Turbomach., **112**, pp. 714–722.
[20] He, L., 1992, “Method of Simulating Unsteady Turbomachinery Flows With Multiple Perturbations,” AIAA J., **30**(11), pp. 2730–2735.
[21] Li, H. D., and He, L., 2005, “Blade Aerodynamic Damping Variation With Rotor-Stator Gap: A Computational Study Using Single-Passage Approach,” ASME J. Turbomach., **127**, pp. 573–579.
[22] Li, H. D., and He, L., 2005, “Toward Intra-Row Gap Optimization for One and Half Stage Transonic Compressor,” ASME J. Turbomach., **127**, pp. 589–598.
[23] Huang, X. Q., He, L., and Bell, D. L., 2006, “Influence of Upstream Stator on Rotor Flutter Stability in a Low Pressure Steam Turbine Stage,” Proc. Inst. Mech. Eng., Part A, **220**, pp. 25–35.
[24] Huang, X. Q., 2006, “Three-Dimensional Unsteady Flow in Oscillating Turbine Blade Row,” Ph.D. thesis, University of Durham, Durham.
[25] Denton, J. D., 1992, “The Calculation of Three-dimensional Viscous Flow Through Multistage Turbomachines,” ASME J. Turbomach., **114**, pp. 18–26.

Experimental Investigation of Flow Field Structure in Mixing Tee

Seyed Mohammad Hosseini
Department of Energy,
Division of Fluid Mechanics,
Lund University,
Lund 22100, Sweden
e-mail: seyed_mohammad.hosseini@energy.lth.se

Kazuhisa Yuki

Hidetoshi Hashizume

Department of Quantum Science and Energy,
Tohoku University,
6-6-01 Aza-Aoba, Aramaki,
Sendai 980-8579, Japan

T-junction is one of the familiar components in the cooling system of power plants with enormous capability of high-cycle thermal fatigue. This research investigates the structure and mixing mechanism of turbulent flow in a T-junction area with a 90 deg bend upstream. According to the wide distribution of turbulent jets in the T-junction, a re-attached jet was selected previously as the best representative condition with the highest velocity fluctuation and the most complex structure. For considering the mixing mechanism of re-attached jet, T-junction is subdivided into few lateral and longitudinal sections, and each section is visualized separately by particle image velocimetry technique. Corresponding to the experimental data, the branch flow acts as a finite turbulent jet, develops the alternative type of eddies, and causes the high velocity fluctuation near the main pipe wall. Three regions are mainly subject to maximum velocity fluctuation: the region close to the jet boundaries (fluctuation mostly is caused by Kelvin–Helmholtz instability), the region above the jet and along the main flow (fluctuation mostly is caused by Karman vortex), and the re-attached area (fluctuation mostly is caused by changing the pressure gradient in the wake area above the jet). Finally, the re-attached area (near the downstream of wake area above the jet) is introduced as a region with strongest possibility to high-cycle thermal fatigue with most effective velocity fluctuation on the main pipe wall above the branch nozzle. [DOI: 10.1115/1.3112383]

Keywords: fluid mixing structure and interaction, mixing tee, PIV, piping system, turbulent flow

1 Introduction

This research investigates fluid mixing phenomena and turbulent jet structure in a T-junction area with a 90 deg bend upstream to understand the basic mechanism of high-cycle thermal fatigue. The problem of thermal fatigue occurs in the pipes where two flows with different temperatures mix together. The T-junction is one of the familiar components with a considerable potential of thermal fatigue and is used in many thermohydraulic systems such as combustion engines, turbines, exhaust systems, hydraulics-pneumatics, and reheat systems. With due attention to the importance of thermal striping phenomenon in the T-junction area, several experiments and analyses have been performed such as the evaluation of the thermal fatigue by Faidy [1], the numerical simulation of the mixing phenomenon by Tanaka [2], the analysis of the flow field structure by Igarashi [3], and the LES study of the high-cycle temperature fluctuation by Hu and Kazimi [4]. These researches consider the T-junction as a single component. Since usually the T-junction is connected to other apparatuses in the piping systems, the 90 deg bend is chosen as one of the common components in most piping systems and it was also connected in the upstream of the T-junction in some familiar leakage accidents of power plants such as Phenix and Civaux in France. A secondary flow is formed by this 90 deg bend and has strong effects on the flow field along with the mixing mechanism. These effects were studied previously by Hosseini and Yuki [5–7]. The interaction between main and branch flows including the effects of secondary flow formed an unstable area above the branch nozzle. This area was shown to be highly loaded and subjected to the temperature fluctuation due to some experimental and numerical researches [8,9]. Depending on the momentum ratio of the branch flow to the main flow, mainly four different types of turbulent jets were identified by Hosseini and Yuki [10] such as wall jet, re-attached jet, turn jet, and impinging jet. Some parameters had main impact on the classification of turbulent jets, namely, secondary flow, temperature difference, pipe geometries, velocity ratio, and momentum ratio. These parameters were defined experimentally by Yuki et al. [11], and the following results were pointed out: The turn jet has the lowest velocity fluctuation near the wall, the 90 deg bend has positive effects for decreasing fluctuation near the main pipe wall, and connecting the branch pipe closer to the bend helps decrease the velocity fluctuation near the wall as well as using a bend with lower curvature ratio.

After evaluating and categorizing many flow patterns in the T-junction, the fluid mixing condition of re-attached jet showed the most complex structure and mechanism in comparison with the other turbulent jets and was selected to provide the precise mechanism of velocity fluctuation. It was difficult to completely figure out the transport mechanism of turbulent flow toward the wall only by the information of the whole flow field so the measuring area was subdivided into small regions to get more accurate close-up data. This close-up measurement method was really helpful in explaining the turbulent wall flow in great detail. According to the strong effect of secondary flow on the mixing mechanism, several lateral sections beside the longitudinal sections are visualized. The interaction between the main and the branch flows creates the complex turbulent structure including the wide distribution types of eddies. The branch jet has three parts based on the theory of turbulent jets by Abramovich [12] such as main, transitional, and initial parts. The initial part is formed by the potential core of jet and acts as flexible obstacle against the main flow. Unsteady separation flow over the bluff body of initial part develops some vortices that look like Karman vortices. The steep velocity gradient between the main and the branch flows in both

---

Contributed by the Fluids Engineering Division of ASME for publication in the Journal of Fluids Engineering. Manuscript received February 13, 2008; final manuscript received February 25, 2009; published online April 13, 2009. Assoc. Editor: Juergen Kompenhans. Paper presented at the 2007 ASME Fluids Engineering Division Summer Meeting and Exhibition (FEDSM2007), San Diego, CA, July 30–August 2, 2007.

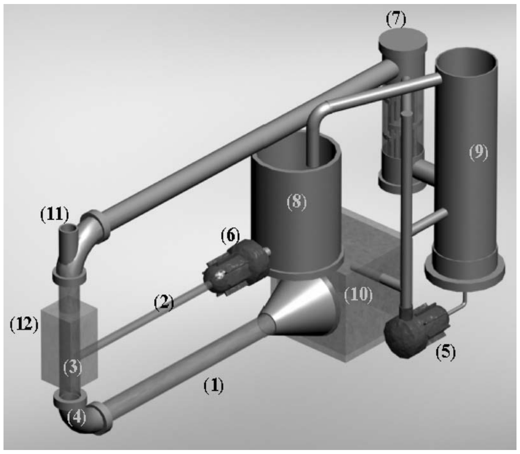

Fig. 1 Experimental apparatuses: (1) main pipe, (2) branch pipe, (3) tee junction, (4) 90 deg bend, (5) main pump, (6) branch pump, (7) heat exchanger, (8) heating tank, (9) mixing tank, (10) straightener tank, (11) measuring window, and (12) water jacket

initial and transient parts of jet causes Kelvin–Helmholtz instability and creates the high vorticity field in the same area. In addition there are many other eddies in the downstream of T-junction that mainly are created by the following mechanisms: the oscillation of the flexible body of jet in the transitional part caused by the frequent drag and lift forces, the structure-interaction between the flow and piping system, the secondary flow created by 90 deg bend in the upstream, the self-developing behavior of turbulent jet in the main part, etc. Finally, the T-junction area was subdivided into few regions based on their intensity of velocity fluctuation near the wall, and the turbulent behavior of the most intense region was analyzed in more detail along with the fluctuation mechanism.

2 Experimental Apparatuses

Figure 1 shows experimental apparatuses including the fluid cycle system to mix two fluids with different physical properties. The mixing area is T-shaped with two main and branch acrylic pipes that connect to each other at the right angle with 3 mm thick and square edged. The main pipe diameter, D_m, is 108 mm and the branch pipe diameter, D_b, is 21 mm. The main pipe runs vertically upward in the test section, which is connected to a measuring window downstream for visualizing the lateral flow field. The 90 deg bend is installed in the upstream of the T-junction. This bend is a stainless steel with 1.41 curvature ratio. There is a straightener tank (which is made of acrylic plates with $30\times30\times30$ cm^3 size) to straighten the main flow before it is injected to a long main pipe and the bend $(13D_m)$, respectively. The branch pipe is also long enough $(60D_b)$ to inject fully-developed flow into the mixing area. The mixing tank is placed to insert small tracers and remove bubbles in the main cycle. This tank is connected to other apparatuses with five pipe connections (heat-exchanger pipe, emergency inlet pipe, heating tank pipe, main pump pipe, and drying outlet pipe). There are two main and branch pumps with 600 l/min and 75 l/min maximum flow rates. The mean velocity of these flows is adjusted by a flow-rate control valve and an inverter individually. A heat-exchanger is used to control the inlet temperature of the main flow and the branch flow in the mixing tee and it is set behind the mixing tank. The heat-exchanger has a secondary cooling system for decreasing the temperature with city water, and the flow is controlled by the inlet heat-exchanger valve. There is a cube water jacket around the T-junction, which is made of acrylic plates the same as the piping material to decrease the effect of refraction on light through the pipe wall during the visualization of longitudinal sections.

3 Experimental Conditions and Analysis Methods

The particle image velocimetry (PIV) system is used to visualize the flow field in the T-junction area with water as the working fluid. In this system, the velocity vectors are derived from subsections of the target area of the particle-seeded flow by measuring the movement of particles between two light pulses. The flow is illuminated in the target area with a light laser sheet. The camera is able to capture each light pulse in separate image frames. Once a sequence of two light pulses is taken, the images are divided into small subsections called interrogation areas. The interrogation areas from each image, frames 1 and 2, are cross correlated with each other pixel by pixel. The correlation produces a signal peak, identifying the common particle displacement. An accurate measure of the displacement—and thus also the velocity—is achieved with subpixel interpolation. A velocity vector map over the whole target area is obtained by repeating the cross-correlation for each interrogation area over the two image frames captured by the charge coupled device (CCD) camera. The correlation of the two interrogation areas, frames 1 and 2, results in the particle displacement represented by a signal peak in the correlation.

The number of particles in the flow is important for obtaining a good signal peak in the cross-correlation. As a rule of thumb, 10–25 particle images should be seen in each interrogation area. When the size of the interrogation area, the magnification of the imaging, and the light-sheet thickness are known, the measurement volume can be defined. Setting up a PIV measurement, the side length of the interrogation area d and the image magnification s_m are balanced against the size of the flow structures to be resolved. One way of expressing this is to require the velocity gradient to be small within the interrogation area:

$$\frac{s_m \,.\, |U_{\max} - U_{\min}| \cdot \Delta t}{d} < 5\% \tag{1}$$

The highest measurable velocity is constrained by particles traveling further than the size of the interrogation area within the time, Δt. The result is a lost correlation between the two image frames and thus loss of velocity information. As a rule of thumb,

$$\frac{s_m \cdot U \cdot \Delta t}{d} < 25\% \tag{2}$$

In this research, two conditions are selected to visualize the flow field: whole flow field (long-shot) and close-up flow field with 150×150 mm^2 and 60×60 mm^2 view sections, respectively. The resolution of each section is 1018×1008 pixels. The interrogation cell is basically divided into 64×64 pixels at each segment for measuring whole flow field and 32×32 pixels for measuring close-up area with 50% area overlap and 100 μs time intervals. The cross section is visualized into two velocity matrices. Both matrices have 30×29 arrays when 64×64 pixels cross correlated is used and have 62×59 arrays when 32×32 pixels cross correlated is used. The laser sheet thickness is 1–3 mm with 200 mJ energy level based on the three parameters such as visualization area, amount of tracer in the fluid, and distance between visualization cross section and the camera's lens. Two kinds of tracer with different diameters are selected, both made from nylon powder with 1.03 g/cm^3 density. The tracer with a diameter of 80 μm is used for visualizing the whole flow field and the tracer with a diameter of 20 μm for close-up flow field condition. The camera starts to shoot at 30 Hz trigger input frequency whose frame rate is 30 fps, and two images are captured in the rapid succession by the camera in the triggered double exposure mode. Each shot captures 99 images continually, and 49 velocity vector maps are obtained with 0.03 s time separation. Five shots are taken, and a total of 240 frames in the each condition is used for evaluating both flow fields. In all experimental conditions, the measurement is done several times and is calibrated really skillfully. There were not any error vector in the experimental data and data are evaluated without using any filtering, masking, smooth-

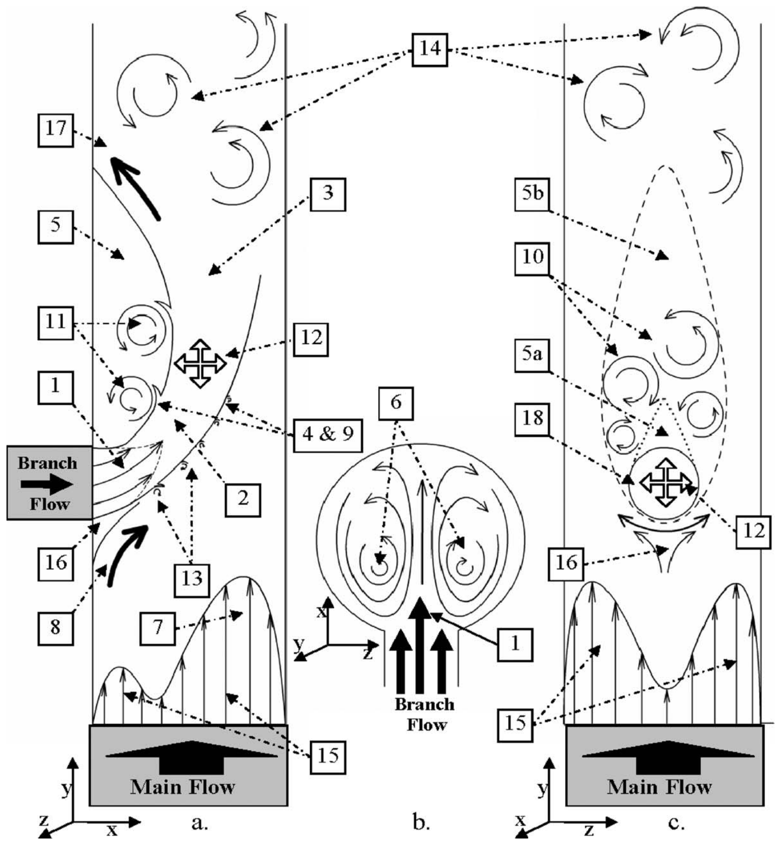

Fig. 2 Flow field structure: (*a*) longitudinal section, parallel to the jet, (*b*) lateral section, and (*c*) longitudinal section, perpendicular to the jet; (1) initial part of the jet, (2) transitional part of the jet, (3) main part of the jet, (4) Kelvin–Helmholtz instability, (5) wake area, (6) secondary flow twin vortex, (7) high velocity area, (8) main flow turning area, (9) interface, (10) vortices act as Karman vortex, (11) large wake eddies, (12) moving cross section of the jet, (13) small eddies, (14) large eddies in the downstream, (15) main flow blow jet, and (16) small area below jet

ing, and peak locking during the process and analysis.

The average flow field and the intensity of velocity fluctuation are evaluated by the following equations:

$$U_{\mathrm{ave}} = \frac{1}{n}\sum_{i}^{n} \sqrt{(u_{r,j}^2 + u_{z,i}^2)} \tag{3}$$

$$s_j = \left(\frac{1}{n}\sum_{i=1}^{n} (u_{j,i} - \overline{u_j})^2\right)^{1/2} \tag{4}$$

$$U_{\mathrm{mix}} = \sqrt{(U_b^2 + U_m^2)} \tag{5}$$

$$I = \sqrt{(s_r + s_z)/2}/U_{\mathrm{mix}} \tag{6}$$

Here, $u_{r,i}$ and $u_{z,i}$ represent the instantaneous radial and axial velocities at the i frame, U_{ave} is the averaged absolute velocity, and n is the total number of the frames. U_b and U_m represent the branch and main velocities, respectively, and s_r and s_z are the standard deviations of the velocity variation in the radial and axial directions. I represents the intensity of velocity fluctuation.

4 Results and Discussion

The mixing mechanism of two fluids in the T-junction is researched by visualizing the flow field instantaneously, and the schematic structure of this mixing is drawn in Fig. 2.

In this figure the different parts of the flow field are numbered, and the experiment related to each part is described in the following paragraphs. To have comprehensive evaluation of every part, the T-junction area is subdivided in the several lateral and longitudinal sections (A, B, C1, C2, C3, and C4), as shown in Fig. 3, and each section is visualized separately with high accuracy. All these experiments are done under the re-attached jet condition

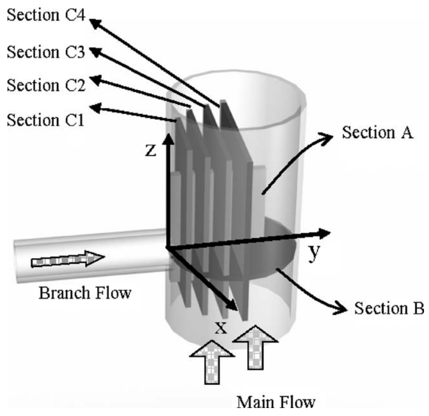

Fig. 3 Positions of lateral and longitudinal sections to visualize the flow field

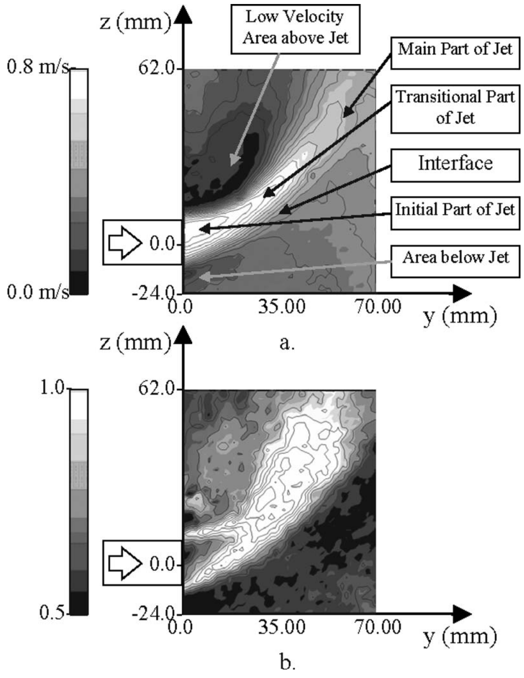

Fig. 4 Flow field in longitudinal section A: (*a*) average velocity distribution and (*b*) intensity of velocity fluctuation

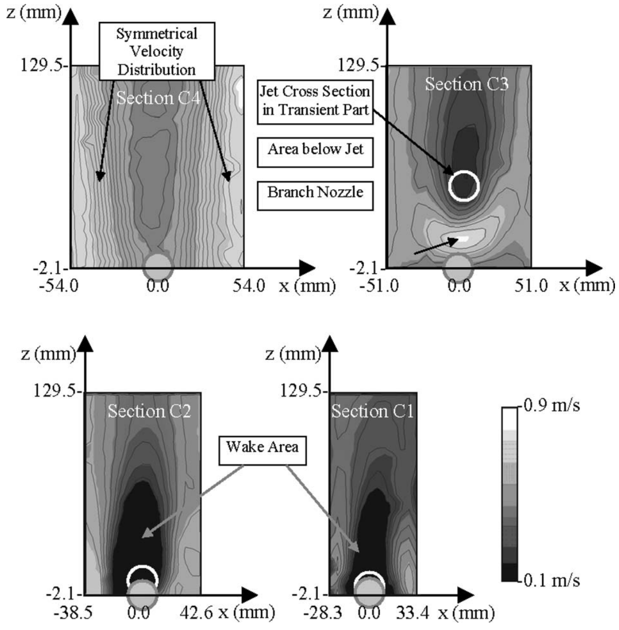

Fig. 5 Average velocity distributions in different longitudinal sections

with almost same branch and main velocities and different Reynolds numbers (Re=53,000 and 10,000, respectively). The complexity of this condition is the basic purpose for choosing it, which was studied previously by Hosseini and Yuki [10].

Figure 4 shows the average velocity distribution and the velocity fluctuation in the longitudinal section A with 0.48 m/s main velocity and 0.47 m/s branch velocity. The different parts of branch jet are easily recognizable in this figure with almost the same structure as the one introduced by Abramovich [12]. The first part is the wedge shape region including the potential core that is called the initial part with the minimum velocity fluctuation and the highest instability compared with other parts. The second part of the branch jet is the transitional part that is distributed from the edge of the initial part to the upright direction along the branch jet axis. The cross section of this area becomes larger in the downstream, and the jet in this part has a flexible structure against the main flow. The main part of the jet is the last part and spreads from the transitional part of the jet to the long downstream. This part is the most flexible, unstable, and self-developed. There is an interface that is raised by the steep velocity gradient between the main flow and the jet in the initial and transient parts. The nature of the interface is caused by the viscous shearing force of two fluids with different velocities, and its thickness depends on the boundary condition in each part. The wake area above the jet has the most steep velocity gradient and has strong temperature fluctuation effects in the case of nonisothermal mixing fluids, and if the interface touches the main pipe wall frequently then it can cause the high-cycle thermal fatigue. The effect of temperature fluctuation on the wall is studied previously by several research groups such as Hosseini and Yuki [10], Yuki et al. [11], Metzner and Wilke [8], and Chapuliot and Gourdin [9].

Figure 5 presents the average velocity distribution in four longitudinal sections (C1, C2, C3, and C4). The main flow is distributed almost symmetrically in all sections, and the cross section of the branch jet and the wake area above it become more visible by getting closer radially to the branch pipe nozzle from section C4 to section C1. The intensity of velocity fluctuation is calculated in the same longitudinal sections, as drawn in Fig. 6. The fluctuation is minor in the region with highest velocity because of instability's law and it is large in the region around the jet along with the edge of the wake area because of the variation in steep velocity gradient.

Figure 7 shows the velocity distribution and the velocity fluctuation of secondary flow in the lateral section B. The symmetrical twin vortex—indicated by the average velocity vectors in Fig. 7(*a*) and basically created by the 90 deg bend in the upstream—has strong effects on the flow field in the mixing area. Three main high velocity regions are observed as well as a high velocity fluctuation region between twin vortices in the lateral section.

The mixing progress will be monitored better by analyzing every frame of the time series data repeatedly. Figure 8 describes four continual velocity vector frames with 0.03 s time separation

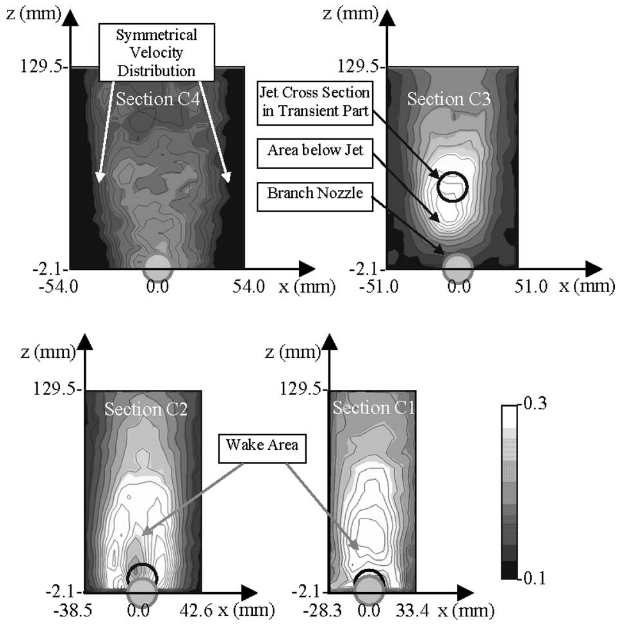

Fig. 6 Intensity of velocity fluctuation in different longitudinal sections

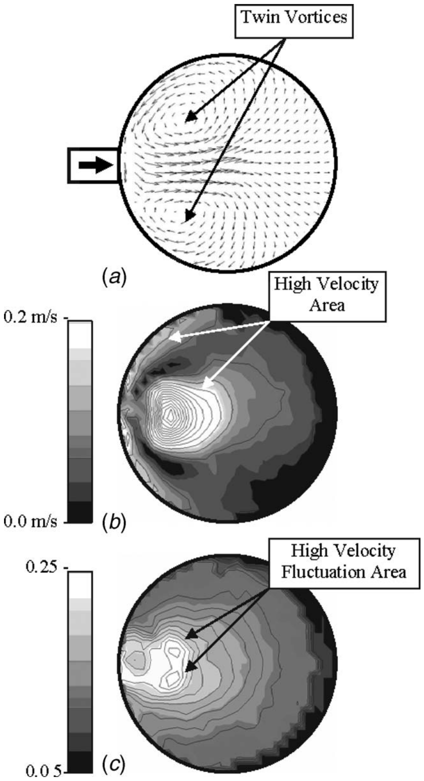

Fig. 7 Lateral section B: (*a*) average velocity vectors, (*b*) mean velocity distribution, and (*c*) intensity of velocity fluctuation

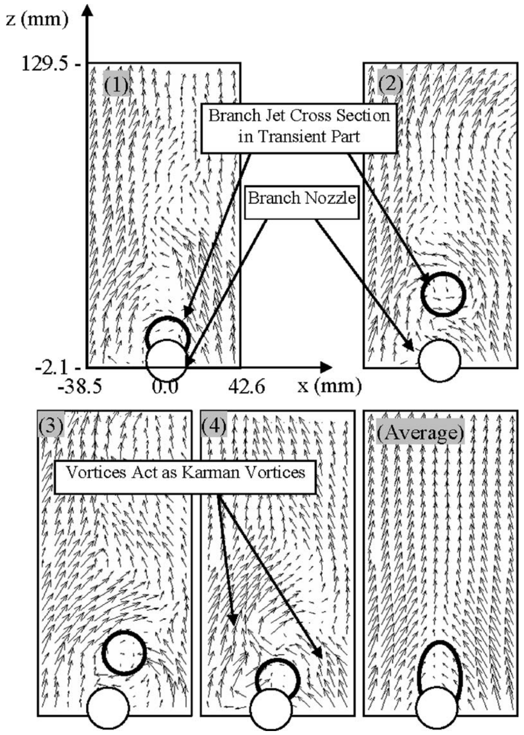

Fig. 8 Velocity vectors of time series and average flow field above the jet in C2 section (t=0.03 s, four continual frames, average of 240 frames, U_b=0.47 m/s, and U_m=0.485 m/s)

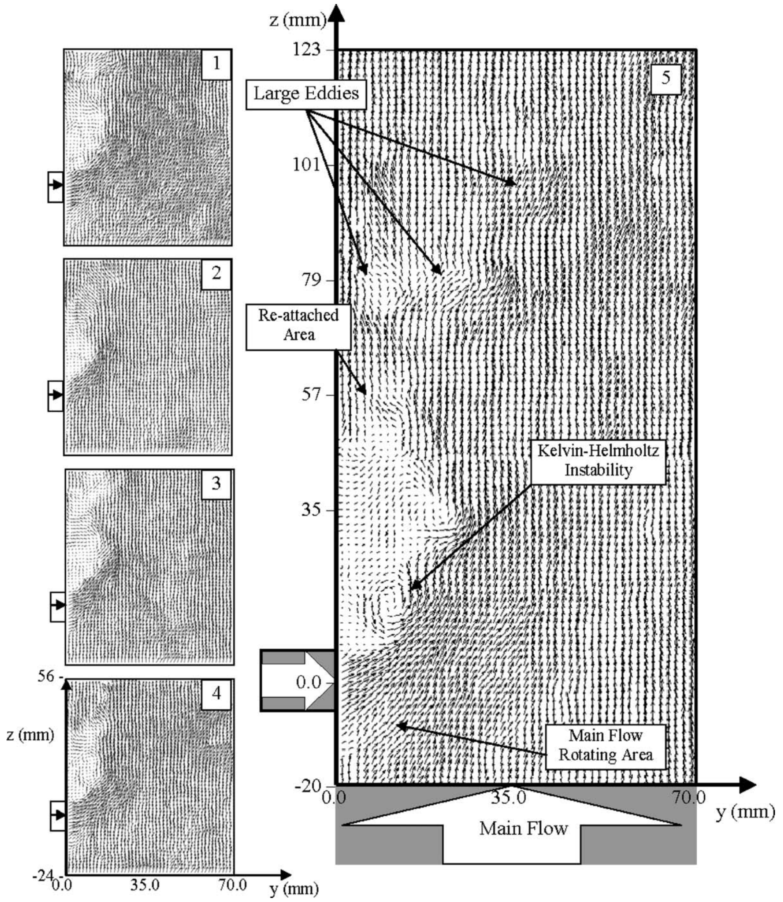

Fig. 9 Five continual frames of time series data with close-up visualization (U_b=0.55 m/s and U_m=0.73 m/s)

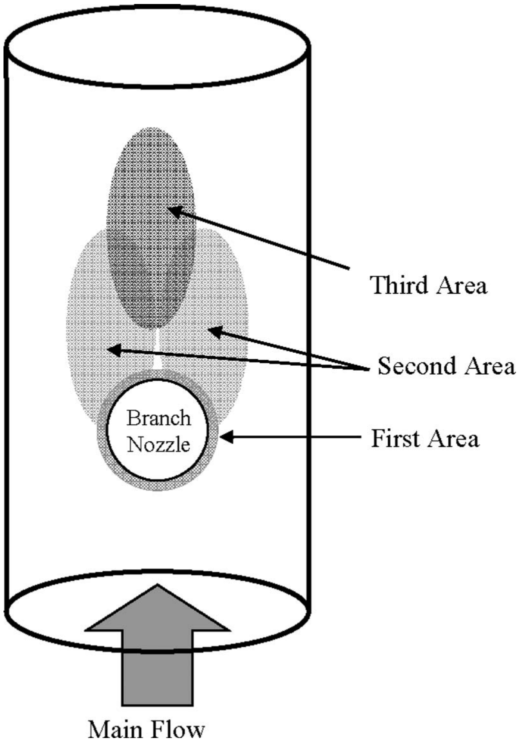

Fig. 10 Schematic of high velocity fluctuation areas near the main pipe wall in the T-junction area

together with the average velocity vectors of 240 frames in the longitudinal section C2. Some vortices are created in the wake area above the branch jet and they look like Karman vortices. The different pressures between the wake area and the main flow below the jet create drag force on the jet body and make the jet move up and down with a low frequency. On the other hand, the formation of Karman vortex causes lift force and moves the jet body to the left and right as well.

Figure 9 shows different time series data in the longitudinal section A with four continual frames. The existence of the wake area above the jet is clear in this section. The gradient velocity between the wake area and the jet causes Kelvin–Helmholtz instability that stretches the flow and produces some anticlockwise vortices in the wake area.

A part of the jet flows over the edge of the wake area and touches the main pipe wall in the region, which is called the re-attached region. By considering the formation mechanism of vortices in the wake area three-dimensionally, the combination of the Kelvin–Helmholtz instability vortex and the Karman vortex creates a type of arch vortex and develops it eventually in the downstream. There are also many other large eddies in the downstream of T-junction with different sources such as the interaction of main flow with the body of the jet, some hidden eddies in the self-developing part of the jet, the fluctuation of the jet structure by the drag and lift forces, the 90 deg bend effects, etc.

5 Conclusion

The fluid mixing mechanism is provided experimentally by particle image velocimetry method to investigate the structure of the turbulent flow field in a T-junction area with a 90 deg bend upstream. For this purpose, several longitudinal and lateral sections in the mixing area are visualized by the high frame rate of velocity distribution, and the statistical analyses of time series data give us the general view of mixing phenomena.

Figure 10 summarizes three regions with the highest velocity fluctuation in the T-junction. The first one surrounds the branch nozzle and is created by the Kelvin–Helmholtz instability between the main flow and the branch jet, and in the case of nonisothermal mixing condition can cause high-cycle thermal fatigue in the same area and sometimes inflict considerable damage on the piping structures. The second region is distributed between the branch nozzle and the re-attached area in the edge of the wake area, and the Karman vortices are the main source of this fluctuation. The frequency of velocity fluctuation in the second region is lower compared to the first one as well as the velocity gradient. The third region is the re-attached region with lowest frequency of the velocity fluctuation. This fluctuation mainly is generated by the lift and drag force between the main flow and the jet body. Due to the fact that the jet body is flexible against the main flow, the high pressure gradient around the jet changes the cross section of the jet in the transitional part from the circular shape to the oval shape periodically. Meanwhile the pressure gradient decreases based on the oval shape and then automatically the cross section of the jet changes back to the circular shape again, which means that the lift and drag forces fluctuate side by side. So the jet body starts to move up and down as well as right and left frequently. This phenomenon causes the low frequency fluctuation of the velocity in the re-attached area. Because of an efficient thermal transfer to the structure, this low frequency fluctuation inflicts the most effective thermal fatigue damage compared with the other two areas and can be improved simply just by changing the momentum ratio between the main and the branch flows or the piping geometry, which is described previously by Hosseini and Yuki [10].

Nomenclature

Δt = time separation
d = side length of the interrogation area
D_b = branch pipe diameter
D_m = main pipe diameter
I = intensity of the velocity fluctuation
$I_{\max}$ = maximum velocity fluctuation
s_m = image magnification
s_j = standard deviation in the j direction
s_r = radial velocity standard deviation
s_z = axial velocity standard deviation
t = time separation
U = mean velocity
U_{ave} = average of the absolute velocity
U_b = branch velocity
U_m = main velocity
$U_{\max}$ = maximum velocity
$U_{\min}$ = minimum velocity
$u_{\underline{i,j}}$ = velocity at the i frame in the j direction
u_j = average velocity in the j direction
$u_{r,i}$ = radial velocity at the i frame
$u_{z,i}$ = axial velocity at the i frame
z = longitudinal distance along the axial direction

References

[1] Faidy, C., 2004, “Thermal Fatigue in Mixing Area,” Third International Conference on Fatigue of Reactor Components, EPRI-US NRC-OECD NEA, Seville, Spain.
[2] Tanaka, M., 2004, Sixth International Conference on Nuclear Thermal Hydraulic, Operation and Safety, NUTHOS-6, Nara, Japan, ID No. N6P334.
[3] Igarashi, M., 2003, “Study on Fluid Mixing Phenomena for Evaluation of Thermal Striping in a Mixing Tee,” Tenth International Topical Meeting on Nuclear Reactor Thermal Hydraulic, NURETH-10, Seoul, Korea.
[4] Hu, L. W., and Kazimi, M. S., 2006, “LES Benchmark Study of High Cycle Temperature Fluctuation Caused by Thermal Striping in a Mixing Tee,” Int. J. Heat Fluid Flow, **27**(1), pp. 54–64.
[5] Hosseini, S. M., and Yuki, H., 2006, “Experimental Investigation of Thermal Hydraulic Characteristics at a Mixing Tee,” International Heat Transfer Conference, Sydney, Australia, FCV-17.
[6] Hosseini, S. M., and Yuki, H., 2005, “Three-Dimensional Study of Flow Mixing Phenomenon,” International Conference Nuclear Energy for New Europe, Bled, Slovenia, September ID: 037.

[7] Yuki, K., and Hosseini, S. M., 2004, 15th International Conference on Nuclear Thermal Hydraulic, Operation and Safety (NUTHOS-6), Nara, Japan, ID No. N6P082.
[8] Metzner, K. J., and Wilke, U., 2005, "European THERFAT Project-Thermal Fatigue Evaluation of Piping System Tee Connections," Nucl. Eng. Des., **235**(2-3), pp. 473–484.
[9] Chapuliot, S., and Gourdin, C., 2005, "Hydro-Thermal-Mechanical Analysis of Thermal Fatigue in a Mixing Tee," Nucl. Eng. Des., **235**(5), pp. 575–5906.
[10] Hosseini, S. M., Yuki, H., and Hashizume, H., 2008, "Classification of Turbulent Jets in a T-Junction Area With a 90-deg Bend Upstream," Int. J. Heat Mass Transfer, **51**(9-10), pp. 2444–2454.
[11] Yuki, K., Sugawara, Y., and Hosseini, S. M., 2008, "Influence of Secondary Flow Generated in a 90-Degree Bend on the Thermal-Hydraulic Characteristics in a Mixing Tee," Nucl. Sci. Eng., **158**, pp. 194–202.
[12] Abramovich, G. N., 1963, *The Theory of Turbulent Jets*, MIT Press, Cambridge, MA, Chap. 1, p. 3.

Experimental Study of a New Flow Conditioner on Disturbed Flow in Orifice Plate Metering

A. Ahmadi
Department of Mechanical Engineering,
Iran University of Science and Technology-Arak
Branch,
Arak,
Markazi 38181-41167, Iran
e-mail: a_ahmadi@iust.ac.ir

The sensitivity to poor conditioned and swirling flow of flow measurements using an orifice plate are subjects of concern to flowmeter users and manufacturers. Measurements of mass flow rate under different conditions and different Reynolds numbers were used to establish a change in discharge coefficient relative to the standard one. The experimental results show that an optimally shaped flow conditioner could attenuate the effects of both swirl and asymmetrical flows. The optimization of the swirler flow conditioner is a main outcome of this work. So far the experimental results show that the cone swirler flow conditioner is the best one for swirling flow. [DOI: 10.1115/1.3114677]

Keywords: orifice plate, asymmetric, swirling flow, flow conditioner, swirler, flow measurement

1 Introduction

The differential pressure flowmeter is one of the most common forms of flowmeter used in industry. It is mainly because the orifice plate is simple to construct, has a low maintenance cost, and wide applicability to different fluids including both liquids and gases. In addition, there is a great weight of experience to confirm its operation and installation, which is documented in BS EN ISO 5167 [1].

The International Standards state that the uncertainty of metering is typically 0.5–1% when supplied with fluid with a well-conditioned velocity profile [2]. The most important assumption of well-conditioned flow is that the flow approaching the orifice plate must be fully developed and free of any asymmetry or swirl. In practical applications, however, pipe fittings and pipe installations such as valves, bends, heat exchangers, compressors, and other devices can generate a distorted and swirling flow profile. These distortions can alter the accuracy of an orifice plate up to 4% for an asymmetric velocity profile [3] and from 3% up to 7% error for swirling flow generated by twin 90 deg elbows [4,5]. In order to produce a fully developed flow, free from all disturbances, a long straight pipe must be installed upstream from the orifice plate. British Standard or ISO recommends a minimum straight length upstream of the meter that depends on the Reynolds number, pipe diameter, orifice diameter, the ratio of pipe diameter to hole diameter, and the pipe fitting [6]. In general, this requirement means that at least 10 pipe diameters of smooth straight pipe is required for orifice plates with small holes increasing to 36 pipe diameters for plates with large ones [6]. In many installations it is impossible to provide a sufficiently long straight pipe upstream of the meter to remove flow disturbances. In these circumstances, flow conditioners and flow straighteners can be placed upstream to remove disturbances in the flow, which reduce the number of straight upstream pipe lengths required for accurate flow measurement.

In general, a flow straightener is a device that removes a swirl from the flow but has little effect on the asymmetrical velocity profile. On the other hand, a flow conditioner is a device that not only removes swirl but also produces a repeatable downstream velocity irrespective of the upstream flow disturbances. Therefore, most flow conditioners are used to avoid unwanted shifts in the meter's calibration by reducing the effect of upstream disturbances on the meter to an insignificant level. It is desirable for a good flow conditioner to fulfill its duty within the following requirements:

- low-pressure loss across the device
- short downstream length from the source of disturbances
- the combination of device and conditioner to be as compact as possible
- easy installation

However, even the best performing flow conditioners need to be installed at least 2 pipe diameters from the disturbances and also 4 or 5 pipe diameters from the orifice plate [7]. So, great efforts have been expended to achieve a flow conditioner that will perform with a lower number of pipe lengths and minimum pressure drop across it [8–10].

There are a large number of flow conditioners used in flow measurement, and some are included in the British and ISO Standards and others can be found in technical reports [1,2]. For instance, a flow conditioner introduced by Canada Pipeline (CPA 50E [11]) is a perforated plate, which can provide a repeatable, swirl free, fully developed velocity profile for high-pressure natural gas applications [11]. A new device, a vane perforated plate (described as meeting the velocity profile requirement of ISO 5167), is positioned 6 pipe diameters upstream of the orifice plate and produces a pressure loss of about 1.4 dynamic heads [12]. Two kinds of new flow conditioner called the in-line flow conditioning plate [13] and the AS-FC flow conditioner [14] claim to produce a fully developed velocity profile with a low-pressure loss. The efficiency of standard flow conditioner in reducing the effect of disturbed flow consisting of asymmetric velocity profile and swirling flow has been described in other references [15].

Generally, all flow conditioners are aiming either to supply a flow in a settled fully developed state through turbulent mixing devices or to achieve a repeatable constant velocity profile independent of source of disturbances as in vortex action devices.

1.1 Recent Experimental Work.

An approach to the flow conditioner, based on vortex action and developed at Sheffield University, is to use a device at the short distance upstream of the orifice plate, which makes a strong swirl or disturbance that will absorb all the other disturbances in a predetermined manner. This device creates a predetermined flow condition, independent of the

---

Contributed by the Fluids Engineering Division of ASME for publication in the JOURNAL OF FLUIDS ENGINEERING. Manuscript received May 7, 2007; final manuscript received March 13, 2009; published online April 13, 2009. Assoc. Editor: Juergen Kompenhans. Paper presented at the 2005 ASME Fluids Engineering Division Summer Meeting and Exhibition (FEDSM2005), Houston, TX, June 19–23, 2005.

upstream conditions. Therefore, the strong disturbed flow that is made by the swirler device can absorb other unknown and unwanted disturbances and achieve a repeatable velocity profile independent of disturbances. An elementary study using a twisted piece of plastic was positioned 1.5 pipe diameters upstream as a flow conditioner was carried out in an experimental rig using air as the working fluid. This experimental work was carried out for a 76 mm pipe with $\beta=0.5$ and a variety of Reynolds numbers from 14,000 to 70,000 for both standard and nonstandard velocity profiles. The flow was disturbed upstream of the orifice plate by fixing different shaped blocks within 3.5–4.5 pipe diameters of the orifice plate [16].

The results showed that block disturbances produced up to 4% shift in measuring flow based on the equation in the ISO Standards [1]. The application of using a swirler flow conditioner for higher Reynolds numbers and different orifice diameters has been conducted in an experimental water rig with β of 0.4–0.7. The effect of these disturbances on mass flow showed that the effect of asymmetric velocity profile is to produce up to 3% shift in discharge coefficient for low Reynolds number and about 1.5% for high Reynolds number for $\beta=0.4$ and $\beta=0.7$, respectively [17]. Finally, the effect of an optimum design for the swirler flow conditioner on disturbed flow shows that this flow conditioner has a positive effect on swirling flow disturbances [18].

Thus the focus of this study is to examine the effect of different shapes of swirler flow conditioner in limiting disturbances due to different kinds of disturbances. These experiments were carried out with water and air flow in two rigs with both high and low Reynolds numbers.

1.2 Theory. The pressure drop (ΔP) across the orifice plate and the mass flow rate (q_m) are linked by an equation from ISO [1].

$$q_m = \frac{C}{\sqrt{1-\beta^4}}\varepsilon\frac{\pi}{4}d^2\sqrt{2\Delta p\rho} \tag{1}$$

where C is the discharge coefficient that depends on the exact type of differential flowmeter being used. For instance, for the D and $D/2$ orifice plate flowmeter, which has been used in this study, this coefficient is

$$\begin{aligned} C = {} & 0.5961 + 0.0261\beta^2 - 0.216\beta^8 + 0.000521\left[\frac{10^6\beta}{\mathrm{Re}}\right]^{0.7} \\ & + \left[0.0188 + 0.0063\left(\frac{19{,}000\beta}{\mathrm{Re}}\right)^{0.8}\right]\beta^{3.5}\left[\frac{10^6}{\mathrm{Re}}\right]^{0.3} \\ & + 0.04289\left[1 - 0.11\left(\frac{19{,}000\beta}{\mathrm{Re}}\right)^{0.8}\right]\frac{\beta^4}{1-\beta^4} \\ & + 0.031\left[\frac{0.94}{1-\beta} - 0.8\left(\frac{0.94}{1-\beta}\right)^{1.1}\right]\beta^{1.3} \\ & + 0.011(0.75-\beta)\left[2.8 - \frac{D}{25.4}\right] \end{aligned} \tag{2}$$

where β is the ratio of the orifice diameter to the pipe diameter ($\beta=d/D$).

It can be seen that the flow rate is calculated from the pressure drop, geometry, and the physical parameters of the fluid and also the Reynolds number of the flow, which is itself a function of the flow rate. So, in order to calculate a mass flow rate from differential pressure, an iterative method must be used. An important point regarding the above correlations is that the profile of the flow approaching the orifice plate should be fully developed. This allows the uncertainty of the measured flow rate to be less than 1%.

1.3 Variation in the Discharge Coefficient. In evaluating the effects of disturbances on mass flow rates, various disturbances and hence variations in the discharge coefficient have been analyzed. According to the ISO Standards the flow rate is determined from the differential pressure measured through the orifice plate [1]. For a fully developed velocity profile, for a known discharge coefficient, the mass flow rate can be calculated or for a known mass flow rate the standard discharge coefficient can be calculated. Nevertheless, the mass flow rate for disturbed flow can be measured by experiment and then new discharge coefficient (C_d) can be calculated from Eq. (2). Thus the percentage shift of the standard discharge coefficient due to disturbances ΔC_d (%) can be determined as

$$\Delta C_d = \left[\frac{C_d - C_{d0}}{C_{d0}}\right] \times 100 \tag{3}$$

This can be used to express the effect of disturbances on metering.

1.4 Pressure Loss Coefficient. In order to compare pressure losses across different flow conditioners, it is customary for this quantity to be expressed according to a specific term called the pressure loss coefficient. This coefficient is defined as

$$PL = \frac{\Delta P}{\frac{1}{2}\rho u^2} \tag{4}$$

where ΔP is a pressure drop caused by the flow conditioner and u is an average velocity in the pipe line or the bulk velocity in the pipe (volume flow divided by the cross-sectional area).

2 Experimental Facility

In order to assess the effect of disturbed flow on the orifice plate, two experimental facilities have been built: one for air and one for water. In these facilities, the mass flow rate of the orifice plate with both standard and nonstandard velocity profiles has been measured for different Reynolds numbers and β ratios. Throughout the experimental work the accuracy of the standard orifice plate without disturbances was also compared with the ISO Standards [1] using Eq. (3).

2.1 Water Rig. For the water rig, a smooth 32 mm internal diameter pipe with 20 and 10 pipe diameters upstream and downstream, respectively, was used (Fig. 1). For measuring the pressure difference, two pressure tappings were used: D upstream and $D/2$ downstream of the plate. The pressure drop across the orifice plate was measured by using both a U-tube water manometer and a pressure transducer.

To measure the mass flow rate, the dynamic weighing scale was used to measure the mass flow rate. This method requires the mass flow rate to be under steady state flow rate conditions. As the mass flow rate was not initially determined, so the pressure drop was fixed for a particular value. This task was achieved by changing a valve, which was installed at the end of a pipeline. After adjusting the pressure drop at a constant value and obtaining steady state mass flow rate, the weighing tank drain valve was closed and mass began to accumulate until the counterbalance weight was lifted. When the balance arm started to move, a timer was triggered to run and the test run began. After a while, the flow rate was accumulated in the weighting tank for a specific interval time. At the end of the interval time the time was stopped manually and the mass flow was measured. Hence, by measuring the discharged water in the weighting tank and its discharging time, experimental mass flow rate was calculated. In the next step, the velocity of the flow was calculated; consequently, the Reynolds number basis of the pipe diameter was calculated. It followed that with having the pressure drop, which was fixed during the experiment, the discharge coefficient from Eq. (2) was calculated. On the other hand by having experimental mass flow rate, the discharge coefficient was calculated using Eq. (1). Finally, these two discharge coefficients (calculated from mass flow rate and from specific correlation stated in the Standards) were compared to investigate a varia-

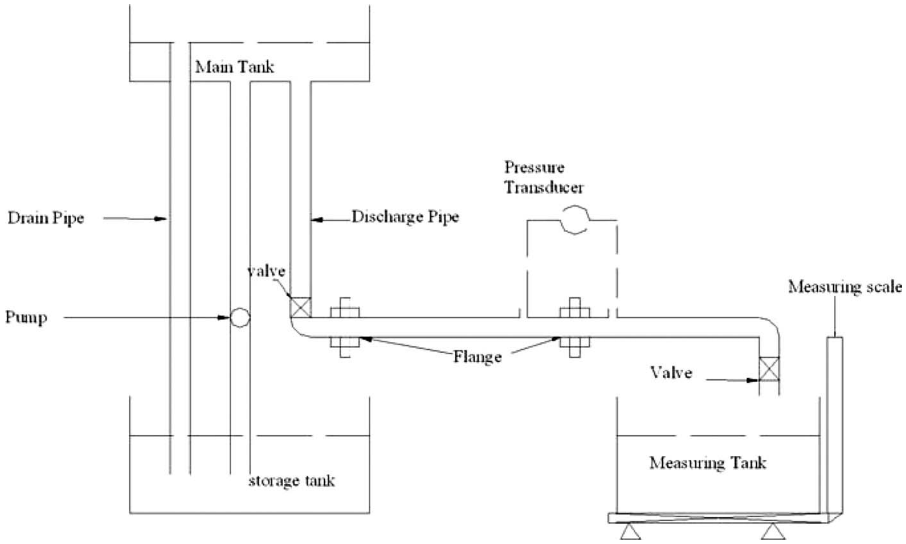

Fig. 1 Sketch of the experimental rig for water

tion in discharge coefficient for different experimental conditions.

Orifice plates with values of β varying from 0.4 to 0.7 were employed in this rig but only the results of 0.5 will be reported here. The experimental mass flow rate for each case was measured by the dynamic weighting method [6]. This mass flow rate was compared with the mass flow rate calculated according to the ISO Standards. The difference between these two flow rates has been investigated in order to estimate likely errors.

2.2 Air Rig. For the air rig, two orifice plates were positioned in a series of smooth and circular pipes of 76.2 mm diameter. The first of these was used as a reference meter and the second was the one where flow approaching the orifice plate was altered. These two pipes were joined together with a large air box to reverse the flow and also to allow it to settle. A sketch of this experimental arrangement is shown in Fig. 2. In the air rig a diameter ratio of $\beta=0.5$ was selected for both orifice meters. The pipes were 3 m (40 diameters) long on either side of each orifice plate. This exceeded the ISO Standards requirements of 20 pipe diameters. However, it should be noted here that the requirement of 20 pipe diameters is still in doubt by several authors and some of them mention the need for a 100 pipe diameters requirement to become fully developed [12].

Liquid filled differential manometers were fitted to either side of the orifice plates again using ISO Standards D and $D/2$ tappings. As the flow rates were calculated using the density of the air, the atmospheric pressure and temperature were measured for each set of experiments. The air was sucked through the system using a fan controlled by a ball valve. All of the measurements were carried out simultaneously on both meters using Reynolds numbers of up to 40,000.

2.3 Swirler Flow Conditioners. The initial shape for the swirler was a piece of plastic with a 90 deg twist in it. The length of the swirler was about 1.5 times the pipe diameter, which was similar to the previous experiments [16]. In the new series of experiments, the development of the suitable swirler conditioner on the disturbed flow was the main goal. The reason for this was that the previous results showed that the original, one piece, swirler conditioner could attenuate the effect of asymmetric flow very well but for swirling flow, it performed less well. So, four different swirler shapes were designed and also tested. The length of these was kept the same, as the original 1.5 pipe diameter and they were positioned in the same position upstream of the orifice plate. These swirler conditioners can be described as follows in Fig. 3:

(a) cone swirler
(b) joint two-piece of the swirler (made of two pieces joined together)
(c) two-piece of the swirler with a gap between these two parts
(d) four-piece of the swirler with a gap between each part

2.4 Disturbances. Velocity profiles different from those formed in fully developed flow can be produced using distur-

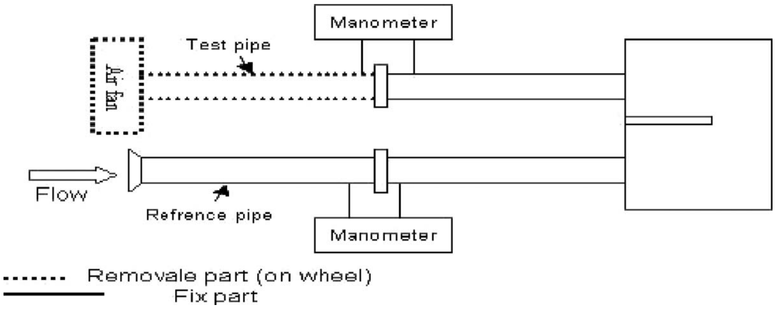

Fig. 2 Sketch of air experimental rig

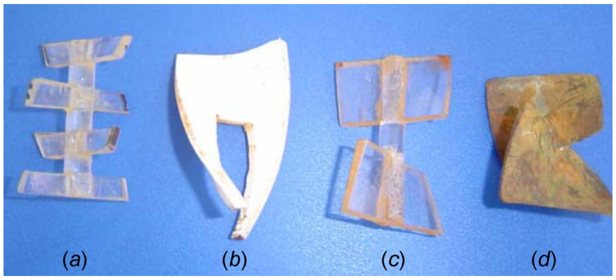

Fig. 3 Swirler flow conditioner shapes; left to right: (*a*) four-piece swirler, (*b*) cone swirler, (*c*) two-piece swirler, and (*d*) joint swirler

bances upstream of the orifice plate. These disturbances can provide a combination of an asymmetric velocity profile and a swirling flow. In order to assess the effect of the swirler flow conditioner on the disturbed flow, both types of disturbances were used in the experimental facilities. To achieve an asymmetric velocity profile, block disturbances were used. These blocks were cut from a circular piece of metal and were placed on the bottom of the pipe. One block, referred to as the 1/4 disturbance, had a cross section of 1/4 of the area of the pipe and caused a significant distribution. The second one, referred to as the 1/8 disturbance, had a cross section of 1/8 of the area of the pipe and caused a weaker disturbance. These block disturbances are shown in Fig. 4.

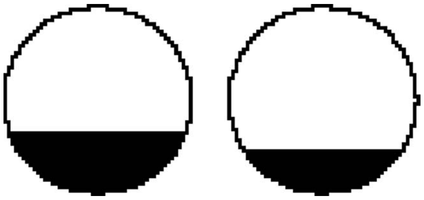

Fig. 4 Block disturbances (left to right: 1/4 and 1/8 disturbances)

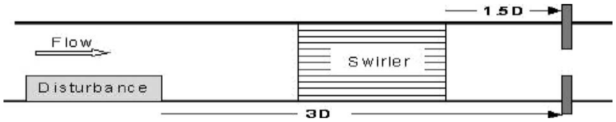

Fig. 5 The positions of disturbance, swirler, and orifice plate

A swirling flow was produced in the pipe using similar devices to the one-piece swirler. The length of each was 1D and they had angles of 90 deg and 180 deg. Also, in the water rig two out of plane elbows were employed. The two-elbow disturbance was two successive bends connected together by a flange without a straight length to set the configuration in and out of plane. The ratio of the radius of the curve to the pipe diameter was 1.5. Consequently, the following disturbances were used in experimental rigs:

- two elbows both in and out of plane
- swirler disturbance with different twist angles
- block disturbance

All of the disturbances were 1.5D in length and were positioned about 3D from the orifice plate. The configuration of the swirler, disturbances, orifice plate, and their position from the upstream face of the orifice plate is shown in Fig. 5.

Four different sets of experiments for measuring mass flow rate were conducted. The first was done for a standard velocity profile to estimate the accuracy of rig and to compare it to the ISO Standards. Then the effect of disturbances was examined. The effect of each swirler flow conditioner on the mass flow rate was then investigated with disturbances. Then, these mass flow rates were used to calculate new discharge coefficients, and the variation in C (Eq. (3)) was calculated to allow a comparison to take place. All of these results were obtained with a β of 0.5.

3 Results and Discussion

3.1 Performance of the Different Swirler Flow Conditioner on Disturbed Flow. The results for the two-piece and joint swirler conditioners are shown in Figs. 6 and 7, respectively. By comparing the two graphs it can be seen that the change in discharge coefficient caused by each swirler conditioner on its own is as much as when using a block disturbance. This means that the swirler flow conditioner can attenuate the effect of an asymmetric velocity profile. Nevertheless, the effect of these two swirler conditioners on the swirling flow caused by the swirler disturbance is totally different. As the same time employment of swirler disturbance causes about 3% change in standard C, using joint and two-piece swirler conditioner for this condition causes about 7% and more than 10% (this line has not been shown in the graph

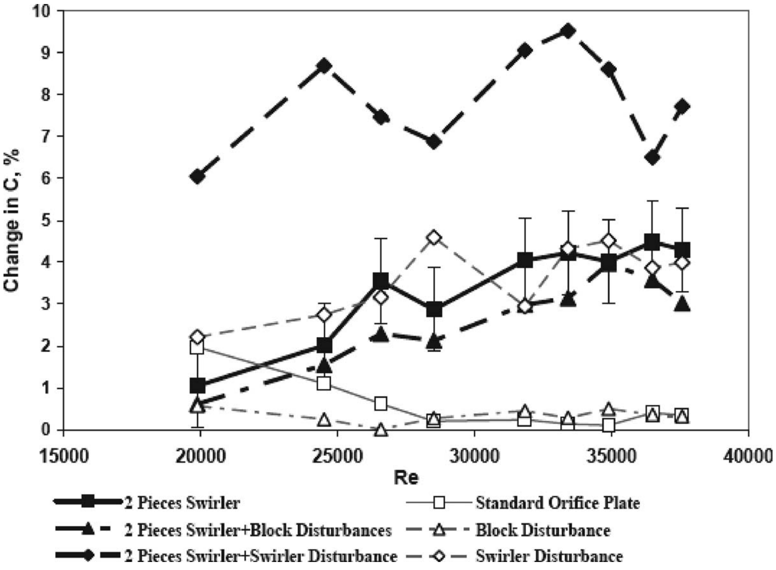

Fig. 6 Change in discharge coefficient with two-piece swirler

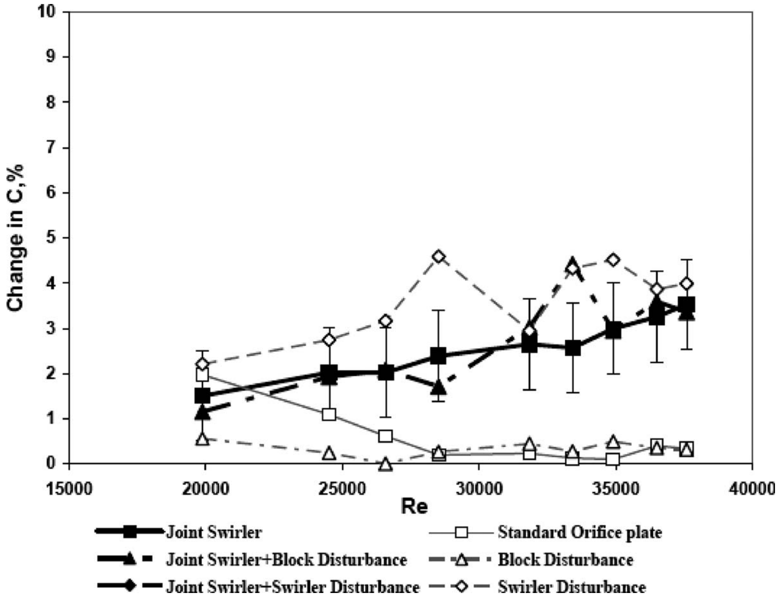

Fig. 7 Change in discharge coefficient with joint swirler

because it is out of scale). Thus, the swirler flow conditioner generally can dampen the effect of block disturbance; however, the effective swirler flow conditioner on the swirling flow is a main task. Therefore, other shapes of the swirler have been designed and their effects on the swirling flow have been tested.

The effect of the four-piece and cone swirler flow conditioner on the disturbed flow was examined, and the results on the discharge coefficient are presented in Figs. 8 and 9. It can be seen from Fig. 8 that the four-piece flow conditioner does not have an attenuating effect on the asymmetry flow caused by the block disturbance and neither has any better effect on the swirling flow relative to previous ones. On the other hand, the result of the cone swirler shown in Fig. 9 illustrates perhaps the best result for implementation of the swirler flow conditioner on the disturbed flow. It can be seen that using the cone swirler by its own changes the discharge coefficient from 4% for low Reynolds numbers to about 6% for high Reynolds numbers. The change in discharge coefficient for both block and swirler disturbance with cone swirler is similar to the change in *C* due to cone swirler by its own with about 1% tolerance. So, it shows that the cone swirler can not only attenuate the effect of asymmetric velocity profile but can also dampen the effect of swirling flow. Thus, it could be concluded that the cone swirler is an optimum shape for swirler flow conditioner, and this device will achieve about a 1% variation in metering when faced with a disturbed flow. This compares well with the standard orifice plate without any disturbances, which can also obtain 1% accuracy [6].

3.2 Implementation of Cone Swirler With Two-Elbow Disturbance.

In order to justify that the cone swirler flow conditioner has a positive effect on dampening swirling flow, the performance of this device was tested on other sources of swirling flow. According to the majority of references, two elbows in and out of plane are the main sources of swirling flow [6,1]. So, these

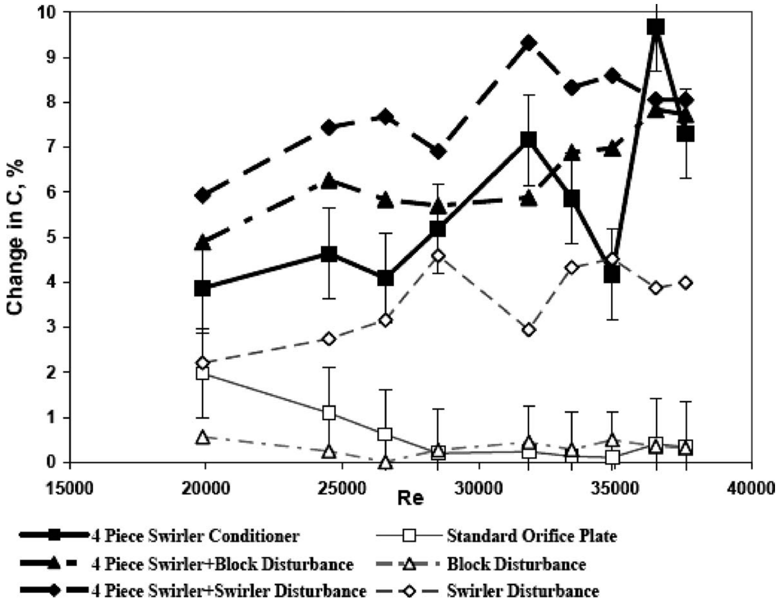

Fig. 8 Change in discharge coefficient with four-piece swirler

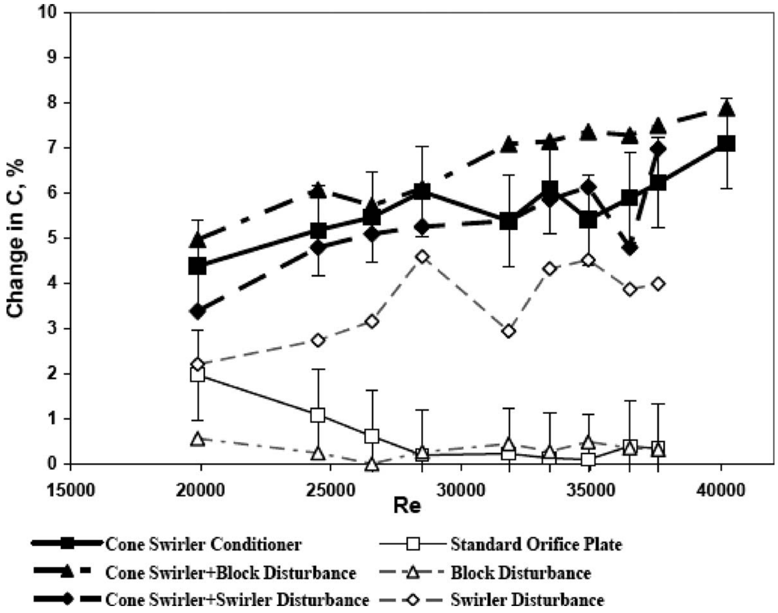

Fig. 9 Change in discharge coefficient with cone swirler

double elbow disturbances were set in the water rig, and the effect of these configurations on the standard orifice plate alongside the cone swirler conditioner was investigated. This result of change in discharge coefficient is given in Fig. 10.

It can be seen from Fig. 10 that the two-elbow disturbances can make a 2–3% shift in the standard discharge coefficient [4]. However, the combination of a cone swirler with a two-elbow disturbance causes a change in discharge coefficient up to 4–6%. It means that the cone swirler conditioner on its own can cause up to a 6% change in standard discharge coefficient, and the combination of this device with other disturbances such as block disturbance, swirler disturbance, and two elbow again causes the change in discharge coefficient (within the 1% error bars). In other words, the cone swirler conditioner can produce a repeatable shift in discharge coefficient independent of sources of disturbance. On the other hand, this graph shows that the result of change in *C* for using the standard orifice plate falls within the 1% error bars too. The latter conclusion confirms the accuracy of the standard orifice metering [1].

3.3 Performance of the Cone Swirler at Low Reynolds Numbers (Air Rig). After the measurement of the cone swirler on a disturbed flow at relatively high Reynolds number, which was achievable for water rigs, this procedure was examined on the air rig with low Reynolds numbers. In the air rig, low Reynolds numbers up to 20,000 were obtained. The results for the air rig with different combinations of disturbances and the cone swirler are shown in Fig. 11.

The graph shows that using a cone swirler conditioner in the upstream changes the standard discharge coefficient by up to 1.5%. This trend is repeated when a combination of block disturbance and cone swirler is placed upstream. This means that the

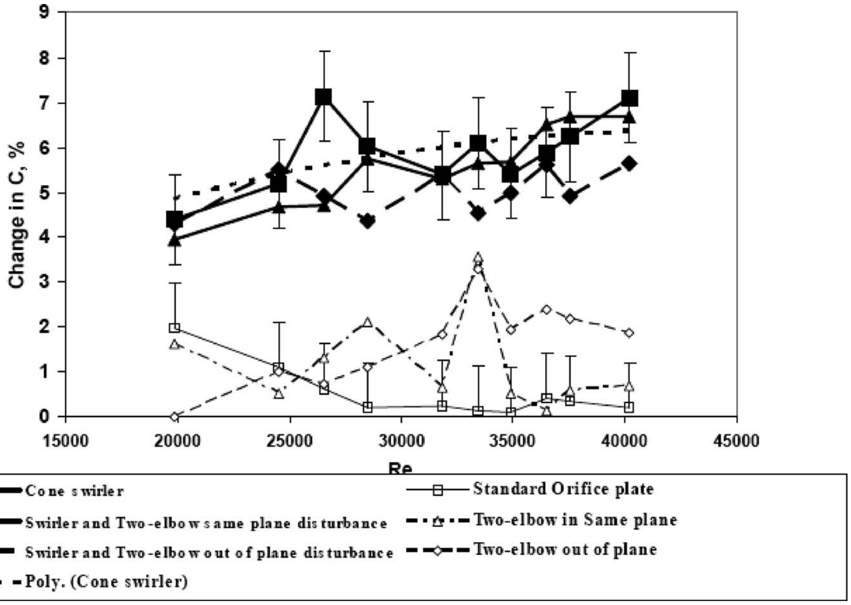

Fig. 10 Change in discharge coefficient for two-elbow disturbance with cone swirler

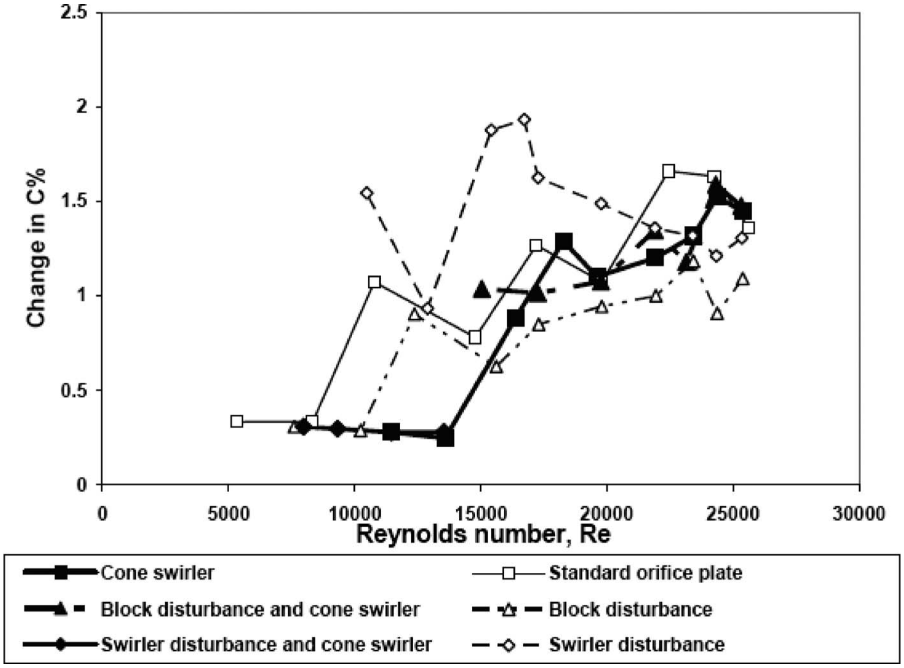

Fig. 11 Change in discharge coefficient for different disturbances and cone swirler (air rig)

cone swirler can attenuate the effect of asymmetric flow with low Reynolds number. On the other hand, employment of swirler disturbance makes up to 1.5% error on metering, and this change when using a cone swirler conditioner can be affected by 0.5% error. This means that the cone swirler cannot compensate the effect of swirling flow as much as for asymmetric flow.

3.4 Calibration of the Cone Swirler. While the swirler conditioner is used in front of an orifice plate, the standard discharge coefficient equation (2) cannot be used to calculate a mass flow rate. So the appropriate discharge coefficient for the combination of the swirler and an orifice plate was determined by curve fitting.

Figure 12 shows the calibration curve for the combination of cone swirler and orifice plate. The experimental mass flow rate in the presence of the cone swirler is plotted versus the calculated mass flow rate of the standard discharge coefficient. It can be seen that the orifice plate and cone swirler combination appears to produce about 7% more flow rate than the orifice plate on its own. To obtain a new discharge coefficient appropriate to the combination of cone swirler and orifice plate, a straight, trend line has been fitted to this curve. This line represents the new discharge coefficient (C^*) for combination of cone swirler and orifice plate flowmeter is 1.079. It means that the new discharge coefficient is 1.079 times the standard orifice plate on its own. So, it can be concluded that the correction factor (K) regarding the employment of cone swirler upstream of a standard orifice plate is 1.0799 for a β of 0.5.

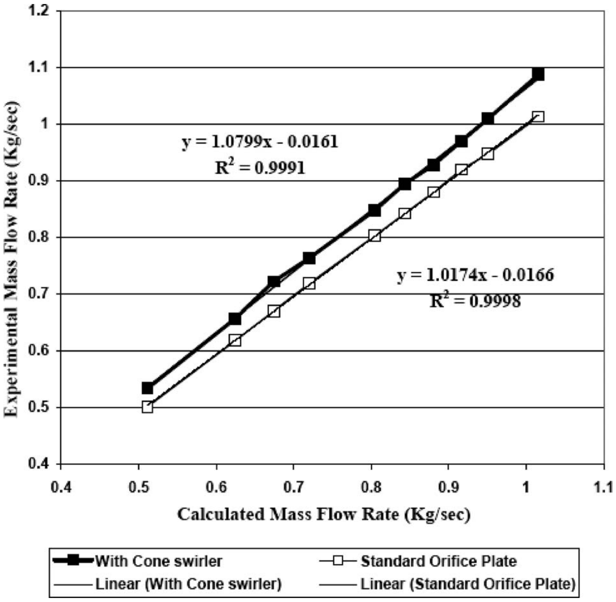

Fig. 12 Calibration of the cone swirler

3.5 Pressure Loss Coefficient for Cone Swirler. As already mentioned, a good flow conditioner should have not only a good performance in dampening the disturbances but also a minimum pressure loss as well. By measuring a pressure difference across 3D in upstream and downstream of the orifice plate with and without flow conditioner, this coefficient can be calculated for cone swirler according to Eq. (4). The reported results for pressure loss coefficient for vortex action devices can be varied from as high as 8 for the "AMCA" flow conditioner to about 1 for "Swirl-van-tab," and this coefficient for "Etoile" flow conditioner reported a factor of 2 [7]. The pressure loss calculation shows this coefficient for cone swirler to be about 2.3.

3.6 Source of Errors. A brief review of error sources associated with measurement of the various parameters is considered in this section. The accuracy of the weighing scale was 0.1% and the stop watch 0.2%. Also, as already mentioned, the pressure drop was measured by two kinds of pressure sensors: a pressure transducer and U-tube manometer. The pressure difference between these two meters was compared, and the difference was about 1.8 cm H_2O or 176 Pa in 3 m, which is negligible in metering. On the other hand, the same procedure was used for measuring the mass flow rate, and so the inaccuracy was the same for the mass flow rate. Thus, it can be concluded that the errors in metering are within those predicted by the Standards.

4 Conclusions

The present study has shown that the novel idea of using a swirler flow conditioner for disturbed flow can reduce the error of metering caused by disturbances to an acceptable standard level. To discover the best design of the swirler flow conditioner, a variety of different shapes was considered and tested in experimental rigs. So far the results show that the cone swirler flow conditioner can reduce the distortion due to asymmetric velocity profile on metering for high and low Reynolds numbers. It is concluded that this kind of swirler conditioner also has a positive effect on swirling flow for high Reynolds numbers but has less effect for low Reynolds numbers. The new discharge coefficient appropriate for the cone swirler flow conditioner can vary from 4% for low Reynolds numbers up to 6–7% of standard discharge coefficient for high Reynolds number.

Regarding other factors for desired flow conditioner, the results show the cone swirler to be positioned about 1.5 pipe diameters upstream of the orifice plate and its pressure loss to be 2.3 of dynamic head. These values clearly describe the advantages of the cone swirler flow conditioner in comparison with other vortex action flow conditioners.

Also, an important feature is that the standard orifice plate is vulnerable for metering of dirty flow because of accumulation of dirt in front of the orifice plate. So the accumulated particles can alter the accuracy of metering dramatically. Thus using the cone swirler conditioner not only gives a mass flow metering independent of upstream disturbance but also keeps particles in suspension and prevents the accumulation of particles in front of the orifice plate.

Nomenclature

d = diameter of the orifice
D = diameter of the pipe
C = discharge coefficient
Δp = differential pressure across the orifice
Re = Reynolds number of the flow (related to the pipe diameter)
P = pressure (static)
u = velocity
C^* = new discharge coefficient with the swirler
C_{d0} = standard discharge coefficient for fully developed flow
C_d = discharge coefficient for nonfully developed flow
K = correction factor for different values of β and for an orifice plate with the swirler
μ = dynamic viscosity
ν = kinematic viscosity
β = ratio of the orifice diameter on the pipe diameter $\beta = d/D$
ε = expansion factor
ρ = density of the fluid

References

[1] BS EN ISO 5167, 2003, "Measurement of Fluid Flow by Means of Pressure Differential Devices Inserted in Circular Cross Section Conduits Running Full," British Standards Publications.
[2] Rogers, S., 2003, "Differential Pressure," available on www.flowcontrolnetwork.com/PastIssues/julaug1999/1.asp.
[3] Ouazzane, A. K., and Benhadj, R., 2002, "Flow Conditioners Design and Their Effects in Reducing Flow Metering Errors," Sens. Rev., **22**(3), pp. 223–231.
[4] Laribi, B., Wauters, P., and Aichouni, M., 2002, "Experimental Study of Aerodynamics Behaviour Downstream of the Three Flow Conditioner," ASME Fluids Engineering Division Summer Meeting, Canada.
[5] Reader-Harris, M. J., Hutton, S. P., and Laws, E. M., 1989, "Flow Straighteners and Flow Conditioning Devices," Flow Measurement and Instrumentation Consortium Report No. 7.
[6] Miller, R. W., 1996, *Flow Measurement Engineering Handbook*, 3rd ed., McGraw-Hill, New York.
[7] National Engineering Laboratory (NEL), 1998, "Flow Conditioners Performance Review," Guidance Note No. 11.
[8] National Engineering Laboratory (NEL), 2002, "Assessment of the Performance of Flow Conditioner at Elevated Reynolds Number," Guidance Note No. 29.
[9] National Engineering Laboratory (NEL), 1999, "CFD Techniques Applied to Differential Pressure Flowmeter Performance," Guidance Note No 20.
[10] Frattolillo, A., and Massarotti, N., 2002, "Flow Conditioners Efficiency a Comparison Based on Numerical Approach," Flow Meas. Instrum., **13**, pp. 1–11.
[11] Canada Pipeline Accessories, 2004, "CPA 50E Flow Conditioner," available on www.flowmeterdirectory.com/flowmeter_flow_conditioners.html.
[12] Laws, E. M., and Ouazzane, A. K., 1995, "A Further Investigation Into Flow Conditioner Design Yielding Compact Installations for Orifice Plate Flow Metering," Flow Meas. Instrum., **6**(3), pp. 187–199.
[13] 2004, "In-Line Flow Conditioning Plate," available on www.sierrainstruments.com/products/pdf/flow-track.pdf.
[14] 2004, "AS-FC Flow Conditioner," available on www.fluidcomponents.com/Aerospace/A_ProdflowCond_ASFC.htlm.
[15] Ouazzane, A. K., and Barigou, M., 1999, "A Comparative Study of Two Flow Conditioners and Their Efficiency to Reduce Asymmetric Swirling Flow Effects on Orifice Meter Performance," Trans. Inst. Chem. Eng., Part A, **77**, pp. 747–753.
[16] Beck, S. B. M., and Mazille, J., 2002, "A Study of Pressure Differential Flow Meter That Is Insensitive to Inlet Conditions," Flow Meas. Instrum., **12**(5-6), pp. 379–384.
[17] Ahmadi, A., Beck, S., and Stanway, R., 2003, "Effect of Diameter Ratio on the Swirling Orifice Plate," Seventh International Symposium on Fluid Control, Flow Measurement and Flow Visualization, Italy.
[18] Ahmadi, A., and Beck, S., 2005, "Development of the Orifice Plate With a Cone Swirler Conditioner," Sens. Rev., **25**(1), pp. 63–68.

2D Navier–Stokes Simulations of Microscale Viscous Pump With Slip Flow

Khaled M. Bataineh[1]
e-mail: k.bataineh@just.edu.jo

Moh'd A. Al-Nimr

Department of Mechanical Engineering,
Jordan University of Science and Technology,
Irbid 22110, Jordan

In this paper we provide numerical solution of the Navier–Stokes equations coupled with energy equation for gaseous slip flow in two-dimensional microscale viscous pumps. A first-order slip boundary condition was applied to all internal solid walls. The objectives are to study the performance of the pumps and to study the effect of velocity slip on its performance. Mass flow rate and pump efficiency were calculated for various pump operation conditions when an external pressure load is applied at the pump exit plane. Geometric parameters were held fixed in this work. Microviscous pump performance was studied in detail for several values of the Reynolds number, pressure load, eccentricity, and slip factors. Our numerical results for no-slip were compared with previously published experimental and numerical data and were found to be in very good agreement. Slip values and eccentricity were found to be major parameters that affect the performance of pump. Pump head decreases with increasing slip factors. Maximum pump efficiency increases with increasing slip factor up to Kn approaching 0.1. However, the maximum value of pump efficiency is found to experience a steep degradation for Kn approaching 0.1. The values of moment coefficient always decrease as both slip factor and distance of the rotor from the lower wall increase. Also, as slip factors and distance of the rotor from the lower wall increase, less net flow rate is predicted. For a given fixed driving force at the rotor surface, there is an optimum value for the behavior of pump efficiency with distance of the rotor from the lower wall. Future research should be conducted to modify the current design to make this concept work for higher Knudsen numbers. [DOI: 10.1115/1.3112390]

Keywords: microfluidics, viscous micropump, slip flow, low Reynolds number, CFD

1 Introduction

Micropumps are important devices in various fields such as medical science, biotechnology, microelectronic cooling, and mechanical engineering, for example, controlled drug delivery systems in medical science, the pressure supplies for micromachines in mechanical engineering, ink jet printing, environmental testing, and so on. Advances in the miniaturization of electromechanical systems have enabled the fabrication of microelectromechanical systems (MEMS) that offer several advantages over conventional devices. The general advantages of using MEMS are small size features, mass production at low cost, sensitivity, and reliability [1,2]. The fluid volumes in these systems are pumped, controlled, or manipulated during operation. Because of their physical and engineering significance, micropumps form an active part among the development of MEMS.

Micropumps can be generally classified as mechanical or nonmechanical micropumps. Mechanical micropumps have mechanical moving parts such as diaphragm and check valves. They require actuators or mechanisms to pump fluids. For example, electrostatic, piezoelectric, and thermopneumatic actuators are used in mechanical micropumps. The pumping action for nonmechanical micropumps does not involve moving parts. They mainly depend on transforming nonmechanical energy into kinetic momentum energy for pumping the fluids. These various types were proposed, researched, and developed to be used for various environments and conditions. For example, drug biocompatibility, safety, and desired flow rates must be met for drug delivery micropumps.

Mechanical pumps based on conventional centrifugal and inertia forces will not work at microscales where Reynolds number is typically small. Microscale reduces the effect of centrifugal forces and inertia forces and amplifies the effect of viscous forces. Hence, viscous force is the dominant force at the microscale [3]. Positive-displacement pumps with a membrane or diaphragm actuated in a reciprocating mode are the typically used method for micropumps. The problem with this type of pumps is that they require even smaller valves and seal mechanism, which are not-too-trivial micromanufacturing challenge. In addition, there are problems of wearing or clogging and consequent leaking around the valves [4]. To overcome the design problems, Stemme and Stemme [5] suggested replacing the check valves with a nozzle at the inlet and a diffuser at the exit. The problem with the idea is that restrictive operating conditions must be met for the pump to operate properly [5].

Several types of nonmechanical micropumps have been developed. The Knudsen pump uses thermal-creep effect to move rarified gases. Ion-drag is used in electrohydrodynamic pumps. They relay on the electrical properties of the fluid and are thus not suitable for many applications [6,7,15]. Electrokinetic pumps, similar to electrohydrodynamic pumps, use the moving electric field to displace the ions in the electric double layer of the electrolyte, rather than the charges in a dielectric fluid [6]. The entire micropump concepts mentioned above, although applicable, are complex and require additional components for pumping action to occur.

It is possible to generate axial fluid motion in open channels through the rotation of a cylinder in a viscous fluid medium. This incorporates both applicability and simplicity in design. Odell and

---

[1] Corresponding author.

Contributed by the Fluids Engineering Division of ASME for publication in the Journal of Fluids Engineering. Manuscript received June 10, 2008; final manuscript received February 2, 2009; published online April 14, 2009. Assoc. Editor: Paul Durbin.

Kovasznay [8] studied a pump based on this principle at high Reynolds number. Sen et al. [9] was the first to propose a novel viscous micropump. They carried out an experimental study on different versions of such pump. The viscous micropump consists simply of a transverse-axis cylindrical rotor eccentrically placed in a channel. The pumping action depends on the net viscous differential resistance between the small and large gaps, which causes net flow along the duct. It depends on viscous force to operate. The viscous force is always dominant for microscale devices. Hence, regardless of the viscosity of the liquid, this pump can pump any kinds of liquids. The study of Sen et al. [9] focused on the effect of the channel height, rotor eccentricity, and angular velocity on the pump performance and on the fluid bulk velocity in the duct. No-slip boundary condition was assumed in their study.

Sharatchandra et al. [10] performed a numerical simulation of the viscous micropump solving Navier–Stokes equations for the case of the cylindrical rotor. Optimal values for optimum performance were obtained. The optimal values were obtained when the channel height is around one and a half times the cylinder diameter for a fixed eccentricity or at the maximum eccentricity for a fixed channel height. The maximum efficiency of the pump was determined to be approximately 2.5% for the optimum channel thickness.

Abdelgawad et al. [11,12] investigated the transient performance of the viscous micropump numerically. They determined that rotor eccentricity is a major parameter that affects the transient performance of the micropump. They assumed no-slip boundary conditions at solid surfaces. da Silva et al. [13] addressed the effect of geometric parameters such as channel height and rotor eccentricity on the mass flow rate and power consumption of two-dimensional microscale viscous pumps. They showed that the rotor eccentricity and the channel height have a major effect on the mass flow rate generated by the rotor and on the shaft power demanded by the rotor. Preliminary simulations showed that mass flow rate is maximized when the eccentricity is small. They studied three different viscous micropump configurations, a straight housed pump (I-shaped housing), and two curved housed pumps (L- and U-shaped housings). They also presented optimal geometric dimensions of several values of the Reynolds number and pressure. Sharatchandra et al. [6] briefly investigated the effect of slip for gas flows. They mentioned that the effect of slip is insignificant when Knudsen number is greater than 0.1. Matthews and Hill [14] used the hydrodynamic theory of lubrication to obtain an analytical solution, which relates flow rate, rotation rate, pressure drop, and applied torque as functions of two geometric parameters for a viscous pump. Their results were valid for very small values of Reynolds number where inertia effect could be neglected. Also they assumed that the gaps between the cylinder and the channel walls are small compared with the radius of the rotor for the lubrication theory to be used. They did not include compressibility effect. Hence, their study could be considered a special case of our present study. It is the objective of this study to have detailed investigations about the effect of slip on the pumping performance of viscous micropump.

In this study, we investigate the effect of slip flow on the pump performance. It has been well documented and shown that fluid flows in small devices differ from those in macroscopic devices. The conventional flow models such as the Navier–Stokes equations with a no-slip boundary condition at a fluid-solid interface cannot predict the operation of MEMS-based devices. We started with a description of micropump configuration and numerical modeling. Next, we validate our numerical results by comparing our present results to those reported by Sharatchandra et al. [6] and Abdelgawad et al. [11]. After the validation of the model we proceed with determining the effect of slip boundary conditions on pump performance. We also investigated the performance for several flow parameters. Finally, we sum up the main findings of this work.

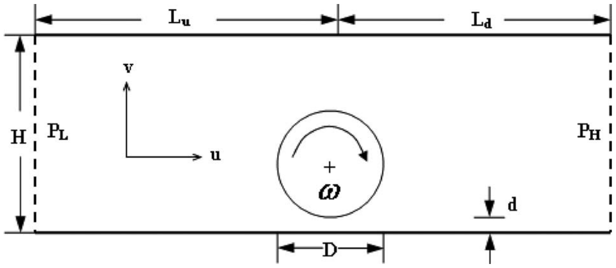

Fig. 1 2D model of viscous micropump

2 Governing Equation

The viscous micropump is composed of two parallel plates with transverse-axis rotating shaft placed asymmetrically within the duct, as shown in Fig. 1. The fluid between the two plates is taken to be Newtonian, compressible, and isothermal with constant properties. Both upper and lower plates are held stationary while the shaft rotates clockwise with constant angular velocity ω.

We take the diameter of the shaft D as our characteristic length scale. Nondimensional geometric parameters are obtained by dividing by length scale D.

$$x^* = \frac{x}{D}, \quad y^* = \frac{y}{D}, \quad H^* = \frac{H}{D}, \quad L_u^* = \frac{L_u}{D}, \quad L_d^* = \frac{L_d}{D}, \quad \varepsilon = \frac{d}{D} \tag{1}$$

where L_d is the downstream distance, L_u is the upper stream distance, H is the channel height, and ε is the cylinder eccentricity.

We define the dimensionless x- and y-component of fluid velocity as

$$u^* = \frac{u}{\omega D/2} \tag{2}$$

$$v^* = \frac{v}{\omega D/2} \tag{3}$$

We define the density as

$$\rho = \rho_r \rho_o \tag{4}$$

where ρ_o is the density at the exit of the channel, which is assumed to be constant, without loss of generality, we assume ρ_r to be equal to unity.

The nondimensional pressure rise (pump load) is defined as:

$$p^* = \frac{P_{\text{out}} - P_{\text{in}}}{\rho \upsilon^2/D^2} \tag{5}$$

where P_{out} is the exit pressure, P_{in} is the inlet pressure, ρ is the density of fluid, ω is the rotational speed of the shaft, and υ is the kinetic viscosity of the fluid.

We define the drag, lift, and moment coefficients as follows:

$$C_D = \frac{F_D}{\frac{1}{2}\rho_o U^2 D} \tag{6}$$

$$C_L = \frac{F_L}{\frac{1}{2}\rho_o U^2 D} \tag{7}$$

$$C_M = \frac{M}{\frac{1}{2}\rho_o U^2 D^2} \tag{8}$$

where F_D, F_L, and M are defined as

$$F_D = -\int_0^{2\pi} Rp\cos\theta d\theta - \int_0^{2\pi} R\tau_{r\theta}\sin\theta d\theta \tag{9}$$

$$F_L = -\int_0^{2\pi} Rp\sin\theta d\theta - \int_0^{2\pi} R\tau_{r\theta}\cos\theta d\theta \tag{10}$$

$$M = -\int_0^{2\pi} R^2\tau_{r\theta} d\theta \tag{11}$$

The above equations represent forces per unit length exerted by the fluid on rotor. R is the rotor radius.

The nondimensional mass and momentum balance equations are as follows:

$$\nabla \cdot \boldsymbol{V}^* = 0 \tag{12}$$

$$\mathrm{Re}^2(\boldsymbol{V}^* \cdot \nabla)\boldsymbol{V}^* = -\nabla P^* + \mathrm{Re}\,\nabla^2\boldsymbol{V}^* \tag{13}$$

where $\mathrm{Re}=\omega D^2/2\upsilon$ is the Reynolds number based on rotor angular velocity and shaft diameter.

A gas flow is classified to be in the slip regime if the Knudsen number Kn is $0.001 < \mathrm{Kn} < 0.1$. Here the Knudsen number is defined as $\mathrm{Kn}=\lambda/H$, where λ is the mean free path of gas molecules. For macrofluidic devices, Kn is very small, and no-slip boundary condition at solid boundaries is a valid assumption. In micromechanics of gases, Kn is not small and there is a slip at solid boundaries [15–17]. The traditionally used no-slip boundary conditions for velocity are no longer valid in the micromechanics of gases. In the slip regime, the gas velocity at a solid surface differs from the velocity at which the wall moves. Following Maxwell [18], it has been proposed by Schaaf and Chambre [19] that at a solid surface in isothermal slip flow, the dimensionless slip velocity is defined as

$$v_s^* = v_g^* + \frac{2-\sigma}{\sigma}\mathrm{Kn}\frac{\partial v_g^*}{\partial n} \tag{14}$$

where v_{s^*} is the dimensionless tangential velocity of the surface, v_g^* is the dimensionless velocity of the gas, n is the coordinate normal to the solid surface, and σ is called the tangential-momentum accommodation coefficient. The equation above is written in nondimensional form with velocities being nondimensionlized by the surface speed of the shaft $\omega D/2$ and channel height H.

We define slip factor S as

$$S = \frac{2-\sigma}{\sigma}\mathrm{Kn} \tag{15}$$

where S takes value from zero to unity. For $S=0$ there is no slip between the wall and the fluid; the slip increases as S becomes larger.

3 Numerical Modeling

It is often difficult to obtain accurate analytical results using governing equations for viscous micropump. Hence numerical simulations become an attractive method to predict the performance of the micropump.

To evaluate the performance of viscous micropumps, the commercial finite volume software FLUENT is used in this study [20]. The 2D Navier–Stokes equations coupled with energy equation were numerically solved. The numerical domain consists of two parallel plates held stationary and an asymmetrically placed shaft rotating clockwise shown in Fig. 1. Due to viscous action, the clockwise-turning shaft impels the fluid from left to right against an external pressure difference defined as $\Delta P = P_{\mathrm{out}} - P_{\mathrm{in}}$. This pressure difference is called backpressure or pump pressure.

It has been shown by Sen et al. [4] that a rotating body, asymmetrically placed within a duct, will produce a net flow due to viscous action. The differential viscous resistance between small gap and large gap produces a net flow. Hence, the performance of a viscous micropump depends on the eccentricity of the shaft with respect to the duct walls. Thus, we introduce dimension d that indicates the distance between the lower wall and the shaft (see Fig. 1).

Table 1 Demonstrates the mesh convergence of dimensionless average flow velocity $\overline{u^*}$, Re=1, H^*=1.5, and ε=0.025

No. of elements	$\overline{u^*}$	$\left\lvert \frac{\overline{u_i^*} - \overline{u_{i+1}^*}}{\overline{u_i^*}} \right\rvert \times 100\%$
639	0.1001	N/A
1563	0.10368	3.466
6413	0.10514	1.40313
22,352	0.1058	0.6076

In numerical simulations, the inlet boundary condition was specified by pressure $P^* = P_{\mathrm{in}}^* = 0$. This value will always be assumed zero gauge pressure at the inlet throughout all simulations. The outlet boundary condition was specified by pressure $P^* = P_{\mathrm{out}}^*$. This value will be varied to simulate different pump loads. In all numerical simulations L_u and L_d were taken to be $8D$ to satisfy the fully developed flow conditions [1]. The eccentricity ε is taken to be 0.025 for all simulations.

FLUENT software adopts Maxwell's models for slip velocity. FLUENT defines the equations below to simulate slip velocity.

$$U_w - U_g = \left(\frac{2-\sigma}{\sigma}\right)\mathrm{Kn}\frac{\partial U}{\partial n} \approx \left(\frac{2-\sigma}{\sigma}\right)\frac{\lambda}{\delta}(U_g - U_c) \tag{16}$$

$$V_g \equiv (\boldsymbol{V} \cdot \boldsymbol{n})_g = V_w \tag{17}$$

Here, **U** and **V** represent the velocity components that are parallel and normal to the wall, respectively. The subscripts **g**, **w**, and **c** indicate gas, wall, and cell-center velocities. The parameter $\boldsymbol{\delta}$ is the distance from the cell-center to the wall, and $\boldsymbol{\sigma}$ is the momentum accommodation coefficient of the gas. The mean free path is computed as follows:

$$\lambda = \frac{k_B T}{\sqrt{2}\pi\sigma_v^2 p} \tag{18}$$

where k_B is the Boltzmann constant equal to 1.38066×10^{-23} J/K. The normal component of gas velocity is the same as the wall normal velocity (no penetration). The tangential component values lie somewhere between the cell-center and the wall values. Slip velocity conditions were used in all internal surfaces of the channel. As a convergence criterion, the solver iterated the equations until the scaled residuals of continuity, x-velocity, y-velocity, and energy were less than 10−6.

4 Validation of the Model

The mesh density was exhaustively tested in order to guarantee that the results were mesh-independent. Table 1 illustrates the mesh convergence of the average fluid velocity. A model that consists of 22,352 elements was used for the entire simulation. Figure 2 shows part of the mesh density numerical domain where a finer mesh was used around the rotor surface.

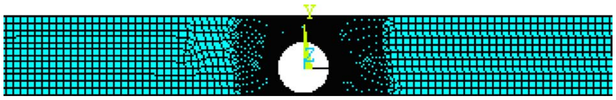

Fig. 2 Part of numerical domain mesh density

Table 2 Validation of the simulation results; Re=1, H^*=1.5, and ε=0.025

ΔP^*	$\overline{u^*}$ Present work	$\overline{u^*}$ [6]	Difference $\left\lvert \frac{\overline{u}^*_{\text{present}} - \overline{u}^*_{\text{Sharatchandra}}}{\overline{u}^*_{\text{Sharatchandra}}} \right\rvert \times 100\%$ (%)
0	0.1058	0.106	0.19
7.5	0.075	0.0736	1.9
15	0.042	0.043	2.3
30	−0.0214	−0.021	1.9

In order to validate the simulation model, the present results were compared against previous results obtained by Sharatchandra et al. [6]. Table 2 compares the effect of the backpressure on the average fluid velocity $\overline{u^*}$ at the outlet plane. Let Re=1, $H^*=1.5$, and $\varepsilon=0.025$, where the average fluid velocity is defined as

$$\bar{u} = \frac{1}{H}\int_0^H u(y)dy \tag{19}$$

Table 2 shows that our present numerical results are in good agreement with previous numerical results throughout ΔP^* range with an average difference on the order of 2%.

5 Results and Discussion

5.1 Effects of Slip Factor and Pump Load. The pump load (pump backpressure) is modeled by increasing the outlet pressure of the pump to simulate the pressure increase needed from the pump to overcome the imposed external pressure. The effect of slip was simulated by changing the values of slip factor. We investigated four different values of slip factor, namely, $S=0$, 0.0027, 0.027, and 0.27. Figure 3 shows the change in the flow rate at different pump loads and slip factors. It is clear that the pump flow rate decreases linearly with increasing pump load. It is also clear that pumping flow rate decreases with increasing slip. When the external imposed pressure exceeds the maximum load the pump can deliver, a backflow occurs and the average velocity becomes negative. The maximum load that pumps can deliver decreases with increasing slip. For example, the maximum pumping load is around 25 for no-slip. This value decreases dramatically to a value around 4 for Kn approaching 0.1 (corresponds to $S=0.27$). Figure 3 shows that for $S=0.0027$ (corresponds to Kn $=0.002$), the deviation from no-slip is small. This behavior agrees very well with the accepted classification of flow regime, that is, for Kn greater than 0.001, the no-slip is a valid condition. From the definition of S, $S=0.27$ corresponds to Kn approaching 0.1 in our simulations. For Kn approaching 0.1, the pump operating conditions degraded significantly. The maximum backpressure (at zero flow rate) is only 0.0252 Pa. The maximum flow rate obtained (at zero pump pressure) is only 0.132 $\mu\text{m}^3/\text{s}$.

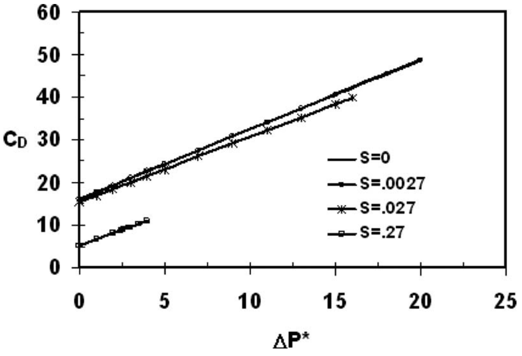

Fig. 4 Total drag coefficient (viscous and pressure) as a function of pump load for different slip factors ε=0.025, H^*=1.5, and Re=1

Figure 4 shows how the drag coefficients vary as a function of pump load for different slip factors. Drag coefficients are always negative and increase with an increase in pump load. The drag coefficient decreases with increasing slip factor. The deviation between no-slip $S=0.0027$ and $S=0.027$ is small. However, for $S=0.27$ there is a significant reduction in drag coefficient and hence reduced traction on the rotor surface. Figure 5 shows how the moment coefficients vary as a function of pump load for different slip factors. It is clear that C_M did not change significantly over a wide range of pump loads. However C_M decreases with increasing slip factor. The moment coefficient for no-slip is greater than that for $S=0.27$ by six times. This is because the magnitude of shear stresses at the rotor surface is proportional to the slip velocity.

In order to determine the efficiency of the micropump and the effect of flow parameters, the pump efficiency is defined as

$$\eta = \frac{\text{flow energy rise}}{\text{mechanical energy input}} \tag{20}$$

where the input mechanical energy is $M \cdot \omega$. M is the torque supplied to the rotor and ω is the angular velocity. The net energy of the flow is only in the form of pressure increase at the pump outlet, since the kinetic energy at the inlet and exit are equal and there is no elevation change. Hence, micropump efficiency can be obtained by

$$\eta = \frac{\dfrac{\dot{m}\Delta p}{\rho}}{M\omega} \tag{21}$$

And in nondimensionless form as

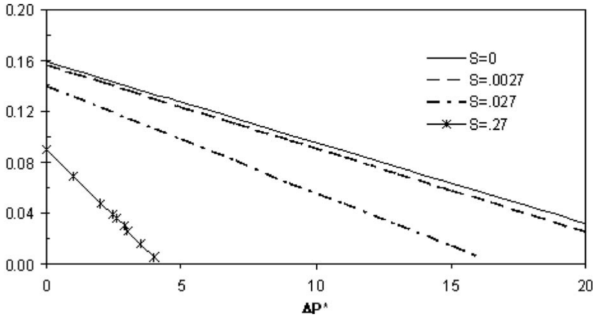

Fig. 3 Effect of slip factor on flow rate versus pump load at Re=1 and ε=0.025, H^*=1.5

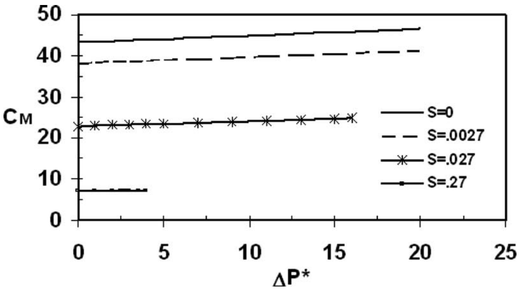

Fig. 5 Moment coefficient as a function of pump load for different slip factors ε=0.025, H^*=1.5, and Re=1

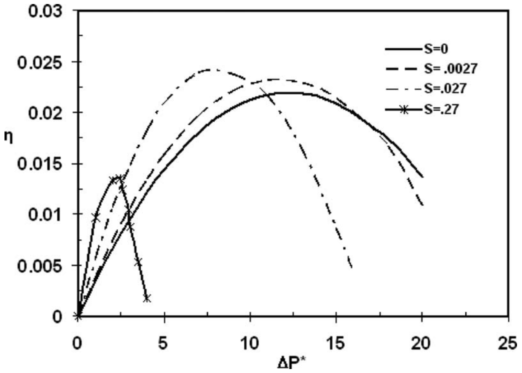

Fig. 6 Efficiency as a function of pressure for different slip factors $\varepsilon=0.025$, $H^*=1.5$. and Re=1

$$\eta=\frac{u^*\Delta p^* H^*}{C_M\,\mathrm{Re}^2} \tag{22}$$

Simulations were carried out to determine the micropump efficiency and the effect of the flow parameters on the performance of the pump. Figure 6 shows how the efficiency η varies as a function of pump load and slip factors. The pump efficiency is high when the flow rate and pump load are high and the coefficient of moment is low. Since for a fixed slip factor, the coefficients of moment do not change considerably, the dominant terms are the pump load and flow rate. Since the flow rate is inversely proportional to the pump load, there should be an optimum operating condition of the pump. Figure 6 shows that the optimum operating condition lies in the middle the pump loads. For example, for no-slip, the pump delivers flow when ΔP^* varies from 0 to 25 (see Fig. 3). Figure 6 shows that the maximum value of efficiency corresponding to pump load is equal to half of the maximum backpressure (zero flow rates). The same is true for different values of slip factor. Generally, the effect of increasing the slip factor is the increase in pump efficiency and the shift of the optimal point to the left. For given values of H^*, ΔP^*, and Re, pump efficiency reduces to the ratio between u^* and C_M. Increasing slip factor reduces both u^* and C_M. Numerical results predict that C_M decreases more than u^* with increasing slip factor. However, when Kn approaches 0.1, average velocity experiences a steeper reduction, while moment coefficient still decreases smoothly. Figure 6 shows that pump efficiency has been greatly degraded for $S=0.27$ compared with $S=0.027$ or smaller. This agrees well with Ref. [6]. For example, for Kn approaching 0.1, maximum efficiency is only about 1.3%. Maximum efficiency for no-slip is about 2.2%, which matches previously published results.

5.2 Effect of Reynolds Number. To investigate the effect of Reynolds number on pump performance, numerical simulations were carried out for various values of Re. External pressure difference was fixed to be 1. Figure 7 shows flow rate variations as a function of Reynolds number and slip factors. The flow rate increases linearly with increasing Reynolds number. Also, flow rate decreases with increasing slip factor.

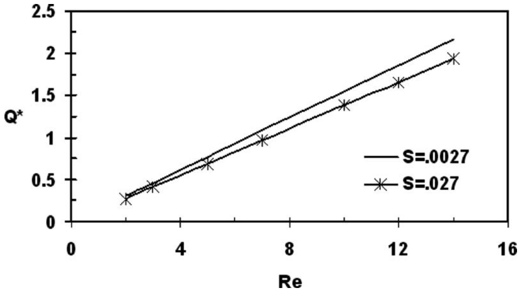

Fig. 7 Flow rate as a function of Reynolds number for different slip factors $\varepsilon=0.025$, $H^*=1.5$, and $\Delta P^*=1$

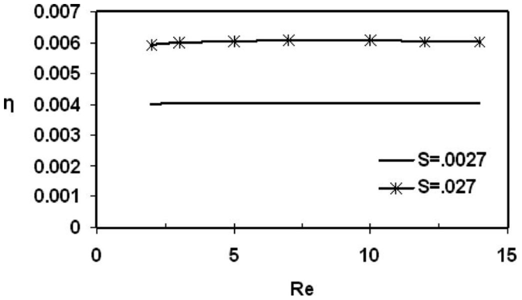

Fig. 8 Efficiency as function of Reynolds number for different slip factors $\varepsilon=0.025$, $H^*=1.5$, and $\Delta P^*=1$

Figure 8 shows that pump efficiency stayed constant as a function of the Reynolds number. This was due to the fact that efficiency is inversely proportional to the product of C_M and Re^2. Figure 9 shows that C_M and C_D decrease with increasing Reynolds number, so the product stayed almost constant.

5.3 Effect of Rotor Eccentricity. Simulations were carried out to investigate the effect of rotor eccentricity on pump performance for several values of slip factors. External pressure was fixed to 1. Reynolds number was fixed to unity. Figure 10 shows flow rate as a function of rotor eccentricity for different slip factors. As S and ε increase, less net flow rate is predicted. Although higher values of S creates more forward flow in the upper gap and more backward flow in the lower gap, but the net effect will be less net flow as S increases. Also, as ε increases, the width of the

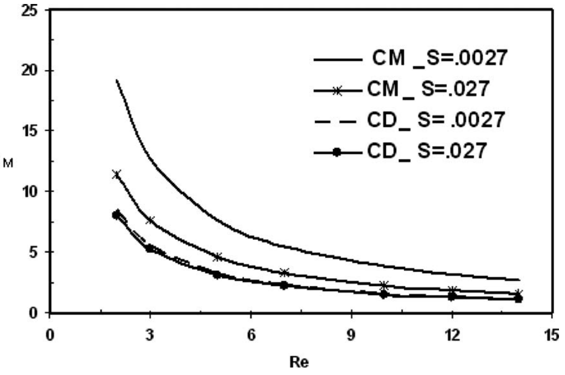

Fig. 9 Moment coefficient as a function of pump load for different slip factors $\varepsilon=.025$, $H^*=1.5$, and Re=1

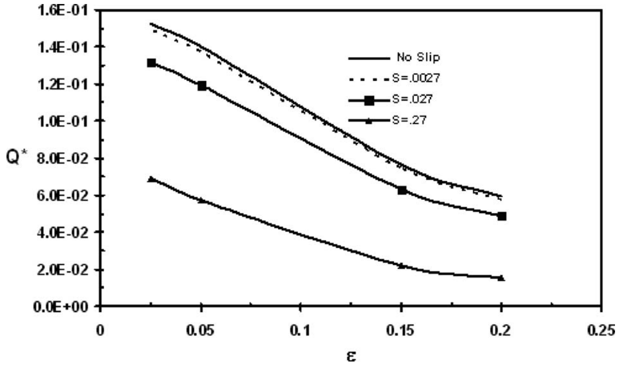

Fig. 10 Flow rate as a function of rotor eccentricity for different slip factors Re=1, $H^*=1.5$, and $\Delta P^*=1$

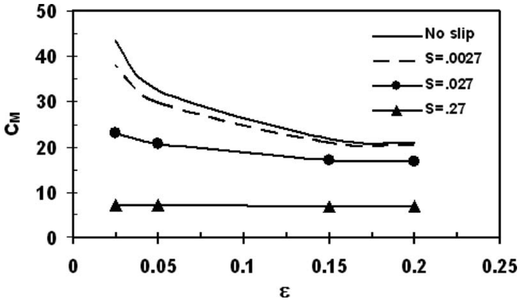

Fig. 11 Moment coefficient as a function of rotor eccentricity for different slip factors Re=1, H^*=1.5, and ΔP^*=1

lower gap increases and that of the upper gap decreases. This causes a reduction in the amount of the forward flow in the upper gap and an increase in the amount of the backward flow in the lower gap. The net effect will be a reduction in Q with increasing ε. Our results agreed well with previously published data that flow rate increases with decreasing ε.

Figure 11 shows the moment coefficient as a function of rotor eccentricity for different slip factors. The values of C_M always decrease as both S and ε increase. Increasing S implies that the slipping effects at the rotor surface increases and this yields less velocity gradients and as a result, less shear forces and C_M. In the same manner, as ε increases, the slipping effects will decrease due to the less velocity gradients near the rotor surface. As a result, less C_M values are predicted. However, for $S=0.27$, the moment coefficient reduces slightly with increasing ε.

Figure 12 shows efficiency variation with S and ε. For small ε as S increases the efficiency increases. For a given fixed driving force at the rotor surface and as S increases, the flow in both the upper and lower gaps will be enhanced by the slipping effects due to the less wall resistance against the flow. This implies that both the forward flow in the upper gap and backward flow in the lower gap will increase as S increases. The flow in the upper wider gap is subject to less slipping effects due to its less velocity gradients, as compared with the flow in the lower gap. But since the upper gap has a larger area the net effect will be enhancing the forward flow as S increases and hence improving pump efficiency. At large ε the lower gap has a significant area and the effect of ε will be to decrease η regardless of the slipping effects. Within this limit of relatively larger ε, the increase in ε will increase the area of the backward flow and decrease the area of the forward flow. The net effect will be a reduction in the net flow as ε increases and this causes a reduction in η regardless of the values of S, because at large values of ε the slipping effects become insignificant.

Tracing the behavior of a single curve one may observe that there is an optimum value for the behavior of η with ε. There are two opposite effects for increasing ε. Increasing ε will increase the area of the lower gap that allows for more backward flow to return back. This causes the reduction in η due to the reduction in the net flow rate Q. On the other hand, increasing ε will reduce the slipping effects within the lower gap, and this reduces the amount of backward flow within the gap and improving η as a result. Now, from Fig. 12 one may observe that as small values of ε increases, the slipping effects within the lower gap decreases (due to the reduction in Kn) and the retardation effects of the wall will overcome the increase in the gap width. As a result, less flow will return within the lower gap, and the net effect will improve the pump efficiency. As ε continues to increase, the slipping effects within the lower gap diminish (lower Kn) but the increase in the gap width allows for more flow to return (less net positive flow rate), and this causes a reduction in η. Note that the optimum behavior for $S=0.27$ still exist, but it appears at lower values of ε that do not appear in the figure.

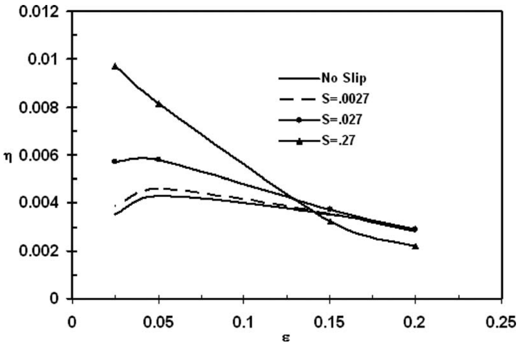

Fig. 12 Efficiency as a function of rotor eccentricity for different slip factors Re=1, H^*=1.5, and ΔP^*=1

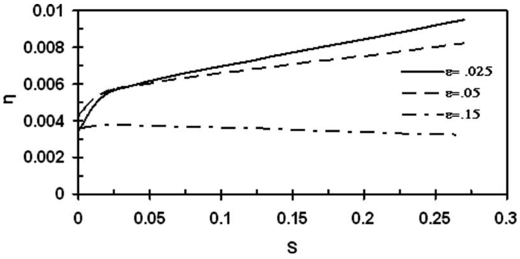

Fig. 13 The effect of S on the optimized eccentricity

A better clarification for the effect of slip factors on pump performance for several values of rotor eccentricity is shown in Fig. 13. Pump performance increases with increasing slip factors for small values of rotor eccentricity. However, for larger values of rotor eccentricity pump performance decreases with increasing slip factors. This agrees well with the explanation given above.

6 Conclusion

The performance of the viscous micropump with slip flow for gaseous were investigated numerically. A solution of 2D Navier–Stokes equations coupled with energy equation was numerically obtained. The geometrical parameters were fixed in this present work except for rotor eccentricity. The effect of varying flow parameters such as varying Reynolds number and backpressure were studied separately for various values of slip factor.

The drag, lift, and moment coefficient were studied for different flow parameters. The drag coefficient was always negative, as expected, and the pressure contribution to the drag force was always higher than the viscous force contribution, sometimes one order of magnitude higher. The drag coefficient increases with an increase in external imposed pressure. The drag coefficient decreases with an increase in Reynolds number. Drag coefficient decreases with increasing slip factor. The lift coefficient is much smaller than the drag coefficient. The moment coefficient does not change significantly with changing external imposed pressure. However, the moment coefficient decreases with increasing slip factor, which also decreases with increasing Reynolds number.

Pump efficiency varies with external imposed pressure and slip factor. However, for fixed slip factor and external pressure, pump efficiency stays almost constant with varying Reynolds number in the present study range. For the given Reynolds number, maximum efficiency occurs around half of the maximum pressure that the pump can deliver. Maximum pump efficiency increases with increasing slip factor.

Slip velocity degraded pump performance when Kn approaches 0.1. Present pump is able to pump fluid against 25 of the nondimensional external pressure for no-slip. On the other hand, it is able to deliver against only four of the nondimensional external pressure for Kn approaching 0.1. Pump performance increases smoothly and slowly with increasing Knudsen number from 0 to 0.02. However, it experiences a steeper degradation when Kn changes from 0.02 to 0.1.

For the given fixed driving force and imposed external pressure, moment coefficient always decreases as both S and ε increases. Also, as S and ε increase, less net flow rate is predicted. Finally, there is an optimum value for the behavior of pump efficiency with ε and S.

Nomenclature

C_D = drag coefficient
C_L = lift coefficient
C_M = moment coefficient
d = rotor distance from lower wall (m)
D = rotor diameter (m)
Kn = Knudsen number
H = channel height (m)
k_B = Boltzmann constant
L = channel length (m)
L_d = down stream distance (m)
L_u = upperstream distance (m)
M = moment $(\mathrm{N/m^2})$
P_{in} = inlet pressure (Pa)
P_{out} = outlet pressure (Pa)
P = pressure (Pa)
Re = Reynolds number
S = slip factor
T = torque (N m)
u = x-component velocity (m/s)
$\bar{u}$ = mean velocity (m/s)
U = rotor surface velocity (m/s)
v_s = tangential velocity of the solid surface (m/s)
x, y = Cartesian coordinates (m)
v = y-component velocity (m/s)
$\boldsymbol{V}$ = velocity vector (m/s)
v_g = velocity of the gas (m/s)
ε = cylinder eccentricity
η = pump efficiency
λ = mean free path (m)
υ = kinematic viscosity $(\mathrm{m^2/s})$
ρ_o = density at channel exit $(\mathrm{kg/m^3})$
ρ = density $(\mathrm{kg/m^3})$
ρ_r = density
σ = tangential-momentum accommodation coefficient
σ_v = Lennard-Jones characteristic length (m)
ω = rotor angular velocity (rad/)
τ = shear stress $(\mathrm{N/m^2})$
* = indicates dimensionless variables

References

[1] Judy, J. W., 2001, "Fabrication, Design and Applications," Smart Mater. Struct., **10**, pp. 1115–1134.
[2] Ziaie, B., Baldi, A., Lei, M., Gu, Y., and Siegel, R. A., 2004, "Hard and Soft Micromachining for BioMEMS: Review of Techniques and Examples of Applications in Microfluidics and Drug Delivery," Adv. Drug Delivery Rev., **56**, pp. 145–172.
[3] Gad-el-Hak, M., 1999, "The Fluids Mechanics of Microdevices—The Freeman Scholar Lecture," ASME J. Fluids Eng., **121**, pp. 5–33.
[4] Sen, M., Wajerski, D., and Gad-el-Hak, M., 1996, "A Novel Pump for MEMS Applications," ASME J. Fluids Eng., **118**, pp. 624–627.
[5] Stemme, E., and Stemme, G., 1993, "Valveless Diffuser/Nozzle-Based Fluid Pump, Sensors and Actuators," Physica, **39**, pp. 159–167.
[6] Sharatchandra, M. C., Sen, M., and Gad-el-Hak, M., 1997, "Navier–Stokes Simulation of a Novel Viscous Pump," ASME Trans. J. Fluids Eng., **119**, pp. 372–382.
[7] Bart, S. F., Tavrow, L. S., Mehregany, M., and Lang, J. H., 1990, "Microfabricated Electrohydrodynamic Pumps," Sens. Actuators, A, **21–23**, pp. 193–197.
[8] Odell, G. M., and Kovasznay, L. S. G., 1971, "A New Type of Water Channel With Density Stratification," J. Fluid Mech., **50**, pp. 535–543.
[9] Sen, M., Wajerski, D., and Gad-el-Hak, M., 1996, "A Novel Pump for MEMS Applications," ASME J. Fluids Eng., **118**, pp. 624–627.
[10] Sharatchandra, M. C., Sen, M., and Gad-el-Hak, M., 1998, "Thermal Aspects of a Novel Viscous Pump," ASME J. Heat Transfer, **120**, pp. 99–107.
[11] Abdelgawad, M., Hassan, I., and Esmail, N., 2004, "Transient Behavior of the Viscous Micropump," Microscale Thermophys. Eng., **8**, pp. 361–381.
[12] Abdelgawad, M., Hassan, I., Esmail, N., and Phutthavong, P., 2005, "Numerical Investigation of Multistage Viscous Micropump Configurations," ASME J. Fluids Eng., **127**, pp. 734–742.
[13] da Silva, A. K., Kobayashi, M. H., and Coimbra, C. F. M., 2007, "Optimal Theoretical Design of 2-D Microscale Viscous Pumps for Maximum Mass Flow Rate and Minimum Power Consumption," Int. J. Heat Fluid Flow, **28**, pp. 526–536.
[14] Matthews, M. T., and Hill, J. M., 2008, "Lubrication Analysis of the Viscous Micro/Nano Pump With Slip," Microfluid. Nanofluid., **4**(5), pp. 439–449.
[15] Fuhr, G., Hagedorn, R., Müller, T., Benecke, W., and Wagner, B., 1992, "Microfabricated Electrohydrodynamic (EHD) Pumps for Liquids of Higher Conductivity," J. Microelectromech. Syst., **1**, pp. 141–146.
[16] Richter, A., Plettner, A., Hofmann, K. A., and Sandmaier, H., 1991, "A Micromachined Electrohydrodynamic (EHD) Pump," Sens. Actuators, A, **29**, pp. 159–168.
[17] Harrison, D. J., Manz, A., and Glavina, P. G., 1991, "Electroosmotic Pumping within a Chemical Sensor System Integrated on Silicon," Proceedings of the International Conference on Solid-State Sensors and Actuators Transducers, pp. 792–795.
[18] Maxwell, J. C., 1879, "On Stresses in Rarified Gases Arising From Inequalities of Temperature," Philos. Trans. R. Soc. London, **170**, 231–256.
[19] Schaaf, S. A., and Chambre, P. L., 1961, *Flow of Rarefied Gases*, Princeton University Press, Princeton, NJ.
[20] FLUENT 6.0 User Guide Manual, 2002, Fluent, Inc., NH.

Pre-Stall Instability Distribution Over a Transonic Compressor Rotor

A. J. Gannon

G. V. Hobson

Turbopropulsion Laboratory,
Naval Postgraduate School,
Monterey, CA 93943

An investigation of the behavior of a transonic compressor rotor when operating close to stall is presented. The specific areas of interest are the behavior and location of low-frequency instabilities close to stall. In running close to stall, compressors can begin to exhibit nonperiodic flow between the blade passages even when appearing to be operating in a stable steady-state condition. The data from the current rotor clearly show that low-frequency instabilities were present during steady-state operation when stall was approached. These frequencies are not geometrically fixed to the rotor and typically appear at 0.3–0.8 of the rotor speed. The presence of these low-frequency instabilities is known and detection is reasonably commonplace; however, attempts to quantify the location and strength of these instabilities as stall is approached have proved difficult. In the current test fast response pressure sensors were positioned in the case-wall; upstream, downstream, and over the rotor blade tips. Simultaneous data from the sensors were taken at successive steady-state settings with each being closer to stall. A time domain analysis of the data investigates the magnitude of the instabilities and their transient effect on the relative inlet flow angle. The data are also presented in the frequency domain to show the development and distribution of the instabilities over the rotor as stall was approached. Initially the instabilities appeared within the rotor row and extended downstream but at operation closer to stall they began to protrude upstream as well. The greatest amplitude of the instabilities was within the blade row in the complex flow region that contains phenomena such as the tip-vortex/normal-shock interaction and the shock/boundary-layer interaction. In addition as stall is approached the growth of the instabilities is nonlinear and not confined to one frequency. [DOI: 10.1115/1.3112388]

Keywords: transonic compressor, near-stall operation, nonaxisymmetric flows

1 Introduction

It has been observed experimentally that during operation near stall in an axial flow fan or compressor rotor the flow can become nonperiodic between blade passages and low frequency; below once-per-revolution, instabilities in the flow field can be present. These instabilities have been measured and reported for the current test rotor [1]. Labels such as spike and modal instabilities have been used to describe them [2,3]. In some early studies the instabilities were detected when stall was imminent and it was thought that these may be a precursor event. More recent work has shown that this phenomenon can be present even in so called steady-state conditions when operating near to stall or surge [4,5]. In this work they are called “low-frequency instabilities” to avoid confusion with precursor, spike, and modal instabilities and with poststall rotating instabilities. While low-frequency instabilities usually indicate that the machine operates near to stall they do not necessarily indicate that stall is imminent. Experimental results indicate that the magnitude of these low-frequency instabilities is significant [1].

Understanding of these structures has significance in the design of compressors with regard to their stable operation near to stall. Simulations that force a periodic assumption may not accurately predict stall or surge points, either being optimistic or pessimistic making design optimization difficult. Close to stall this periodic assumption becomes less accurate and it appears that in order to properly model the flow field an unsteady simulation of the complete rotor needs to be performed. The instabilities that resulted in the rotor meant it experienced as much as a 2 deg change in the inlet flow angle near stall over a 5–10 revolution period [1].

This study aims to more accurately quantify and present the magnitude and frequency of these instabilities in a transonic rotor. To do this simultaneous results of a number of sensors are combined to show the distribution of the instabilities over the rotor. The frequency and distribution of the instabilities are shown at various operating points each successively closer to stall. The distributions are of interest as the region of greatest magnitude of the instabilities occurred in the complex flow region containing the tip-vortex shock interaction and shock boundary-layer interaction. In addition as stall was approached the low-frequency instabilities are detectable well upstream and downstream of the rotor.

The detection of these low-frequency instabilities required the use of high-speed pressure sensors and good signal processing techniques. It will be shown that the instabilities do not behave in either a linear fashion toward stall nor do they occur at predictable frequencies. In addition the magnitudes of the instabilities were significant, which resulted in observable changes in the bulk flow properties.

There may be many possible mechanisms for the production of these low-frequency instabilities. The fact that the present test case was a rotor-only machined blisk seemed to indicate that they were inherent in the flow without the need for external excitation. Further improvement to stall margin for stable operation of future compressors close to stall will demand better methods to simulate these low-frequency instabilities and better understanding of their causes and effects on machine operation.

Contributed by the Fluids Engineering Division of ASME for publication in the Journal of Fluids Engineering. Manuscript received August 18, 2008; final manuscript received January 29, 2009; published online April 23, 2009. Assoc. Editor: Chunill Hah. Paper presented at the ASME Turbo Expo 2008: Land, Sea and Air (GT2008), Berlin, Germany, June 9–13, 2008.

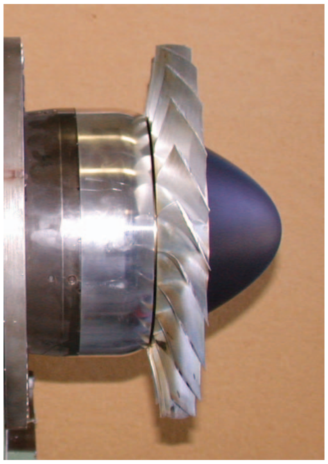

Fig. 1 Transonic test rotor

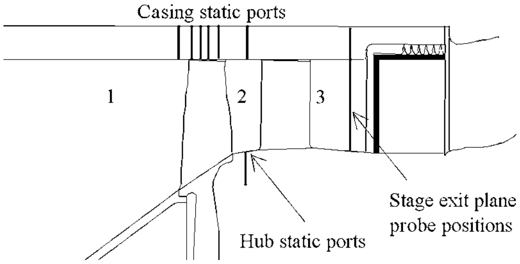

Fig. 2 Transonic test rotor

2 Experimental Apparatus

The rotor used, as shown in Fig. 1, was designed by Sanger [6] and subsequently tested by Gannon et al. [7]. A detailed description of the stage, instrumentation, and test rig, as well as methods to accurately determine the efficiencies, is contained in the papers [6,7]. To summate the rotor consisted of 22 blades of aspect ratio 1.2 with a design tip speed of 396.2 m/s (1300 ft/s), diameter of 0.2794 m (11 in.), and axial chord of 22.4 mm (0.884 in.). The rotor-only and stage design pressure ratios are 1.61 and 1.56, respectively, with a design mass flow rate of 7.75 kg/s (17.05 lb/s). The rotor was driven by an air turbine with the pressure ratio controlled by an upstream throttle.

2.1 Tip-Gap. An abradable strip was positioned over the rotor and before any runs took place the cold tip-gap was measured. Initially the machine was run to a particular low speed, shut down, and the new increased cold tip-gap measured. While this does cause a casing groove it ensures a small tip-gap. This process was repeated in steps until the design speed was reached. At 100% speed the rotor tip-gap was 25 μm (0.001 in.). This allowed the hot tip-gap to be inferred for different speeds as shown in Table 1.

2.2 Instrumentation. Two types of instrumentation, one set for steady-state performance measurement and a second for high-speed data capture, were installed on the rig. The steady-state instrumentation consisted of 2 upstream and 20 downstream Kiel stagnation-pressure probes. Stagnation-temperature probes to measure the efficiency consisted of two upstream and nine downstream [7]. An additional temperature sensor was embedded in a static port downstream of the rotor in the case-wall. The number of temperature probes has been increased from six to nine as this allows for more accurate efficiency measurement especially at off design conditions when the downstream temperature profile was distorted. The Kiel probe angles were also turned away from axial as no stator row was present. The angles were based on the streamline curvature code output from the design report of the rotor [8]. The angles are measured from axial, range from 45 deg at the hub to 39 deg at the tip. The stagnation Kiel probes used to measure the stagnation pressure have a high accuracy in the region of ±54 deg in yaw and ±49 deg in pitch. The probes were arranged at 15 deg intervals on a plane four axial chord lengths downstream of the rotor trailing tip as shown in Fig. 2.

The high-speed data system consisted of nine Kulite static-pressure transducers (referred to as high-speed sensors) over the rotor as shown in Fig. 3. Kulite sensors (1), (7), (8), and (9) were upstream of the rotor while sensor (2) was positioned at the leading edge and acted as the position reference. Sensors (3)–(5) were over the rotor and sensor (6) downstream of the rotor. One impact or stagnation Kulite sensor (10) was positioned upstream of the rotor facing the flow. It was positioned 0.44 of the rotor diameter upstream of the rotor at midspan (45 mm upstream of the nose cone) of the blade to measure the strength of the low-frequency instabilities upstream of the rotor. The sensors were sampled at 196.6 kHz giving 19.6 readings per blade passage at design speed. This was sufficiently high enough to ensure that the magnitude of any aliased higher frequencies was small.

3 Experimental Program

The present test program concentrated on compressor operation near to stall. The basic performance of the machine and the location of the stall lines were previously determined [7,9]. In addition the operating region for the appearance of the flow instabilities for the rotor-only case was known [1].

Detailed data at various speeds from the subsonic to the transonic region were taken. The compressor was not stalled at 100% speed in the rotor-only configuration due to concerns about the high overspeed during stall. For brevity, only the 70% speed, subsonic operation, and the 90% and 95% speeds, transonic operation are presented. Although the two transonic speeds are close the behavior of the low-frequency instabilities close to stall is markedly different.

To measure data for a particular speed line the compressor was set to operate in a steady-state condition at a point near to stall but far enough away that low-frequency instabilities were not expected to be significant. A sample of high-speed data was then taken. The compressor operating point was then moved incrementally closer to the stall point and data taken again. This allowed the development of these low frequencies to be observed as stall was approached. Data samples of 0.5 s were taken, which was sufficient to resolve the low frequencies of interest. At 95% speed this was equivalent to 214 rotor revolutions and approximately 100 cycles of the low-frequency flow variations.

Figure 4 shows the performance maps for the rotor-only configuration. Points at which the high-speed data were taken are shown with (A) being closest to stall and (F) farthest away. Point

Table 1 Rotor tip gaps

Speed (%)	70	90	95
Tip-gap	127 μm (0.005 in.)	25.4 μm (0.001 in.)	12.7 μm (0.0005 in.)
Tip-gap/blade chord	0.0025	0.0005	0.0002

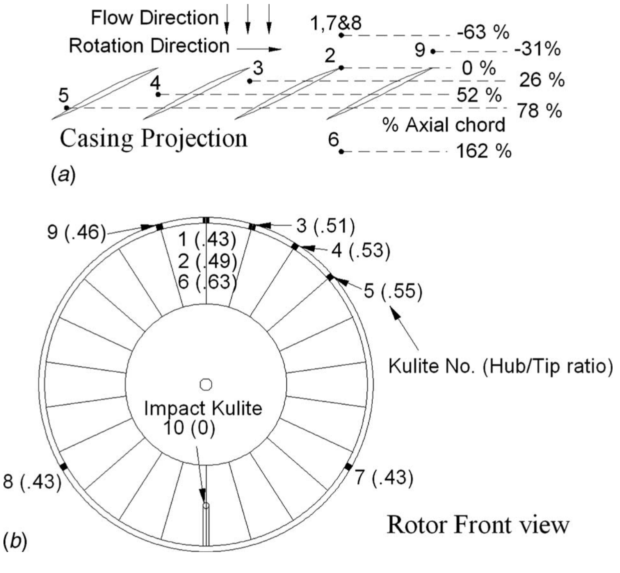

Fig. 3 Kulite sensor positions

(F) was at the full open throttle position of the test rig, point (E) was at peak efficiency, and point (D) was where low-frequency instabilities first appeared. These points are used for reference throughout the rest of the paper.

4 Postprocessing

4.1 Time Domain. In order to isolate the signals of interest in the time domain a selective filtering technique was required. These are well documented in the fields of signal processing but a basic outline found to be applicable to the current field is described here. A digital convolution filter method was used [10]. The steps are as follows: (1) A suitable filter was constructed in the time domain. (2) The sampled signal and filter are both transformed into the frequency domain using a fast Fourier transform (FFT). It was important to note that the FFT of the sampled signal and filter had to be of the same length. (3) A simple element by element complex multiplication of the filter and sample in the frequency domain was performed. (4) The product was converted back to the time domain using an inverse fast Fourier transform (IFFT) again of the same length to give the resultant filtered signal. The method for designing a low-pass digital filter was as

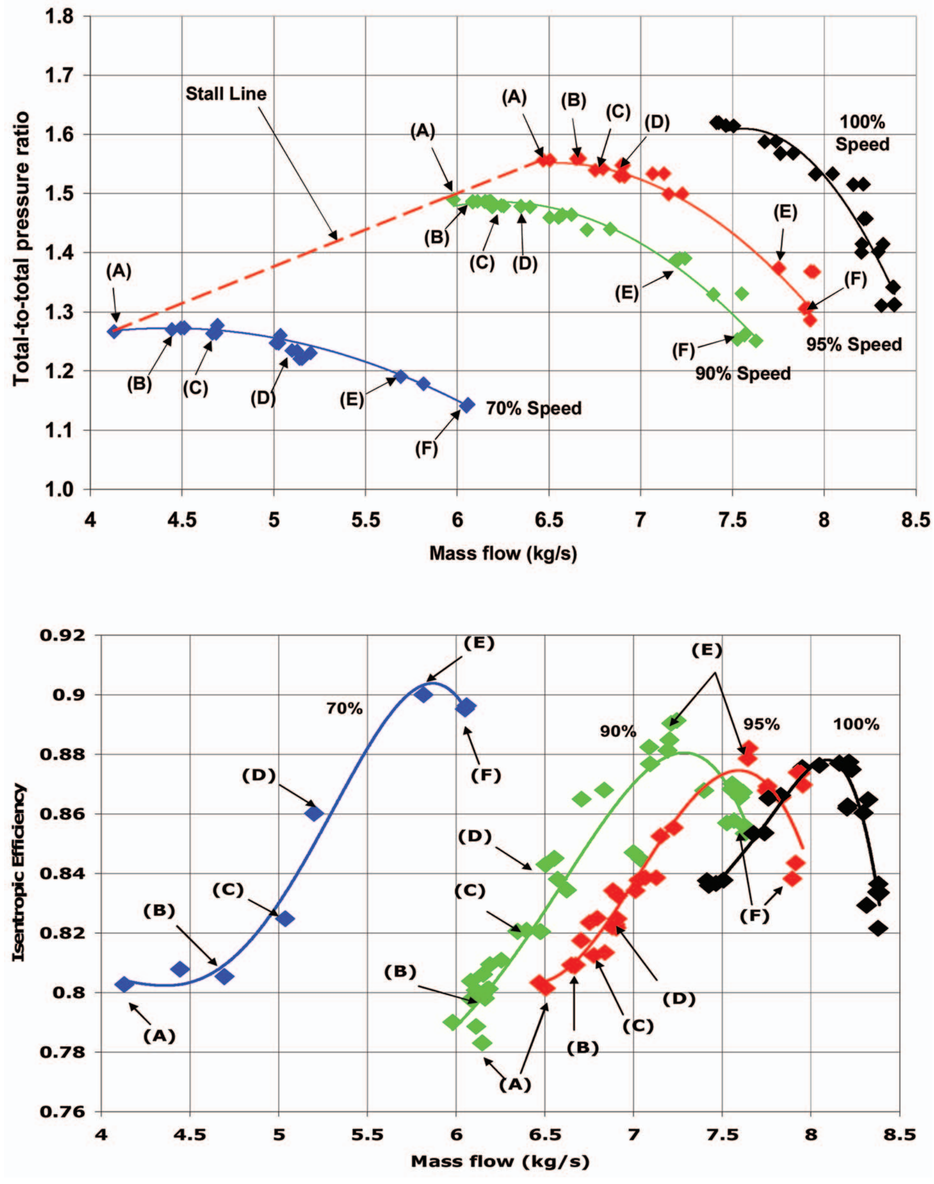

Fig. 4 Rotor-only performance maps

follows. The desired cutoff frequency f_c must be nondimensionalized by the sampling frequency

$$f_c = \frac{\text{cutoff frequency}}{\text{sampling frequency}} \tag{1}$$

The roll-off bandwidth (BW) was defined as the desired frequency width where the signal dropped from 99% to 1% in strength. The constant BW was defined as follows

$$\text{BW} = \frac{\text{roll-off width}}{\text{sampling frequency}} \tag{2}$$

The bandwidth of the roll-off determined the number of points required for the digital filter and BW was used to construct a vector M from –2/BW to 2/BW in steps of 1 (2/BW must be rounded to an integer value)

$$M = -\frac{2}{\text{BW}}:1:\frac{2}{\text{BW}} \tag{3}$$

The so called sinc function was used to create an ideal low-pass filter vector h_{sinc} as follows

$$h_{\text{sinc}} = \frac{\sin(2\pi f_c M)}{2\pi f_c M} \tag{4}$$

Due to the filter length being finite a truncation error occurs that requires correction. To achieve this, a Blackman window is used (w_{Black}) and results in near unity gain in the band-pass region

$$w_{\text{Black}} = 0.42 - 0.5\cos\left(\frac{2\pi}{M}\right) + 0.08\cos\left(\frac{4\pi}{M}\right) \tag{5}$$

An element by element vector multiplication of the sinc filter h_c and Blackman window w_{Black} gave the filter shape h_{Black}. The filter must be normalized to ensure a unity gain in the pass region to get the final filter h as follows

$$h_{\text{Black}} = h_{\text{sinc}} \times w_{\text{Black}} \Rightarrow h = h_{\text{Black}} / \sum h_{\text{Black}} \tag{6}$$

To create a high-pass filter, all the elements of h_{Black} were multiplied by -1 and unity added to the central sample. A low-pass, h_1, and high-pass, h_2, filter were then combined to form a band-pass filter. Multiple band-pass filters can be added together but only one was used here. With the desired digital filters constructed the steps outlined earlier can be used to filter the sampled signal S to obtain the filtered signal S_f

$$S_f = \text{IFFT}(\text{FFT}(S) \times (\text{FFT}(h_1) \times \text{FFT}(h_2))) \tag{7}$$

MATLAB was used to perform the filtering techniques, which had built in functions to perform the above listed operations. All frequencies were normalized to the rotor speed in rpm. The band-pass frequency filter was from 0.3 to 0.85 with a roll-off of 0.05 rpm.

4.2 Frequency Domain. Observation of the signals in the frequency domain was also useful. In order to better isolate the low-frequency signals the signals were transformed into the frequency domain using FFTs as these were computationally cheap and easily implemented. A spectral analysis of the frequency data showed the magnitude and frequency of the sampled pressures over the rotor. The long data samples and high sampling rate ensured minimal aliasing and a good signal to noise ratio. To ensure that the correct magnitude of a particular frequency was captured the sampled signals were padded with zeros, usually eight times the length of the sample. Practically this was done by performing a longer FFT than the number of points in the sample. If this very simple method was not used the magnitude would often be cropped especially at lower frequencies [10], which were of special interest in this research.

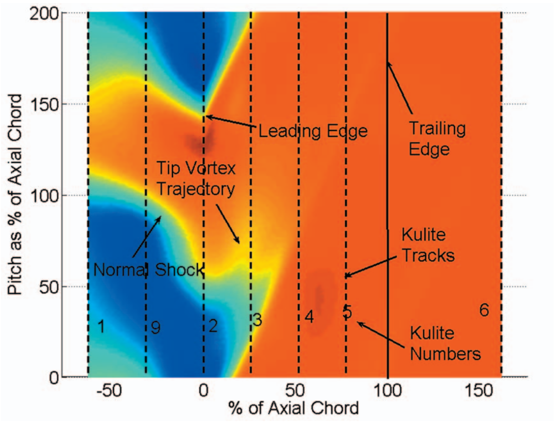

Fig. 5 Experimental pressure contours near stall, 95% speed (A)

5 Results

Figure 5 shows the experimentally obtained projection of the pressure contours by the rotor on the casing. Superimposed in this figure are the measurement locations of the Kulite sensors as the rotor passes over them. It was obtained using 0.5 s of data at 95% speed (214 rotations=4717 blade passages). A full set of these figures is presented in Ref. [11]. The sensor positions can be cross referenced with the low-speed frequency data presented in the figures that follow. In addition the detached shock typical of near-stall flow, as well as the track of the tip-vortex as it impinges on the shock, is indicated.

5.1 Time Domain. Observation of the filtered signals is useful in that is shows that their magnitude is not insignificant as compared with the raw signal. The three main regions of interest at near-stall operation are focused on the inlet just upstream of the rotor, the rear part of the blade where the large low-frequency instability magnitudes are found, and downstream of the blade as this would affect any following blade rows.

Figure 6 shows an example of a signal passed through a band-pass filter with a pass band of 0.25–0.9 of rotor revolution. The flow condition was at 95% speed at the closest stable operating point near to stall (point (A) Fig. 4). Results from three Kulite sensors, (1) upstream, (4) within the blade row, and (6) downstream are shown. Underlying the filtered signals are the raw data to give a visual comparison of the magnitudes. The data are presented for 50 rotor revolutions. A closer inspection of the raw signal would show that the blade passing frequency is dominant as expected.

It should be noted that if the flow was periodic in the blade-to-blade sense, the filtered signal would be constant. This is clearly not the case as shown in Fig. 6. Upstream of the rotor at sensor (1) the filtered signal was fairly small when compared with the raw signal, which was dominated by the blade passing frequency. Once inside the blade row at sensor (4) the magnitude of the instabilities increased while the blade passing amplitude decreases and the instabilities became an appreciable fraction of the pressure variations. Once the flow had exited the rotor the instabilities were still present and would affect downstream blade rows. In addition to wake effects variations in the bulk flow would affect downstream blade row performance. In Fig. 6, for sensor (6) downstream of the rotor, the effects of the underlying instabilities can be seen on the raw signal, which correspond to the underlying low-frequency instabilities. In a simulation where a periodic assumption is made these would not be captured.

Figure 7 presents only the filtered signals on a larger scale with the upstream impact-sensor included. It can be seen that there is an amplification of the signal from the upstream impact-sensor (10) to the over-rotor sensor (4) and a slight decrease downstream

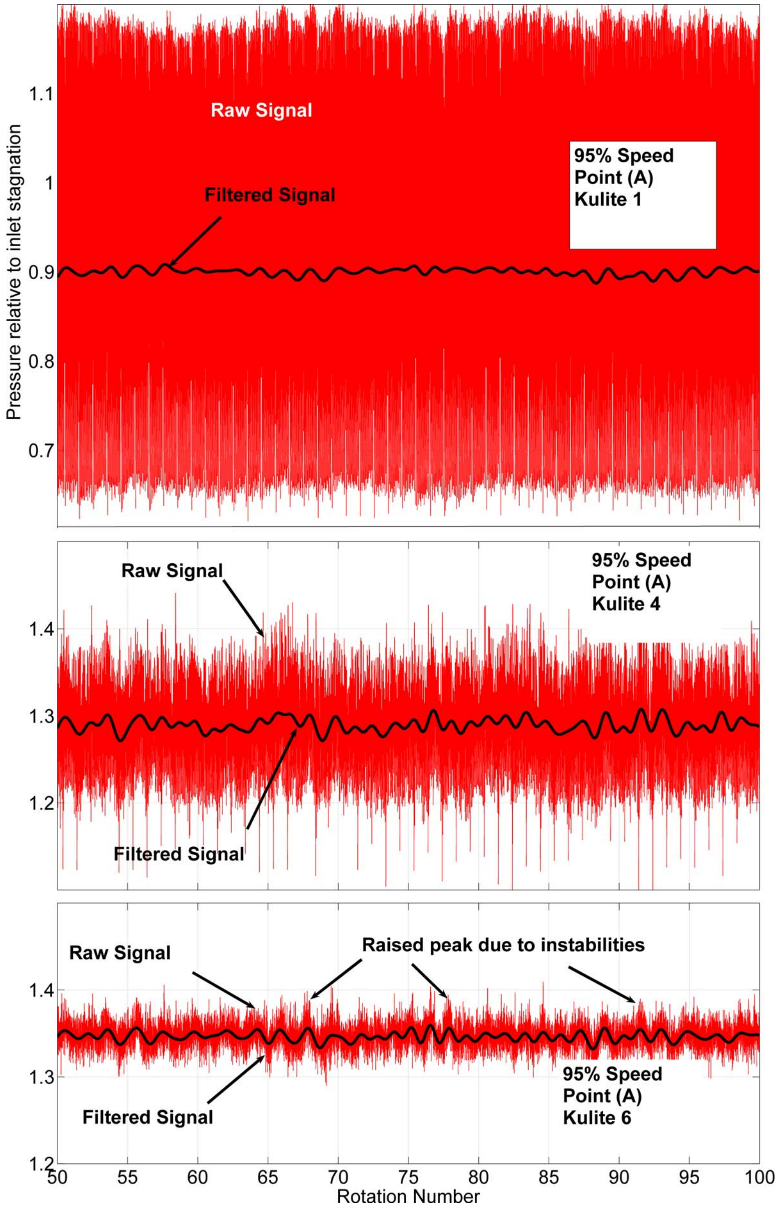

Fig. 6 Resultant filtered signal (95%)

of the rotor to sensor (6). These signals would be responsible for variations in the bulk flow not associated with the blade passing frequencies. The above signals were sampled simultaneously so it is also interesting to note that there are quite significant differences in the peaks. Where sensor (1) shows a small amplitude, sensor (4) shows a large one. The spectral analysis shows this in more detail.

Initial results looking at the variations of the inlet flow angle at 95% were presented by Gannon and Hobson [1]. Here too the assumption was made that the upstream stagnation pressure was constant. The amplitude of this filtered signal at the inlet is small when compared with the filtered static signal at the casing and assuming it is constant results in a more conservative calculation of the change in relative inlet angle.

Knowing the inlet static and stagnation pressures and using the measured upstream stagnation temperature allow the inlet Mach number to be calculated. Here the filtered signals derived from the Kulite sensors were used. In addition to the flow Mach number the blade tip speed was known and this allowed the low-frequency variation in the relative inlet angles to be calculated using a basic velocity triangle. Zero tangential inlet velocity was assumed but in the presence of changing circumferential static pressures such as those shown in Fig. 7 this was not strictly accurate. Figure 8 shows the variation in the rotor relative inlet angle for operation near to stall. In the figure the low frequency of the variations is evident with about 5 cycles for every ten rotor revolutions. A very low-frequency cycle was also observed at 95% speed but this was thought to be either a system oscillation or "beats" resulting from interference between the different frequencies.

Table 2 shows the amplitude of the variation for near 200 revolutions. The table shows that the effects of the low-frequency instabilities are significant. While it is not thought that the flow separates at the leading edge of the rotor blade, changes in inlet flow angle would affect the flow through the blade passage. As the frequencies of the instabilities are known we see that one peak-to-trough is roughly 0.75 of a revolution. Knowing the inlet speed we can then show through a rough calculation that the blade will have 14 chord lengths of flow from one peak-to-trough of a low-frequency signal. This would be sufficient time for the boundary

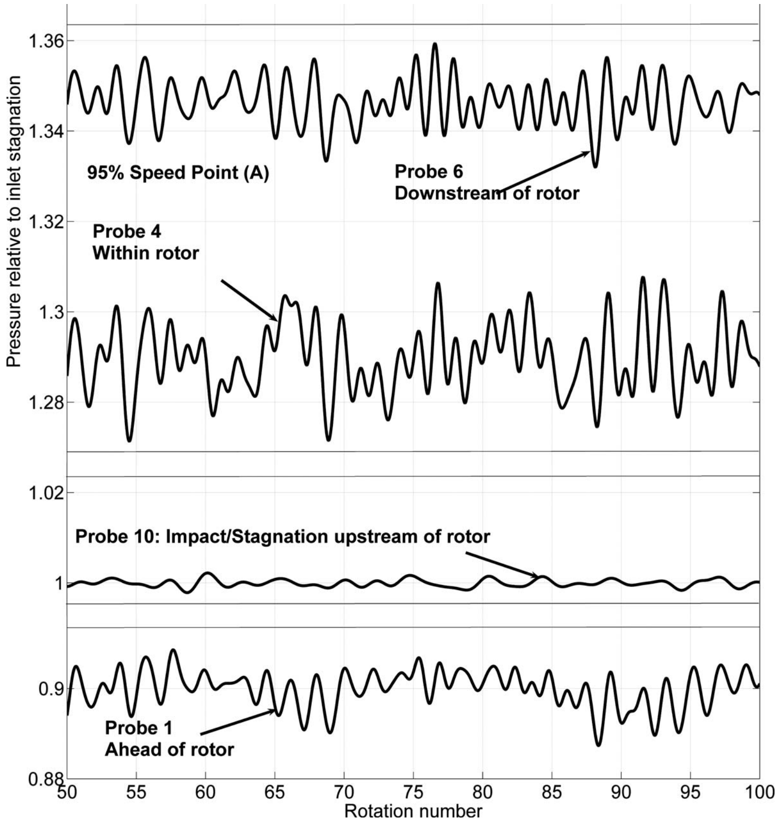

Fig. 7 Filtered signals through the rotor (95%)

layer to respond to these signals and thus each rotor passage would likely be operating along the relevant machine characteristic for a particular speed.

Tables 3–5 compare the peak-to-peak values of pressure for the raw unfiltered signal and the filtered signal for 95%, 90%, and 70% speeds, respectively, when operating close to stall. The tabulated 95% speed data correspond to those from Figs. 6 and 7. The filtered peak-to-peak values are a measure of the passage unsteadiness. At all speeds once the flow entered the blade row, the magnitudes of the low-frequency instabilities increased from the leading edge to the rear of the rotor. This is typical of diffuser type devices that tend to amplify flow distortions. This contrasted with the raw signal that was largest near the leading edge and decreased through the rotor thus increasing the ratio between the raw and filtered peak-to-peak amplitude through the rotor. The ratio of the peak-to-peak filtered over peak-to-peak raw data shown in the fifth column allows for comparison between speeds. This is most evident at probe (6) downstream of the rotor, which grows from 0.097 at 70% speed to 0.241 at 95% speed.

It is probable that it would be a peak and not a mean adverse pressure gradient that would precipitate a stall. The data in Tables 3–5 indicate that a downstream blade row may be subjected to a greater magnitude of instability than the one upstream of it. In the present rotor forcing periodicity would cause a simulation to fail to capture the nonaxisymmetry of the flow. It is thought that this would cause the greatest error in the prediction of the stability limit of the machine. Each individual passage would still be expected to operate along the unique characteristic of the machine.

5.2 Frequency Domain.

A spectral analysis allowed for better observation of the distribution and magnitude of the low-frequency instabilities over the blade row. The spectral analyses were performed on the signals once they had been nondimensionalized to the inlet stagnation pressure (Figs. 6 and 7).

A brief summary of the method is shown in the following figures. Figure 9 shows the complete spectral power distribution from the single Kulite sensor (4) at 95% speed. The low-frequency region of interest below the once–per-revolution signal is indicated. The once-per-revolution signal was an indication of imperfections in the rotor. The largest magnitude was as expected at the blade passing frequency. Due to the high sampling speed a significant roll-off at high frequencies was found meaning that aliasing was minimal.

Figure 10 expands the low-frequency region presented in Fig. 9 on a linear scale. It shows the low-frequency instabilities that are present when operating close to stall. No clear higher-frequency harmonics of the signals were observed indicating that the instabilities are fairly pure sinusoidal signals. Recalling that the physical axial position of the Kulite sensors relative to the blade was known (Fig. 5) it is possible to present the distribution of the signals over the blades as shown in the next sets of figures.

Figure 11 shows the combined signals of the Kulite pressure sensors over the rotor presented as a waterfall plot. At each sensor position the relevant low-frequency spectrum similar to that shown in Fig. 10 is plotted. The four operating points presented correspond to those in Fig. 4 at 95% speed. All magnitudes from points (A) to (D) are plotted on the same vertical scale. A cursory observation of the figures indicates that there is a substantial change in the distribution and frequency of the low-frequency instabilities as stall is approached.

At point (D) small instabilities were present at the leading edge of the rotor row and decayed toward the trailing edge of the blade. At point (C), where the rotor was operating closer to stall, the first significant low-frequency instabilities occurred in the aft portion of the rotor at sensors (4) and (5). An inspection of Fig. 5 showed this to be behind where the normal-shock wave impinged on the blade suction surface. This region contains a thick boundary layer especially when operating close to stall. Moving even closer to stall to point (B) the dominant instability frequency abruptly

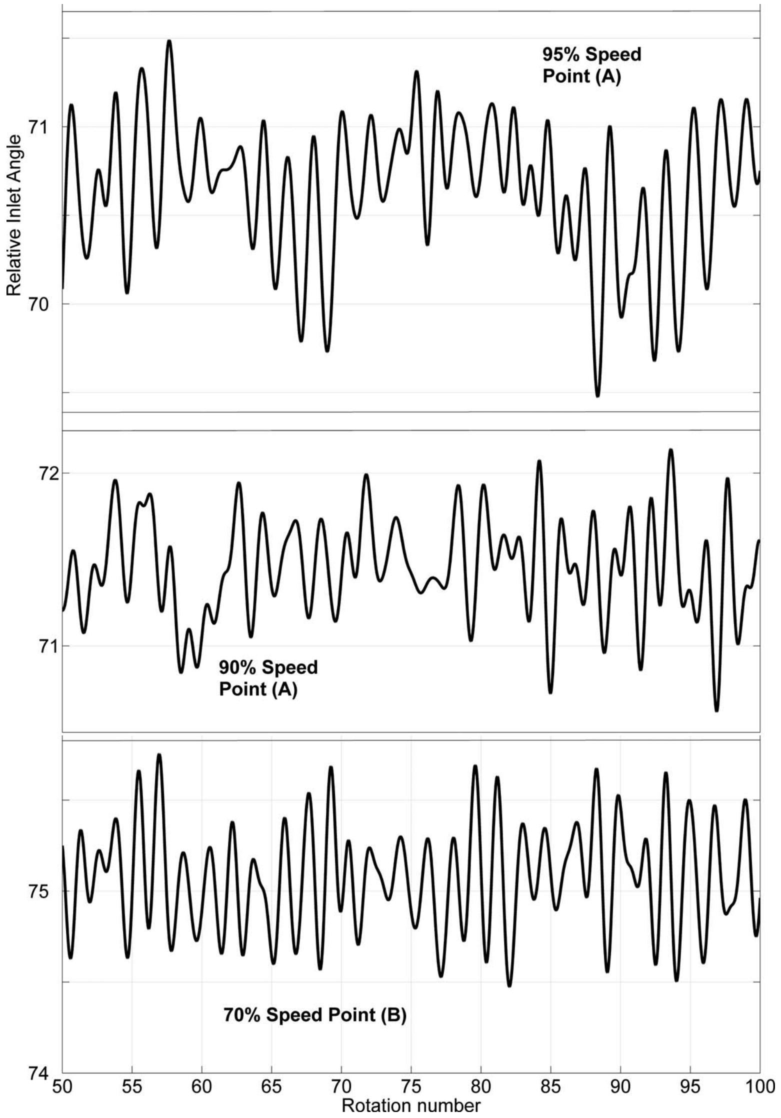

Fig. 8 Relative inlet angle variation close to stall

changed and in addition began to protrude ahead of the rotor blade. This could be due to the tip-vortex shock interaction becoming stronger and more complex. At point (A), the closest stable operating point before stall, one dominant frequency emerged. The position of greatest magnitude was found again at sensors (4) and (5) from midrotor to the trailing edge of the blade within the thick boundary-layer region. It could also be seen that

Table 2 Variation in inlet flow angle when operating near to stall

Speed and point	Mean inlet flow angle (deg)	rms variation (deg)	Peak-to-peak variation (deg)
95% (A)	70.6	0.351	2.04
90% (A)	71.5	0.341	2.21
70% (B)	75.1	0.269	1.65

Table 3 Variations in sensor pressure at 95% speed

Sensor No.	Mean pressure	Raw peak to peak	Filtered peak to peak	Ratio
10	1.00	0.094	0.0096	0.102
1	0.90	0.6069	0.0215	0.035
4	1.29	0.3767	0.0406	0.107
6	1.35	0.1453	0.0351	0.241

Table 4 Variations in sensor pressure at 90% speed

Sensor No.	Mean pressure	Raw peak to peak	Filtered peak to peak	Ratio
10	1.00	0.0502	0.0048	0.092
1	0.92	0.5649	0.0200	0.035
4	1.25	0.3281	0.0359	0.109
6	1.30	0.1269	0.0234	0.184

Table 5 Variations in sensor pressure at 70% speed

Sensor No.	Mean pressure	Raw peak to peak	Filtered peak to peak	Ratio
10	1.00	0.0335	0.0022	0.065
1	0.97	0.1426	0.0074	0.052
4	1.14	0.1826	0.0193	0.106
6	1.17	0.1029	0.0100	0.097

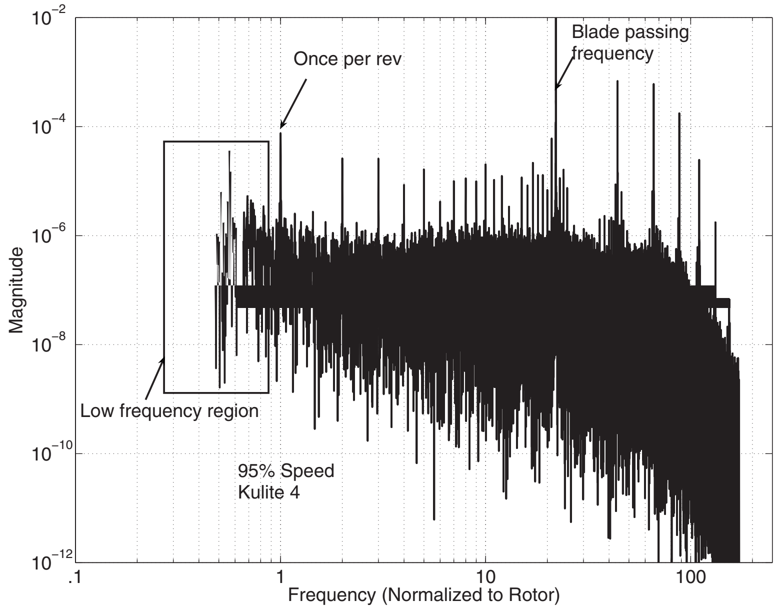

Fig. 9 Spectral analysis from FFT (log-log scale)

this instability was detectable upstream of the rotor in sensors (1) and (9) and as a small peak at the impact-sensor (10) more than five axial chords upstream.

For completeness Fig. 12 shows the low-frequency regions for peak efficiency and choked operation of the rotor at 95% speed. It can be seen that any low-frequency instabilities are barely detectable above the background noise. There was a slight increase in their strength as the compressor loading increased from a choked condition to peak efficiency.

Figure 13 presents the low-frequency instabilities for the 90% speed case again showing the four points closest to stall (Fig. 4). Again a constant vertical scale was used throughout the series of figures. The vertical scale is smaller than for 95% speed due to the lower speed. What was notable is that the relatively small difference in speeds caused a significantly different type of behavior in the instabilities as stall was approached. Point (D) was the first point where instabilities were significant. Operating slightly closer to stall at point (C) the magnitude of the instabilities increased. The largest magnitudes were again in the midchord region of the blade and a small instability was seen to protrude upstream. Moving closer to stall to point (B) four dominant frequencies began to emerge and the first significant signs of instabilities protruding upstream began to occur. As at 95% speed the largest region of instability was in the rear to trailing part of the blade and as stall was approached the instabilities did not decay behind the blade row. At point (A), the closest stable operating point to stall, two dominant instabilities emerged at 0.5 and 0.75 of rotor speed. The lower frequency protruded and was detectable well upstream of the blade row. The higher frequency had a larger magnitude but increased toward the rear of the blade row. Unlike at 95% speed, at 90% speed no single frequency emerged dominant suggesting that the mechanisms that cause these instabilities can act indepen-

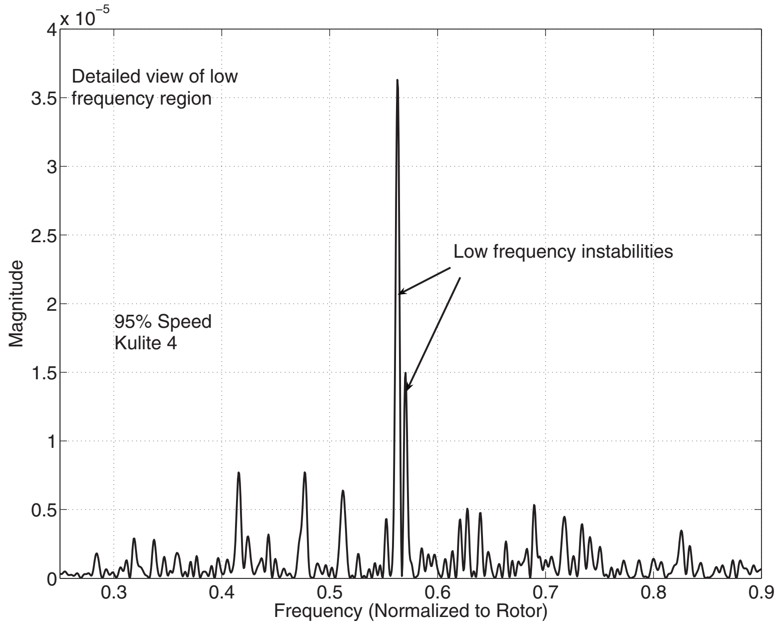

Fig. 10 Low-frequency region (linear scale)

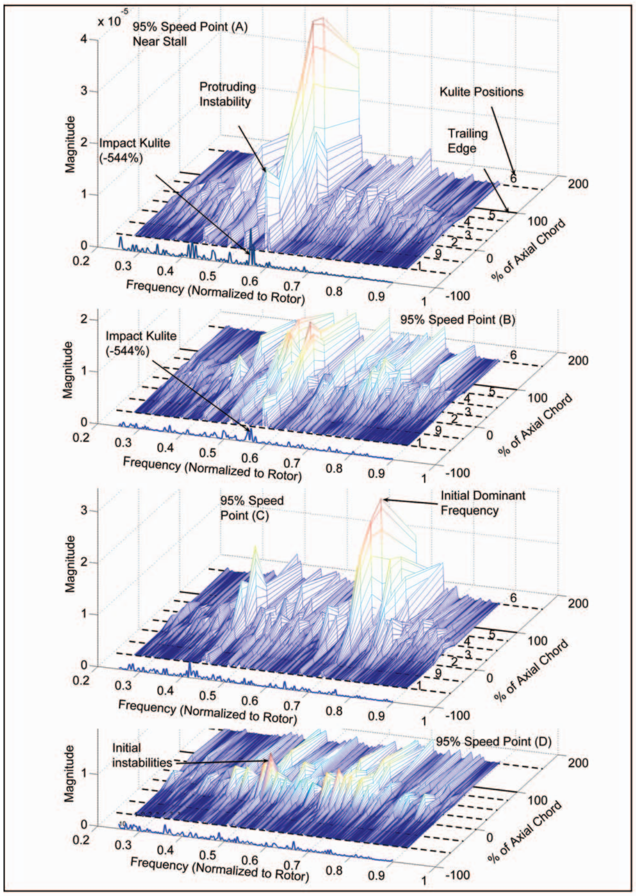

Fig. 11 Near-stall low-frequency instabilities (95%)

dently of each other.

Figure 14 shows the low-frequency instabilities for a subsonic case at 70% speed. The magnitude of the instabilities was lower at 70% speed but still detectable. Again a nonlinearity in the growth of the instabilities toward stall was present. At point (D) the instabilities first appeared and increased noticeably when approaching stall to point (C). Here two peak instabilities appeared, once again in the rear section of the blade passage. When moving closer to stall to point (B) more instability frequencies appeared but the peak magnitude was reduced. As with the transonic cases some instabilities protruded upstream of the rotor row.

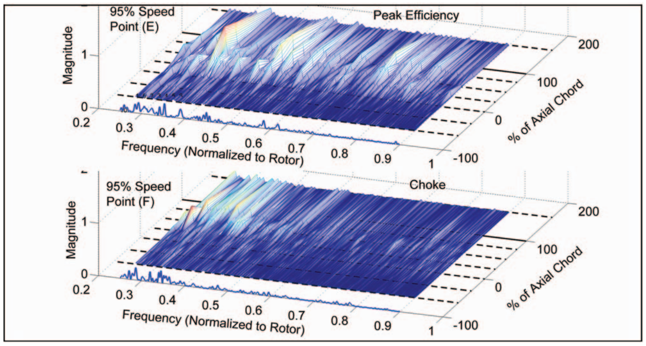

Fig. 12 Far from stall low frequencies (95%)

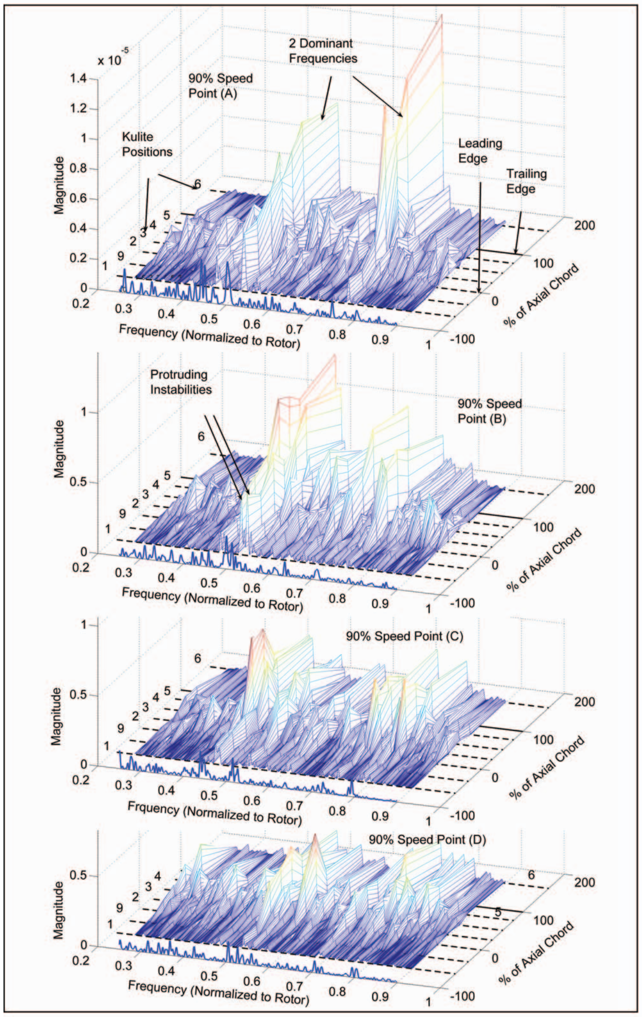

Fig. 13 Near-stall low-frequency instabilities (90%)

6 Discussion

The ability to observe the collective behavior of the low-frequency instabilities allowed some insight into their possible causes and the prestall characteristics of some transonic machines. It is important to recall that the periodic assumption of the flow in each passage being the same and steady relative to the blade does not always hold when operating close to stall [1,5]. Typical near-stall flow of a transonic machine contains a normal detached shock ahead of the blades with a tip-vortex that intersects the shock, which distorts it as shown in Fig. 5. The shock impinges on the suction surface of the blade ahead of it.

6.1 Protruding Instabilities. The so called protruding instabilities indicated in the previous figures were most likely due to the movement of the normal shock relative to the blade row as the shock clearly protruded upstream of the blade. At peak efficiency the shock in a transonic rotor is attached to the leading edge and thus geometrically fixed to the rotor. A detached normal shock would be affected by any change in the passage blockage and a changing position relative to the blade would have been detected upstream of the rotor. This movement may be due to multiple mechanisms as indicated by the more than one protruding-instability that were sometimes present (Fig. 13, (A) and (B)). The tip-vortex may also not be steady near stall and could affect the normal shock, which of course in turn would affect the following blade's flow.

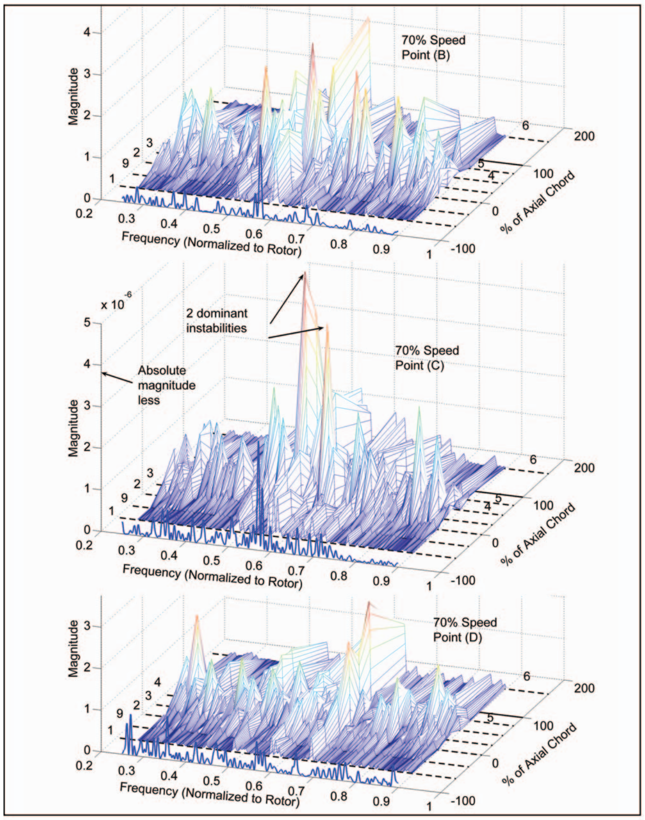

Fig. 14 Near-stall low-frequency instabilities (70%)

6.2 Peak Instability Region. The largest instabilities that appeared were within the blade passage at sensors (3)–(5) at all speeds. In this region the tip-vortex would have been interacting with the detached normal shock as mentioned before. This also corresponded axially to the location of the shock impinging on the blade suction surface. While the vortex-shock interaction has a strong influence in the tip region the shock-boundary impingement region occurs for a significant part of the span in a transonic machine especially at higher Mach number.

6.3 Instability Behavior. The behavior of the instabilities was generally nonlinear when approaching stall with different frequencies becoming dominant as stall was approached. It is important to note, however, that as long as they remain below a certain magnitude stall would not occur. The main difference between 95% and 90% speeds was that at 95% speed the two main instabilities coalesced. At 95% speed, one of the instabilities presumably acted as a strong forcing function causing the other to follow suit (Fig. 11). At 90% speed (Fig. 13) the two instabilities remained independent.

The exact mechanism that causes the instabilities can only be hypothesized here. They clearly moved relative to the rotor but only appeared when the compressor began to approach stall. The types of flow found in a rotor, such as the tip-vortex, its interaction with the shock, and the detached normal shock would vary with small disturbances in the external flow field. A variation due to a small disturbance in one passage would affect the flow in the following passage akin to a stall cell. This type of behavior could reinforce itself after a number of trips around the rotor and eventually lead to the larger detectable variations that were observed. As stall is approached the adverse pressure gradients increase and flows with adverse pressure gradients such as in diffusers and rotors tend to amplify flow disturbances.

6.4 Influence on Stall. It is thought that the eventual cause of stall in a transonic rotor is a region of separated flow that spreads and becomes large enough to cause a change in the operation of the compressor at a macroscale, usually detectable by a large reduction in the pressure ratio and mass flow rate. This distinction is important as rotors can operate with localized regions of separated flow with no adverse affects. The actual stall event itself is usually very rapid and develops in a stall cell within five to ten revolutions [4,9]. The low-frequency instabilities may cyclically increase the risk of a region of flow becoming a large scale separation.

6.5 Stall Prediction Improvements. The presence of instabilities, especially at multiple frequencies, makes the exact prediction of stall difficult. As noted it may take a number of revolutions of the machine for the conditions in the passage that cause a stall to be present. This may be different for each stall event. When simulating the flow making using of a periodic boundary assumption for the blade rows this in effect numerically damps out the low-frequency instabilities. Whether this makes the simulated prediction of stall pessimistic or optimistic depends on the machine. Ideally full rotor simulations are needed and the simulations will have to be conducted over many revolutions. If a full annulus, transient simulation was performed the shocks, tip-vortex, and boundary layers would be allowed to vary between passages. As was noted though the actual change in the flow of a single passage is quite slow, around 14 chord lengths peak-to-trough, which may leave some scope to using existing single passage steady-state methods to improve designs. A design change that would indicate a stall-margin improvement in a steady-state simulation is likely to lead to a stall-margin improvement in the real machine. However, if the low-frequency instabilities increased in magnitude as this study seems to indicate the magnitude of the improvement is likely to be less than predicted.

7 Conclusions

The distribution and magnitude of low-frequency instabilities in a transonic compressor rotor operating close to stall have been presented. Using effective sampling techniques, instrumentation, and appropriate numerical methods they can be isolated and observed. In isolating these low-frequency signals through the use of filtering techniques their magnitude in the time domain can be measured. It is shown that their magnitude was significant when compared with the dominant blade passing frequency. A spectral analysis of the instability region in the frequency domain was used to investigate the development and distribution of the instabilities over the rotor blade as stall was approached. Three different speeds, one in the subsonic and two in the transonic region, were investigated. The different behaviors served to demonstrate the unpredictable nature of the development of low-frequency instabilities. The instabilities were present upstream of the rotor and suspected to be due to the normal shock protruding ahead of the rotor and moving relative to the blade leading edge. The region of greatest magnitudes was found at midchord on the blade row, which contained the tip-vortex interacting with the detached normal shock and the normal shock impinging on the blade suction surface. The clear presence of these low-frequency instabilities means that the periodic boundary condition commonly used in simulations becomes less accurate as stall is approached. This could be one possible reason for the difficulty in predicting stall points with current methods.

Acknowledgment

The present study was part of the compressor research program sponsored by the Propulsion and Power Department of the Naval Air Warfare Centre, Patuxent River, MD with Ravi Ravindranath as the technical monitor.

References

[1] Gannon, A. J., and Hobson, G. V., 2007, "Pre-Stall Modal Instabilities in a Transonic Compressor Rotor," ISABE, Beijing, China.

[2] McDougall, N. M., Cumpsty, N. A., and Hynes, T. P., 1990, "Stall Inception in Axial Compressors," ASME J. Turbomach., **112**, pp. 116–125.

[3] Camp, T. R., and Day, I. J., 1997, "A Study of Spike and Modal Stall Phenomena in a Low-Speed Axial Compressor," ASME Turbo, Orlando, FL, Paper No. 97-GT-526.

[4] Bergner, J., Kinzel, M., Schiffer, H.-P., and Hah, C., 2006, "Short Length-Scale Rotating Stall Inception in a Transonic Axial Compressor: Experimental Investigation," ASME Turbo, Barcelona, Spain, Paper No. GT2006-90209.

[5] Hah, C., Bergner, J., and Schiffer, H. P., 2007, "Rotating Instability in a Transonic Compressor," ISABE, Beijing, China.

[6] Sanger, N. L., 1996, "Design of a Low Aspect Ratio Transonic Compressor Stage Using CFD Techniques," ASME J. Turbomach., **118**(3), pp. 479–491.

[7] Gannon, A. J., Hobson, G. V., and Shreeve, R. P., 2004, "A Transonic Compressor Stage Part 1: Experimental Results," ASME Turbo Expo, Vienna, Austria, Paper No. GT2004-53923.

[8] Sanger, N. L., 1999, "Design Methodology for the NPS Transonic Compressor," TPL Technical Note 99-01, Naval Postgraduate School, Monterey, CA.

[9] Gannon, A., Hobson, G., Shreeve, R., and Villescas, I., 2006, "Experimental Investigation During Stall and Surge in a Transonic Fan Stage and Rotor-Only Configuration," ASME Turbo, Barcelona, Spain, Paper No. GT2006-90925.

[10] Smith, S. W., 1997, *The Scientist & Engineer's Guide to Digital Signal Processing*, California Technical Publication.

[11] Gannon, A. J., Hobson, G. V., and Shreeve, R. P., 2005, "Measurement of the Unsteady Casewall Pressures Over the Rotor of a Transonic Fan and Comparison With Numerical Predictions," Paper No. ISABE-2005-1099.

Front Condition for Gravity Currents in Channels of Nonrectangular Symmetric Cross-Section Shapes

B. M. Marino
CONICET Researcher
Associate Professor
e-mail: bmarino@exa.unicen.edu.ar

L. P. Thomas
CONICET Researcher
Associate Professor
e-mail: lthomas@exa.unicen.edu.ar

Instituto de Física Arroyo Seco,
Universidad Nacional del Centro,
Pinto 399,
B7000GHG Tandil, Argentina

We study the variation of the Froude number at the front of gravity currents developed in uniform channels whose cross-section shape depends on a parameter usually used in many numerical and theoretical models. The thickness and front velocity of the dense currents running on the bottom are greater for all the cases studied, resulting in a Froude number greater than that corresponding to the rectangular cross-section shape. The light currents developing along the upper boundary show the opposite trend. It is found that the results are not related to the depth and width of the channel. The relationships obtained agree with the results of laboratory experiments in which open and closed channels of different cross-section shapes are used. [DOI: 10.1115/1.3089537]

1 Introduction

Gravity currents are flows driven by horizontal buoyancy differences of a fluid running inside another fluid of slightly different density, at the top, at the bottom, or at an intermediate level. As they are present in numerous important natural and industrial events, the comprehension of the motion of its frontal region is particularly important for a variety of practical situations. For example, the analysis of gravity currents is relevant for water quality management in reservoirs as they carry suspended matters and dissolved solids across the lake, often determining the distribution of pollutant substances. Analogous environmental flows are caused by the spreading of the cooling water from a power plant in a river, the spreading of cool marine air under the warmer air overlying land (which is known as the sea-breeze), avalanches of airborne snow particles, fiery avalanches and base surges formed from gases and solids issuing from volcanic eruptions, and the spread of accidentally released liquid natural gas. The properties of this diverse range of dynamically related flows have been described and comprehensively reviewed by Simpson [1].

In particular, estuaries also exhibit a variety of phenomena driven ultimately by the density differences associated with freshwater discharge, which may be understood in terms of gravity current theory. One characteristic of the estuarine phenomenon is the tidal intrusion of brackish water formed under low energy conditions of the estuary and characterized by a range of small magnitude tides and weak effects of the wind over the flow, as typically occurs in narrow canals. The penetration of this salt-water wedge may (and frequently does) contaminate and become useless the supply of potable water and water for industrial use in coastal cities upstream, with serious consequences from the ecological and economical points of view. Although typical of estuaries with constricted connections to the sea, these tidal intrusion fronts have been observed in reservoirs and lakes where cold turbid river inflow may plunge below the less dense ambient water [2].

The main physic phenomena underlying in many natural situations can be analyzed by means of a simple experimental system constituted by a channel that is temporarily divided into two sections by a thin vertical barrier. Fresh water fills one section and salt water the other, and the levels are made equal. As soon as the barrier is raised, the dense fluid starts to collapse and countercurrents begin to flow in opposite directions, as illustrated in Fig. 1. However, the geometry for inflow channels to lakes, reservoirs, and impoundments uses to play a non-negligible role [3]. Most of the experimental works related to these situations have been conducted in channels with a constant width and sloping bottom (see Refs. [4,5] and references therein) and few researchers have dealt with a varying-width channel or diffusers (e.g., Refs. [6–10]). It is well known that the density underflow and plunge line in a diverging channel may have different regimes, and that the flow field strongly depends on several parameters: inflow Froude number, inflow aspect ratio (width/depth), the divergent angle, and the bed slope. In addition, a water course may expand its width and depth, the flow may have a significant momentum, turbulence may be important, and so on. However, as most studies are conducted in idealized geometric setups where effects of individual parameters are analyzed separately (e.g., Ref. [9]), it is not possible to generalize the available experimental results to fit all cases, especially for field applications. Supplementing the existing experimental results and providing insight into processes that are too difficult to measure in the field or in a laboratory, computational analysis was also performed (see, for example, Ref. [11]).

We are particularly interested in the influence of the transversal variations of the properties of many currents in estuaries, rivers, and natural or man-made channels. Even though the influence of the factors mentioned above deserves additional separated investigations, some indication of their effects might be inferred from previous studies. For example, Britter and Linden [4], and later Monaghan [12], found that the front velocity parallel to the slope is constant for angles less than 45 deg on rectangular cross-section channels; similarly such an unimportant effect might be expected for nonrectangular cross-section channels. Fronts in river flows with significant momentum may be analyzed on a moving frame of reference but taking into account the change in the stress of the channel contours. Britter and Simpson [13] studied the influence of the bottom stress on gravity currents generated in rectangular cross-section channels in the laboratory, and Zhou [14] in estuaries. They found that the bottom stress may dramatically change the height profile of the dense current, so the influence of the momentum of the flow should be carefully analyzed for nonrectangular cross-section shapes as well.

Although in most previous studies, authors assumed that the properties of the flow are independent of the cross-coordinate as

---

Contributed by the Fluids Engineering Division of ASME for publication in the JOURNAL OF FLUIDS ENGINEERING. Manuscript received May 13, 2008; final manuscript received January 21, 2009; published online April 1, 2009. Assoc. Editor: James A. Liburdy.

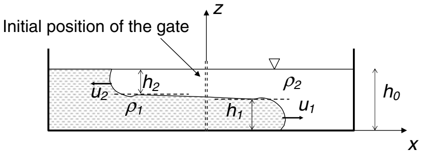

Fig. 1 Sketch of the lateral view of the lock-exchange gravity currents generated after removing the gate

occurs, in fact, in flows evolving along rectangular cross-section channels, some attempts to model theoretically the flow driven by lateral variation of the bathymetry were made. Nunes and Simpson [15] modeled the secondary transverse circulation in the Conwy estuary (North of Wales) with a parabolic cross-section, while Wong [16] and Wong and Munchow [17] modeled the gravitational circulation in Delaware Bay with a triangular cross-section, and Valle-Levinson and Lwiza [18] simulated the flow field in a coastal estuary through a rectangular cross-section with a triangular depression in the middle. Engqvist and Hogg [19] used a simple relationship for the cross-section shape to derive analytical solutions, corroborated by three dimensional numerical simulations, describing unidirectional stratified flow through a flat-bottomed nonrectangular channel.

Simpson [1] reported the empirical values of the ratio between the initial front velocities of the salt-water and freshwater flows and the thickness of the channel provided by laboratory experiments carried out in trapezoidal, triangular, and circular cross-section flumes. More recently, Thomas and Marino [20] presented an analytical model based on global balances of mass and momentum, which concerns lock-exchange flows generated in open channels of triangular cross-section shape based on a few experiments. They found that the ratio between the front velocities corresponding to the light and dense currents depends on an empirical parameter related to the ratio of the depths determined at the position of the gate that initially separates the fluids. That is, the front velocity evolutions for each flow were coupled by means of a relationship, simplifying the calculus, but the results do not allow analyzing each front dynamics separately.

The goal of this paper is to introduce a theoretical treatment describing the dynamics of both counterflows, which only includes the effect of the cross-section shape. The front condition for steady-state currents generated in nonrectangular cross-section channels is analytically derived independently for each flow improving the previous model reported by Thomas and Marino [20]. Thus, as the front velocity is related to the height of the following flow, the results can be used to study situations where the attention is focused on a single current as in geophysical and engineering flows. The theoretical findings are compared with those provided by laboratory experiments where lock-exchange flows in open and closed channels of rectangular, triangular, and parabolic cross-sections are generated.

2 Theoretical Model

The front condition of an energy-conserving gravity current propagating into a rectangular channel of finite depth was studied by Benjamin [21]. He used the mass and momentum conservation equations to obtain the value of the relationship between the velocity u of the frontal zone and the depth h of the following fluid layer with a density excess $\Delta\rho$ over that of the ambient, which is the Froude number

$$\mathrm{F} = \frac{u}{\sqrt{g'h}} \tag{1}$$

where $g' = (\Delta\rho/\rho)g$ is the reduced gravity, g is the acceleration due to gravity, and F is of the order of unity. This relationship coincides with that previously reported by von Karman [22] applying (erroneously) Bernoulli's theorem to the lighter fluid along a streamline in a turbulent region around the head.

The front condition (1) has been extensively applied at the frontal zone of gravity currents propagating at high Reynolds number $\mathrm{Re} = uh/\nu$, where ν is the kinematic viscosity of the current fluid. The value of the Froude number at the front is a function of the ratio between the thickness of the current and the total depth of the fluid (or fractional depth), being also affected by the friction at the rigid bottom, mixing, and a large-density-difference (non-Boussinesq case—see Refs. [23,24] and references therein).

Now, consider a uniform nonrectangular cross-section channel divided by a vertical gate in two parts, which initially contain a fluid of density ρ_1 and a lighter fluid of density $\rho_2 = \rho_1 - \Delta\rho$. The upper contour may be either a solid boundary as in ducts or pipes or a free surface; the latter case may be also thought as a half of a cross-section of a duct. Removing the gate, two opposite gravity flows produce a two-layer stratification, the lower layer with depth $h_1(x)$ and the upper one with depth $h_2(x)$, as illustrated in Fig. 1.

Although mixing is generated for high Reynolds number flows, it is possible to consider an equivalent layer of unmixed dense fluid for which the main properties of the flow are maintained as noted by Marino et al. [25], and then the theoretical findings for the no-mixing case can be extended to realistic cases.

The channel cross-section contour is assumed to be given by

$$y(z) = \begin{cases} bz^{\alpha} & \text{for} \quad y \geq 0 \\ -bz^{\alpha} & \text{for} \quad y < 0 \end{cases} \tag{2}$$

where z and y are the vertical and transversal coordinates, respectively, and α and b are constants. In particular, $b = w/h_0^{\alpha}$ is determined by the width w of the channel and the height h_0 of the denser fluid at the initial time. The cross-section area s that is occupied by the denser fluid up to a height h is

$$s = \int_0^h \int_{-bz^{\alpha}}^{bz^{\alpha}} dy dz = \frac{2bh^{\alpha+1}}{\alpha + 1} \tag{3}$$

The use of the relationship (2) simplifies the analysis of the basic properties of the flows generated in channels of nonrectangular cross-section shape, and is similar to the use of other functions as in most theoretical and numerical studies cited above. The value $\alpha \to 0$ corresponds to a rectangular cross-section, $\alpha = 1$ defines a triangular cross-section, $\alpha < 1$ provides convex cross-sections, and $\alpha > 1$ indicates sections with a distinctive central depression.

Figure 2 illustrates the frontal zone of gravity currents developing on the bottom (Fig. 2(*a*)) and along the top of a closed channel (Fig. 2(*b*)). The motion is assumed to be steady, and the current heads are at rest in a frame of reference moving with the corresponding constant velocity; the contact points O are stagnation points. Control volumes used in the following analysis are marked by dashed lines.

2.1 Dense Current. We take into account an approximation in which a mean velocity is considered over the channel cross-section in each layer. In Fig. 2(*a*) the light fluid is entering through the vertical plane AB with velocity u_1. It overcomes the head of the dense current, and the velocity u_{1D} of the light fluid is again uniform in plane CD located far enough from the front for any perturbation originated in the head to be neglected. Continuity implies that

$$u_1 = u_{1D}(1 - H_1^{\alpha+1}) \tag{4}$$

where $H_1 = h_1/h_0$ is the dimensionless thickness of the current at CD.

The pressure distribution is assumed to be hydrostatic in both planes so that in AB the pressure as function of the height is given by

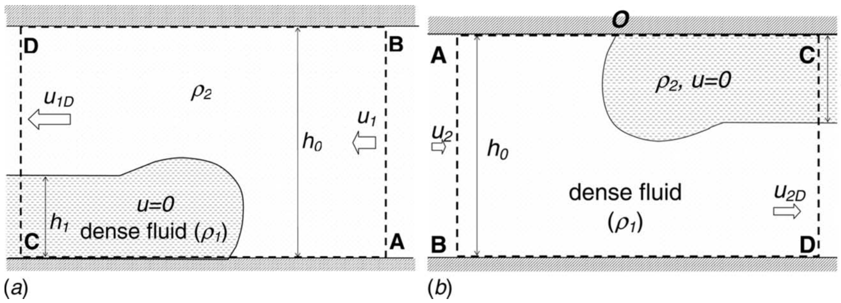

Fig. 2 Schematic of the frontal zone of dense (*a*) and light (*b*) gravity currents

$$p = p_A - \rho_2 g z \tag{5}$$

The pressure p_A is related to the pressure at the stagnation point O by means of the Bernoulli equation

$$p_A = p_O - \tfrac{1}{2}\rho_2 u_1^2 \tag{6}$$

Pressure on section CD is

$$p = \begin{cases} p_C - \rho_1 g z & \text{for} \quad 0 \le z \le h_1 \\ p_C - \rho_1 g h_1 - \rho_2 g (z - h_1) & \text{for} \quad h_1 < z \le h_0 \end{cases} \tag{7}$$

where p_C is the pressure at point C in Fig. 2(*a*), with $p_C = p_O$ if the internal flow within the dense current is negligible.

The momentum function for a given cross-section is

$$\Pi = \int\int p\,dy\,dz + \int\int \rho_2 u^2\,dy\,dz \tag{8}$$

Using Eqs. (4)–(7) on section AB, we obtain

$$\Pi_{AB} = \frac{2bh_0^{\alpha+1}}{\alpha+1}\left(p_O + \frac{1}{2}\rho_2 u_1^2 - \frac{\alpha+1}{\alpha+2}\rho_2 g h_0\right) \tag{9}$$

and

$$\Pi_{CD} = \frac{2bh_0^{\alpha+1}}{\alpha+1}\left[p_O - \frac{\alpha+1}{\alpha+2}\rho_2 g h_0 - \frac{\alpha+1}{\alpha+2}(\rho_1-\rho_2) g h_0 H_1^{\alpha+2} - (\rho_1-\rho_2) g h_0 H_1 (1 - H_1^{\alpha+1}) + \rho_2 u_{1D}^2 (1 - H_1^{\alpha+1})\right] \tag{10}$$

on section CD.

Since there are no external horizontal forces acting on the flow, the net flux of momentum into the control volume including the head is zero. Conservation of the horizontal component of the momentum may then be written as $\Pi_{AB} = \Pi_{CD}$. Using the mass conservation (4), the Froude number F_1 for the dense current is

$$\mathrm{F}_1^2 = \frac{u_1^2}{g'_1 h_0 H_1} = \frac{(1 - H_1^{\alpha+1})\left(2 - \dfrac{2}{\alpha+2}H_1^{\alpha+1}\right)}{(1 + H_1^{\alpha+1})} \tag{11}$$

where $g'_1 = g(\rho_1 - \rho_2)/\rho_2$.

Equation (11) is found by relating the velocities and heights corresponding to two sections, AB and CD, separated by a horizontal distance of the order of the head length. If the length of the head is much smaller than the total current length, planes AB and CD may be considered to be near to each other so that Eq. (11) is valid at a "front" where the fluid velocity and the current height are discontinuous functions of the horizontal coordinate x, as usual in the theoretical analyses.

As expected, Eq. (11) with $\alpha = 0$ becomes the well known relationship for the rectangular cross-section channels proposed first by Benjamin [21] and confirmed later by other authors (see, for instance, Ref. [26]),

$$\left[\frac{u_1^2}{g h_0}\right]_{\alpha=0} = \frac{(1-\gamma)}{\gamma}\frac{(1-H_1)(2-H_1)H_1}{(1+H_1)} \tag{12}$$

where $\gamma = \rho_2/\rho_1$.

While Bernoulli's equation is valid between points A and O (see Eq. (6)) because of the laminar flow existing there, it is not always valid between O and any point on plane CD since there is usually energy dissipation in the head. But for currents in which dissipation can be considered negligible, Bernoulli's equation may be also applied along a streamline between points on planes AB and CD as, for example, the upper boundary of the channel to find

$$\frac{u_1^2}{g'_1 h_0 H_1} = 2(1 - H_1^{\alpha+1})^2 \tag{13}$$

Equating Eqs. (11) and (13), the nontrivial solution for the current depth results

$$H_{1c} = \left(\frac{1}{\alpha+2}\right)^{1/(\alpha+1)} \tag{14}$$

and the Froude number given by Eq. (11) for a dense energy-conserving gravity current becomes

$$\mathrm{F}_{1c}^2 = 2\left(1 - \frac{1}{\alpha+2}\right) \tag{15}$$

2.2 Light Current. The Froude number in this case is also based on the mass and momentum balances as done in Sec. 2.1. As shown in Fig. 2(*b*), the denser fluid is entering through the vertical plane AB with uniform velocity u_2 and plunges under the light fluid. In plane CD, which is located far enough from the front for any perturbation originated in the head to be neglected, the fluid velocity u_{2D} is again uniform. Continuity implies that

$$u_2 = u_{2D} H_1^{\alpha+1} \tag{16}$$

where H_1 is now related to the thickness of the dense fluid layer below the light current (Fig. 2(*b*)).

Assuming that the pressure at the stagnation point O is $p_O = 0$, and applying Bernoulli's equation between points O and A, the pressure on plane AB is

$$p = p_O - \tfrac{1}{2}\rho_1 u_2^2 + \rho_1 g (h_0 - z) \tag{17}$$

and

$$p = \begin{cases} p_O - \rho_2 g (h_0 - h_1) + \rho_1 g (h_1 - z) & \text{for} \quad 0 \le z \le h_1 \\ p_O + \rho_2 g (h_0 - z) & \text{for} \quad h_1 < z \le h_0 \end{cases} \tag{18}$$

on plane CD. Calculating Π_{AB} and Π_{CD} by means of Eq. (8) and using Eqs. (16)–(18), the conservation of the horizontal component of the momentum ($\Pi_{AB} = \Pi_{CD}$) gives the Froude number F_2 of the light current as a function of H_2 and $g'_2 = g(\rho_1 - \rho_2)/\rho_1$ as

$$F_2^2 = \frac{u_2^2}{g'_2 h_0 H_2} = \frac{2}{(\alpha+2)}\frac{[1-(1-H_2^{\alpha+2})](1-H_2)^{\alpha+1}}{[2-(1+H_2^{\alpha+1})]H_2} \tag{19}$$

For rectangular cross-section channels, Eq. (19) is reduced to

$$\left[\frac{u_2^2}{gh_0}\right]_{\alpha=0} = (1-\gamma)\frac{(2-H_2)(1-H_2)H_2}{(1+H_2)} \tag{20}$$

When $\gamma = 1-\varepsilon$ with $\varepsilon \ll 1$, Eq. (20) differs from Eq. (12) by a factor $O(\varepsilon)$; that is, the front velocities of the dense and light currents are the same in the Boussinesq approximation as it is well known. For nonrectangular cross-section channels the front velocities of the flows developed are not the same even in the Boussinesq approximation (see Eqs. (11) and (19) with $\gamma \approx 1$ and $\alpha \neq 0$).

If there is no flow dissipation in the head of the light gravity current, Bernoulli's equation applied along the streamline that coincides with the channel bottom boundary suggests that

$$\frac{u_2^2}{gh_0} = 2(1-\gamma)H_2(1-H_2)^{2(\alpha+1)} \tag{21}$$

Equating Eqs. (19) and (21), the height H_{2c} for an energy-conserving light gravity current is found to be the solution of the algebraic equation

$$(1-H_{1S}^{\alpha+2}) - (\alpha+2)(1-H_{1S})H_{1S}^{\alpha+1}(2-H_{1S}^{\alpha+1}) = 0 \tag{22}$$

where $H_{1S} = 1 - H_{2c}$. Thus, the Froude number for a light energy-conserving gravity current is

$$F_{2c}^2 = \frac{2}{(\alpha+2)}\frac{[1-(1-H_{2c}^{\alpha+2})](1-H_{2c})^{\alpha+1}}{[2-(1+H_{2c}^{\alpha+1})]H_{2c}} \tag{23}$$

3 Experimental Results

Six sets of laboratory experiments were performed in Perspex channels with nonrectangular cross-sections, which are considered as half the shapes defined by Eq. (2) with $\alpha = 0.44$ (concave, Fig. 3(*a*)), 1.00 (triangular, Fig. 3(*b*)), and 1.79 (convex, Fig. 3(*c*)). This experimental setup therefore includes a vertical wall at the centerline of the flow to reduce the optical distortion when it is observed laterally. The effects of this wall were found negligible after comparing the results obtained using the triangular cross-section channel with those coming from the use of a rectangular cross-section tank tilted 45 deg. The results for a half cross-section may be extrapolated to the complete cross-section by symmetry without losing validity.

The channels are 2.00 m long, 0.20 m wide, and 0.29 m high. In addition, two sets of experiments were carried out in a rectangular cross-section channel, where known results were reproduced. Four sets of experiments were performed in channels with a Perspex upper boundary (closed channels) and another four sets with a free surface. A central gate separates initially one part of the channel containing fresh water from another with salt water. Each set includes four or five experiments with density relative difference $\Delta\rho/\rho_1 = 1-\gamma = 0.5\%$, 0.75%, 1%, 2%, and 4% approximately. Densities were measured by an Anton Paar 4500 densimeter with a precision of 5×10^{-5} g/cm^3.

The nonrectangular channels were placed inside a greater rectangular cross-section tank (depicted with dashed lines in Fig. 3) filled with fresh water to reduce the optical distortion due to the nonparallel or curved lateral walls. The experiment starts when the gate is removed, giving place to two opposite gravity currents as illustrated in Fig. 1. The flows were observed laterally with a charged-coupled device (CCD) video-camera located 6 m away from the tank. Experimental setup and image processing are similar, as done by Marino et al. [25]. An anamorphic lens is used in order to magnify the vertical scale, reduce the horizontal scale, and improve the resolution of the images. A fluorescent strip light and a light-diffusing screen located behind the tank provide nearly uniform backlighting. A calibrated quantity of dye is added to the salt water to provide visualization. The light attenuation due to the dyed water allows the cross-current averaged concentration to be measured from which the cross-current average density may be inferred, taking into account the nonrectangular cross-section shape of the channel. Figure 4 shows an instantaneous image that corresponds to the lock-exchange flows generated in a parabolic cross-section open channel for an initial density relative difference of 2%. Vertical and horizontal scales are different, and the light intensity is proportional to the cross-current average density and independent of the width of the channel in each point.

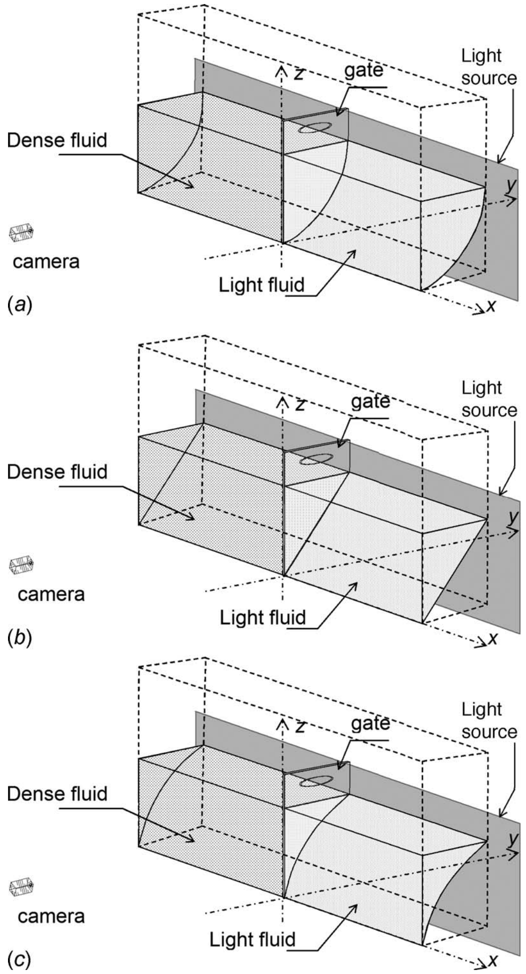

Fig. 3 Experimental setup to generate gravity flows in a channel of concave (*a*), triangular (*b*), and convex (*c*) cross-section shapes

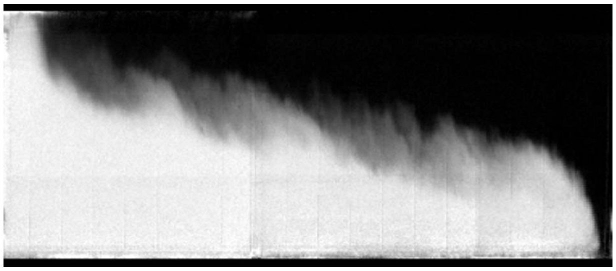

Fig. 4 Instantaneous image of the counterflows generated in a parabolic cross-section shape tank after applying the image processing. A dense current (white) moving to the right and a light current (black) running in the opposite direction are clearly distinguished.

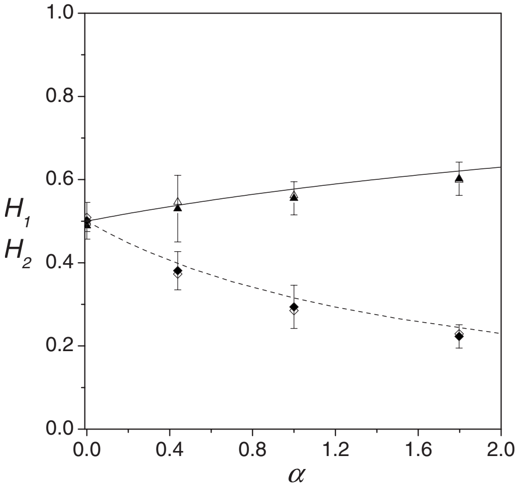

Fig. 5 Theoretical thickness of dense (solid line) and light (dashed line) gravity currents for different cross-section shapes. The experimental results obtained in closed and open channels are represented by solid and open symbols, respectively, and by triangles and diamonds for dense and light currents, respectively.

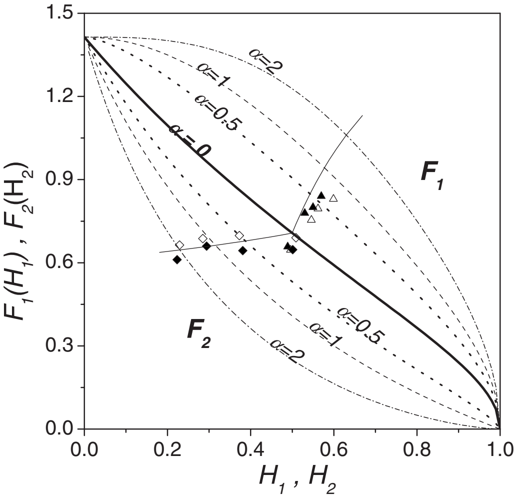

Fig. 6 Froude numbers of the dense F_1 and light F_2 currents as function of the respective heights H_1 and H_2 for different α. The energy-conserving solutions $F_{1c}(H_{1c})$ and $F_{2c}(H_{2c})$ given by Eqs. (15) and (23), respectively, are plotted by thin solid lines.

From the density distribution, the front velocity and the height of the opposite flows may be estimated. A few seconds after the release, the currents enter into the constant velocity or slumping phase that is maintained practically until the fronts reach the corresponding end-walls. Two layers with the most advanced point separated from the bottom/top (rigid) contour are quickly developed. Then the height of each fluid layer, that is, h_1 and h_2 marked in Fig. 1, was measured almost at the end of the run and at a density relative difference of 90% with respect to the initial value. Other criteria tested do not modify the results significantly (more details can be found in Ref. [25]). The values of the front velocity and current height lead to Reynolds numbers between 7000 and 35,000. Due to Reynolds number independence for density currents moving along boundaries when $\mathrm{Re} \geq 10^3$ [27], laboratory flows reproduced well many of the problems to which the results of this paper might be directed. It is found that each set of experiments (that is, different relative densities for the same cross-section shape) gives similar results when dimensionless variables H, $u/(g'h_0)^{1/2}$, and F are determined; hence they are averaged in the following.

It is worthwhile noting that the reduced gravity g' enters into Eqs. (1), (11), and (19) through the product $g'h$. That is to say, the global results will not be strongly affected by mixing that reduces g' but increases h or viceversa, in approximately the same extent as shown by Marino et al. [25]. Therefore, the model is expected to provide the correct scaling laws even if a strong mixing is present. So, the Froude numbers F_1 and F_2 at the front should not be modified significantly by the particular values of the Richardson numbers after the head.

Figure 5 shows the variation with α of the dimensionless thicknesses of the currents obtained from Eqs. (14) and (22). In addition, symbols and vertical bars indicate the average values and the standard deviations, respectively, calculated from the experimental data for different cross-section shapes. Theoretical and experimental results agree well. Note that $H_1+H_2=1$ only for rectangular cross-section (α=0); in such a case, both currents occupy half the channel depth $\left(H_{1c}=H_{2c}=\frac{1}{2}\right)$ as well known [1]. For a nonrectangular cross-section channel $H_{1c}>1/2>H_{2c}$ being greater the difference between the thicknesses for increasing α, and $H_1+H_2 \neq 1$. A significant difference between the thicknesses obtained with open and closed channels was not detected.

Figure 6 shows the Froude numbers $F_1(H_1)$ (above the line corresponding to α=0) and $F_2(H_2)$ (below the line for α=0), for different values of α obtained from Eqs. (11) and (19), respectively. The standard deviations for F and H (shown in Fig. 4) are similar, but are not included in Fig. 4 as horizontal and vertical bars for the sake of clarity. The central thick line corresponds to the classical solution for rectangular cross-section channels (α =0). There is no difference between the predictions for light and dense currents provided that the reduced gravity for each current is defined as done in the Sec. 2. This is not the case for nonrectangular cross-section channels ($\alpha \neq 0$). In these cases, the dense fluid flow is faster than the light current of the same depth, and this effect increases with α. This is because, even though both H_1 and u_1 increase with α, u_1 increases faster than $\sqrt{H_1}$. The opposite occurs for the light current; in such a case F_2 decreases with increasing α.

The experimental values corresponding to closed channels (solid symbols) fall near the energy-conserving solutions (thin solid lines) obtained from Eq. (15) for the dense currents (triangles), and from Eq. (23) for the light ones (diamonds). In particular, the values of Froude numbers at the front of dense currents fall close to the curve representing the energy-conserving relationship derived theoretically as expected. The high slope of this curve implies that any variation of $F_1(H_1)$ should be noted mainly in the front velocity.

For $\alpha>1$ the experimental values for dense currents are close to the theoretical predictions but do not seem to follow them as well as the light currents do. In these cases the lateral walls are quite closer to each other as they reach the bottom of the channel and the fluid finds it difficult to flow there. A complete description of the flow up to the apex should include the effects of the walls, but this problem deserves deeper study.

4 Conclusions

The values of the Froude number obtained at the front of gravity currents developed in uniform nonrectangular cross-section channels are studied as a function of a simplified cross-section shape. Mass and momentum balances in the frontal region of both dense and light currents running on the bottom and along the upper boundary, respectively, are considered. It is shown that the usual relationships obtained for rectangular cross-sections have to be modified in order to include the effects of the cross-section shape on the flow. For example, for triangular cross-section shapes ($\alpha=1$), the theoretical values of the front velocity and thickness corresponding to the dense current are 92% and 83%, respectively, greater than those for the light current.

The analytical findings are in reasonable agreement with the results obtained in laboratory experiments performed in closed and open channels with four cross-section shapes. In open channels, we find faster light currents and slower dense currents than those developed in closed channels. The Froude number of the light currents in open channels is 1.07 ± 0.02 times the value corresponding to the currents generated in closed channels. This value is in agreement with 1.08, approximately, suggested by Hartel et al. [28] (see their Fig. 4) for gravity currents developing along slip and nonslip boundaries for $\alpha=0$ in the range of experimental Reynolds numbers here reported. In addition, the Froude number of the bottom currents results 0.98 ± 0.01 times the value corresponding to closed channels. These factors seem to be independent of the cross-section shape.

The Eqs. (11) and (19) do not depend on the scale of the depth h_0 or width w of the channel (that is, the coefficient b in Eq. (2)), but only on the exponent α associated with the cross-section contour shape. Thus, the same relationship may be held for wide and shallow natural estuaries and narrow laboratory channels provided that the same value of α is used in both cases, which is a convenient advantage for the laboratory modeling of natural environments. It is also suggested that if the depth and/or width of a river changes smoothly maintaining the value of α, the dimensionless Froude number of a gravity current should tend to be the same, though the actual front velocity scales with the square root of the corresponding height of the current ($\sqrt{h}$, see Eq. (1)).

We study here a stratified environment in which the frontal zones of dense and light fluid flows are distinguished. This happens for a wide range of natural situations where turbulence is not dominant. Thus the solutions obtained represent an advance from the theoretical and practical standpoints of the study of the gravity currents in complex-shaped cross-section channels, which may help to understand the features of the exchange flows in geophysical and engineering events. Laboratory experiments also give information about mixing in the interface between dense and light fluids, which are not described here because they do not modify the front movement appreciably. These aspects are under investigation and will be reported in a near future.

Acknowledgment

This work was supported by CONICET and ANPCyT (Argentina) under Grant No. PIP 5893 and Grant Nos. PICT 34088/05 and 1185/06, respectively.

Nomenclature

F = Froude number
g = acceleration due to gravity
g' = reduced gravity
h = height of the current behind the head
H = dimensionless thickness of the current
p = hydrostatic pressure
Re = Reynolds number
s = area of the channel cross-section occupied by the denser fluid
u = frontal zone velocity
x, y, z = longitudinal, transversal, and vertical coordinates
w = width of the laboratory channel
α, b = parameters associated with the shape of the channel cross-section
γ = relationship between light and dense fluid densities
ρ = density
ν = kinematic viscosity

Subscripts

0 = initial value
1 = dense fluid
2 = light fluid
AD, CD = vertical planes limiting the control volume
c = energy-conserving current
O = stagnation point

References

[1] Simpson, J. E., 1997, *Gravity Currents: In the Environment and the Laboratory*, Cambridge University, Cambridge, p. 258.
[2] Imberger, J., and Hamblin, P. F., 1982, "Dynamics of Lakes, Reservoirs and Cooling Pounds," Annu. Rev. Fluid Mech., **14**, pp. 153–187.
[3] Farrell, G., and Stefan, H., 1988, "Mathematical Modeling of Plunging Reservoir Flows," J. Hydraul. Res., **26**, pp. 525–537.
[4] Britter, R. E., and Linden, P. F., 1980, "The Motion of the Front of a Gravity Current Travelling Down an Incline," J. Fluid Mech., **99**, pp. 531–543.
[5] Alavian, V., Jirka, G. H., Denton, R. A., Johnson, M. C., and Stefan, H. G., 1992, "Density Currents Entering Lakes and Reservoirs," J. Hydrol. Eng., **118**, pp. 1464–1489.
[6] Akiyama, J., and Stefan, G., 1987, "Onset of Underflow in Slightly Diverging Channels," J. Hydrol. Eng., **113**, pp. 825–844.
[7] Johnson, T. R., Farell, G. J., Ellis, C. R., and Stefan, H. G., 1987, "Negatively Buoyant Flow in a Diverging Channel. I: Flow Regimes," J. Hydrol. Eng., **113**, pp. 716–730.
[8] Johnson, T. R., Ellis, C. R., Farell, G. J., and Stefan, H. G., 1987, "Negatively Buoyant Flow in a Diverging Channel. II: 3-d Flow Field Descriptions," J. Hydrol. Eng., **113**, pp. 731–742.
[9] Johnson, T., Ellis, C., and Stefan, H., 1989, "Negatively Buoyant Flow in Diverging Channel. IV: Entrainment and Dilution," J. Hydrol. Eng., **115**, pp. 437–456.
[10] Stefan, H., and Johnson, T., 1989, "Negatively Buoyant Flow in Diverging Channel. III: Onset of Underflow," J. Hydrol. Eng., **115**, pp. 423–436.
[11] Bournet, P. E., Dartus, D., Tassin, B., and Vinçon-Leite, B., 1999, "Numerical Investigation of Plunging Density Current," J. Hydrol. Eng., **125**, pp. 584–594.
[12] Monaghan, J. J., 2007, "Gravity Current Interaction With Interfaces," Annu. Rev. Fluid Mech., **39**, pp. 245–261.
[13] Britter, R. E., and Simpson, J. E., 1978, "Experiments on the Dynamics of a Gravity Current," J. Fluid Mech., **88**, pp. 223–240.
[14] Zhou, M., 1998, "Influence of the Bottom Stress on the Two-Layer Flow Induced by Gravity Currents in Estuaries," Estuarine Coastal Shelf Sci., **46**, pp. 811–825.
[15] Nunes, R. A., and Simpson, J. H., 1985, "Axial Convergence in a Well Mixed Estuary," Estuarine Coastal Shelf Sci., **20**, pp. 637–649.
[16] Wong, K. C., 1994, "On the Nature of Transverse Variability in a Coastal Plain Estuary," J. Geophys. Res., **99**, pp. 209–222.
[17] Wong, K. C., and Munchow, A., 1995, "Buoyancy Forced Interaction Between Estuary and Inner Shelf-Observation," Cont. Shelf Res., **15**, pp. 59–88.
[18] Valle-Levinson, A., and Lwiza, K. M. M., 1995, "The Effects of Channels and Shoals on Exchange Between the Chesapeake Bay and the Adjacent Ocean," J. Geophys. Res., **100**, pp. 18551–18563.
[19] Engqvist, A., and Hogg, A., 2004, "Unidirectional Stratified Flow Through a Non-Rectangular Channel," J. Fluid Mech., **509**, pp. 83–92.
[20] Thomas, L. P., and Marino, B. M., 2004, "Lock-Exchange Flows in Non-Rectangular Cross-Section Channels," ASME J. Fluids Eng., **126**, pp. 290–292.
[21] Benjamin, T. B., 1968, "Gravity Currents and Related Phenomena," J. Fluid Mech., **31**, pp. 209–248.
[22] von Karman, T., 1940, "The Engineer Grapples With Non-Linear Problems," Bull. Am. Math. Soc., **46**, pp. 615–683.
[23] Lowe, R. J., Rottman, J. W., and Linden, P. F., 2002, "A Laboratory Study of the Velocity Structure in an Intrusive Gravity Current," J. Fluid Mech., **456**, pp. 33–48.
[24] Birman, V. K., Martin, J. E., and Meiburg, E., 2005, "The Non-Boussinesq Lock-Exchange Problem. Part 2. High Resolution Simulation," J. Fluid Mech., **537**, pp. 125–144.
[25] Marino, B. M., Thomas, L. P., and Linden, P. F., 2005, "The Front Condition for Gravity Currents," J. Fluid Mech., **536**, pp. 49–78.
[26] Shin, J. O., Dalziel, S. B., and Linden, P. F., 2004, "Gravity Currents Produced by Lock Exchange," J. Fluid Mech., **521**, pp. 1–34.
[27] Simpson, J. E., and Britter, R. E., 1979, "The Dynamics of the Head of a Gravity Current Advancing Over a Horizontal Surface," J. Fluid Mech., **94**, pp. 477–495.
[28] Hartel, C., Meiburg, E., and Necker, F., 2000, "Analysis and Direct Numerical Simulation of the Flow at a Gravity-Current Head. Part 1. Flow Topology and Front Speed for Slip and No-Slip Boundaries," J. Fluid Mech., **418**, pp. 189–212.

Vortex Dynamics and Shedding of a Low Aspect Ratio, Flat Wing at Low Reynolds Numbers and High Angles of Attack

Daniel R. Morse

James A. Liburdy

Mechanical Engineering,
Oregon State University,
Corvallis, OR 9733

This study focuses on the detection and characterization of vortices in low Reynolds number separated flow over the elliptical leading edge of a low aspect ratio, flat plate wing. Velocity fields were obtained using the time-resolved particle image velocimetry. Experiments were performed on a wing with aspect ratio of 0.5 for velocities of 1.1 m/s, 2.0 m/s, and 5.0 m/s corresponding to chord length Reynolds numbers of 1.47×10^4, 2.67×10^4, and 6.67×10^4, respectively, and angles of attack of 14 deg, 16 deg, 18 deg, and 20 deg. A local swirl calculation was used on proper orthogonal decomposition filtered data for vortex identification and corresponding vortex centers were tracked to determine convective velocities. The swirl function was also analyzed for its temporal frequency response at several discrete points in both the shear layer and in the separated recirculation region. A peak frequency was detected in the shear layer with a corresponding Strouhal number of approximately 3.4 based on the flow direction projected length scale. The Strouhal number increases with both angle of attack and Reynolds number. The shear layer convective length scale, based on the vortex convection velocity, is found to be consistent with the mean separation distance between vortices within the shear layer. This length scale decreases with increasing Re_c. [DOI: 10.1115/1.3112385]

1 Introduction

Low and ultralow Reynolds number aerodynamics are of increasing interest in a number of application areas, such as micro-air vehicles, autonomous vehicles, as well as animal and insect flight. Low Reynolds numbers based on the freestream velocity and chord length are typically characterized as less than 10^6, while ultralow is typically less than 10^3. Of concern in the design of small aircraft is the ability to maintain acceptable lift characteristics over a wide range of angles of attack and to reduce the susceptibility for unstable operation. McCullough and Gault [1] discussed the generally accepted three main types of airfoil stall: trailing edge, leading edge, and thin airfoil stall. Flow over thin airfoils at high angles of attack displays attributes of stall where by the flow separates at the leading edge with a re-attachment point that moves downstream as the angle of attack increases. McCullough and Gault likened this to the separation of flow past a sharp edge because at sufficiently high angles of attack the stagnation point moves below the leading edge.

In this present study, a low aspect ratio, thin wing at high angles of attack results in leading edge separation with a recirculation bubble extending over a significant portion of the wing. The separation results in a strong shear layer that yields to a Kelvin–Helmholtz instability. Consequently, as the disturbances grow into vortical structures along the shear layer, they are convected downstream. Figure 1 illustrates the flow characteristics for the current study with time averaged velocity vectors and associated streamlines showing the extent of the separation bubble along the centerline for $\mathrm{Re}_c=1.47\times10^4$ and $\alpha=20$ deg. For all cases studied, flow reattachment occurs near $x/c=0.3$. A flow visualization image of this using a smoke wire technique is shown in Fig. 2, where flow is from left to right at a chord Reynolds number of approximately 1.47×10^4 and 20 deg angle of attack. The view is of approximately 20% of the chord length from the leading edge. The separated region contains larger, generally weaker swirl components, and at high angles of attack is more consistent with the von Kármán instability of vortex shedding from bluff bodies.

Increased knowledge of the low Reynolds number flow events leading up to and during separation will be valuable to the development of unmanned and autonomous aircraft. Moreover, detailed understanding of the time dependent nature of separation conditions may lead to the ability for new control algorithms to improve overall performance. A better understanding of the leading edge separation may lead to improved techniques for delaying or counteracting separation effects under these conditions.

1.1 Low Reynolds Number Flow Over a Wing. Separation of airflow over a wing has been a topic of interest for many decades. Studies of high Reynolds flows have direct application to traditional aircraft. In contrast, Carmichael [2] compiled a detailed survey of low Reynolds number wing performance and identified various flow regimes based on Reynolds number, as well as separation and characteristics of the separation bubble. In the regime of Re_c from 10^4 to 3×10^4, Carmichael noted that small gliders operate in a completely laminar manner and that trip devices had little benefit. At larger Reynolds numbers, from 3×10^4 to 7×10^4, wings may have significant induced drag penalties. This regime received additional attention by Re et al. [3] because it also coincided with aircraft operating in rarefied environments such as extremely high altitude or the Martian atmosphere.

The investigation of low Reynolds number flows has increased as a result of interest in autonomous and micro-air vehicle development. In general, these craft operate at Reynolds numbers less than or equal to 10^5. Mueller and DeLaurier [4] reviewed the performance of small air vehicles, which included the aerodynamics for fixed and flapping wings, with discussion of the Reynolds number effects on the separation bubble. At very low Reynolds numbers, less than 5×10^4, there is no re-attachment of the flow for leading edge separation. They concluded that distinct differ-

---

Contributed by the Fluids Engineering Division of ASME for publication in the Journal of Fluids Engineering. Manuscript received April 16, 2008; final manuscript received January 26, 2009; published online April 14, 2009. Assoc. Editor: Juergen Kompenhans. Paper presented at the 2007 ASME International Mechanical Engineering Congress (IMECE2007), Seattle, WA, November 10–16, 2007.

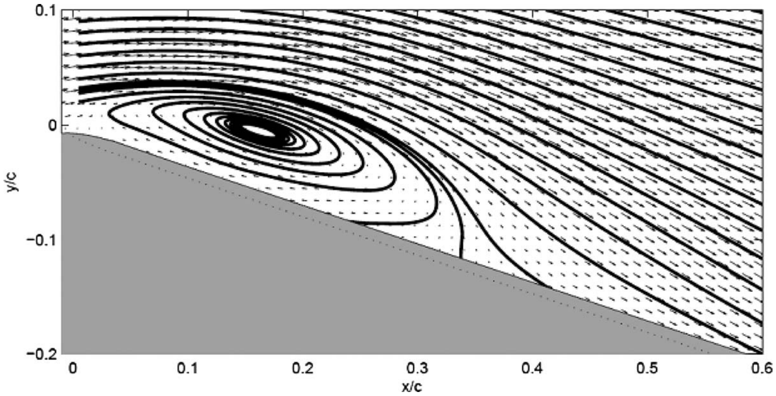

Fig. 1 Mean flow PIV data obtained at the wing centerline. Streamlines illustrate the extent of the separated region. The light gray region represents an area of no data below the wing. An approximation of the wing contour is shown with a dotted line.

ences in flight characteristics between high Reynolds number, greater than 5×10^5, and low Reynolds number operations necessitate a different design approach for emerging micro-air vehicles, defined based on a characteristic size on the order of 15 cm.

A study by Torres and Mueller [5] details the lift and drag characteristics of 12 micro-air vehicle wings. All have low aspect ratio designs, between 0.5 and 2.0 (ratio of wing span to chord). They found that the 0.5 aspect ratio rectangular wing has somewhat superior lift at high angles of attack for $\mathrm{Re}_c=7\times10^4-1\times10^5$. Broeren and Bragg [6] discussed the advantage of thin wings at low Reynolds numbers, but a consequence is unsteady stall characteristics. Their results, for 12 thin wing designs and a single $\mathrm{Re}_c=3\times10^5$, show fluctuations in lift near the stall condition varying on the order of 12–20% depending on angle of attack, α. The associated Strouhal number, St_h, based on projected height, $h=c\sin\alpha$, increases almost linearly with angle of attack, a direct result of increasing frequency, in addition to the increase in the projected height. The spectra indicate two dominant values of St_h, one in the range 0.008–0.030 and the other 0.12–0.22 depending on the wing design. They discussed how this behavior may be related to separation bubble effects.

The effect of periodic flow can be significant on the body forces in low Reynolds number regimes, giving rise to von Kármán vortex shedding. Much work has been done to analyze this phenomenon for flow over blunt bodies. Bishop and Hassan [7] and Berger and Wille [8] described the phase synchronization of fluctuations for a cylinder in cross flow and its wake at low Reynolds numbers. Mair and Maull [9] discussed the three dimensional effects of vortex formation on the body forces. The strongest effect was seen when the vortices were large in the spanwise direction along the length of the cylinder. This phenomenon was also seen for wings with blunt trailing edges. They proposed the introduction of a serrated trailing edge that produces streamwise vortices to disrupted the formation of longitudinal vortex structures.

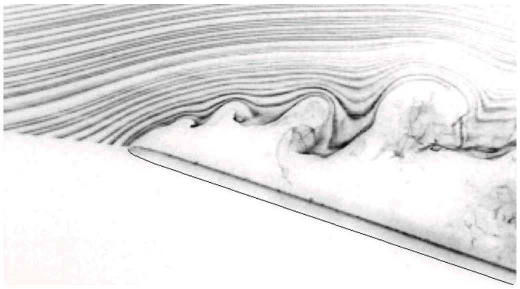

Fig. 2 Flow visualization of leading edge Kelvin–Helmholtz instability rollup forming spanwise vortices, $\mathrm{Re}_c=1.47\times10^4$, $\alpha=20$ deg.

Yarusevych et al. [10] studied the effect of periodic excitation of an airfoil as a method of flow control. They investigated matching the excitation frequency with the dominant frequency of separation to improve performance of an airfoil at $\mathrm{Re}_c=10^4$ and low angles of attack. Tinar and Cetiner [11] analyzed the self-induced vibration frequencies of a spring supported airfoil at Reynolds numbers between 5.9×10^4 and 14.8×10^4. Accelerometer data were paired with particle image velocimetry (PIV) data to determine natural vibration frequencies and vorticity patterns during the vibration cycle. Among others, Cheng and Chen [12] performed a numerical study evaluating flow control for the body forces on a bluff shape and found that dominant frequencies of vortex shedding corresponded to imposed body force frequencies.

Abernathy [13] investigated flow over an inclined flat plate and studied the frequency of shed vortices. When analyzing pressure in the wake of the flat plate, it was seen that the Strouhal number was nearly constant at 0.17 for angles of attack greater than 35 deg, which corresponds to completely separated flow. This is consistent with the results of Roshko [14] who observed a low range of Strouhal numbers ($0.14<\mathrm{St}_h<0.21$) for various bluff bodies and Reynolds numbers.

Burgmann et al. [15] examined the vortex structure of a low Reynolds number airfoil in water using two-component, time-resolved PIV (2C-TR PIV) and scanning PIV. They identified the development of convex shaped vortex structures ejecting from the separation bubble behind the leading edge. Derksen and Rimmer [16] employed a vortex cloud model in the simulation of flow over a low Reynolds number airfoil. This model used free vortices in the flow that convect over time. The results highlight the importance of such structures in separated flows when considering body forces such as lift and drag.

1.2 Flow Structure Identification.

During the past 2 decades with the advance of digital PIV, as well as computational fluid dynamics, large sets of discrete two dimensional velocity fields have become more readily available for study. While vorticity is a commonly, and often an appropriately, used measure for detecting swirl, it is also sensitive to shear and the smallest fluctuations in the data because it is resolved at the grid level. Several researchers have set forth alternative methods for quantitatively identifying coherent structures. Jeong and Hussain [17] identified criteria using the Hessian of the pressure field to identify a vortex core based on a local pressure minimum. This approach neglects viscous and advective effects in the flow and is based on instantaneous velocity strain rate data. Adrian et al. [18] discussed large eddy simulation (LES) decomposition on experimental data for visualizing vortices by the removal of the larger structures. This method employs the use of a low pass Gaussian filter on the flow field, which is subtracted from the total velocity field leaving the high frequency, small structures. Graftieaux et al. [19] used a structure detection technique based on the local swirl velocity component. This was done by integrating the circumferential velocity component about an area bounded by a closed path of selected diameter for each point in the flow.

Shinneeb et al. [20] recently performed an experimental investigation of structures in the far field of a jet at $\mathrm{Re}_c=2.25\times10^4$. Traditional PIV was used to determine the velocity flow field. The proper orthogonal decomposition (POD) was used to filter high frequency flow features based on modes containing 40% of the variance of the velocity field. The local circulation was determined using the concept of closed streamlines and was used to show that the number of structures decreased along the flow direction. This same algorithm was used by Agrawal and Prasad [21]. Troolin et al. [22] performed TR PIV analysis of a wing with a Gurney flap. Up to 1000 PIV fields were sampled at 1 kHz, 2 kHz, and 4 kHz resulting in total sampling times of 1 s, 0.5 s, and 0.25 s. They show good comparison of spectral analyses of TR PIV data and hot wire data. Additionally, Druault et al. [23] performed TR PIV measurements of an internal combustion engine at 276 Hz and 423 Hz over approximately 1.6 s, reported as data covering 32 cycles at 20 counts/s. The TR PIV results were analyzed using POD using 100 modes and phase averaged to examine cycle to cycle variation of flow in the cylinder. Recently, Weiland and Vlachos [24] using vortex detection coupled with TR PIV analyzed the vortical unsteady flow associated with leading edge blowing control. They used the first several POD modes to distinguish frequency characteristics influenced by blowing. Kutulus et al. [25] used TR PIV to study the unsteady forces acting on a square cylinder in cross flow. Through the use of the instantaneous Navier–Stokes equations, they calculated the transient lift and drag forces from the 2D velocity vector field.

1.3 Objectives. The primary goal of this study is to characterize vortex shedding during leading edge separation from a flat low aspect ratio wing using time-resolved vortex detection. Time resolved PIV data are collected for a range of high angles of attack (14–20 deg) for low values of Re_c $(1.47-6.67)\times10^4$. The POD and a tracking filter algorithm are used to assist in the identification and characterization of these structures. Furthermore, the temporal frequency of vortex shedding and the characteristic length scale of vortex separation are analyzed by examining the time series of local swirl events.

2 Experimental Method

Tests were carried out in a large recirculating wind tunnel with internal dimensions of $1.37\times1.52\ \mathrm{m}^2$. A Laskin nozzle was used to generate airborne particles in the tunnel using vegetable oil. Particle size distribution was centered around 6 μm, or on the order of 1 pixel spacing. This corresponds to a particle response time limit of 5 kHz using a Stokes flow drag model described by Hinze [26]. A 532 nm New Wave Pegasus Laser was used to illuminate the flow from the downstream direction. A Dantec Dynamics 9080×0651 light sheet module was used to convert the beam to a 1 mm wide light sheet. This light sheet was placed in the spanwise center of the wing.

The wing was a flat plate of aspect ratio AR=0.5 (span to chord ratio) and chord length of 20.5 cm. The plate leading and trailing edges were elliptical with a major to minor axis ratio of 5:1. The side edges were semicircular. The thickness of the wing was 4 mm, which is approximately 2% of the chord length. Torres and Mueller [5] studied several wing configurations for small unmanned aerial vehicle (UAV) applications. They noted that a flat wing of aspect ratio equal to 0.5 at $\mathrm{Re}_c=7\times10^5$ had an increasing lift coefficient with an angle of attack up to 40 deg. This high lift coefficient at high angles of attack is a feature that makes low aspect ratio wings beneficial to small UAV applications.

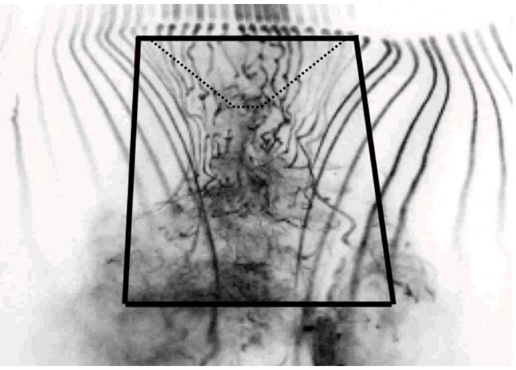

Fig. 3 Downstream view (looking upstream) of a low aspect ratio wing using smoke wire visualization for $\mathrm{Re}_c=1.47\times10^4$, $\alpha=20$ deg. The wing outline is highlighted in bold and the separated flow region is outlined with a dashed line. Streamwise tip vortices are shown with smoke lines curving toward the center and leading edge instabilities are observed to disrupt the smoke lines along the centerline increasing smoke diffusion.

The wing cross-sectional area as seen by the incoming flow is defined as the product of the projected height, h, and width of the wing, $A_c=hw=c\sin(\alpha)w$. The total wind tunnel blockage, at the maximum angle of attack of 20 deg, was 0.3%, and at the lowest angle of attack of 14 deg was approximately 0.2%. In order to obtain the desired field of view, the wing was located approximately 20 cm from the near side optical window of the wind tunnel. This was well outside the wall boundary layer. This wing was located approximately 6 m downstream from the contraction. The wind tunnel has a freestream turbulence level of approximately 1% [27].

The wing was supported from the underside trailing edge using a mounting plate that was 2.5 mm thick by 15 mm wide and 30 mm along the wing. This plate was connected to an aluminum support rod approximately 70 cm long. The angle was fixed using a four-bar linkage mechanism. The trailing edge of the wing was held at a height of approximately 40 cm from the wind tunnel floor. The total cross-stream width of the rod and linkage was less than 2 cm. This system was rigid in the relatively low velocities used in this study, $\leq 5.0\ \mathrm{m/s}$. The wing surface was not observed to oscillate throughout each of the 1000 image pair sequences obtained in each data set.

Smoke wire flow visualization was performed to understand the basic flow configuration around the wing. A nickel wire was placed approximately 10 cm upstream of the leading edge. The results for $\mathrm{Re}_c=1.47\times10^4$ and $\alpha=20$ deg are shown in Figs. 2 and 3. The negative image shown in the figures reveals the presence of streamwise tip vortices, as well as the leading edge disturbances, which increased smoke line diffusion. The separated region on the wing shown in Fig. 3 occupied a roughly triangular shaped region extending from the leading edge and tapering downstream to a point at approximately 60 mm, or $0.3c$, from the leading edge along the wing centerline. This re-attachment point was also confirmed using the mean flow PIV data obtained at the centerline, as shown in Fig. 1. Typically, thin wings of large aspect ratio develop a leading edge separation bubble just prior to stall. In the case of this low aspect ratio wing, the streamwise tip vortices act to reduce the spanwise separation bubble size by increasing the downward flow of air on the suction side of the wing, and thereby delay stall. Consequently, the dynamic characteristics of the separated region can be expected to be impacted by the tip vortices in a low aspect ratio wing.

Hot wire anemometry was used to confirm the TR PIV frequency spectra for a single angle of attack, $\alpha=20$ deg, at each Reynolds number. A TSI IFA-300 constant temperature anemometer was used in conjunction with a single axis, TSI 1201-20 model probe. The probe was mounted in the wind tunnel, supported from the downstream direction, and placed in the separation bubble at the centerline approximately $0.25c$ downstream from the leading edge. The probe was also placed in the shear region approximately $0.05c$ downstream and $0.01c$ above the leading edge. Data were obtained using a personal computer (PC) with analog capture board and LABVIEW® 8.2.

Three freestream velocities were used for this study: 1.1 m/s, 2.0 m/s, and 5.0 m/s, which correspond to chord Reynolds numbers of 1.47×10^4, 2.67×10^4, and 6.67×10^4. Four angles of attack were investigated at each velocity: 14 deg, 16 deg, 18 deg, and 20 deg, for a total of 12 experimental cases. For each case images were obtained using an iNanosense high speed digital camera equipped with an image intensifier. The pixel resolution of the charge coupled device (CCD) was 1280×1024 and the field of view was approximately $55\times42\ \text{mm}^2$.

Synchronization with the laser pulse was obtained using Dantec Dynamics FLOWMANAGER software. The time delay between laser pulses for these data was 50 μs for the $\text{Re}_c=6.67\times10^4$ cases and 100 μs for the $\text{Re}_c=1.47\times10^4$ and 2.67×10^4 cases resulting is an average particle displacement of approximately 6 pixels. The time-resolved sampling of velocity fields was performed at 500 Hz. The total sample time was 2.0 s due to hardware memory limitations. This results in a 0.5 Hz frequency resolution when determining the velocity spectra. It is understood that this may not be appropriate for analysis of very low frequency events but it provides adequate results for the higher frequency vortex shedding observed in this study. To help confirm spectral the results, the TR PIV data were also collected using a 10 s sampling period for $\alpha=20$ deg and $\text{Re}_c=1.32\times10^4$, with a sampling rate of 100 Hz. The lower Re_c condition was chosen to compare with since it is the one susceptible to high uncertainty with its lower frequency. One angle of attack was compared as it has been noted by Abernathy [13] that angle of attack has small influence on normalized separated flow fluctuations. Overall, the mean velocity vector values and the local standard deviations were all within 2% and 5%, respectively. Hot wire anemometry, mentioned previously, was also used to compare low and high frequency events observed in the TR PIV data and are shown with the results. It should be noted that the goal of this study is to determine direct spectral characteristics of detected vortical structures rather than velocity components. This data analysis is discussed later.

Postprocessing of the images was done to reduce glare from the wing surface. This was done by calculating the mean pixel intensity and removing this mean value from each image. The subregion size for each PIV cross-correlation calculation was 32×32 pixels, with an average of 6–8 particles per subregion. A 50% overlap was used resulting in a vector field of 79×63 grid points with a spacing of approximately 0.6 mm. The results were obtained using FLOWMANAGER® software from Dantec Dynamic Denmark® using fast Fourier transform (FFT) cross correlation. Numerical experiments were carried out with the same seeding density and particle size as used in the experiments and an adaptive cross-correlation scheme was not found to improve the results of the swirl detection describe later in a highly curved flow regions [27]. The velocity data were filtered using a 3×3 median filter since large scale flow structures are of interest. No vectors were removed from the data set. The PIV velocity uncertainties were investigated in the same wind tunnel, with the same field of view, while using the same particle generator system and seeding levels [27]. For the same pixel resolution, approximately 6 μm particle diameter, and a 32×32 pixel subregion as used in this study, the uncertainties were found to be approximately 1% and velocity gradient bias is small by virtue of estimated particle displacement variation over the subregion domain.

3 Data Analysis

The vortex detection method used in this study was introduced by Graftieaux et al. [19] and used by Dano and Liburdy [27] for vortex detection in a pulsed jet in cross flow. This technique is based on the orientation of the velocity vectors relative to radial lines from a local point. The local swirl function, Γ^*, is calculated for a given subregion, A_M, centered about point P. This vortex detection function is defined as

$$\Gamma^* = \frac{1}{A_M}\int_A \frac{(PM\times U_M)\cdot\bar{Z}}{\|PM\|\cdot\|U_M\|}dA = \frac{1}{A_M}\int_A \sin(\theta_M)dA \tag{1}$$

where PM is the vector from the center point P to subregion point M, U_M is the velocity at point M within the subregion, Z is the unit vector perpendicular to the plane of data, and θ_M is the angle between position vector PM and velocity vector U_M. This locally normalized function allows the detection of vortical structures in both the shear layer and the slower recirculating region in the wake of the wing leading edge.

It should be noted that in using this technique the local swirl is not equivalent to an average of spanwise vorticity within the domain specified by A_M. That is, the function Γ^* includes all velocity vectors within the domain not just the line integral around the domain boundary. Consequently, it weights the vorticity near the central point, P.

The value of Γ^* varies between -1 and 1 where $\Gamma^*<0$ represents a clockwise vortex and $\Gamma^*>0$ represents a counterclockwise vortex. This technique allows the user to provide a prescription of the mask size, A_M, used to evaluate the local value of swirl. In this study the domain was set to a 9×9 grid centered about each data point, which corresponds to approximately $4.0\ \text{mm}^2$ region. This is equivalent to $0.02c$ and is equal to the wing thickness. A further discussion of the effects of the subregion size and the vortex strength based on velocity magnitude can be found in Ref. [28]. Additional comparison of the Γ^* function with other structure detection techniques is given by Chen et al. [29] such as the λ_2 criteria proposed by Jeong and Hussein [17], as well as various vector field topological structures. It should be noted that Γ^* is sensitive to swirl features smaller than the subdomain, A_m. Structures that are larger than A_m will yield Γ^* values large at the swirl center but will decay as the subregion center moves away from the swirl center. In addition, Γ^* is sensitive to opposing shear flow within a subregion. A pure shear flow with opposing flow centered around zero in the subregion results in $\Gamma^*=0.65$, whereas pure unidirectional shear flow produces $\Gamma^*=0$. A threshold value of Γ^* can be set to help filter out opposing flow shear gradients. In the current study, this type of flow occurs within the separation. A threshold of 0.7 was used to filter out shear flow while capturing the strong swirl elements. Additional filters were applied to aid in vortex tracking and are discussed later.

Since a time series of vector fields are available using the TR PIV method, individual vortical structures are tracked over time. In doing this, the local convective velocity of the vortex is approximated as the change in position of the vortex center over a given time interval: $U_{\Gamma^*}=\Delta x/\Delta t$ and $V_{\Gamma^*}=\Delta y/\Delta t$, which represent the x and y convection velocity components, respectively. Here the vortex center was calculated at each time step based on the area geometric center of an enclosed structure. The structure is defined as a contour of Γ^* at the given threshold value.

The POD was applied to the velocity field to isolate the large scale energetic flow structures. A brief overview for the sake of notation is given here. A more detailed discussion of the concept and its applications include Refs. [30–32]. The velocity data, $f(x,y,t)$, can be approximated as follows:

$$f(x,y,t) \sim \sum_k d_k(x,y)a_k(t) \tag{2}$$

where $d_k(x,y)$ is the relative spatial distribution of velocity for each mode k and $a_k(t)$ is the amplitude time series of that mode. The modes, beginning at mode 1, are organized from the mode with the most variance (energy), to the least variance, highest mode. Mode 0 is simply the time averaged velocity field. Typically, as the mode energy decreases, the frequency of fluctuation increases for its associated amplitude time series, $a(t)$, and the spatial size of the features seen in the mode map, $d(x,y)$, decreases. Therefore, used as a filter, a low order reconstruction will capture much of the energy and behavior of the larger, lower frequency features of the flow and eliminate the smaller, high frequency variations.

The procedure used here is the same as was applied to TR PIV data by Morse and Liburdy [33] for separated flows. Determination of the POD modes was carried out in MATLAB. The first step was removing the time averaged flow. The remaining fluctuating values of u and v were concatenated into a single design matrix $\mathbf{D}$, of M locations by N time steps. Using the "svd" function in MATLAB, a singular value decomposition was performed on the design matrix. The resultant set of matrices denoted U_{NxM}, S_{MxM}, and V_{MxM} can be combined as $\mathbf{U}^*\mathbf{S}^*\mathbf{V}^T$ to recreate the design matrix. In this case the $\mathbf{U}$ matrix is the set of modal spatial velocity distribution maps. The amplitude time series matrix, $\mathbf{A}$, is equal to $\mathbf{V}^*\mathbf{S}$. Each column of $\mathbf{U}$ represents a mode map and each column of $\mathbf{A}$ represents the amplitude time series for the mode map in $\mathbf{U}$. A truncation to the decomposition was done for efficiency using the number of modes equal to the limiting dimension, in this case $N=1000$, the number of time steps. The results show that 90% of the energy is contained in less than 600 modes so this truncation had negligible effect on modal distribution.

In order to more clearly identify vortical structures, the higher frequency velocity fluctuations were filtered using the POD of the velocity data. This was done by reconstructing the flow using the first 30 modes which accounts for 30–55% of the total variance in the flow. This reconstruction represents the high energy, lower frequency features of the flow while eliminating the low energy, high frequency fluctuations.

To better determine of the convective velocity of individual flow field structures, a tracking filter method was used. A minimum lifespan criterion $\tau_l = t/t_c$ (where t is the detected lifetime of the vortex and $t_c = c/U_\infty$ is the convective timescale using the freestream velocity) was used to filter out vortices, which may appear in only one or two frames but were not observed over a sufficiently long time. This method determines vortex paths by seeking out the nearest vortex location in the subsequent time steps. If there exists no vortex within this specified distance in the next time step, then that vortex is no longer tracked. The specified threshold distance was determined by multiplying 150% of the freestream velocity by the time period between frames, $\Delta x_{\text{limit}} = 1.5 \cdot U_\infty \cdot \Delta t$. This corresponds to a length threshold, $l_{\text{threshold}} = 0.017c$, $0.030c$, and $0.075c$ for $\text{Re}_c = 1.47\times 10^4$, 2.67×10^4, and 6.67×10^4, respectively. Similarly, identified vortex locations without an associated previously identified vortex were marked as origin points for further tracking in time. In essence, the tracking filter requires a vortex to exist for a given number of frames and places an upper limit on the vortex convection velocity based on the magnitude of the freestream velocity.

Spectral analysis was performed on individual velocity components and the Γ^* function with the aim of detecting the presence of any dominant frequencies. Because Γ^* is a locally normalized swirl function, its fluctuations are equally detectable in the high speed shear region and the low speed recirculation region. The TR PIV data field provides time series data and frequency response at each location within the grid. The root mean square of fluctuations of Γ^*, denoted $\sigma(\Gamma^*)$, indicates locations of the most intense fluctuations of Γ^* over time.

An alternative to examining the fluctuation of Γ^* is to look for cyclic behavior in Γ^*. One approach is to examine the time based autocorrelation of Γ^*, denoted as ρ_{Γ^*}. A periodic autocorrelation function represents a cyclic event, and the root mean square of the autocorrelation of Γ^*, $\sigma(\rho_{\Gamma^*})$, at each TR PIV location is used to provide an indication of where Γ^* has the most intense cyclic fluctuations.

A vortex separation length scale was determined and used to assure consistency between vortex detection frequency data and vortex spatial separation data. Two lengths scales are defined as (i) the average separation distance between the identified vortex centers in all time frames for the entire time series, l_{track} (note that this does not require time-resolved data), and (ii) the length defined by dividing the convection velocity of vortex centers by the characteristic frequency, l_{freq}. These two results would be expected to be reasonably close if the measured convection velocity and frequency are consistent.

In summary, two primary analyses are presented (i) vortex detection with tracking and (ii) frequency analysis of the local nondimensional swirl function, Γ^*. The velocity field was filtered using the POD to remove high frequency variations prior to calculation of Γ^*. The Γ^* function was used to determine areas of swirl and a threshold was set to identify discrete regions of high swirl. The centers of these swirl regions were tracked over time to determine the convective velocity of these structures. A vortex tracking filter based on vortex lifespan was applied to reduce the noise in the vortex velocity signal. Frequency analysis of the Γ^* function was carried out. A vortex separation length scale in the shear layer is evaluated using two methods to check the consistency of the measurements.

4 Results

4.1 Vortex Detection and Tracking. The data consist of the planar TR PIV results at three chord Reynolds numbers and four angles of attack. Figures 4(*a*)–4(*d*) illustrate instantaneous velocity vector data at four angles of attack for $\text{Re}_c = 1.47\times 10^4$ with the x and y coordinates, originating at the leading edge, are normalized by the chord length, c. The field of view is of the leading edge comprising approximately 25% of the chord length; this view is slightly smaller than that shown in Fig. 1. The region below the wing surface was not illuminated by the laser and contains no velocity data. The vector plots clearly identify the regions of separated flow and the corresponding large recirculation region. The mean vector fields are similar for the other Re_c values, with separation occurring at the leading edge and approximately the same reattachment location.

Figures 4(*e*)–4(*h*) show instantaneous contours of Γ^* at the times and conditions corresponding to the vector plots in Figs. 4(*a*)–4(*d*), respectively. The regions of highest clockwise local swirl ($\Gamma^* < 0$) are located in the high shear region beginning near the leading edge. The vortices in the shear region form very near the leading edge and extend along a line, which projects further from the wing surface as α increases. That is, the angle of the line of Kelvin–Helmholtz instability beginning at the separation location forms an angle greater than α with the wing surface as α increases. Close to the surface the shear flow results in a relatively weak layer of $|\Gamma^*|$ due to the near surface velocity gradient, not swirl. A threshold applied to Γ^* was used to filter out weak shear flows during vortex tracking. The separated recirculation region beneath the shear layer does not contain strong swirl components, although the flow is seen to clearly recirculate from the vector plots shown in Figs. 4(*a*)–4(*d*).

Figure 5(*a*)–5(*e*) illustrate a time-resolved sequence of TR PIV vectors and Γ^* contours sampled at every time step, or 2 ms time separation, for the case of $\alpha = 14$ deg and $\text{Re}_c = 1.47\times 10^4$. The large vortical structures can be seen to convect downstream. Since their motion is relatively fast (and are shown later to be dependent on Re_c), the resolution of the local convective velocity is limited

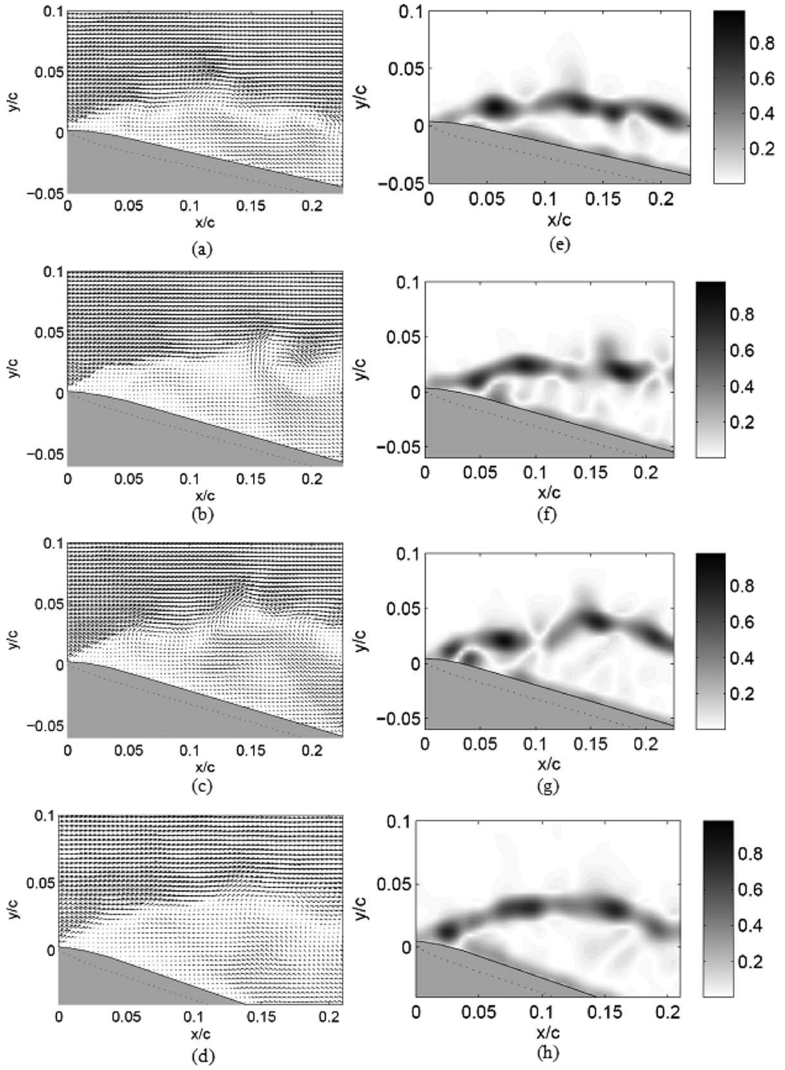

Fig. 4 TR PIV vector field for $\mathrm{Re}_c = 1.47 \times 10^4$ at four angles of attack: (*a*) 14 deg, (*b*) 16 deg, (*c*) 18 deg, and (*d*) 20 deg; grayscale plots of Γ^* are shown in (*e*)–(*h*), which were calculated from the velocity fields in (*a*)–(*d*).

by the time resolution of the TR PIV, in this case 500 Hz sampling rate. To illustrate the time evolution of Γ^* contours, Figs. 5(*f*)–5(*j*) illustrate a time sequence for the same conditions given in Figs. 5(*a*)–5(*e*). In the identification of the strongest vortical structures, a threshold of $|\Gamma^*| \geq 0.7$ was applied, which eliminates the near surface results. The magnitude of the large swirl elements does not change significantly during tracking, which is discussed later. The position denoted above the contours in Figs. 5(*f*)–5(*j*) is the downstream position of the centers of the vortices as defined by the geometric mean position of the contour. The structures in the shear layer convect downstream in a systematic manner in most cases, although they occasionally are observed to stall or temporarily reverse direction, as is shown in the final two frames of this sequence. This unsteady motion of detected vortices occurs regularly and is illustrated further in the vortex tracking results.

The POD of the velocity field was used to filter out high frequency fluctuations in the flow. This was desirable in order to more clearly track the vortical structures over time. Figure 6 shows the cumulative modal energy distribution for all Re_c and α values. In general, the amount of energy in the lower order modes increases with increasing angle of attack for $\alpha = 14$, 16, and 18 deg. However, for $\alpha = 20$ deg the energy drops for the $\mathrm{Re}_c = 1.47 \times 10^4$ case. This can be seen more clearly in the inset, which shows only the first 30 modes. The velocity field at higher angles of attack contained more energy, or variance, in fewer modes when compared with the lower angle of attack cases. The higher velocity cases show a greater disparity in lower mode energy content for all angles of attack. For example, in Fig. 6(*a*), the energy contained in the first 100 modes varies about 7% over all angles of attack. In contrast, in Fig. 6(*b*), the energy contained in the first 100 modes varies as much as 13% depending on the angle of attack. Additionally, the energy contained in lower modes for the highest angle of attack, $\alpha = 20$ deg, does not decrease significantly with increasing Reynolds number. Therefore, increasing Reynolds number is seen to cause the velocity field to be less ordered for the lower angles of attack while not showing a significant effect for the $\alpha = 20$ deg case.

Figures 7(*a*)–7(*c*) show the unfiltered set of vortex locations for the first 200 ms of a time sequence of 2000 ms for each Reynolds number at $\alpha = 14$ deg. The progression of detected vortex structures in the downstream direction can be more clearly seen in Figs. 7(*a*) and 7(*b*) as the local slope of the line connecting these positions over time is used to represent the vortex convective velocity. The highest Re_c data shown in Fig. 7(*c*) is much more difficult to use to determine a convection velocity. A vortex tracking filter coupled with the POD reconstruction of the velocity field was used to more clearly identify the convection of structures downstream. The results of applying these methods for tracking

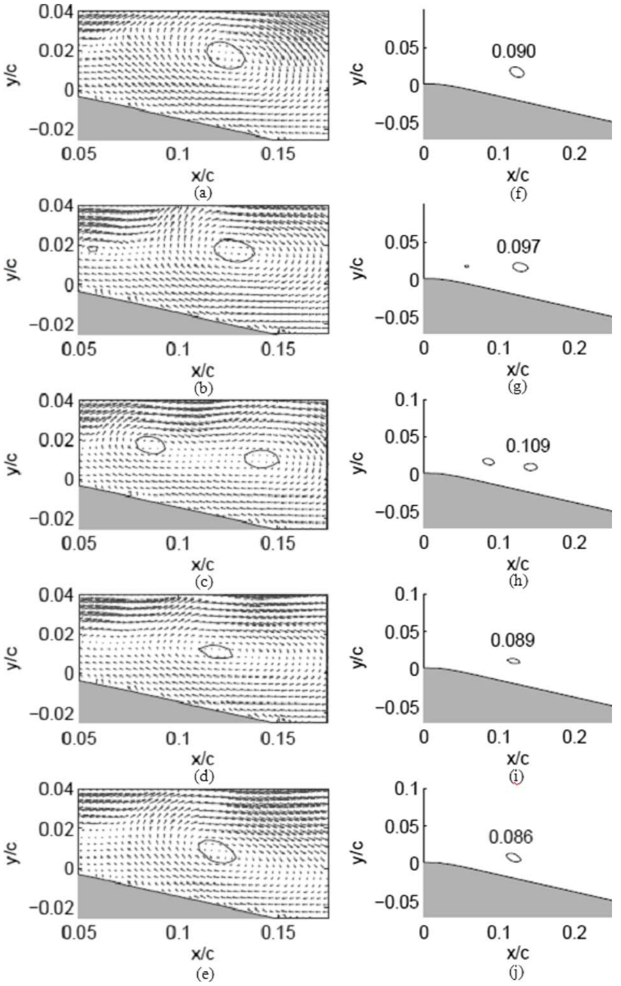

Fig. 5 Time sequence of (*a*)–(*e*) $\Gamma^* = -0.70$ contours and TR PIV vectors for $\mathrm{Re}_c = 1.47 \times 10^4$ and $\alpha = 14$ deg from $t = 64$ ms to $t = 72$ ms; (*f*)–(*j*) corresponding isolated contours of Γ^* shown over a larger field of view with vortex center *x*-position plotted above each contour.

are shown in Figs. 7(*d*)–7(*f*) for the $\alpha = 14$ deg cases. The origin points for tracking are denoted with a shaded star and path lines are traced through the vortex centers. These results use a POD filter based on the first 30 modes and a tracking filter time scale, $\tau_l = 0.05$ or 5% of the convective time scale based on U_∞. By removing smaller scale fluctuations, the POD filter allows for more consistent detection and tracking of vortex positions over time as seen by comparing the vortex position markers (circles) between Figs. 7(*a*)–7(*c*) and Figs. 7(*d*)–7(*f*). This is especially useful for the highest Re_c case.

The centers of the detected swirl regions were determined at all time steps for each time series. These time series were 2 s long resulting in 1000 data sets for each flow condition. The centers are defined based on the geometric mean of contours of $|\Gamma^*| = 0.7$ similar to those given in Figs. 5(*f*)–5(*j*). The distance traveled per sample time was used to calculate the *x* directional velocity component of these structures. The velocity vector is not strictly only along the *x* direction but also the *x* component is chosen to determine the downstream convection rate for vortical structures generated from leading edge separation. Table 1 lists the calculated convective velocity, U_{Γ^*}, normalized by the freestream velocity, U_∞, for all cases. The standard deviation of U_{Γ^*}, σ, normalized by the freestream velocity is also listed for all cases. Note that no filtering of the calculated velocities was applied. The convective velocities show weak variation with angle of attack, less than 5% for all cases. The dependence on Reynolds number is significant with a decrease of approximately 50% from $\mathrm{Re}_c = 1.47 \times 10^4$ to 6.67×10^4. Averaging the convective velocities for all angles of attack, the freestream normalized convective velocity is shown to decrease with increasing Reynolds number from 0.43 to 0.22. These three convective velocities vary approximately as $\mathrm{Re}_c^{-0.45}$ although more data are needed to verify this relationship.

The standard deviation of the convective velocity is on the order of the convective velocity and shows an increase for the $\mathrm{Re}_c = 6.67 \times 10^4$ case. This high standard deviation is in part due to jitter or stall and reversal of flow of the detected vortices illustrated in Fig. 5. Figure 7(*f*) shows the furthest downstream vortex between $t = 50$ and 100 ms moving downstream and upstream in alternating fashion for approximately 40 ms. More variation in movement is seen in the highest Re_c case in Fig. 7(*f*), which is consistent with a higher standard deviation of U_{Γ^*}. This is seen in Table 1 as a decrease in U_{Γ^*}/U_∞ with increasing Re_c while σ/U_∞ increases.

4.2 Spectral Analysis.

The time dependent nature of the detected vortices was studied using the transient characteristics of Γ^* at all grid location with no threshold applied. The strategy for evaluating the transient nature of Γ^* was to examine the regions where the rms of Γ^*, $\sigma(\Gamma^*)$, are high as well as the regions where the rms of the autocorrelation of Γ^*, $\sigma(\rho_{\Gamma^*})$, are high. An example of the nature of the temporal variations of Γ^* is shown in Fig. 8. The data shown are taken from a point within the vortex shedding shear layer at $x/c = 0.1$, $y/c = 0.025$. Note that the time span is only shown for the first 200 ms out of a total of 2000 ms. The autocorrelation of Γ^* indicates a highly cyclic process with a strong rms value of the autocorrelation. The associated spectra of Γ^* indicates a peak at a Strouhal number, St_h of approximately 2.4.

The distribution of $\sigma(\Gamma^*)$ for $\mathrm{Re}_c = 1.47 \times 10^4$, $\alpha = 20$ deg is shown in Fig. 9(*a*) and indicates that fluctuations of Γ^* are maximum in the shear region. A white line has been added to show the region of maxima of $\sigma(\Gamma^*)$. Figure 9(*b*) shows the distribution of $\sigma(\rho_{\Gamma^*})$, which are interpreted as regions of high cyclic characteristics of Γ^* Two regions of high $\sigma(\rho_{\Gamma^*})$ are identified by enclosed dashed lines, one just above the region of high rms values of Γ^* and the other in the recirculation region. Interestingly, the region of high rms values of Γ^* has a relative low cyclic characteristic. In addition, the high cyclic characteristics within the recirculation region do not correspond to large amplitude fluctuations since Fig. 9(*a*) shows relatively low rms values in the recirculation region.

To help determine the frequency of the cyclic processes within the shear layer, several experimental results were used. Representative spectra are shown in Fig. 10 for $\mathrm{Re}_c = 1.47 \times 10^4$ and $\alpha = 20$ deg. These plots are the results averaged over four points located in the high amplitude cyclic region denoted by the dashed line above the shear layer shown in Fig. 9(*b*). Using the TR PIV data at 500 Hz, the average spectrum of the vertical velocity fluctuations, v', is shown in Fig. 10(*a*) and the horizontal velocity fluctuation, u', in Fig. 10(*b*). Both spectra show a peak near $\mathrm{St}_h = 3.5$, with the v' spectrum peak being more dominant. The average spectral for the Γ^* fluctuations, $\Gamma^{*\prime}$, is shown in Fig. 10(*c*) revealing a similar peak near $\mathrm{St}_h = 3.5$. These spectra show a broad low frequency peak in the range of $\mathrm{St}_h = 0.1 - 0.3$. For all cases the resolution limit based on the length of the sampling period is $\mathrm{St}_h \sim 0.006 - 0.03$, depending on the Reynolds number and angle of attack. For comparison, hot wire data taken at approximately the same location in the shear layer were obtained at 10 kHz over 10 s and the resulting spectrum is shown in Fig. 10(*d*), showing a similar high frequency peak.

The average spectra using six points in the recirculation region identified in Fig. 9(*b*) were obtained using the same methods stated above for Fig. 10. The average spectra for v' and $\Gamma^{*\prime}$ are shown in Figs. 11(*a*) and 11(*b*) using the TR PIV data at 500 Hz for $\mathrm{Re}_c = 1.47 \times 10^4$, $\alpha = 20$ deg. To better illustrate the results, a

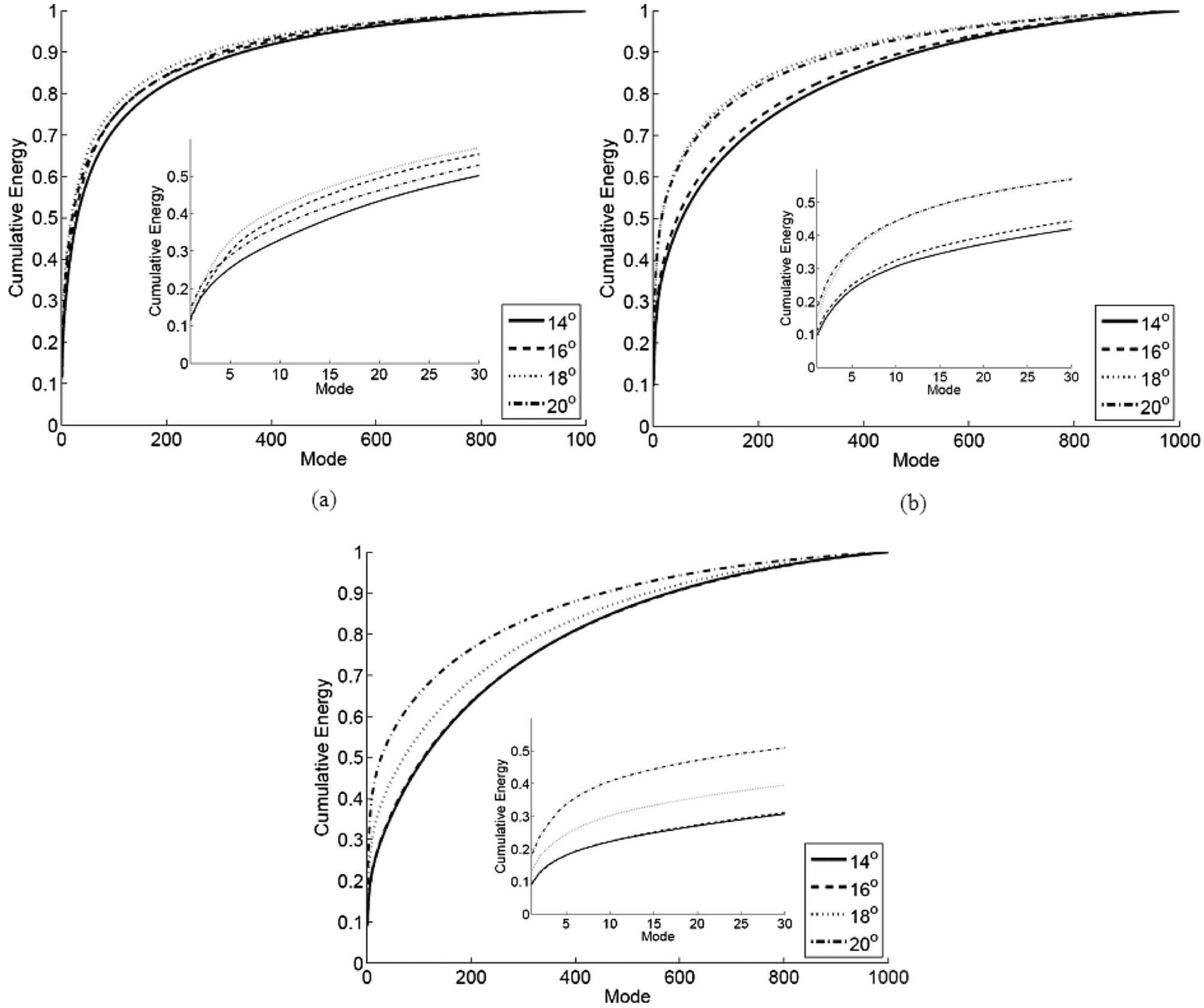

(a)

(b)

Fig. 6 The POD distribution of energy across modes and angles of attack for (*a*) $Re_c=1.47\times10^4$, (*b*) $Re_c=2.67\times10^4$, and (*c*) $Re_c=6.67\times10^4$

linear plot is used. The results are shown only up to $St_h=5.0$ since no peaks at higher frequencies were found. Both spectra show broad maxima near $St_h=0.2$. Comparing Figs. 10 and 11 indicates that the higher frequency peaks in the shear layer occur at approximately an order of magnitude higher value of St_h than any peaks in the recirculation region. Comparative tests using the hot wire results and longer time period TR PIV were carried out for a limited number of cases. Hot wire data obtained at 10 kHz over 10 s are presented in Fig. 11(*c*) and TR PIV data sampled at 100 Hz, over 10 s, are shown in Fig. 11(*d*). These spectra are similar to those found for the 500 Hz TR PIV data for both v' and $\Gamma^{*\prime}$ with peaks in the same range of St_h.

For all cases of Re_c and α, the average spectra of $\Gamma^{*\prime}$ were determined using the four points in the high shear region, which correspond with regions of high values of $\sigma(\rho_{\Gamma *})$. In addition, the average spectra of $\Gamma^{*\prime}$ using five points in the recirculation region were also calculated. To illustrate the results, the spectra for $\alpha=20$ deg and $Re_c=1.47\times10^4$ and 2.67×10^4 are shown in Fig. 12 using the TR PIV data at 500 Hz. Similar to the results shown in Fig. 10 for the high shear region, Figs. 12(*a*) and 12(*b*) show the spectra with peaks occurring at the high frequencies, with broad low frequency maxima. The average spectra in the recirculation region are shown in Figs. 12(*c*) and 12(*d*) for $\alpha=20$ deg, $Re_c=1.47\times10^4$ and 2.67×10^4. A broad low frequency maximum occurs near $St_h=0.2$ for both values of Re_c, which is similar to the lower frequency maxima found in the high shear region. Based on these results, it can be concluded that there is no pronounced frequency response in the recirculation region comparable to that observed for the leading edge separation, equivalent to a Strouhal number on the order of 3.5. However, the shear layer shedding frequency spectra does include a lower frequency component in the same range as that found in the recirculation region.

The results of the identification of dominant high frequency peaks for the low and middle Re_c cases were compiled and the results versus the angle of attack are shown in Fig. 13. Due to the TR PIV sampling rate limitation of 500 Hz, the maximum measurable St_h for the $Re_c=6.67\times10^4$ case is 3.4, whereas the limits for the lower two Re_c cases are 15.5 and 8.6. Consequently, the higher Re_c shear region results are too high to measure accurately and are not included. Shown in Fig. 13 is a nearly linear increase in St_h with increasing α for both values of Re_c, with a shift toward higher St_h for the higher Re_c case. Further data would be required to substantiate this trend over a larger range for both α and Re_c.

The previously identified average length scales, l_{track} and l_{freq}, were calculated for the two lower Re_c cases for which shear region Γ^* fluctuation signals were measured, $Re_c=1.47\times10^4$ and 2.67×10^4. The results are given in Table 2 normalized by the chord length. The length scale, l_{track}, was based on POD filtered reconstructed instantaneous snapshots of TR PIV data. The length scale, l_{freq}, was determined using the measured vortex convection

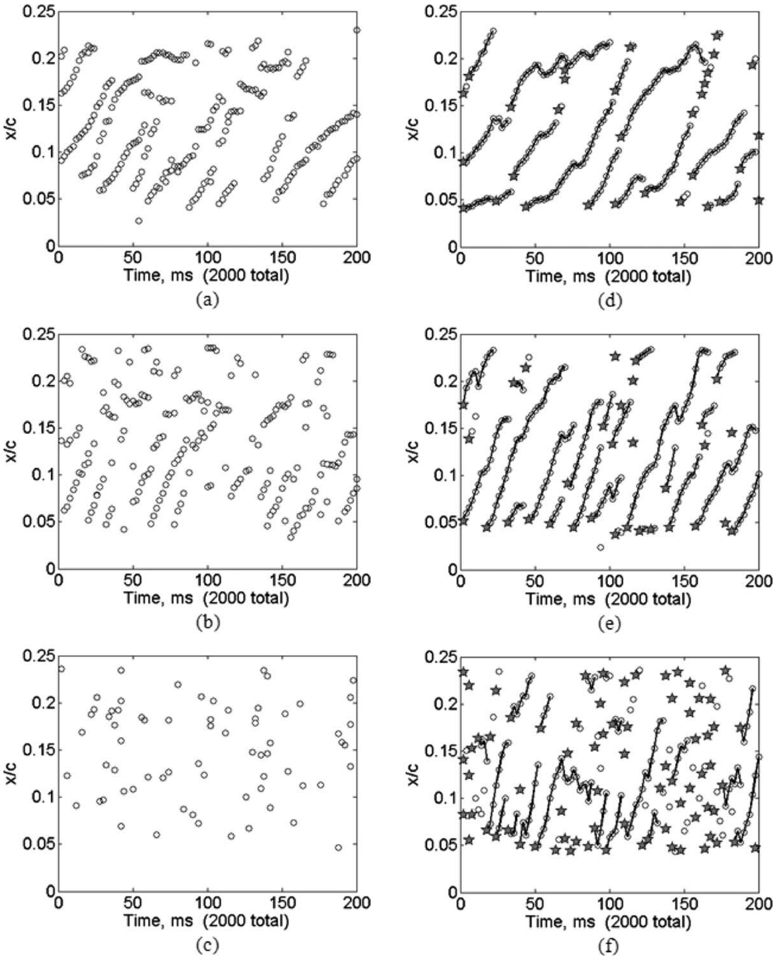

Fig. 7 Detected vortex positions shown for the first 200 ms of a total of 2000 ms with and without filtering. Unfiltered detected vortex positions for $\Gamma^*=-0.70$ at =14 deg and (*a*) $Re_c=1.47\times10^4$, (*b*) $Re_c=2.67\times10^4$, and (*c*) $Re_c=6.67\times10^4$. POD reconstructed detected vortex positions filtered for path lifetime greater than $0.05\tau_c$ for (*d*) $Re_c=1.47\times10^4$, (*e*) $Re_c=2.67\times10^4$, and (*f*) $Re_c=6.67\times10^4$ at $\alpha=14$ deg.

velocity and frequency data. The two length scales are shown to be within 10% for all α values for $Re_c=1.47\times10^4$ and 4% for $Re_c=2.67\times10^4$, with no observable trend with angle of attack for the range studied. Based on the variability of $U_{\Gamma*}$ and the resolution of the peak frequencies, the results for both length scales show very good agreement. The length scale is shown to decrease with increasing Re_c, which indicates a relative increase in rate of vortex generation within the shear layer as Re_c increases.

Table 1 Vortex convective velocity and its standard deviation for all Re_c and α

	$U_{\Gamma*}/U_\infty$			σ/U_∞		
α	Re_c					
(deg)	14,700	26,700	66,700	14,700	26,700	66,700
4	0.44	0.36	0.23	0.41	0.40	0.46
16	0.41	0.38	0.22	0.40	0.42	0.49
18	0.42	0.35	0.21	0.37	0.41	0.49
0	0.45	0.33	0.20	0.42	0.38	0.50
Avg.	0.43	0.36	0.22	0.40	0.40	0.49

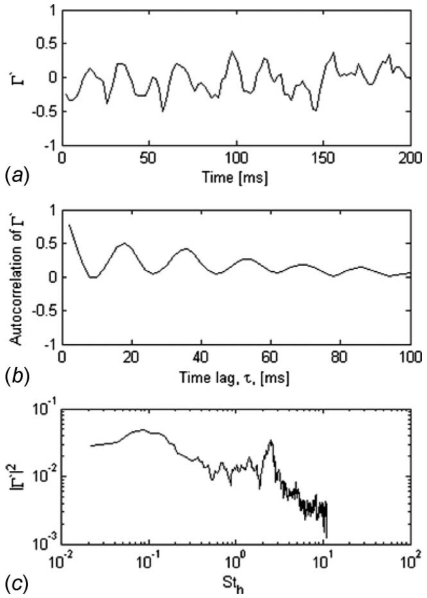

Fig. 8 (*a*) Time trace of $\Gamma^{*\prime}$ at $x/c=0.1$ and $y/c=0.025$ for the first 200 of 2000 total milliseconds of data for the $\alpha=14$ deg, $Re_c=1.47\times10^4$ case. (*b*) Corresponding autocorrelation of $\Gamma^{*\prime}$ shown for time lag values up to 100 ms. (*c*) Corresponding spectrum of $\Gamma^{*\prime}$ shown with observed peak near $St_h=2.4$.

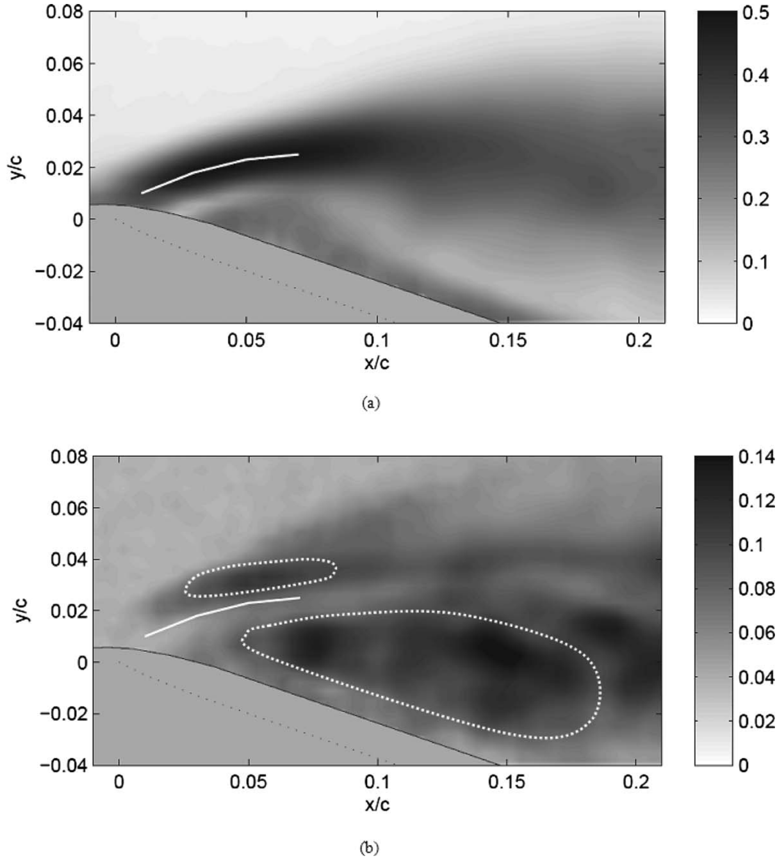

Fig. 9 (*a*) rms value of Γ^*, $\sigma(\Gamma^*)$, for the $Re_c=1.47\times10^4$, $\alpha=20$ deg case. The solid white line identifies the region of highest amplitude. (*b*) rms value of the temporal autocorrelation of Γ^*, $\sigma(\rho_{\Gamma*})$. The two areas outlined with dashed lines represent regions of large amplitude cyclic activity of Γ^*.

5 Conclusions

This study presents the results of the detection of strong vortical structures evolving from the leading edge of a flat wing for a range of low Reynolds numbers and angles of attack from 14 deg to 20 deg. These structures were identified based on a local measure of swirl. The region of interest coincides with the region of Kelvin–Helmholtz type instability extending from the separation point to approximately one-quarter of the chord length. The time resolved PIV data are used to generate velocity vector maps and these data were used to detect spanwise vortices sampled at 500

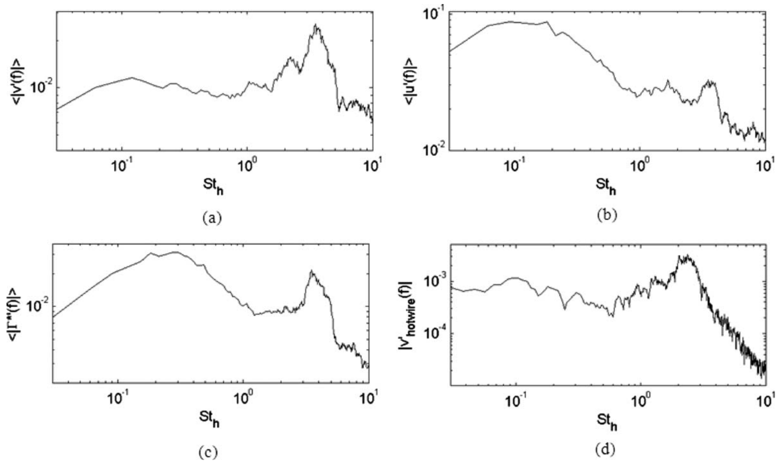

Fig. 10 Average spectral results using four points in the high cyclic shear region shown in Fig. 9(*b*) for $Re_c=1.47\times10^4$, $\alpha=20$ deg. TR PIV data at 500 Hz over 2 s: (*a*) averaged spectrum of v', (*b*) averaged spectrum of u', (*c*) averaged spectrum of Γ^*, and (*d*) hot wire data spectrum for a single point in the shear region using data at 10 kHz for 10 s.

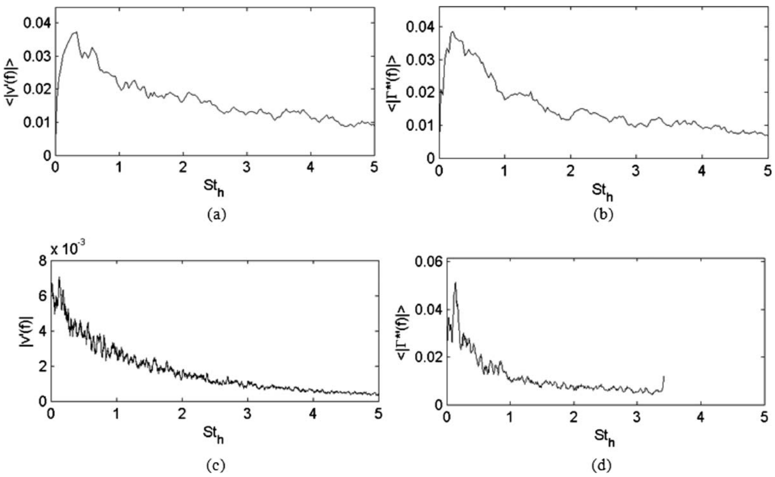

Fig. 11 **Average spectra of selected points in the recirculation region for $\mathrm{Re}_c=1.47\times10^4$ and $\alpha=20$ deg. (a) TR PIV data of v' at 500 Hz for 2 s, (b) TR PIV data of $\Gamma^{*\prime}$ at 500 Hz for 2 s, (c) hot wire spectrum of v' at 10 kHZ for 10 s, and (d) TR PIV data of $\Gamma^{*\prime}$ at 100 Hz for 10 s.**

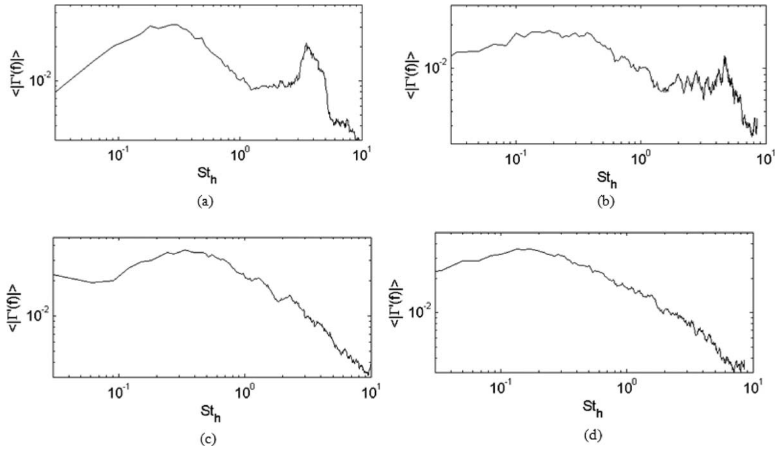

Fig. 12 **Average spectra of $\Gamma^{*\prime}$ for $\alpha=20$ deg using TR PIV data at 500 Hz for 2 s of data obtained from (a) the high cyclic shear region shown in Fig. 10(b) for $\mathrm{Re}_c=1.47\times10^4$, ($b$) the high cyclic shear region shown in Fig. 10(b) for $\mathrm{Re}_c=2.67\times10^4$, ($c$) the recirculation region shown in Fig. 10(b) for $\mathrm{Re}_c=1.47\times10^4$, and ($d$) the recirculation region shown in Fig. 10(b) for $\mathrm{Re}_c=2.67\times10^4$**

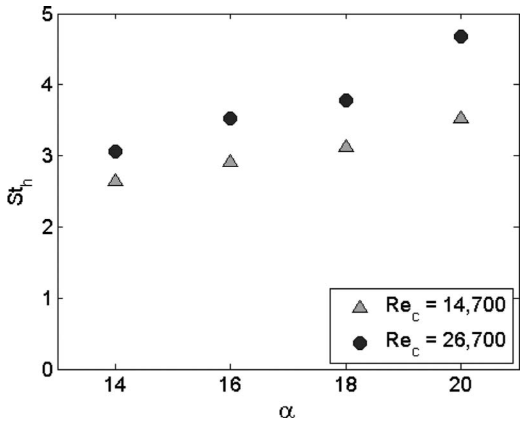

Fig. 13 **Average Strouhal number versus angle of attack for the high frequency component determined in the shear region**

Hz. Lower modes of the POD of the velocity field were used to reconstruct a low-pass filtered velocity field, which assisted in tracking vortices. A vortex convection velocity was determined for three relatively low Reynolds numbers and was not seen to

Table 2 **Length scales based on (i) the average separation distance between tracked vortices, l_{track}, and (ii) the frequency and convection velocity of detected vortices, l_{freq}**

	Re_c			
α	14,700		26,700	
(deg)	l_{track}/c	l_{freq}/c	l_{track}/c	l_{freq}/c
14	0.034	0.040	0.025	0.030
16	0.036	0.038	0.028	0.028
18	0.038	0.035	0.032	0.028
20	0.032	0.041	0.028	0.023
Avg.	0.035	0.038	0.028	0.027

change over angles of attack between 14 deg and 20 deg. The vortex convection velocity, $U_{\Gamma*}$, decreases with increasing Re_c, although more data are needed to accurately describe this trend. The rms values of the autocorrelation of Γ^*, $\sigma(\rho_{\Gamma*})$, were combined with spectral analysis of $\Gamma^{*\prime}$ to determine a region of time correlated events in the shear region, in which high frequency events on the order of $\mathrm{St}_h=3.4$ are observed. These leading edge vortices are shed at increasing rates for increasing Re_c and α. The vortex separation length scale using the instantaneous TR PIV data compares well with the length scale calculated from the dominant frequencies and vortex convection velocities observed in the shear region. Further detailed studies are needed to define the Re_c effects on dominant shear layer vortex frequencies and convection velocities.

Acknowledgment

Funding for this work was partially provided by AFOSR under Grant No. FA-9550-05-1-0041 and is gratefully acknowledged.

Nomenclature

$\mathbf{A}$ = amplitude time series matrix
A_M = area of swirl calculation subregion
c = wing chord length
$\mathbf{D}$ = $M \times N$ matrix of velocity data
h = approach height of wing section, $=c\sin(\alpha)$
l_{freq} = vortex separation length scale defined by the frequency of events and vortex convection velocity, U_{Γ^*}
l_{track} = vortex separation length scale observed in PIV frames containing multiple vortices
M = number of TR PIV grid locations
N = number of TR PIV time steps
PM = vector from subregion center
Re_c = Reynolds number based on chord length, $=U_\infty \cdot c/\upsilon$
$\mathbf{S}$ = singular values of the design matrix
St = Strouhal number based on chord length, $=fc/U_\infty$
St_h = Strouhal number based on wing approach height, $=fh/U_\infty$
$\mathbf{U}$ = left singular vectors of design matrix
U_M = velocity vector at point M
U_∞ = freestream velocity
U_{Γ^*} = convective velocity of vortex structure, x-direction
w = wing span
$\mathbf{V}$ = right singular vectors of design matrix
Z = perpendicular unit vector $\{0, 0, 1\}$

Greek Notation

α = angle of attack
ρ_{Γ^*} = temporal autocorrelation of Γ^*
$\sigma(\rho_{\Gamma^*})$ = root mean square of ρ_{Γ^*}
$\sigma(\Gamma^*)$ = root mean square of Γ^*
θ_M = angle between PM and U_M
Γ^* = swirl detection parameter
t_c = convective time scale, $=c/U_\infty$
τ_l = tracking filter time scale, $=t/t_c$

References

[1] McCullough, G. B., and Gault, D. E., 1951, "Examples of Three Representative Types of Wing-Section Stall at Low Speeds," NACA Technical Note 2502.

[2] Carmichael, B. H., 1981, "Low Reynolds Number Wing Survey, Volume 1," NASA Contractor Report No. CR-165803.

[3] Re, R. J., Pendergraft, O. C., Jr., and Campbell, R. L., 2006, "Low Reynolds Number Aerodynamic Characteristics of Several Airplane Configurations Designed to Fly in the Mars Atmosphere at Subsonic Speeds," NASA Report No. 214312.

[4] Mueller, T. J., and DeLaurier, J. D., 2003, "Aerodynamics of Small Vehicles," Annu. Rev. Fluid Mech., **35**, pp. 89–111.

[5] Torres, G. E., and Mueller, T. J., 2001, "Aerodynamic Characteristics of Low Aspect Ratio Wings at Low Reynolds Numbers," Prog. Astronaut. Aeronaut., **195**, pp. 115–142.

[6] Broeren, A. P., and Bragg, M. B., 2001, "Unsteady Stalling Characteristics of Thin Wings at Low Reynolds Number," Prog. Astronaut. Aeronaut., **195**, pp. 191–213.

[7] Bishop, R. E. D., and Hassan, A. Y., 1964, "The Lift and Drag Forces on a Circular Cylinder in a Flowing Fluid," Proc. R. Soc. London, Ser. A, **277**, pp. 32–50.

[8] Berger, E., and Wille, R., 1972, "Periodic Flow Phenomena," Annu. Rev. Fluid Mech., **4**, pp. 313–40.

[9] Mair, W. A., and Maull, D. J., 1971, "Bluff Bodies and Vortex Shedding—A Report on Euromech 17," J. Fluid Mech., **45**(2), pp. 209–224.

[10] Yarusevych, S., Sullivan, P. E., and Kawall, J. G., 2005, "Wing Boundary Layer Separation and Control at Low Reynolds Numbers," Exp. Fluids, **38**, pp. 545–547.

[11] Tinar, E., and Cetiner, O., 2006, "Acceleration Data Correlated With PIV Images for Self-Induced Vibrations of a Wing," Exp. Fluids, **41**, pp. 201–212.

[12] Cheng, M., and Chen, B. K., 2007, "A Numerical Study on Fluid Force Reduction of a Square Cylinder by Flow Control," Fluids Engineering Conference, San Diego, CA, Jul. 30–Aug. 2, Paper No. FEDSM2007-37025.

[13] Roshko, A, 1954, "On the Drag and Shedding Frequency of Two Dimensional Bluff Bodies," NACA Technical Note 3169.

[14] Abernathy, F. H., 1962, "Flow Over an Inclined Plate," ASME J. Basic Eng., **84**, pp. 380–388.

[15] Burgmann, S., Brücker, C., and Schröder, W., 2006, "Scanning PIV Measurements of a Laminar Separation Bubble," Exp. Fluids, **41**, pp. 319–326.

[16] Derksen, R. W., and Rimmer, J., 2006, "Aerodynamic Flow Simulation," *Int. Conference on Advances in Fluid Mechanics VI*, Skiathos, Greece, pp. 59–67.

[17] Jeong, J., and Hussain, F., 1995, "On the Identification of a Vortex," J. Fluid Mech., **285**, pp. 69–94.

[18] Adrian, R. J., Christiansen, K. T., and Liu, Z.-C., 2000, "Analysis and Interpretation of Instantaneous Velocity Fields," Exp. Fluids, **29**, pp. 275–290.

[19] Graftieaux, L., Michard, M., and Grosjean, N., 2001, "Combining PIV, POD and Vortex Identification Algorithms for the Study of Unsteady Turbulent Swirling Flows," Meas. Sci. Technol., **12**, pp. 1422–1429.

[20] Shinneeb, A.-M., Balachandar, R., and Bugg, J. D., 2008, "Analysis of Coherent Structures in the Far-Field Region of an Axisymmetric Free Jet Identified Using Particle Image Velocimetry and Proper Orthogonal Decomposition," ASME J. Fluids Eng., **130**, p. 011202.

[21] Agrawal, A., and Prasad, A. K., 2002, "Properties of Vortices in the Self-Similar Turbulent Jet," Exp. Fluids, **33**(4), pp. 565–577.

[22] Troolin, D. R., Longmire, E. K., and Lai, W. T., 2006, "Time Resolved PIV Analysis of Flow Over a NACA 0015 Airfoil With Gurney Flap," Exp. Fluids, **41**, pp. 241–254.

[23] Druault, P., Guibert, P., and Alizon, F., 2005, "Use of Proper Orthogonal Decomposition for Time Interpolation From PIV Data," Exp. Fluids, **39**, pp. 1009–1023.

[24] Weiland, C., and Vlachos, P., 2007, "Analysis of the Parallel Blade Vortex Interaction With Leading Edge Blowing Flow Control Using the Proper Orthogonal Decomposition," ASME Fluids Engineering Summer Conference, San Diego, CA, Paper No. FEDSM2007-37275.

[25] Kurtulus, D. F., Scarano, F., and David, L., 2007, "Unsteady Aerodynamic Forces Estimation on a Square Cylinder by TR-PIV," Exp. Fluids, **42**, pp. 185–196.

[26] Hinze, J. O., 1959, *Turbulence*, McGraw-Hill, New York.

[27] Dano, B. P. E., and Liburdy, J. A., 2006, "Vortical Structures of a 45° Inclined Pulsed Jet in Crossflow," Fluid Dynamics Conference, San Francisco, CA, AIAA Paper No. 2006-3543.

[28] Morse, D. R., and Liburdy, J. A., 2007, "Dynamic Characteristics of Flow Separation from a Low Reynolds Number Wing," Fluids Engineering Conference, San Diego, CA, Jul. 30–Aug. 2, Paper No. FEDSM20070-37083.

[29] Chen, G., Lin, Z., Morse, D., Snider, S., Apte, S., Liburdy, J., and Zhang, E., 2008, "Multiscale Feature Detection in Unsteady Separated Flows," IJNAM, **5**, pp. 17–35.

[30] Chatterjee, A., 2000, "An Introduction to the Proper Orthogonal Decomposition," Curr. Sci., **78**(7), pp. 808–817.

[31] Sirovich, L., 1987, "Turbulence and the Dynamics of Coherent Structures—Part I: Coherent Structures," Q. Appl. Math., **45**(3), pp. 561–571.

[32] Berkooz, G., Holmes, P., and Lumley, J. L., 1993, "The Proper Orthogonal Decomposition in the Analysis of Turbulent Flows," Annu. Rev. Fluid Mech., **25**, pp. 539–575.

[33] Morse, D. R., and Liburdy, J. A., 2008, "Experimental Time Resolved Flow Features of Separation Over an Elliptic Leading Edge," 46th AIAA Aerospace Sciences Meeting and Exhibit, Reno, NV, Jan. 7–10, AIAA Paper No. 2008-655.

Drag Reduction in Turbulent Flow With Polymer Additives

Shu-Qing Yang
Associate Professor
School of Civil, Mining and Environmental Engineering,
University of Wollongong,
New South Wales 2522, Australia
e-mail: shuqing@uow.edu.au

The mean velocity profile and friction factor in turbulent flows with polymer additives are investigated using Prandtl's mixing-length theorem. This study reveals that the mixing-length theorem is valid to express the drag-reducing phenomenon and that the presence of polymer additives increases the damping factor B in van Driest's model; subsequently reducing the mixing-length, this interprets that the polymer hampers the transfer of turbulent momentum flux, the velocity is increased, and flow drag is reduced. This study also discusses the onset Reynolds number for drag reduction to occur. The predicted velocity, friction factor, and onset Reynolds number are in good agreement with the measured data in the literature. [DOI: 10.1115/1.3111255]

Keywords: drag reduction, velocity distribution, van Driest's model, damping factor, friction factor

1 Introduction

It has been widely observed that addition of a small amount of macromolecular polymer to a Newtonian fluid may lead to a dramatic reduction in fluid resistance. Such phenomenon was first discovered by Toms [1], and many research studies and publications had been devoted to the subject over the past 50 years. The drag reduction (DR) flow has technological applications from fire engines to oil pipes. Scientists and engineers have conducted many studies on this phenomenon, including theoretical, experimental, and numerical approaches. However, the fundamental mechanism has still remained under debate.

For drag-reducing flows, the onset of drag reduction is an interesting phenomenon. Virk [2] observed that if the Reynolds number is larger than a certain value, the drag reduction occurs, and the log-law is shifted by an amount ΔB in the turbulent core, with no change in slope; below which the flow behaves like a Newtonian fluid, i.e., no drag reduction can be observed in the flow of dilute polymer solutions, and the flow resistance is similar to that of Newtonian fluid in the absence of additives. But the threshold Reynolds number has not been clearly identified; thus it is useful to determine the onset Reynolds number for drag reduction.

Virk [2] also divided the velocity profile of drag-reducing flow into three regions, i.e., the viscous sublayer, a buffer or elastic layer, and the turbulent core. This division appears to provide better insight for understanding the mechanisms of the drag-reducing phenomena; thus Virk's three-layer model has been widely adopted by researchers, such as by Larson [3], Min et al. [4,5], Gasljevic et al. [6], and Ryskin [7].

Since Virk's [2] systematical observations, with the advent of particle image velocimetry (PIV) (Warholic et al. [8], White et al. [9], etc.) and laser Doppler anemometry (LDA), e.g., Durst et al. [10], Willmarth et al. [11], Luchik and Tiederman [12], Harder and Tiederman [13], and Wei and Willmarth [14], turbulent structures can be observed, and their results showed that the root-mean-square (rms) of the fluctuations in the streamwise velocity increases while the rms of the fluctuations in the wall-normal direction decreases with drag reduction. Although the obtained results provide valuable insights into drag reduction for flow containing polymer additives, there is as yet no clear picture of why or how polymer additives reduce drag, and the physical mechanisms of drag reduction are still tentative [15,16]. Of the most important result from these turbulent measurements by LDA and PIV is the "stress deficit," i.e., the total shear stress in drag-reduced flow is greater than the sum of viscous shear stress ($=\nu du/dy$) and the measured Reynolds shear stress ($=-\overline{u'v'}$). Willmarth et al. [11], Den Toonder et al. [17], Warholic et al. [18], and Gyr and Tsinober [19] attributed this stress deficit to the effects of the long-chain polymer in the fluid. Gyr and Tsinober [19] expressed this shear deficit as

$$G(y) = \frac{\tau}{\rho} - \left[\nu \frac{du}{dy} + (-\overline{u'v'}) \right] \tag{1}$$

where ν is the kinematic viscosity, u is the time-averaged velocity, ρ is the fluid density, y is the distance from the wall, G is the shear deficit and $G \geq 0$, and τ is the total shear stress. For a pipe/channel flow $\tau = \rho u_*^2(1-y/h)$, where u_* is the friction velocity and h is the pipe radius or channel water depth. The existence of "shear deficit" suggests that the viscoelasticity as modified by the presence of the long-chain polymers should be an important property of a dilute polymer solution [4,5,17].

$G(y)$ was first called the Reynolds stress deficit or elastic stresses by Schümmer and Thielen [20] who found that $G(y)$ is essentially non-negligible. Gyr and Tsinober [19] commented that $G(y)$ must be positive. Based on experimental data, Gyr and Tsinober [19] and Giesekus [21] expressed the function of shear deficit as

$$G(y) = \nu_{\text{eff}} \frac{du}{dy} \tag{2a}$$

where ν_{eff} is the effective viscosity.

Using an analogy with Boussinesq's expression for the eddy viscosity in turbulence, Yang and Dou [22] postulated that the effective viscosity can be expressed by

$$\nu_{\text{eff}} = \alpha_* u_* h \tag{2b}$$

where α_* is an elastic factor that only depends on polymer species and concentration and is independent of turbulent characteristics.

Investigators found that the shear deficit can be derived from the constitutive equations governing turbulent flows with polymer additives, e.g., Min et al. [4,5] from the Oldroyd-B model, Dou [23] and Den Toonder et al. [17] from the Maxwell model, and Berman [24] and Ptasinski et al. [25] from the FENE-P model.

Benzi et al. [26] derived the following momentum equation for visco-elastic flows from the FENE-P model:

Contributed by the Fluids Engineering Division of ASME for publication in the Journal of Fluids Engineering. Manuscript received May 28, 2007; final manuscript received August 2, 2008; published online April 10, 2009. Assoc. Editor: Steven Ceccio.

$$\frac{\tau}{\rho} = -\overline{u'v'} + \nu\frac{du}{dy} + \nu_p\langle R_{yy}\rangle\frac{du}{dy} = u_*^2\left(1-\frac{y}{h}\right) \tag{3}$$

where $\langle R_{yy}\rangle$ is the ensemble average dimensionless extension tensor of the dyadic product of the end-to-end vector distance of the polymer chains in the y direction and ν_p is a viscosity parameter that is related to the concentration of the polymer. The right-hand side of Eq. (3) is simply the rate at which momentum is produced by the pressure head, and on the left-hand side the Reynolds stress is the momentum flux [2].

Gyr and Tsinober's [19] expression shown in Eq. (1) can be rewritten as follows:

$$\frac{\tau}{\rho} = -\overline{u'v'} + \nu\frac{du}{dy} + \nu_{\text{eff}}\frac{du}{dy} = u_*^2\left(1-\frac{y}{h}\right) \tag{4}$$

By comparing Eqs. (3) and (4), one has

$$\nu_{\text{eff}} = \nu_p\langle R_{yy}\rangle \tag{5}$$

Equation (5) establishes the relationship between the effective viscosity and properties of polymer solution in drag-reducing flows. If $\langle R_{yy}\rangle$ and ν_p can be determined from the polymer concentration and the vector distance of the polymer molecules, then one is able to determine ν_{eff}. Equation (4) provides a useful tool to assess the effective viscosity ν_{eff} from the measured Reynolds shear stress and velocity gradient. In other words, if the FENE-P model is correctly expressed as the interaction of polymer molecules and turbulence, then the obtained $\nu_p\langle R_{yy}\rangle$ from the property of polymer and concentration must be the same as ν_{eff} obtained from the properties of turbulence using Eq. (4); this conclusion can be extended to other models, such as Oldroyd-B model and Maxwell model.

Instead of solving Eq. (3) directly, Benzi et al. [2] and L'vov et al. [16] introduced the energy balance equation and other assumptions, such as $u_*^2(1-y/h)\approx u_*^2$ and $-\overline{u'v'}\approx 0$, then they claimed that the velocity equation they obtained is valid even for the whole flow region.

Different from the approach used by Benzi et al. [2] and L'vov et al. [16], the present study makes an attempt on the direct solution of Eq. (3). By inserting Eq. (2*b*) into Eq. (4), one obtains the dimensionless Reynolds shear stress

$$-\frac{\overline{u'v'}}{u_*^2} = \left(1-\frac{y^+}{h^+}\right) - D_*\frac{du^+}{dy^+} \tag{6}$$

where $u^+=u/u_*$, $y^+=u_*y/\nu$, $h^+=u_*h/\nu$, and

$$D_* = 1 + \alpha_* h^+ \tag{7}$$

Equation (6) becomes the governing equation for a Newtonian flow when $\nu_{\text{eff}}=0$ or $D_*=1$. Equation (7) shows that the drag-reducing parameter D_* varies linearly with the Reynolds number h^+, and the proportionality factor α_* depends on visco-elastic effect caused by polymer additive.

Based on Maxwell model, Dou [23] obtained the following expression for α_*:

$$\alpha_* = A[\eta]C\alpha_o \exp(-B_1\alpha_o^{0.7}C_w) \tag{8}$$

where $A=\pi^2/15$, $B_1=25{,}500$, $[\eta]$ is the intrinsic viscosity of the polymer, C is the concentration of the solution (g/cm^3), C_w is the concentration of the solution as a mass ratio (g/g), and α_o is a coefficient that depends on polymer's characteristics for drag reduction.

To solve Eq. (6), one has to model the Reynolds shear stress in drag-reducing flow. Now there are many equations available in the literature to express the Reynolds shear stress in Newtonian fluid flow, and one of the most widely cited is the mixing-length equation developed by Prandtl. Hence, it would be interesting to investigate whether Prandtl's formula is valid in drag-reducing flows.

Yang and Dou [22] investigated the velocity profiles in turbulent boundary layer flows; the emphasis of this study will be placed on the pipe flows. The objectives of this study are as follows: (1) to theoretically investigate the mean velocity profile and friction factor of drag reduction flow, (2) to quantitatively express the onset Reynolds number for drag reduction, and (3) to determine the relation between the damping factor in van Driest's [27] model and D_*.

2 Velocity Profile in Drag-Reduced Flows

The Reynolds shear stress in a turbulent flow can be modeled by Prandtl's mixing-length formulation, i.e.,

$$-\overline{u'v'} = l^2\left(\frac{du}{dy}\right)^2 \tag{9}$$

where l is the mixing-length over which the turbulence characteristics remain unchanged [28]. Inserting Eq. (9) into Eq. (6), one has

$$l^{+2}\left(\frac{du^+}{dy^+}\right)^2 + D_*\frac{du^+}{dy^+} - (1-\eta) = 0 \tag{10}$$

where $l^+=lu_*/\nu$ and $\eta=y^+/h^+$.

By solving the quadratic equation shown in Eq. (10), one obtains du^+/dy^+ as follows:

$$\frac{du^+}{dy^+} = \frac{2(1-\eta)}{D_* + \sqrt{D_*^2 + 4l^{+2}(1-\eta)}} \tag{11}$$

The velocity profile can be obtained by integrating Eq. (11) with respect to y^+,

$$u^+ = \int_0^{y^+} \frac{2(1-\eta)}{D_* + \sqrt{D_*^2 + 4l^{+2}(1-\eta)}}dy^+ \tag{12}$$

The most commonly employed expression of mixing-length for pipe, channel, and boundary layer flows is the one developed by van Driest [27]:

$$l^+ = ky^+\Gamma(y^+) \tag{13}$$

where k is the von Karman constant. $\Gamma(y^+)$ is van Driest's damping function, which can be expressed as follows:

$$\Gamma(y^+) = 1 - \exp(-y^+/B) \tag{14}$$

Equations (13) and (14) state that increasing B leads to decreasing l. If B approaches infinity, then $\Gamma(y^+)=0$ and $l=0$. Therefore, one can conclude that if the polymer hampers the transfer of turbulent momentum flux, i.e., $(-\overline{u'v'})$, then the mixing-length l will be reduced and consequently the parameter B becomes larger. In other words, the parameter B could reflect the damping effect caused by polymer additives.

If the effective viscosity $\nu_{\text{eff}}=0$, Eq. (2*b*) gives $\alpha_*=0$, and Eq. (7) shows $D_*=1$, subsequently Eq. (12) becomes the velocity profile of the Newtonian fluid flow. Hence, one may conclude that Prandtl's mixing-length is valid for both drag-reducing flow and Newtonian fluid flow if the damping factor is properly defined.

According to van Driest, the damping factor B needs to be determined empirically; he suggested that for a Newtonian fluid flow, the damping factor B is 26 ($=B_o$). Cebeci and Smith [29] found that the damping factor should be a function of dimensionless quantities involving other factors such as mass transfer, compressibility, etc. Thus, it can be inferred that the damping factor should be a function of D_*.

In fact, Lumley [15] and Berman [24] realized that polymer stretching damp cross-stream or wall-normal velocity fluctuations hamper eddy movement in the wall-normal direction. Hence, it is natural that the damping factor in drag-reducing flows will be different from that in Newtonian flows.

Lumley also found that in drag-reducing flows the polymer molecules are expanded in the flow outside the viscous sublayer

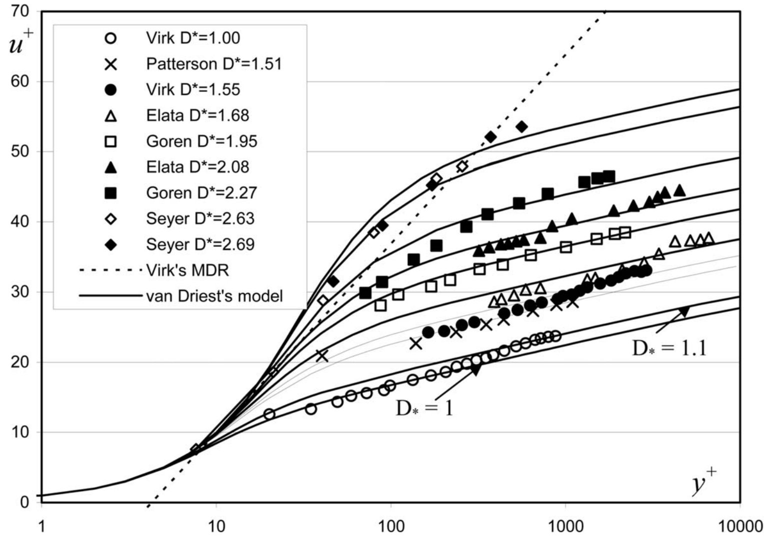

Fig. 1 The velocity distribution in flows containing polymer additives after Virk [2]

due to possible stretching of the polymer molecules; this leads to a thickening of the viscous sublayer leading to a decrease in the velocity gradient at the wall. The thickness of the viscous sublayer, δ^+, can be assessed by $\delta^+=11.6D_*^3$ [22]. It is well known that inside the viscous sublayer, the velocity can be expressed by $u^+=y^+$, but Eq. (11) gives $u^+=y^+/D_*$ if $y^+\approx 0$. Hence Eq. (11) is valid only in the flow outside the viscous sublayer. White and Mungal [30] (page 239) commented that "in wall-bounded turbulent shear flows, polymer are primarily believed to be stretched just outside the viscous sublayer;" this means that in the viscous sublayer $D_*=1$ should be used.

To test this postulation, the experimental data compiled by Virk's [2] are shown in Fig. 1. The solid lines are calculated from Eq. (12) using the popular and most accurate fourth-order Runge–Kutta method, the damping factor B is adjusted to fit the experimental data best, and the values of D_* are obtained using Eq. (7).

It can be seen from Fig. 1 that the difference between $D_*=1.1$ and $D_*=1.0$ falls into the measurement uncertainty; thus the onset of drag reduction could be defined as $D_*=1.1$. If $D_*>1.1$, the velocity shift becomes discernible. From Eq. (7), one can estimate the threshold Reynolds number for the occurrence of drag reduction as follows:

$$\left(\frac{u_*h}{\nu}\right)_c > \frac{0.1}{\alpha_*} \tag{15}$$

where $(u_*h/\nu)_c$ is the threshold Reynolds number. Equation (15) indicates that the onset Reynolds number for drag reduction depends only on the kind and concentration of polymer additives. This is consistent with experimenters' observations, such as Virk [2] and Gyr and Bewersdorff [31].

It can be seen from Fig. 1 that in the turbulent core, the predicted velocity is shifted by an amount ΔB from the standard log-law in Newtonian fluid flow, with no change in slope, and the velocity distribution can be expressed by

$$u^+ = 2.5 \ln y^+ + 5.5 + \Delta B \tag{16}$$

It can be seen clearly from Fig. 1 that Virk's three-layer model can be expressed by a single equation, i.e., Eq. (12).

In Fig. 1, the dotted line represents Virk's asymptote of maximum drag reduction (MDR), i.e.,

$$\frac{u}{u_*} = 11.7 \ln\frac{u_*y}{\nu} - 17.0 \tag{17}$$

Equation (17) was empirically proposed by Virk [2]. But Benzi et al. [26] and L'vov et al. [16] obtained Eq. (17) by solving Eq. (3). Prandtl's model shown in Fig. 1 gives continuous velocity gradient from the subviscous layer to the elastic layer and the turbulent core. The theoretical results state that in the turbulent core, the solid lines are parallel to the log-law and ΔB in Eq. (16) depends on D_*.

Virk's asymptote or Eq. (17) makes the drag-reducing effect an intriguing topic for research on turbulent flow because Virk stated that this asymptote must be a feature of the turbulent flow. However, several experimenters, e.g., Gyr and Bewersdorff [31], show that Virk's assumption of the ultimate velocity profile may not be generally true, i.e., whether or not a specific additive has its own MDR asymptote is still an open question. From Fig. 1, one may find that the lines with $D_*=2.63$ and 2.69 are very close to the data points that were used by Virk to obtain MDR asymptote or Eq. (17).

Figure 1 shows that in the so-called buffer layer the calculated velocity deviates noticeably from that of Newtonian fluid flow ($D_*=1$), and the deviation becomes larger if D_* is higher. This transition is achieved because the strain rate and vorticity fields associated with the buffer layer are suitable to cause full extension of polymers, leading to a corresponding large increase in the elongational viscosity [32,33]; therefore a large increase in the effective viscosity or D_* just outside the viscous sublayer will suppress turbulent fluctuations, increase the buffer-layer thickness, and reduce the wall friction [34]. Therefore, it can be seen that the mechanism of drag reduction by polymer additives has been well expressed mathematically by changing the effective viscosity or D_* from the viscosity sublayer to the buffer layer.

In Fig. 1, the value of damping factor B is obtained by the best-fit technique; the relationship between the obtained B and D_* is shown in Fig. 2. As expected, the experimental data show that the damping factor depends on D_*, and the relation can be expressed as follows:

$$\frac{B}{B_o} = D_*^m \tag{18}$$

where $B_o=26$ and $m=2.5$.

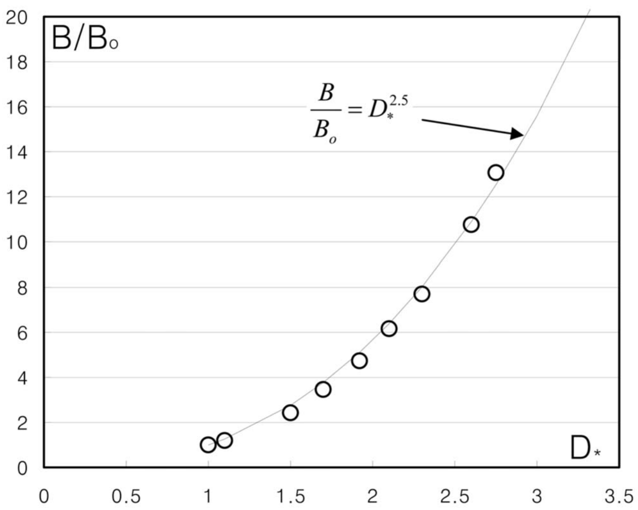

Fig. 2 Relation between the damping factor B and D_* based on the data shown in Fig. 1

Figure 1 includes the experimental data presented before 1971. In order to illustrate the validity of Eq. (18), more recently published experimental data are given in Fig. 3. The data sets published by Den Toonder et al. [17], Luchik and Tiederman [12], Warholic et al. [8], Ptasinski et al. [35], and Harder and Tiederman [13] are included in Fig. 3. The type of polymer, its concentration C, pipe radius/flow depth h, and DR are listed in Table 1. Since some experimental researchers did not report the polymer molecular weight and intrinsic viscosities in their experiments, the parameter D_* is estimated by the best-fit to experimental data instead of using Eq. (8), and the damping factor B is calculated from Eq. (18) based on D_*.

It can be seen from Fig. 3 that the agreements between the measured velocity profiles in drag-reduced flows and Eq. (12) are reasonable. Virk's asymptote is also included in Fig. 3 for comparison. From Fig. 3, one finds that Virk's asymptote does not represent a universal relationship for the maximum drag reduction; the experimental data of Ptasinski et al. [25,35] begin to exceed Virk's asymptote significantly at $y^+=80$. Warholic et al. [18] also concluded that Virk's asymptote may not be universal. However, it can be seen from Figs. 1 and 3 that Eq. (12) can represent the data points. In the turbulent core, the solid lines shown in Figs. 1 and 3 are parallel to the log-law for Newtonian fluid flows with a shift of ΔB without change in slope, as stated by Eq. (16).

This study assumes that the velocity distribution in the viscous sublayer follows Eq. (11) because in the near wall region the distribution of the velocity must follow $u^+=y^+$, not $u^+=y^+/D_*$ as Eq. (11) gives. Thus it is necessary to test the hypothesis using the velocity data in the near wall region. Figure 4 shows the measured velocity distribution inside the viscous sublayer. It can be seen clearly from Fig. 4 that this model can express the velocity distribution very well, indicating that the assumption is reasonable.

Currently, many researchers used direct numerical simulation (DNS) to model the mechanism of drag-reducing flow, such as De Angelis et al. [36], Min et al. [4,5], Housiadas and Beris [37], and Ptasinski et al. [25], and their results show that DNS is a powerful tool to understand the drag-reducing flow. This study uses a different approach to express the drag-reducing effect; thus it would be useful to compare the proposed model with DNS method.

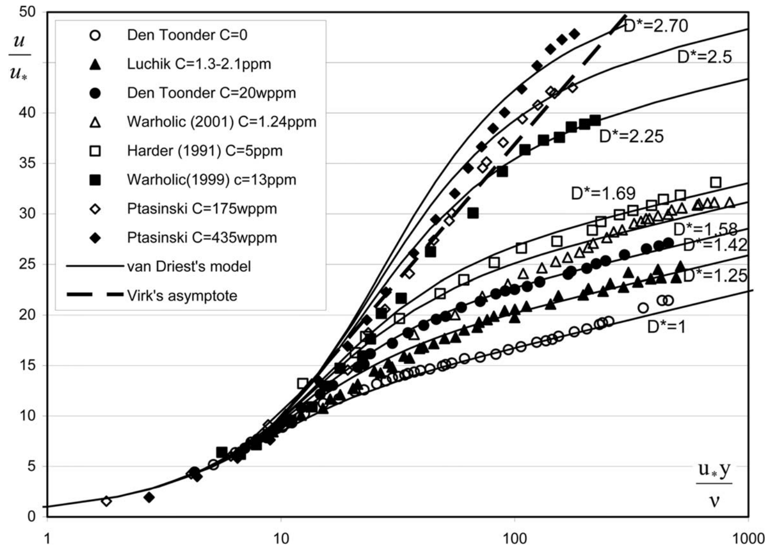

Fig. 3 Comparison of Eq. (12) with the measured velocity profiles

Table 1 Summary of mean velocity profile data shown in Fig. 3

Source	Solvent	Polymer	Polymer concentration, C (wppm)	Pipe radius/water depth, h (cm)	Drag reduction (DR)
Den Toonder et al. [17]	Water	Superfloc A110	20	4	24.2%
Luchik and Tierderman [12]	Water	Separan AP-273	1.3–2.1	1.25	22.0%
Warholic et al. [8]	Water	Percol 727	1.24	2.54	42.0%
Harder and Tiederman [13]	Water	Separan AP-273	5	3.0	
Warholic et al. [18]	Water	Percol 727	13	2.54	64.0%
Ptasinski et al. [25]	Water	Superfloc A110	175, 435	4.0	65%, 70%

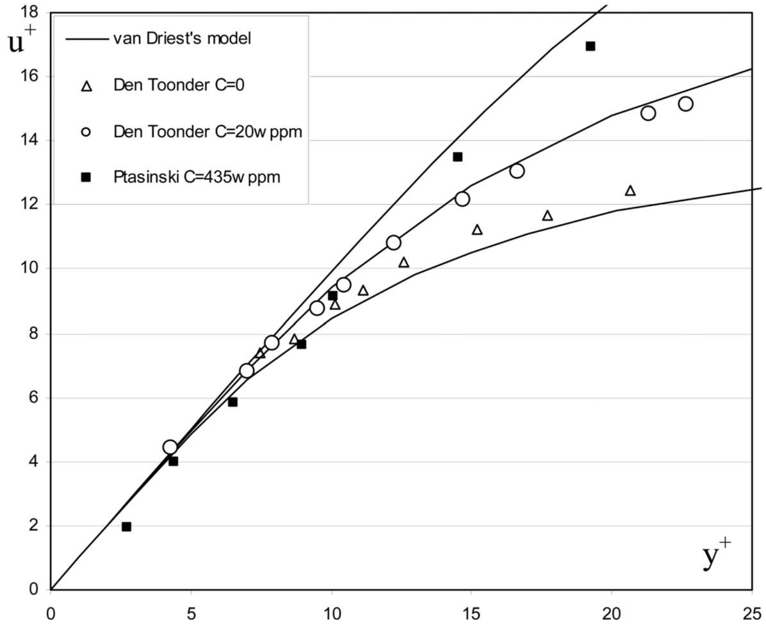

Fig. 4 Velocity distribution inside the near wall region

Ptasinski et al. [35] measured the velocity profiles in drag-reducing flows, and the comparison of the measured data with the present model is included in Fig. 3, in which the discrepancy is noticeable. Ptasinski et al. [25] modeled their measurements in 2001 using DNS, and the comparison between the same measured data as shown in Fig. 3 with DNS's results is included in Fig. 5. Based on the data of Ptasinski et al. [35] in Figs. 3 and 5, one could find that the present model yields the best agreement relative to DNS's results as well as Virk's asymptote of maximum drag reduction.

3 Relation Between Reynolds Number and Drag-Reducing Parameter

Figures 1 and 2 show that the measured velocity profiles in drag-reduced flows can be described by van Driest's model, and the difference between the drag-reducing flow and the Newtonian fluid flow is caused by the effective viscosity or the single parameter D_*, which contains the effects of polymer and turbulence characteristics. Equation (7) states that D_* varies linearly with the Reynolds number. Therefore, it is worthwhile to investigate whether the linear relationship exists. Reischman and Tiederman's [38] experimental data are selected for this purpose. Their experiment was conducted in a channel (305 mm high and 28.4 mm wide), and the velocity was measured by LDA. Magnifloc 837A was used as the polymer additive. The concentration of dilute polymer solution was maintained at 100 ppm by weight. All measured velocity profiles are shown in Fig. 6 in which DR stands for drag reduction. The drag-reducing parameter D_* is determined by the best-fit to the data. The relation between the obtained D_* and the Reynolds number u_*h/ν is shown in Fig. 7, in which the data points collapse into a linear relationship, as predicted by Eq. (7). The linear relation shown in Fig. 7 is understandable because Reischman and Tiederman [38] did not change the polymer species and concentration in their experiment, but only changed the

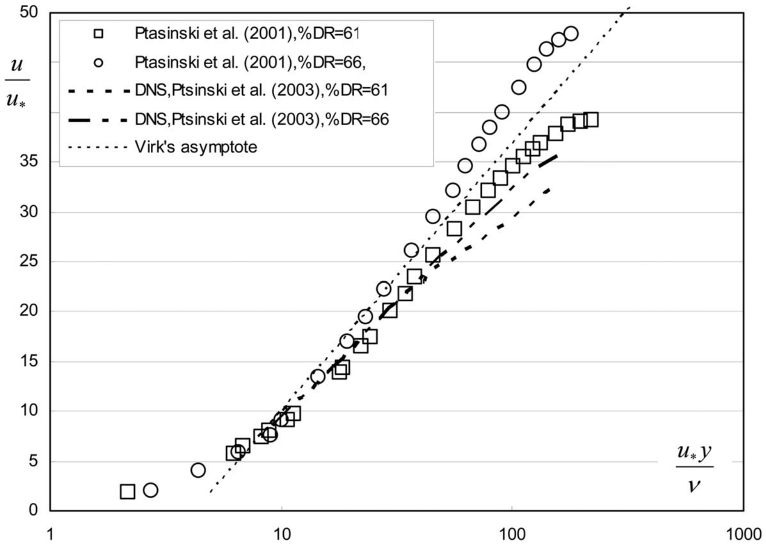

Fig. 5 Comparison of measured velocity profiles in drag-reducing flows with DNS's model after Ptasinski et al. [25,35]

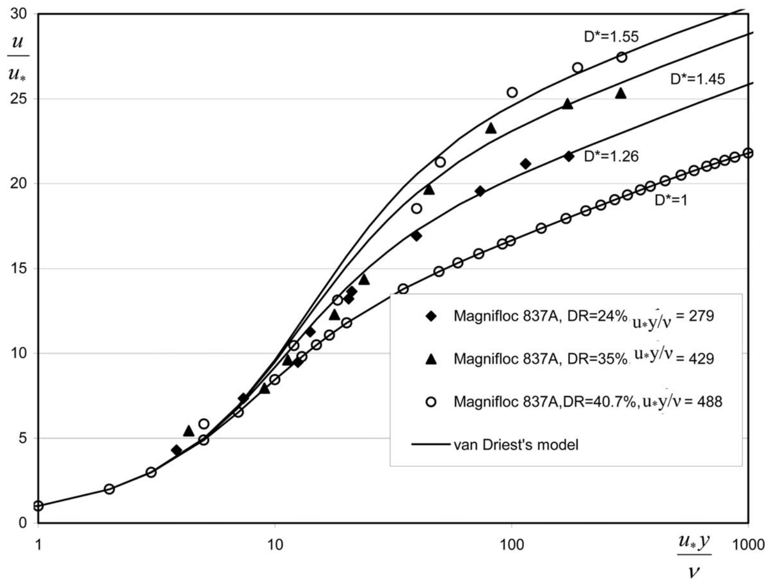

Fig. 6 Mean velocity profiles measured by Reischman and Tiederman [38]; DR stands for drag reduction

Reynolds number. In other words, the straight line in Fig. 7 interprets that polymer species and concentration only affect the value of α_*. For Magnifloc 837A at 100 ppm used by Reischman and Tiederman [38], the coefficient $\alpha_*=0.0011$. Therefore, one can conclude from Reischman and Tiederman's [38] measurements that the effective viscosity is proportional to $u_* h$, as shown in Eq. (2*b*).

4 Friction Factor

Equations (7) and (8) state that the elastic factor α_* is independent of flow strength, and D_* varies linearly with the Reynolds number, i.e., $u_* r/\nu$; this has been proved in Fig. 7. It would be interesting to investigate how the factor α_* changes with the polymer concentration. To do so, the friction factor of drag-reducing flows f defined as follows is investigated:

$$f=2\left(\frac{u_*}{V}\right)^2 \tag{19}$$

where V is the cross-sectional averaged velocity.

In a laminar flow, $-\overline{u'v'}=0$, Eq. (4) becomes

$$u_*^2\left(1-\frac{y}{h}\right)=\nu\frac{du_l}{dy} \tag{20}$$

where u_l is the velocity in a laminar flow. Integrating Eq. (20) and imposing the nonslip boundary condition, i.e., $u_l=0$ at $y=0$, one obtains

$$u_l^+=y^+\left(1-\frac{\eta}{2}\right) \tag{21}$$

For the transitional region from the laminar to the turbulent state, Yang and Dou [22] obtained the following velocity distribution:

$$u_t^+=r_l u_l^+ + (1-r_l)u^+ \tag{22}$$

where u_t^+ is the dimensionless velocity in the transitional region, u_l^+ is determined using Eq. (21), and u^+ is determined using Eq. (12). The parameter r_l is the probability of laminar occurrences and may be expressed as follows [22]:

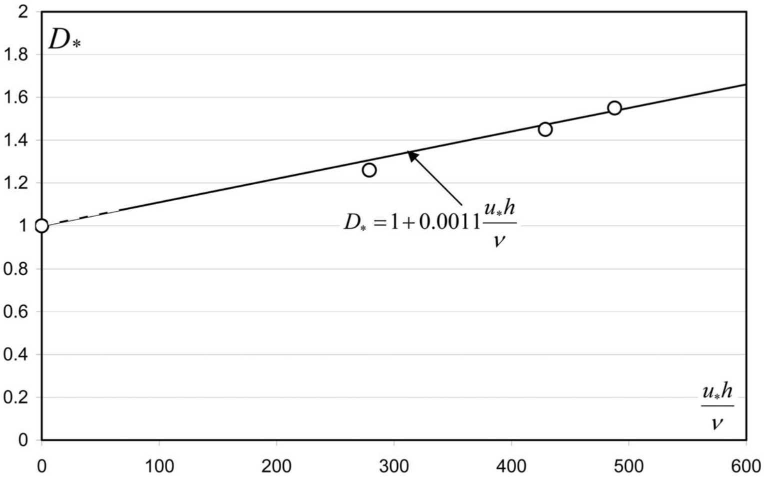

Fig. 7 Linear relation between D_* and Reynolds number based on Reischman and Tiederman's [38] data

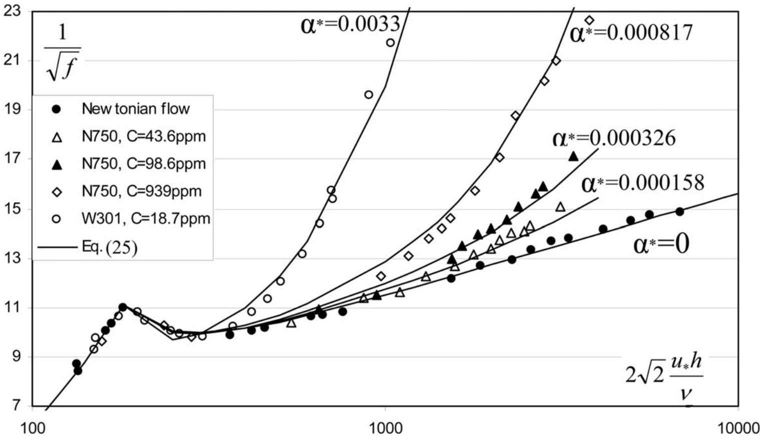

Fig. 8 Comparison of friction factor between the measured results by Virk [2] and Eq. (24)

$$r_l = \begin{cases} \frac{1}{e}\left[\sum_{n=1}^{\infty} \frac{n}{n!}\left(\frac{R_{*k}}{R_*}\right)^{2n}\right] & \text{for } R_* \geq R_{*k} \\ 1 & \text{for } R_* < R_{*k} \end{cases} \tag{23}$$

where R_* is the Reynolds number $(=u_*h/\nu)$ and R_{*k} is the threshold Reynolds number at which the flow becomes unstable and turbulence appears. For a pipe flow $R_{*k}=67.82$ or $2Vh/\nu=2300$. Therefore, one is able to obtain the drag coefficient f from the mean velocity, which is determined by integrating Eq. (12),

$$\sqrt{\frac{1}{f}} = \frac{1}{\sqrt{2}}\frac{V}{u_*} = \frac{1}{\sqrt{2}}\left[r_l\frac{R_*}{4} + \frac{1-r_l}{\pi R_*^2}\int_0^{R_*} 2\pi(R_* - y^+)u^+dy^+\right] \tag{24}$$

The comparison of $1/\sqrt{f}$ given by Eq. (24) and Virk's [39] experimental data in smooth pipes is presented in Fig. 8, which shows that Eq. (24) ($\alpha_*=0$) represents the data points obtained in Newtonian fluid flows well. For drag-reducing flows, Virk used polyethyleneoxide N750 ($\alpha_o=0.019$) as the polymer additive with the following polymer concentrations: 43.6 ppm, 98.6 ppm, and 939 ppm; Eq. (8) gives the corresponding elastic factors $\alpha_* = 0.000158, 0.000326, 0.000817$. In Fig. 8, the experimental data for polyethyleneoxide W301 ($\alpha_o=0.166$) with a concentration of 18.7 ppm are also included for comparison; Eq. (8) gives $\alpha_* = 0.0033$ for this case. Figure 8 indicates that for each line, the parameter α_* holds constant over the full range of Reynolds numbers, i.e., u_*h/ν. The good agreement between the measured and predicted friction factors indicates that α_* is independent of the Reynolds number.

For the drag reduction flows shown in Fig. 8, the calculated onset Reynolds number $\mathrm{Re}\sqrt{f}(=2\sqrt{2}u_*h/\nu)$ from Eq. (15) is 1790 for $\alpha_*=0.000158$, which is very close to the measured value of 1500; for $\alpha_*=0.000326$, the calculated $\mathrm{Re}\sqrt{f}$ is 867 and the observed value is 960; thus, Eq. (15) can express the onset of drag reduction [40–43].

5 Conclusions

The applicability of Prandtl's mixing-length theorem in drag-reducing flows is investigated, and the mixing-length equation developed by van Driest is used. This study finds that the damping factor B in van Driest's model depends on the effective viscosity caused by polymer additives, and the velocity in visco-elastic fluid flow can be well predicted by Prandtl's theorem. Based on the comparison between measured and predicted velocity and friction factors in pipe/channel flows, this study reaches the following conclusions.

1. The difference between the drag-reducing flow and Newtonian fluid flow is caused by the stress deficit, which can be well represented by the sole parameters, D_* or α_*. The experimental data confirm that D_* is proportional to the Reynolds number.
2. The mixing-length model can be applied to drag-reducing flows, and the mixing-length is reduced after the polymer is added to the Newtonian fluid flow, or the damping factor in van Driest's expression increases with D_*. The calculated results show that the mean velocity becomes higher with the increase in D_*. The measured velocity profiles can be described by Eq. (12) from the viscous sublayer through the buffer layer to the turbulent core.
3. The measured friction factor shows that the elastic factor α_* or effective viscosity ν_{eff} is independent of Reynolds number (u_*r/ν). The friction factor can be expressed by the derived equation.
4. The theoretical results show that the onset Reynolds number only depends on the drag-reduction parameter α_*. The onset Reynolds number decreases with the increase in α_*. If $D_* < 1.1$, the velocity profile and friction factor for drag-reducing flows perform as the Newtonian fluid flow.

Acknowledgment

The author would like to express his sincere appreciation to the anonymous referees for their careful review that greatly improves this paper's quality.

References

[1] Toms, B. A., 1949, "Some Observation on the Flow of Linear Polymer Solutions Through Straight Tubes at Large Reynolds Numbers," Proceedings of the First International Congress on Rheology, Vol. 2, pp. 135–141.

[2] Virk, P. S., 1971, "An Elastic Sublayer Model for Drag Reduction by Dilute Solutions of Linear Macromolecules," J. Fluid Mech., **45**, pp. 417–440.

[3] Larson, R. G., 2003, "Analysis of Polymer Turbulent Drag Reduction in Flow Past a Flat Plate," J. Non-Newtonian Fluid Mech., **111**(2–3), pp. 229–250.

[4] Min, T., Choi, H., and Yoo, J. Y., 2003, "Maximum Drag-Reduction in a Turbulent Channel Flow by Polymer Additives," J. Fluid Mech., **492**, pp. 91–100.

[5] Min, T., Yoo, J. Y., Choi, H., and Joseph, D. D., 2003, "Drag Reduction by Polymer Additives in a Turbulent Channel Flow," J. Fluid Mech., **486**, pp. 213–238.

[6] Gasljevic, K. Aguilar, G., and Matthys, E. F., 2001, "On Two Distinct Types of Drag-Reducing Fluids, Diameter Scaling, and Turbulent Profiles," J. Non-Newtonian Fluid Mech., **96**(3), pp. 405–425.

[7] Ryskin, G., 1987, "Turbulent Drag Reduction by Polymers: A Quantitative Theory," Phys. Rev. Lett., **59**, pp. 2059–2062.

[8] Warholic, M. D., Heist, D. K., Katcher, M., and Hanratty, T. J., 2001, "A Study With Particle-Image Velocimetry of the Influence of Drag-Reducing Polymers on the Structure of Turbulence," Exp. Fluids, **31**, pp. 474–483.

[9] White, C. M., Somandepalli, V. S. R., and Mungal, M. G., 2004, "The Turbu-

lence Structure of Drag-Reduced Boundary Layer Flow," Exp. Fluids, **36**, pp. 62–69.

[10] Durst, F., Keck, T., and Kline, R., 1985, "Turbulence Quantities and Reynolds Stresses in Pipe Flow of Polymer Solutions," Proceedings of the First International Conference on Laser Anemometer-Advances and Applications, BHRA, p. 31.

[11] Willmarth, W. W., Wei, T., and Lee, C. O., 1987, "Laser Anemometer Measurements of Reynolds Stress in a Turbulent Channel Flow With Drag Reducing Polymer Additives," Phys. Fluids, **30**, pp. 933.

[12] Luchik, T. S., and Tierderman, W. G., 1988, "Turbulent Structure in Low-Concentration Drag-Reducing Channel Flows," J. Fluid Mech., **190**, pp. 241–263.

[13] Harder, K. J., and Tiederman, W. G., 1991, "Drag Reduction and Turbulent Structure in Two-Dimensional Channel Flows," Philos. Trans. R. Soc. London, Ser. A, **336**, pp. 19–34.

[14] Wei, T., and Willmarth, W. W., 1992, "Modifying Turbulent Structure With Drag-Reducing Polymer Additives in Turbulent Channel Flows," J. Fluid Mech., **245**, pp. 619–641.

[15] Lumley, J. L., 1969, "Drag Reduction by Additives," Annu. Rev. Fluid Mech., **1**, pp. 367–384.

[16] L'vov, V. S., Pomyalov, A., Procaccia, I., and Tiberkvich, V., 2004, "Drag Reduction by Polymers in Wall Bounded Turbulence," Phys. Rev. Lett., **92**, p. 244503-4.

[17] Den Toonder, J. M. J., Hulsen, M. A., Kuiken, G. D. C., and Nieuwstadt, F. T. M., 1997, "Drag Reduction by Polymer Additives in a Turbulent Pipe Flow: Numerical and Laboratory Experiments," J. Fluid Mech., **337**, pp. 193–231.

[18] Warholic, M. D., Massah, H., and Hanratty, T. J., 1999, "Influence of Drag-Reducing Polymers on Turbulence: Effects of Reynolds Number, Concentration and Mixing," Exp. Fluids, **27**, pp. 461–472.

[19] Gyr, A., and Tsinober, A., 1997, "On the Rheological Nature of Drag Reduction Phenomena," J. Non-Newtonian Fluid Mech., **73**, pp. 153–162.

[20] Schümmer, P., and Thielen, W., 1980, "Structure of Turbulence in Viscoelastic Fluids," Chem. Eng. Commun., **4**, pp. 593–606.

[21] Giesekus, H., 1981, *Structure of Turbulence in Drag Reducing Fluids*, Lecture Series 1981-86, von Karman Institute for Fluid Dynamics, Rhode-Sain-Genèse, Belgium.

[22] Yang, S. Q., and Dou, G., 2005, "Drag Reduction in Flat-Plate Turbulent Boundary Layer Flow by Polymer Additive," Phys. Fluids, **17**(6), p. 065104.

[23] Dou, G. R., 1996, "Basic Law in Mechanics of Turbulent Flows," China Ocean Eng., **10**(1), pp. 1–44.

[24] Berman, N. S., 1989, *Drag Reduction in Fluids Flows: Techniques for Friction Control*, R. H. J. Sellin and R. T. Moses, eds., Ellis Horwood Limited, Chichester.

[25] Ptasinski, P. K., Boersma, B. J., Nieuwstadt, F. T. M., Hulsen, M. A., Van den Brule, B. H. A. A., and Hunt, J. C. R., 2003, "Turbulent Channel Flow Near Maximum Drag Reduction: Simulations, Experiments and Mechanisms," J. Fluid Mech., **490**, pp. 251–291.

[26] Benzi, R., Angelis, E. D., L'vov, V. S., Procaccia, I., and Tiberkevich, V., 2006, "Maximum Drag Reduction Asymptotes and the Cross-Over to the Newtonian Plug," J. Fluid Mech., **551**, pp. 185–195.

[27] Van Driest, E. R., 1956, "On Turbulent Flow Near a Wall," J. Aeronaut. Sci., **23**, pp. 1007–1010.

[28] Hinze, J. O., 1975, *Turbulence*, 2nd ed., McGraw-Hill, New York.

[29] Cebeci, T., and Smith, A. M. O., 1974, *Analysis of Turbulent Boundary Layers*, Academic, New York, Chap. 6.

[30] White, C. M., and Mungal, M. G., 2008, "Mechanics and Prediction of Turbulent Drag Reduction With Polymer Additives," Annu. Rev. Fluid Mech., **40**, pp. 235–256.

[31] Gyr, A., and Bewersdorff, H. W., 1995, *Drag Reduction of Turbulent Flow by Additives*, Kluwer Academic, Dordrecht.

[32] Hinch, E. J., 1977, "Mechanical Models of Dilute Polymer Solutions in Strong Flows," Phys. Fluids, **20**, pp. 22–30.

[33] Metzner, A. B., and Metzner, A. P., 1970, "Stress Level in Rapid Extensional Flow of Polymeric Fluids," Rheol. Acta, **9**, pp. 174–181.

[34] Lumley, J. L., 1973, "Drag Reduction in Turbulent Flow by Polymer Additives," J. Polym. Sci. Macromol. Rev., **7**, pp. 263–290.

[35] Ptasinski, P. K., Nieuwstadt, F. T. M., Van Den Brule, B. H. A. A., and Hulsen, M. A., 2001, "Experiments in Turbulent Pipe Flow With Polymer Additives at Maximum Drag Reduction," Flow, Turbul. Combust., **66**, pp. 159–182.

[36] De Angelis, E., Casciola, C. M., and Piva, R., 2002, "DNS of Wall Turbulence: Dilute Polymers and Self-Sustaining Mechanisms," Comput. Fluids, **31**, pp. 495–507.

[37] Housiadas, K. D., and Beris, A. N., 2003, "Polymer-Induced Drag Reduction: Effects of the Variations in Elasticity and Inertia in Turbulent Viscoelastic Channel Flow," Phys. Fluids, **15**, pp. 2369–2384.

[38] Reischman, M. M., and Tiederman, W. G., 1975, "Laser-Doppler Anemometer Measurements in Drag-Reducing Channel Flows," J. Fluid Mech., **70**(2), pp. 369–392.

[39] Virk, P. S., 1971, "Drag Reductions in Rough Pipes," J. Fluid Mech., **45**, pp. 225–246.

[40] Edwards, M. F., and Smith, R., 1980, "The Use of Eddy Viscosity Expressions for Predicting Velocity Profiles in Newtonian, Non-Newtonian and Drag-Reducing Turbulent Pipe Flow," J. Non-Newtonian Fluid Mech., **7**, pp. 153–169.

[41] Gust, G., 1976, "Observations on Turbulent=Drag Reduction in a Dilute Suspension of Clay in Sea-Water," J. Fluid Mech., **75**(1), pp. 29–47.

[42] Virk, P. S., Merrill, E. W., Mickley, H. S., and Smith, K. A., 1967, "The Toms Phenomenon: Turbulent Pipe Flow of Dilute Polymer Solutions," J. Fluid Mech., **30**(2), pp. 305–328.

[43] Yang, S. Q., and Dou, G., 2008, "Modeling of Viscoelastic Turbulent Flow in Open Channel and Pipe," Phys. Fluids, **20**(6), p. 065105.

Shuhong Liu[1]
e-mail: liushuhong@mail.tsinghua.edu.cn

Liang Zhang

State Key Laboratory of Hydro Science and
Hydraulic Engineering,
Tsinghua University,
Beijing 100084, China

Michihiro Nishi
Department of Mechanical Engineering,
Kyushu Institute of Technology,
Sensui-cho 1-1,
Tobata, Kitakyushu 804-8550, Japan
e-mail: nishi@mech.kyutech.ac.jp

Yulin Wu
State Key Laboratory of Hydro Science and
Hydraulic Engineering,
Tsinghua University,
Beijing 100084, China

Cavitating Turbulent Flow Simulation in a Francis Turbine Based on Mixture Model

As a numerical method to study the cavitation performance of a Francis turbine, the mixture model for the cavity/liquid two-phase flow is adopted in the cavitating turbulent flow analysis together with the re-normalization group (RNG) k-ε turbulence model in the present paper. The direct coupling numerical technique is used to solve the governing equations of the mixture model for the two-phase flow. Unsteady cavitating flow simulation around a hydrofoil of ALE15 is conducted as preliminary evaluation. Then, the cavitating flow in a Francis turbine is treated from the steady flow simulation since the feasibility of the cavitation model to the performance prediction of the turbine is the present major concern. Comparisons of the computational results with the model test data, i.e., the cavitation characteristics of hydraulic efficiency and the overload vortex rope at the draft tube inlet being reproduced reasonably, indicate that the present method has sufficient potential to simulate the cavitating flow in hydraulic turbines. Further, the unsteady cavitating flow simulation through the Francis turbine is conducted as well to study the pressure fluctuation characters caused by the vortex rope in the draft tube at partial load operation. [DOI: 10.1115/1.3112382]

Keywords: cavitation, turbulent flow simulation, Francis turbine, mixture model

1 Introduction

A Francis turbine is usually designed under the cavitation-free condition at the rated load. But, unfavorable phenomena to affect the reliability and smooth operation of the turbine have frequently happened due to the occurrence of cavitation since its operation at the condition far from the rated load is not a rare case. Thus, it is desirable if we can predict the cavitating flow in the turbine reasonably at the designing stage. One of such studies was made by Susan-Resiga et al. [1], who showed the predicted results of the initial cavitation number of a Francis turbine runner. And from literature survey on this topic, we can see many contributions summarized as follows.

At the first stage, simplified cavitating flow models have been demonstrated based on the ideal fluid assumption and the singularity method for simulating the cavity flows around hydrofoils and in hydraulic machinery. For instance, using a cavitating flow model proposed by Yamaguchi and Kato [2], Brewer and Kinnas [3] and Pellone and Peallat [4] calculated the flow around 2D, 3D hydrofoils and predicted the local cavities near the hydrofoil surfaces. De Lange and De Bruin [5] simulated the periodic variation in bubble in potential flow. Recently, Watanabe et al. [6] used the singularity method to analyze the thermodynamic effect of partial cavitation.

There are such papers where the inviscid flow simulation by solving Euler equations is conducted for analyzing the cavitating flow. Chen and Heister [7] simulated the cavitating flow around an axisymmetric body by using the marker and cell method. Ventikos and Tzabiras [8] calculated the cavitating flow around a hydrofoil and considered the temperature variation in the flow by using the pressure-correction method. Horiguchi et al. [9] proposed a method for predicting the steady cavitation in turbopumps based on the assumption that the fluid was inviscid and the stream surface is rotationally symmetric.

The single-phase turbulent flow model is regarded as one of the popular numerical methods. Though it has been developed extensively, it may be applicable to the fixed-bubble cavitating flow and not to the dissociative bubble flow and bubble cloud since the momentum and mass transfer between bubble and liquid cannot be taken into account.

It should be noted that some attractive results were obtained through a barotropic model [10,11] to capture the main physics of complex cavitation wake flows. The simulation methodology was based on large eddy simulation (LES), using a barotropic phase model to couple the continuity and momentum equations.

The other method is the simulation of two-phase flow consisting of the continuous liquid phase and the dispersed phase [7,12], where the two-fluid model and the mixture model have been developed. In the former model, the dispersed (cavity or bubble) phase is treated as a pseudofluid in the Eulerian approach, i.e., the flow of the dispersed phase is described by conservation equations of mass, momentum, and energy in continuum mechanics. In this model, there exists not only the slip between the carrier fluid and the dispersed phase but also the different diffusion between them. Rieger [13] applied the two-fluid model to his simulation of cavitating flows. Grogger and Alajbegovic [14] calculated the cavitating flow in the Venturi tube with this model. Liu et al. [15] used the k-ε-A_c turbulence model (i.e., the k-ε model for liquid phase, the local following model for cavity phase) to calculate the bubble flow in the Francis turbine.

In the mixture model, it is assumed that there exist the dynamic balance and the diffusion balance in both the liquid phase and the cavity phase of the cavitating flow, and velocities, temperatures, and densities of both phases are identical to each other at every position in the whole two-phase flow field. There are contributions to simulate the turbulent cavitating flow by Navier-Stokes (N-S) equations of the mixture and an additional equation of cavity (or liquid) volume (or mass) fraction. Singhal et al. [16] used the mass fraction equation and k-ε turbulence model to simulate the cavitating mixture flow around a foil. Kunz et al. [17] and Brewer

---

[1] Corresponding author.

Contributed by the Fluids Engineering Division of ASME for publication in the JOURNAL OF FLUIDS ENGINEERING. Manuscript received October 20, 2007; final manuscript received February 11, 2009; published online April 13, 2009. Assoc. Editor: Chunill Hah.

and Kinnas [3] used multiple species approaches with additional establishment of a mass transfer law between liquid and vapor. This model was applied even when the relative motion between the phases should be taken into account in the calculation. Senocak and Shyy [18] used the mass fraction equation and k-ε turbulence model, as well as the pseudocompressibility method to simulate the 3D and axisymmetric cavitating flows. The mixture model has been developed further by introducing various mass transfer expressions. One of these expressions is based on the bubble dynamics, another is established from the mechanics of evaporation and condensation between the cavity and liquid phase. Singhal et al. [19] presented the full cavitation model of mixture from the Rayleigh–Plesset equation with considering phase change rate, turbulence, and nondissolved gas effects. Aschenbrenner et al. [20] used the mixture model to compute the unsteady cavitating flow and compared it with experiment.

From evaporation and condensation mechanism between vapor and liquid and the assumption of unchanged pressure in cavity, the mass change rate of cavity should be proportional to the difference between liquid and vapor pressures. Saito et al. [21] derived cavitation phase change rate expression from the plane evaporation and evaluated it by calculating the cavitation flow around NACA0015 foil. Okita and Kajishima [22] showed a cavitation change expression in volume fraction form. Guo et al. [23] used this equation to calculate the cavitating flow in the draft tube of the Francis turbine. Though the Reynolds averaged N-S equations' model is widely used to simulate the cavitating flow [24–26] at present, there are attempts to apply the direct numerical simulation to bubbly flow calculation [27,28].

Though the nature of the cavitating two-phase flow is highly dynamic and unstable, its appropriate modeling is still necessary for engineering application. Liu et al. [29] demonstrated that the numerical method based on a mixture model for the cavity/liquid two-phase flow together with the RNG k-ε turbulence model was acceptable to simulate the cavitating flow around a hydrofoil. Thus, for the development of a numerical method to predict the cavitation performance of a hydraulic turbine, we have examined the applicability of the proposed method from two kinds of cavitating flow simulation in this paper. One is unsteady cavitating flow simulation around a hydrofoil of ALE15. The other is the steady and unsteady numerical simulation of cavitating flow in a Francis turbine at three operating conditions, i.e., overload, rated, and part load.

2 Numerical Simulation of Cavitating Flow

2.1 Governing Equations of Mixture Model. The following are governing equations of the present mixture model of the cavity/liquid two-phase flow, including those effects of nondissolved gas, turbulence, tension of interface at cavity, and phase change rate based on the evaporation and condensation mechanism.

(1) Continuity equation of mixture

$$\frac{\partial \rho}{\partial t} + \frac{\partial}{\partial x_j}(\rho u_j) = 0 \tag{1}$$

(2) Continuity equation of cavity phase

$$\frac{\partial \alpha_{\text{ca}}\rho_{\text{ca}}}{\partial t} + \frac{\partial}{\partial x_j}(\alpha_{\text{ca}}\rho_{\text{ca}}u_j) = S \tag{2}$$

(3) Momentum equations of mixture

$$\frac{\partial \rho u_i}{\partial t} + \frac{\partial}{\partial x_j}(\rho u_j u_i) = \rho g_i - \frac{\partial p}{\partial x_i} + \frac{\tau_{ji}}{\partial x_i} \tag{3}$$

It is noted that Eq. (2) is the cavitation model equation for the calculation of cavitating flow based on the evaporation and condensation mechanism proposed by Okita and Kajishima [22], where the static pressure p and vapor pressure p_v are replaced with p^* and p_v^*, respectively, in cavities to consider those effects of the surface tension, the turbulence effect, and the nondissolved gases in this paper as follows,

If the surface tension γ is considered, the pressure p^* is given by

$$p^* = p + \frac{2\gamma}{r} \tag{4}$$

Equation (5) for the apparent vapor pressure p_v^* is introduced to describe the turbulence effect [16] in the vapor pressure p_v.

$$p^* = p_v + 0.195\rho k \tag{5}$$

The source term S in Eq. (2) is adopted to express the mass transfer rate per volume proposed by Cammenga [30]

If $p^* > p_v^*$ (condensation being dominant),

$$S = \frac{3\alpha_{\text{ca}}}{r} C_1 \left(\frac{M}{2\pi R}\right)^{1/2} \left(\frac{p_v^*}{\sqrt{T}} - \frac{p^*}{\sqrt{T}}\right) \tag{6}$$

If $p^* < p_v^*$ (evaporation being dominant),

$$S = \frac{3(1-\alpha_{\text{ca}}-\alpha_u)}{r} C_2 \left(\frac{M}{2\pi R}\right)^{1/2} \left(\frac{p_v^*}{\sqrt{T}} - \frac{p^*}{\sqrt{T}}\right) \tag{7}$$

where correction coefficients of $C_1=0.13$ and $C_2=0.01$ are used to consider the effect of phase change rate.

And considering the effect of nondissolved gases [19], the density of mixture is expressed as

$$\rho = \alpha_{\text{ca}}\rho_{\text{ca}} + \alpha_u\rho_u + (1-\alpha_{\text{ca}}-\alpha_u)\rho_l \tag{8}$$

where $\rho_{\text{ca}}=\rho_v$ is the density of saturated vapor and ρ_u is the density of nondissolved gases, both of which are in the following forms from ideal gas assumption:

$$\rho_{\text{ca}} = \frac{M}{R}\frac{p^*}{T} \tag{9}$$

$$\rho_u = \frac{M_u}{R}\frac{p^*}{T} \tag{10}$$

Equations (1)–(3) are closed in laminar flow or in turbulent flow with additional turbulence model equations, assuming that the cavity radius r is constant. In the case of water as the working liquid, it may be determined that the initial mass fraction of cavity phase $f_{\text{ca}}=\rho_{\text{ca}}\alpha_{\text{ca}}=1-77\ \text{mg/m}^3$ and the initial nuclei radius $r_0=3-10\ \mu\text{m}$. Using them, we can get the number of cavities in a unit volume, which is assumed to be constant in the computation. Thus, the new cavity radius is calculated from parameter of α_{ca} data in each step of iteration of the computation.

2.2 Numerical Algorithm. The time-dependent governing equations are discretized both in space and time. The unsteady second order implicit formulation is used to calculate the unsteady flow. And the RNG k-ε turbulence model is applied for the unsteady turbulent flow with the wall function near walls. The finite volume algorithm, with the second order central difference for the source terms and with the second order upstream difference for the convective terms of the spatial discrete governing equations, is used for the numerical simulation.

Though the cavitating flow was simulated by using a pressure-correction method derived from the semi-implicit method for pressure-linked equations (SIMPLE) algorithm and a finite volume discretization in the work made by Fortes-Patella et al. [26], the direct coupling method is used to solve the incompressible flow in the present simulation [31]. The discrete momentum equations and the continuity equations for the complete flow field are solved together without iteration and corrections. This numerical method will need large computer storage, but it will improve the

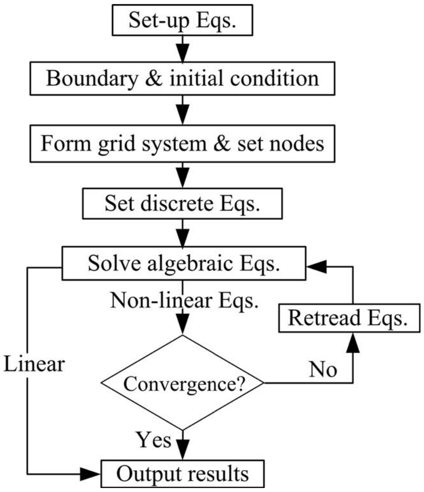

Fig. 1 The direct coupling procedure for incompressible flow

stability in the numerical procedure, as shown in Fig. 1, where the iteration is made in the case of nonlinear cavitating turbulent flow.

2.3 Turbulence Model. As the Reynolds averaged Navier–Stokes solver (CFX code) is used to solve the turbulent flow of cavity/liquid two-phase flow in the present work, the turbulence model is necessary. Coutier-Delgosha et al. [32] evaluated the influence of turbulence model on the numerical results of unsteady cavitating flow. In this paper the RNG k-ε is used on the two-phase flow in the mixture model [33], which is similar to single flow except the definition of viscosity of the mixture as follows [34]:

$$\mu = \alpha_{\text{ca}}\mu_{\text{ca}} + \alpha_u\mu_u + (1 - \alpha_{\text{ca}} - \alpha_u)\mu_l \tag{11}$$

where μ_{ca} is the viscosity of cavity phase, μ_l is the water viscosity, and μ_u is the viscosity of nondissolved gas in water.

2.4 Boundary Conditions for Steady Flow. The following boundary conditions are used to get steady solution of cavity/liquid turbulent flow in the present simulation.

(1) Input data of all physical variants are prescribed at the inlet boundaries of the flow field.
(2) The gradients of all physical variants normal to the boundaries are given at the outlet.
(3) On solid walls of the domain, the nonslip flow condition is adopted. The velocity distribution in the boundary layer is expressed as the wall function near the solid walls.
(4) Zero pressure gradient normal to the surface is used for all boundaries of the domain except a point corresponding to the reference pressure. In order to satisfy the continuity condition from the inlet to the outlet of calculation domain, correction of velocity magnitude to the outlet distribution is made based on the difference between the inflow and the outflow during the calculation.

3 Cavitating Flow Around a Hydrofoil

The steady cavity/liquid turbulent two-phase flow around the ALE15 hydrofoil was simulated by using the turbulent flow analysis with the cavitating flow mixture model described in Sec. 2.1 [29]. The hydrofoil parameters for the calculation were set using the experimental conditions made by Dular et al. [35]. The boundary conditions are as follows:

(1) inflow plane: uniform velocity of 13 m/s
(2) outflow plane: constant pressure of 197.2 kPa
(3) solid walls: nonslip condition

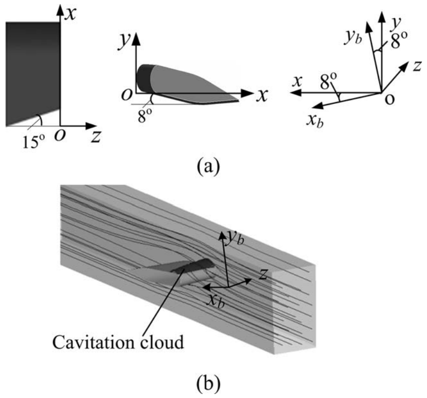

Fig. 2 Cavitating flow around ALE15 hydrofoil: (*a*) geometry of the hydrofoil and calculation coordinate system and (*b*) streamlines around the hydrofoil and bubbly cloud

Simulation of the unsteady cavity/liquid turbulent two-phase flow around the hydrofoil is conducted in this paper, using steady flow results as the initial condition. An example of calculated results is shown in Fig. 2, where Fig. 2(*a*) is the geometry of ALE15 hydrofoil with the calculation coordinate system. Figure 2(*b*) displays the streamlines around the foil and bubbly cloud appeared on the foil surface. The boundary of the bubbles is obtained from a cavity volume fraction of 10% proposed by Okita and Kajishima [22], who explained that the interface between water and bubble could be observed clearly if the cavity volume fraction was more than 10%.

As an example of steady flow results, the numerical result of velocity distribution being compared with the particle image velocimetry (PIV) measurement and the result from the full cavitation model [19] are shown in Fig. 3, where the ordinate is the velocity and the abscissa is y or the distance from the hydrofoil surface at the location of $x=13$ mm and $z=-5$ mm. From Fig. 3, it can be seen that the calculated result from the full cavitation model underestimates the velocity, and the present simulation reasonably corresponds to the experimental data.

As a typical result of unsteady flow simulation, four snapshots of cavitation bubbles on the top surface being taken with the time interval of about 0.1 s are displayed in Fig. 4, where Fig. 4(*a*) corresponds to the view in $-y_b$ and Fig. 4(*b*) is the view in x_b. It is suspected from this result that the area of cavitation bubbles varies from time to time in the tested condition.

4 Cavitating Flow in Francis Turbine

4.1 Francis Turbine Parameters. The cavitating turbulent flow through a model Francis turbine (see Table 1) has been simulated. Figure 5(*a*) shows the calculation domain of the turbine,

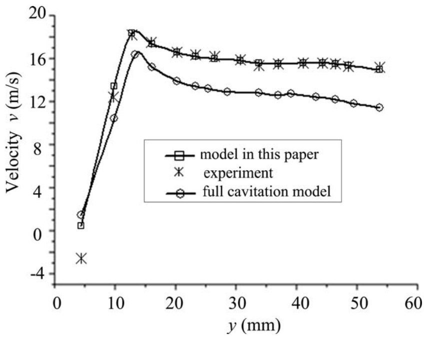

Fig. 3 Comparison of velocity distribution at $x=13$ mm and $z=-5$ mm

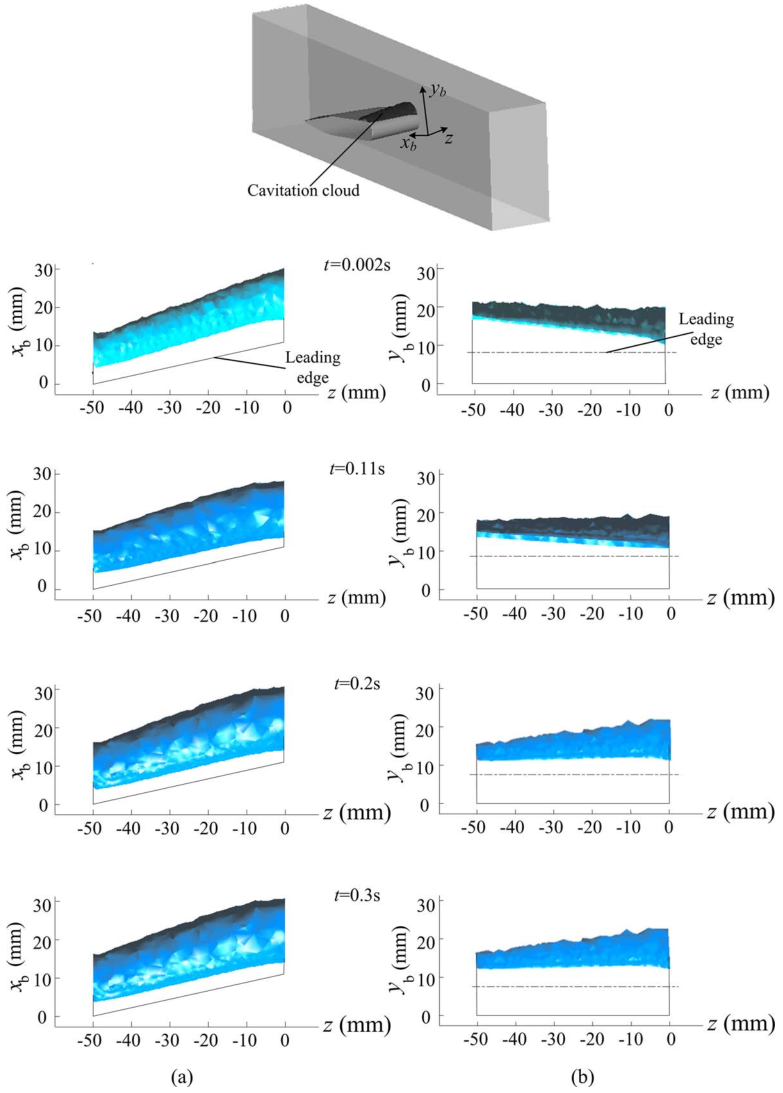

Fig. 4 Numerical snapshots of cavitation bubbles on the top surface of hydrofoil: (*a*) view in $-y_b$ and (*b*) view in x_b

which is a complete flow passage of the turbine consisting of spiral casing (SC), stay vanes (SVs), guide vanes (GVs), runner, and the draft tube (DT). The advantages of adopting the complete flow passage of turbine as the calculated domain are as follows.

(1) Reasonably accurate boundary conditions can be prescribed at the entrance section of spiral casing as the inlet boundary and at the exit section of draft tube as the outlet boundary.
(2) The interaction between a rotating runner and stationary guide vanes and that between the runner and the draft tube can be included in the calculation. Figure 5(*b*) indicates the

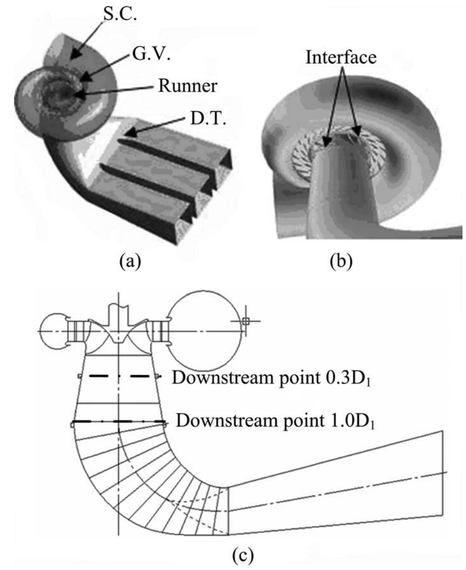

Fig. 5 Model Francis turbine: (*a*) calculation domain, (*b*) interaction surfaces, and (*c*) survey points of pressure in draft tube

Table 1 Geometrical parameters of the model turbine

Parameter	Value
No. of stay vanes	$Z_S=24$
No. of guide vanes	$Z_0=24$
Reference diameter of GV	$D_0=1.111D_1$
Height of GV	$B_0=0.288D_1$
Inlet diameter of runner	$D_1=372.2$ mm
Outlet diameter of runner	$D_2=366.0$ mm
No. of runner blades	$Z=15$

Table 2 Grid system model with predicted turbine torque

Grid model	Total elements	Runner elements	Runner element size (mm)	Torque (N m)
1	1,180,000	100,000	6	1129.792
2	1,880,000	780,000	3	1149.769
3	3,710,000	2,630,000	2	1149.767

Table 4 Prediction of runner torque (experiment: σ=0.142)

Cases	Experiment (N m)	Single-phase (N m)	Cavitating flow (N m)
Case1 (small flow rate)	744.5	682.3	683.9
Case2 (optimum)	1178.4	1149.7	1149.7
Case3 (large flow rate)	1450.3	1393.6	1395.3

two fluid-fluid interfaces upstream and downstream of the runner, which rotate in the reference frame. Namely, the frozen mesh of the runner was used to consider the interaction between a rotating runner and stationary components in the steady cavitating flow simulation. And the slipping mesh of the runner was used to consider the interaction in the unsteady cavitating flow simulation.

In order to examine the independence of the numerical simulation on the grid system, as shown in Table 2, three unstructured tetrahedron grid models with different numbers of elements were tested as the preliminary calculation. Grid model 2 is selected in the following calculation based on the predicted results of torque acting on the runner, which are also shown in Table 2.

Table 3 shows three test cases corresponding to those turbine operating conditions of part load, rated load, and overload, which are set by guide vane openings in the experiment. Following the experimental conditions, the constant test head of 30 m and the rotating speed of 1122 min^{-1} (unit rotational speed of 75 rpm) are used in the calculation.

Another parameter to show the operating condition is the cavitation number given by

$$\sigma = \frac{H_a - H_{\text{VA}} - H_S - H_V}{H} \tag{12}$$

where H_{VA} is the vacuum head in the draft tank of the test rig, which indicates the pressure level at the outlet of the draft tube. H_a is the atmospheric pressure head. H_S is the suction head of the turbine. H is the test head acting on the turbine. H_V is the vapor pressure head at the test temperature.

In the cavitating flow simulation, the following assumptions were used:

(1) radius of cavitation nuclei, r_0=0.5 μm
(2) volume fraction of nondissolved gas, $\alpha_u=5\times10^{-5}$
(3) temperature at the inflow plane, T=298 K

4.2 Validation of Simulation. Since applicability of the cavitation model to the performance prediction of a hydroturbine is our major concern, its validation is conducted from the steady flow simulation.

Predicted torque. Table 4 shows the predicted values of runner torque with and without cavities for three cases. We see that the differences between the results of the single-phase simulation and those of the cavitating flow are almost negligible. This is because of the higher cavitation number around σ=0.142 at the corresponding operating condition. Though the underestimation is observed in the results, the difference of 3% at optimum load (Case 2) and that of 4% at overload (Case 3) are regarded as tolerable in the present study. One of the causes for the difference of 8% in Case 1 may be due to the steady flow simulation since unsteadiness of the flow in the turbine must be large at part load.

Critical cavitation number. Figure 6 is the cavitation characteristics of hydraulic efficiency at another overload operating condition with a unit flow rate of Q_{11}=0.99 m^3/s and a unit speed of n_{11}=83.4 rpm, where both numerical and experimental results are shown for comparison. Similar to the runner torque in Table 4, the hydraulic efficiency is predicted a little bit smaller than the experimental result. Based on the international code IEC193A-1972, we determined the critical cavitation number σ_c, which is defined as the intersection of two approximate curves for $\eta=f(\sigma)$, namely, η=const and $\eta=A\sigma+B$. The predicted critical cavitation number is 0.09 (see Fig. 6), which is much closer to the experimental value of 0.08. Thus, we will be able to evaluate that the steady cavitating flow simulation is reasonably usable to predict the cavitation characteristics of a Francis turbine. To see the macroscopic appearance of cavities in the runner, Fig. 7 shows those at typical conditions, i.e., near the initial cavitation σ_i and the severe condition. As suspected, appreciable cavities on the suction side near the trailing edge of runner blades are predicted at the operating condition near σ_c.

Cavitated vortex rope. If the flow from the runner has strong swirl, the cavitated vortex rope is observed in the draft tube under the low σ condition. Using the steady flow analysis, the rope at overload is investigated. To see the configuration of vortex rope in the inlet cone of the draft tube, it is visualized from the numerical results by using the criterion that the rope boundary is given by the cavity volume fraction of 10%, which was proposed by Okita and Kajishima [22]. Figure 8 shows the result for overload of 130% (Case 3). And a snapshot photograph taken at the model test is shown for comparison. It is seen that the nearly straight vortex rope appears from the runner cone to the draft tube, as shown in Figs. 8(*a*) and 8(*b*). From them, we will be able to say that fairly well reproduction of cavitated vortex rope is achieved by the present numerical simulation, though the numerical vortex rope has a little bit larger diameter and shorter length than those of the snapshot in Fig. 8(*a*).

Unsteady cavitating flow at part load. It is known that large pressure fluctuation caused by the cavitated vortex rope is sometimes observed in the draft tube of the Francis turbine at part load operation, and it deteriorates the stable operation and reliability of the turbine. As the vortex rope orbits in the draft tube depending on time, unsteady flow analysis is essential to simulate the flow at

Table 3 Calculation conditions for three cases

Cases	GV opening (mm)	Head (m)	Flow rate (m^3/s)	Rotational speed (min^{-1})	Q_{11} (m^3/s)	n_{11} (rpm)
Small flow rate (σ=0.143)	10	30	0.322	1122	0.466	75
Optimum (σ=0.144)	15	30	0.497	1122	0.678	75
Large flow rate (σ=0.132)	22	30	0.647	1122	0.882	75

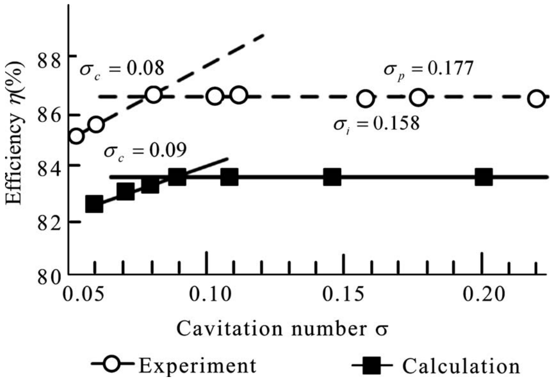

Fig. 6 Cavitation characteristics of efficiency (Q_{11} =0.99 m^3/s, n_{11}=83.4 min^{-1})

such operating points. To see the usability of the present numerical method for predicting the pressure fluctuation, Case 1 in Table 3 is treated as a typical example under the cavitation condition of σ=0.07. Here, the time step of 0.001 s was adopted in the unsteady turbulent flow analysis. Thus, the time step corresponds to the runner rotation of 6.72 deg, as the rotational speed of the runner is 1122 min^{-1}. Following IEC-60193, peak-to-peak amplitude and fundamental frequency of pressure fluctuation are evaluated at two survey points, as shown in Fig. 5(*c*). One of them is expressed as the downstream point 0.3D_1, and the other is the downstream point 1.0D_1. They are located at the distances of 0.3 and 1.0 times the runner inlet diameter from the runner exit, respectively.

The predicted results of dimensionless peak-to-peak amplitude $\Delta H/H$ and the fundamental frequency are listed in Table 5, where the test data and those results from single-phase flow simulation are added for comparison. And the pressure in time domain and that of frequency domain for the point 1.0D_1 are shown in Figs. 9(*a*) and 9(*b*), respectively. The frequency of test data exactly corresponds to the rotating frequency of vortex rope in the draft tube, though it is outside the 0.22–0.31(n/60) range of draft tube surging. And the amplitude decreases toward downstream. These features are qualitatively reproduced in the numerical results. It is seen that much better prediction is achieved in the results being considered the cavitating flow.

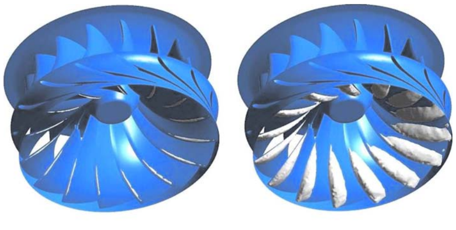

(a) (b)

Fig. 7 Appearance of cavity in the runner: (*a*) initial cavitation (σ_i=0.157) and (*b*) severe cavitation (σ=0.08)

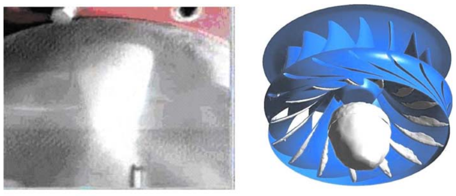

(a) (b)

Fig. 8 Cavitated vortex rope in draft tube at large flow rate (Case 3) under σ=0.054: (*a*) snapshot and (*b*) cavitating flow simulation

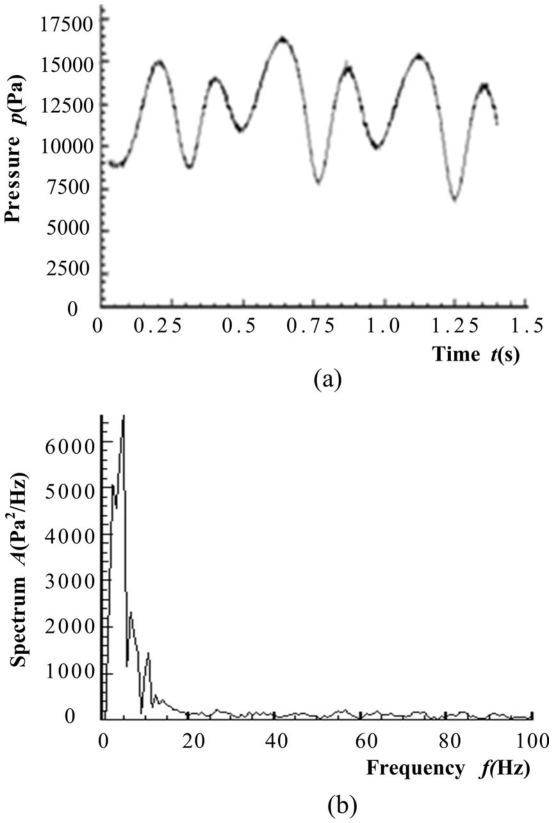

Fig. 9 Wall pressure fluctuation at the 1.0D_1 point for Case 1 from unsteady cavitating flow analysis (σ=0.07): (*a*) variation in pressure with time and (*b*) frequency spectrum

5 Conclusions

From the numerical study on the cavitating flow in a Francis turbine, the following conclusions are drawn.

1. The critical cavitation number σ_c and hydraulic performance of a Francis turbine are reasonably predicted by the steady cavitating flow simulation based on a mixture model.
2. The cavitated vortex rope in the draft tube at overload operation was reasonably displayed from the numerical re-

Table 5 Pressure fluctuation at partial load operation (Case 1) at σ=0.07

	Test data		Single-flow calculation		Cavitating flow calculation	
Survey point	Amp. $\Delta H/H$ (%)	Fundamental freq. (Hz)	Amp. $\Delta H/H$ (%)	Fundamental freq. (Hz)	Amp. $\Delta H/H$ (%)	Fundamental freq. (Hz)
0.3D_1	3.91	3.43	4.32	4.98	4.25	4.12
1.0D_1	3.66	3.42	4.1	4.98	3.2	4.12

sults by using the Okita and Kajishima [22] criterion that the rope boundary is given by the cavity volume fraction of 10%.

(3) From a qualitative viewpoint, pressure fluctuation caused by the cavitated vortex rope at part load operation is reasonably predicted by the present numerical method for unsteady cavitating turbulent flow.

Acknowledgment

The research work was funded by Chinese National Foundation of Natural Science (Contract No. 90410019).

Nomenclature

C_1, C_2 = correction coefficients
g = gravitational acceleration
H = test head acting on the turbine
H_a = atmospheric pressure head
H_S = suction head of the turbine
H_V = saturated vapor pressure head
H_{VA} = vacuum head in the draft tank
k = kinetic energy of turbulence
M = Moore molecule weight
n = rotational speed
n_{11} = unit speed, $=nD/\sqrt{H}$
p = local pressure
Q = flow rate
Q_{11} = unit flow rate, $=Q/D^2\sqrt{H}$
R = gas constant
r = radius of the bubble
S = mass transfer rate
T = temperature
t = time
u = velocity
x,y,z = coordinates
α = volume fraction
γ = surface tension
ε = turbulent kinetic energy dispassion rate
η = efficiency
μ = viscosity
ρ = density
σ = cavitation number, see Eq. (12)
σ_i = initial cavitation number
σ_c = critical cavitation number
τ_{ji} = stress

Subscripts

ca = cavity phase
l = liquid
u = undissolved gas
v = vapor

Appendix: Experimental Uncertainty

The experiment of the turbine performances was carried out in the high accurate test rig in Harbin Large Electric Machinery Institute in China. The flow parameters were measured in the following measuring range and the accuracy, as shown in Table 6.

Table 6 Measurement accuracy (99%)

No.	Performance	Unit	Measuring range	Uncertainty
1	Flow rate Q	m^3/s	0–1.0	±0.20%
2	Head H	MPa	0–2.07	0.075%
3	Force on arm (K)	E pound	0–1000	±0.02%
4	Angular speed (ω)	rad/s	0–3000	±0.05%

References

[1] Susan-Resiga, R. F., Muntean, S., and Anton, I., 2002, "Numerical Analysis of Cavitation Inception in Francis Turbine," Proceedings of the 21st IAHR Symposium on Hydraulic Machinery and Systems, F. Avellan, G. Ciocan, and S. Kvicinsky, eds., Lausanne, Switzerland, pp. 431–438.
[2] Yamaguchi, H., and Kato, H., 1983, "On Application of Nonlinear Cavity Flow Theory to Thick Foil Section," Proceedings of the Second International Conference of Cavitation, ImechE, Paper No. C209/83, pp. 167–174.
[3] Brewer, W. H., and Kinnas, S. A., 1995, "Experimental and Computational Investigation of Sheet Cavitation on a Hydrofoil," Proceedings of the Second Joint ASME/JSME Fluids Engineering Conference and ASME/EALA Sixth International Conference on Laser Anemometry, Hilton Head Island, SC, pp. 1–15.
[4] Pellone, C., and Peallat, J. M., 1995, "Non-Linear Analysis of Three-Dimensional Partially Cavitating Hydrofoil," Proceedings of the International Symposium on Cavitation, Deauville, France, pp. 63–67.
[5] De Lange, D. F., and De Bruin, G. J., 1998, "Sheet Cavitation and Cloud Cavitation Re-Entrant Jet and Three-Dimensionality," Appl. Sci. Res., **58**(1–4), pp. 91–114.
[6] Watanabe, S., Hidaka, T., Horiguchi, H., Furukawa, A., and Tsujimoto, Y., 2007, "Steady Analysis of the Thermodynamic Effect of Partial Cavitation Using the Singularity Method," ASME J. Fluids Eng., **129**(2), pp. 121–127.
[7] Chen, Y., and Heister, S. D., 1994, "A Numerical Treatment for Attached Cavitation," ASME J. Fluids Eng., **116**, pp. 613–618.
[8] Ventikos, Y., and Tzabiras, G., 2000, "A Numerical Method for the Simulation of Steady and Unsteady Cavitating Flows," Comput. Fluids, **29**, pp. 63–88.
[9] Horiguchi, H., Arai, S., Fukutomi, J., Nakase, Y., and Tsujimoto, Y., 2004, "Quasi-Three-Dimensional Analysis of Cavitation in an Inducer," ASME J. Fluids Eng., **126**, pp. 709–715.
[10] Arndt, R. E. A., Kjeldsen, M., Song, C. C. S., and Keller, A., 2002, "Analysis of Cavitation Wake Flows," Proceedings of the 21st IAHR Symposium on Hydraulic Machinery and Systems, F. Avellan, G. Ciocan, and S. Kvicinsky, eds., Lausanne, Switzerland, pp. 395–402.
[11] Qin, Q., Song, C. S. S., and Arndt, R. E. A., 2003, "Numerical Study of Unsteady Turbulent Wake Behind a Cavitating Hydrofoil," Fifth International Symposium on Cavitation, Osaka, Japan, Paper No. EM 003.
[12] Deshpande, M., Feng, J., and Merkle, C. L., 1997, "Numerical Modeling of the Thermodynamic Effects of Cavitation," ASME J. Fluids Eng., **119**, pp. 420–427.
[13] Rieger, R., 1992, "Mehrdimensionale Berechnung Zweiphasiger Stroemungen," Ph.D. thesis, Technical University Graz, Graz, Austria.
[14] Grogger, H. A., and Alajbegovic, A., 1998, "Calculation of the Cavitating Flow in Venturi Geometries Using Two Fluid Model," Proceedings of the ASME Fluids Engineering Division Summer Meeting, Washington, DC, Paper No. FEDSM98-5295.
[15] Liu, S. H., Wu, Y. L., and Luo, X. W., 2005, "Numerical Simulation of 3D Cavitating Turbulent Flow in Francis Turbine," Proceedings of the ASME FEDSM, Houston, TX, Paper No. FEDSM2005-77017.
[16] Singhal, A. K., Vaidya, N., and Leonard, A. D., 1997, "Multi-Dimensional Simulation of Cavitating Flows Using a PDF Model for Phase Change," Proceedings of the ASME Fluids Engineering Division Summer Meeting, Vancouver, BC, Vol. 4, pp. 1–8.
[17] Kunz, R. F., Boger, D. A., Stinebring, D. R., Chyczewski, T. S., Lindau, J. W., Gibeling, H. J., Venkateswaran, S., and Govindan, T. R., 2000, "A Preconditioned Navier-Stokes Method for Two-Phase Flows With Application to Cavitation Prediction," Comput. Fluids, **29**, pp. 849–875.
[18] Senocak, I., and Shyy, W., 2002, "A Pressure-Based Method for Turbulent Cavitating Flow Computation," J. Comput. Phys., **176**, pp. 363–383.
[19] Singhal, A. K., Athavale, M. M., Li, H. Y., and Jiang, Y., 2002, "Mathematical Basis and Validation of the Full Cavitation Model," ASME J. Fluids Eng., **124**(3), pp. 617–624.
[20] Aschenbrenner, T., Otto, A., and Moser, W., 2006, "Classification of Vortex and Cavitation Phenomena and Assessment of CFD Prediction Capabilities," Proceedings. of the 23rd IAHR Symposium on Hydraulic Machinery and Systems, J. Kurokawa, ed., Yokohama, Japan, Paper No. F132.
[21] Saito, Y., Takami, R., Nakamori, I., and Ikohagi, T., 2007, "Numerical Analysis of Unsteady Behavior of Cloud Cavitation Around a NACA0015 Foil," Comput. Mech., **40**, pp. 85–96.
[22] Okita, K., and Kajishima, T., 2002, "Numerical Simulation of Unsteady Cavitating Flow Around a Hydrofoil," Trans. Jpn. Soc. Mech. Eng., Ser. B, **68**, pp. 637–644.
[23] Guo, Y., Kato, C., and Miyagawa, K., 2006, "Large-Eddy Simulation of Non-Cavitating and Cavitating Flow in Venturi Geometries Using Two Fluid Model," Proceedings of the 23rd IAHR Symposium on Hydraulic Machinery and Systems, J. Kurokawa, ed., Yokohama, Japan, Paper No. F195.
[24] Lindau, J. W., Kunz, R. F., Boger, D. A., Stinebring, D. R., and Gibeling, H. J., 2002, "High Reynolds Number, Unsteady, Multiphase CFD Modeling of Cavitating Flows," ASME J. Fluids Eng., **124**(3), pp. 607–616.
[25] Medvitz, R. B., Kunz, R. F., Boger, D. A., Lindau, J. W., and Yocum, A. M., 2002, "Performance Analysis of Cavitating Flow in Centrifugal Pumps Using Multiphase CFD," ASME J. Fluids Eng., **124**(2), pp. 377–383.
[26] Fortes-Patella, R., Coutier-Delgosha, O., Perrin, J., and Reboud, J. L., 2007, "Numerical Model to Predict Unsteady Cavitating Flow Behavior in Inducer Blade Cascades," ASME J. Fluids Eng., **129**(2), pp. 128–135.
[27] Xing, T., Li, Z. Y., and Frankel, S. H., 2005, "Numerical Simulation of Vortex Cavitation in a Three-Dimensional Submerged Transitional Jet," ASME J. Flu-

ids Eng., **127**(4), pp. 714–725.

[28] Lu, T. S., Samulyak, R., and Glimm, J., 2007, "Direct Numerical Simulation of Bubbly Flows and Application to Cavitation Mitigation," ASME J. Fluids Eng., **129**, pp. 595–604.

[29] Liu, S. H., Li, S. C., Zhang, L., and Wu, Y. L., 2008, "A Mixture Model With Modified Mass Transfer Expression for Cavitating Turbulent Flow Simulation," Eng. Comput., **25**, pp. 290–304.

[30] Cammenga, H. K., 1980, "Evaporation Mechanisms of Liquids," Curr. Top. Mater. Sci., **5**, pp. 335–446.

[31] Vanka, S. P., 1986, "Block-Implicit Multigrid Solution of Navier-Stokes Equations in Primitive Variables," J. Comput. Phys., **65**(1), pp. 138–158.

[32] Coutier-Delgosha, O., Fortes-Patella, R., and Reboud, J. L., 2003, "Evaluation of the Turbulence Model Influence on the Numerical Simulations of Unsteady Cavitation," ASME J. Fluids Eng., **125**(1), pp. 38–45.

[33] Speziale, C. G., and Thangam, S., 1992, "Analysis of an RNG Based Turbulence Model for Separated Flows," Int. J. Eng. Sci., **30**(10), pp. 1379–1388.

[34] Lam, S. H., 1992, "On the RNG Theory of Turbulence," Phys. Fluids, **4**, pp. 1007–1017.

[35] Dular, M., Bachert, R., Stoffel, B., and Širok, B., 2005, "Experimental Evaluation of Numerical Simulation of Cavitating Flow Around Hydrofoil," Eur. J. Mech. B/Fluids, **24**, pp. 522–538.

R. Asmatulu
Department of Mechanical Engineering,
Wichita State University,
1845 Fairmount,
Wichita, KS 67260-0133

S. Kim

F. Papadimitrakopoulos

Nanomaterials Optoelectronics Laboratory,
Polymer Program,
Institute of Materials Science,
University of Connecticut,
Storrs, CT 06269-3136

H. Marcus
Department of Materials Science and Engineering,
Institute of Materials Science,
University of Connecticut,
Storrs, CT 06269-3136

Parallel-Plate Conductive Electrodes for the Fabrication of Larger 2D Colloidal Photonic Crystals

A new dielectrophoretic force-induced parallel-plate assembly technique was used to achieve close-packed 2D large colloidal photonic crystals on gold electrodes (~200 nm thick). The electrodes were patterned on a glass substrate using a conventional UV lithography technique. The experimental tests conducted with 5.3 μm carboxyl functionalized polystyrene particles at various ac and dc voltages, frequencies, and particle concentrations showed that larger size (0.25×3 mm^2) colloidal photonic crystals were fabricated on the ground electrode rather than on the working electrode. To date, this is the largest colloidal photonic crystal fabricated using this method. The reason behind this phenomenon can be attributed to the electro-osmotic flow in the colloidal system and dipole-dipole attractions between the colloidal particles. [DOI: 10.1115/1.3111257]

Keywords: parallel-plate gold electrodes, colloidal PS particles, 2D photonic crystals

1 Introduction

Photonic crystals (PCs), with periodicity comparable to the wavelength of light, have been considered one of the most attractive optical materials in a wide range of scientific arenas because of their unique property known as photonic band gap (PBG). This property forbids light over a range of wavelengths at certain frequencies and permits other light in the crystal [1–5]. These materials could be used in many areas: high reflectance mirrors, narrow lossless waveguides with sharp corners, zero-threshold lasers, and superprisms, as well as optical telecommunication, switches, and computing [6–10]. The integration of photonic crystals will allow a large number of components to be produced from a single crystal for industrial applications [11–14].

Based on selected materials (e.g., photoresists, polymeric films, dielectric rods, symmetric holes, and colloidal particles) and crystal dimensions, a number of fabrication techniques have been proposed to achieve photonic crystals. These techniques include lithography, chemical etching, gravity sedimentation, vertical depositions, Langmuir–Blodgett (LB), centrifugation, convective self-assembly, electrophoresis, and dielectrophoresis (DEP). There are a number of advantages of DEP in micro- and nanofabrication systems over the other methods: (i) Higher and lower electric field strengths and gradients can be achieved with a lower potential, (ii) electrodes can be integrated in a small circuit without any dissociation at various frequencies, and (iii) higher electric field can be applied without creating an excessive heat [15,16]. In addition to these, DEP is a simple, inexpensive, practical, and rapid assembly technique, and has great potential for the future fabrication of colloidal PCs in the photonic industry [8–12].

The phenomenon of DEP involves the creation of electric forces on particles to generate momentum in nonuniform electric fields, usually coming from ac electric fields [13–15]. The direction and magnitude of the forces rely on several factors, including applied voltage and frequency, polarizability of the particle, conductivity, and permittivity of both medium and particles, as well as dielectric properties of the particles and the medium. DEP forces can be utilized to characterize, handle, and manipulate colloidal photonic materials for the purposes of sorting, trapping, aligning, and separating. Additionally, other micro- and nanoscale organic (cells, viruses, bacteria, and DNA) and inorganic (nanoparticles, nanotubes, and nanowires) objectives can be directed using the same method [17–23].

Although significant progress has been made during the past decades for increasing the fabrication of colloidal photonic crystals in different dimensions, the problem of fabricating larger size PCs has not been solved yet. Most of the 2D colloidal photonic crystals produced to date are below 2 mm in diameter [5,24,25]. Therefore, the lack of efficient fabrication processes is forcing many government agencies (e.g., ARMY) and private companies to find novel solutions in these areas. This paper presents the fabrication of larger size 2D colloidal photonic crystals on parallel-plate conductive electrodes using a 5.3 μm polystyrene (PS) at various ac and dc voltages, frequencies, and solid contents.

2 Theory

Dielectrophoretic force relies on the difference in the polarizability of the system compared with its surrounding fluid medium (e.g., water). Consider an isolated/dispersed spherical colloidal particle or biological cell with known diameter and dielectric constant in a liquid medium. Under the nonuniform electric field, the induced dipole moment drives the particle in a direction. The dielectrophoretic force acting on the spherical body is expressed as [13]

$$F_{\mathrm{DEP}} = 2\pi\varepsilon_m \,\mathrm{Re}|K(\omega)| r^3 \,\nabla E_{\mathrm{rms}}{}^2 \qquad (1)$$

where r is the sphere radius, ε_m is the permittivity of the suspending medium, ∇E_{rms} is the gradient of the root mean square electric field, and $\mathrm{Re}|K(\omega)|$ is the real part of the Clausius–Mossotti factor given by

---

Contributed by the Fluids Engineering Division of ASME for publication in the JOURNAL OF FLUIDS ENGINEERING. Manuscript received April 20, 2008; final manuscript received September 22, 2008; published online April 14, 2009. Assoc. Editor: Theodore Heindel.

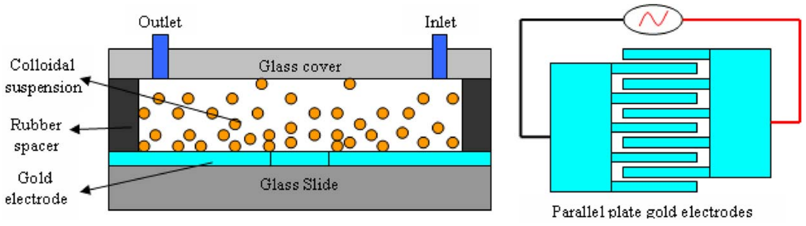

Fig. 1 Schematic outline of the experimental procedure (left) utilized to assemble larger 2D colloidal photonic crystals on the parallel-plate gold electrodes (right) connected to a power supplier. The red line is the working electrode, while the dark line is the ground electrode on which the photonic crystals were formed (not to be scaled).

$$K(\omega) = \frac{\varepsilon_p^* - \varepsilon_m^*}{\varepsilon_p^* + 2\varepsilon_m^*} \tag{2}$$

where ε_m^* and ε_p^* are the complex permittivities of the medium and particle, respectively. The complex permittivity of the medium is defined as

$$\varepsilon^* = \varepsilon - \frac{j\sigma}{\omega} \tag{3}$$

where σ is the conductivity, ε is the permittivity, and ω is the angular frequency of the applied electric field [13]. The direction and intensity of the driving force acting on the particles depend on the dielectric properties of the particles and the suspending fluid medium, electrode configurations, applied voltage, and frequency. The movement of particles toward the strong electric field gradient region is referred to as positive dielectrophoresis (p-DEP) and toward the opposite direction as negative dielectrophoresis (n-DEP).

The dipoles induced in the particles of a suspension by either field also interact with each other, resulting in a "chaining" force F_{chain}, which depends on the field strength E. A generalized expression for the force between adjacent polarized particles is given as [13]

$$F_{\text{chain}} = -C\pi\varepsilon \,\mathrm{Re}|K(\omega)|^2 r^2 E^2 \tag{4}$$

In this expression, the coefficient C ranges between 3 and 1000, depending on the distance among the particles and the length of the particle chains.

ac electro-osmosis is a fluid flow that occurs when a nonuniform ac electric field is applied to the electrical double layer (EDL) of particles, which forms as a result of the interaction of the ionized solution with static charges on dielectric surfaces. The interaction produces a steady flow over the microelectrode surface. In this process, charged particles tend to migrate toward less-charged and turbulent areas. Thus, this phenomenon may possibly affect colloidal particles that are concentrated in specific locations [26–31].

The electro-osmotic velocity v prediction of ac electro-osmosis, which is modeled using the EDL on the surface of parallel electrodes, is given as [32–34]

$$\langle \nu \rangle = \frac{1}{8}\frac{\varepsilon V_0^2 \Omega^2}{\mu a (1+\Omega^2)^2} \tag{5}$$

where V_0 is the potential applied to the electrodes, μ is the viscosity of the electrolyte, and a is the distance from the center of the electrode gap to the point of interest. In this model, the nondimensional frequency Ω is given by

$$\Omega = \omega r \frac{\varepsilon}{\sigma}\frac{\pi}{2}\kappa \tag{6}$$

where κ is the reciprocal Debye length of the EDL, the distance from the wall where the electrokinetic potential energy becomes equal to the thermal energy. The fluid motion caused by ac electro-osmosis varies, based on the geometry of the parallel electrodes, and can be numerically calculated using the equations above.

3 Experimental

3.1 Material. A sample of 5.3 μm carboxyl functionalized polystyrene particles was purchased from Polysciences, Inc. (Warrington, PA). This monodispersed, negatively charged colloidal sample was diluted to desired concentrations using de-ionized (DI) water (Barnstead Nanopure Water System, http://www.thermo.com/com/cda/product/detail/1,,10131329,00.html), and then the *p*H values of the dispersions, determined using a highly sensitive *p*H meter, were adjusted to *p*H 8 with the addition of a few drops of triethylamine (Sigma-Aldrich, http://www.sigmaaldrich.com/sigma-aldrich/home.html) solution before the tests. The reason for using a slightly alkaline medium was to decrease nonspecific binding between particles and substrates. All samples prepared in our facility were refrigerated until used.

3.2 Method. Parallel-plate gold electrodes were patterned using a conventional photolithography technique followed by gold deposition (plasma sputtering). In the surface-patterning step, a photoresist (S1813 Shipley (http://www.microchem.com/products/pmma.htm) positive type) was spin-coated on a clean glass substrate (5×7.5 cm^2) at 5000 rpm for 30 s before 2 min of soft-baking at 115°C. An UV light was exposed with the desired mask for 40 s at 180 μW/cm^2, and then the sample was soft-baked again at 115°C for 1 min. After the developing process was completed using a Shipley MF 351 at a 1:3.5 ratio with water, a thin layer of gold (200 nm) was evaporated on the surface using a plasma-sputtering unit. In the final step, the photoresist was washed out with acetone in a sonicator for 10 min to create the parallel-plate gold electrodes. The width and length of the parallel plates were 280 μm and 3 mm, respectively. Schematic views of the electrode and experimental setup are shown in Fig. 1 (not to scale).

Throughout the experiments, one side of the parallel plates was connected to the working electrode (ac, dc, or both) where the electric current was applied, whereas the other side was connected to the ground electrode. This geometry allowed for an electrically driven assembly of 2D colloidal crystals resulting in a long-range ordering. The electrical fields were applied to the PS particles in an aqueous media of a fluid chamber separated by a rubber spacer (0.75 mm thickness) after the particles had completely settled on the surface of the substrate. Tests were performed on an optical table using an optical microscope equipped with a charge-coupled device (CCD) camera, close-loop TV, sealed microfluidic device made of Plexiglas®, function generator, and oscilloscope to monitor the sine waves, ac and dc voltages, and frequency levels. During the tests, particle settlement and crystallization times were optimized at 30 min and 10 min, respectively.

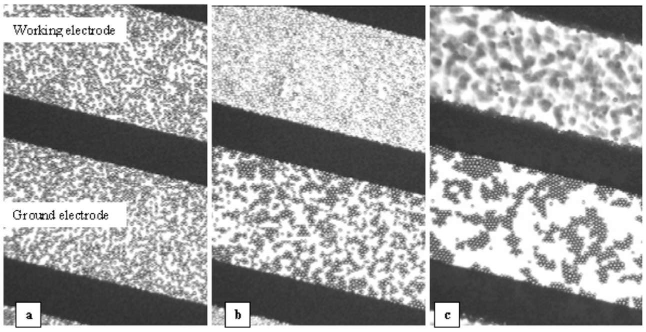

Fig. 2 Photographs showing (*a*) particles settled after 30 min, and crystallized forms at (*b*) 0.1 dc V and (*c*) 0.5 dc V on top of the ground electrodes. Note that the white parts show the gold substrate surface, while the dark stripes show the glass substrate with the PS particles decorating the gold surfaces.

4 Results and Discussion

4.1 Effect of dc Voltage. In order to determine the effects of dc bias voltage on the crystallization of colloidal photonic crystals, a number of tests were conducted with the 5.3 μm PS particles. Figure 2 shows the test results performed at 0.4% solid content, *p*H 8, and 10 min of crystallization time. The particles settled on the ground electrodes (Fig. 2(*a*)) were barely gathered on the ground electrode at 0.1 dc V (Fig. 2(*b*)). However, when the voltage was increased to 0.5 V, localized crystallization of photonic crystals was gradually enhanced. Note that similar effects were also noticed using negative dc charges throughout the tests. Meanwhile, all the particles that originally settled on the working electrode started vibrating (Fig. 2(*c*)). At higher dc voltages (over 0.5 V), it was observed that the working electrodes were debonded from the glass substrate.

In the second step of the experiments, we optimized testing conditions using dc voltage only. Figure 3 shows the gold electrode (Fig. 3(*a*)) and electrophoretic test results conducted on the same particles at 0.5% solid content and 0.4 dc V. The PS particles were initially settled (Fig. 3(*b*)) and crystallized on the ground electrode to form randomly oriented 2D multicrystals (Fig. 3(*c*)). Once again, it was determined that regardless of the sign and intensity of the applied dc voltage, PS particles were formed on the ground electrodes, which can be attributed to the long-range dipole-dipole interactions. However, the other particles on the working electrode were not collected and crystallized, and mostly tended to remain at their original positions. Additionally, particles between the electrodes were not affected much by the applied voltage.

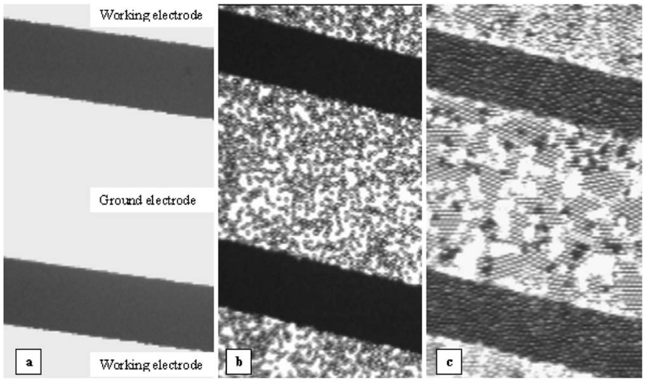

Fig. 3 Photographs showing (*a*) parallel-plate gold electrode (white parts) patterned on a glass substrate (dark parts), (*b*) particles settled on the surface, and (*c*) colloidal particle localized crystallization at 0.4 dc V

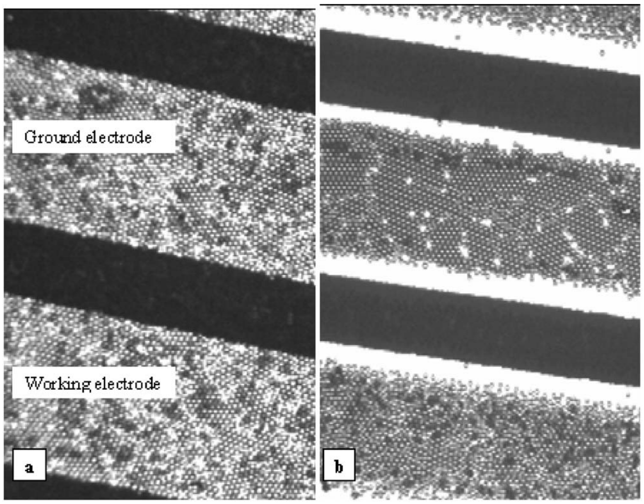

Fig. 4 Photographs showing (*a*) larger colloidal photonic crystal collected on the electrodes and (*b*) crystallization at 2 ac V, 1 MHz frequency, 0.5% solid content, and *p*H 8

4.2 Effect of ac Voltage. ac dielectrophoretic tests were performed on the PS particles at various ac voltages (0.1–4 V), frequencies (10 kHz–10 MHz), and solid contents (0.3–0.5%). Figure 4 shows the fabrication of 2D colloidal crystals at 0.4% solid content, 2 ac V, and 1 MHz frequency after 10 min of crystallization time. These parameters were the optimum conditions obtained for the ac tests. Test results confirmed that the initially settled PS particles were laterally squeezed under the ac voltage and became a larger multidomain PC on top of the ground electrode. No particles were left on both edges of the ground electrodes. In contrast, PS particles on the working electrode were not crystallized and started vibrating in the same manner as during the dc voltage tests. The crystallization of particles under the ac voltage can be due to the electro-osmosis flow (see Eq. (5)) and long-range dipole-dipole attractions on the PS particles [26–31].

Parallel-plate DEP tests were also performed on 0.2% solid content of 5.3 μm PS particles at 2 ac V and 1 MHz to further determine the concentration effects on the accumulation of the colloidal photonic crystals. Figure 5 shows the experimental test

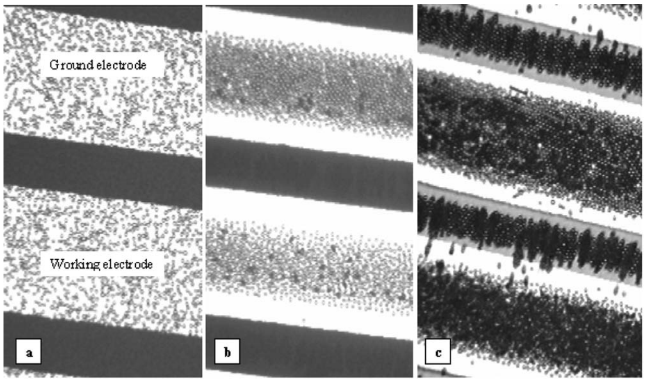

Fig. 5 Photographs illustrating (*a*) PS particles settled on the electrodes; (*b*) parallel-plate DEP tests conducted at 2 ac V, 1 MHz, *p*H 8.0, and 0.2% solid content; and (*c*) formation of pearl chains between the electrodes and second layer on the first layer of the crystal on the ground electrode at 4 ac V and 0.5% solid content

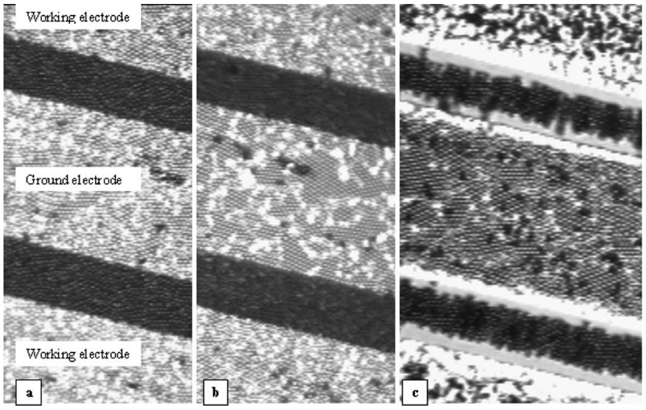

Fig. 6 Crystallization of larger colloidal photonic particles (*a*) after settlement on the electrodes under (*b*) 0.4 dc V, and (*c*) both 0.4 dc and 3 ac V with 1 MHz. This is the largest known colloidal PC to date.

results on the PC fabrication at a lower solid content. Test results illustrate that the PS particles that settled on the electrodes (Fig. 5(*a*)) showed less tendency to crystallize on the ground electrodes. This may be because of the lack of lateral forces acting on the PS particles, or the higher liquid turbulence and Brownian motion at lower concentrations.

The other interesting finding during the tests was that at higher ac voltages and solid content, a second layer of colloidal particles collected on top of the first crystallized layer, which may be because of the higher lateral forces acting on the particles at these testing conditions. Figure 5(*c*) shows the second layer formation at 4 ac V and 0.5% solid content. Additionally, a chaining effect (pearl chains) of PS particles between the working and ground electrodes (see Eq. (4)) was clearly observed in the test, which may be due to the higher polarity of ac voltage applied to the electrodes and PS particles.

4.3 Effect of Both ac and dc Voltages. For the fabrication of larger colloidal photonic crystals, varying ac and dc fields were applied together on the PS particles with 0.5% solid content. Figure 6 shows the test results obtained at 0.4 dc V (Fig. 6(*b*)) and 0.4 dc+3 ac V with 1 MHz (Fig. 6(*c*)). The test results clarified that the colloidal particles were initially crystallized on the ground electrode using dc bias voltage, and then small domains became a larger multidomain (about 250 μm in width and 3 mm in length) after the application of 3 ac V and 0.4 V dc together. To the best of our knowledge, this is the largest multicrystalline colloidal PC produced using this kind of methods. Figure 6 also shows that there are a few point defects (missing particles) and second layers of particles on the crystals, which may be a result of lateral forces on the edges of the electrodes. Particles on the working electrode were again lifted from the surface, while the other particles in between neighboring electrodes formed pearl chains under the ac/dc voltage.

After the experimental studies were completed, the fabrication device was washed out several times using DI water. However, the evidence indicated that some of the colloidal particles still remained on the ground electrodes. The reason for this may be attributed to the excess amount of current/charge on the electrodes and particles, which created a long-range attraction force to hold the particles together. Figure 7 shows the crystalline PS particles on the ground electrode photographed after washing with DI water.

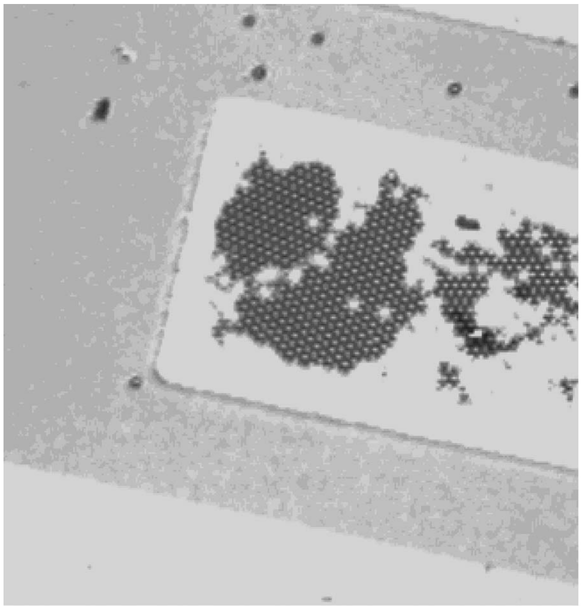

Fig. 7 Photograph illustrating the remaining colloidal particles in mostly crystalline form after washing several times with DI water

4.4 Schematic Illustration of Crystallization Process. In the electro-osmosis process (high-velocity streamlines on the edge of the electrodes), the charged particles tend to migrate toward the lesser charged and turbulence areas as is specified in Eq. (5) [28–30]. Thus, this phenomenon may possibly affect the colloidal particles concentrated in specific locations. In the presence of electrically charged ions in an aqueous system, the ions possibly transfer onto the surface of the PS particles and increase the long-range dipole-dipole (particle-particle) interactions for the crystallization of the polarized particles [31]. Based on the test results, it is believed that this can be one of the major mechanisms of the colloidal particle accumulation and crystallization on the ground electrodes. Additional reasons may be electrohydrodynamic, electric field gradient, and thermal effects on the particles [26–30]. Figure 8 depicts the possible schematic views of the larger PC particle crystallization on the ground electrode using dc and ac voltages.

Crystallization was not achieved on the working electrode, which could be because of induced charges greatly increasing the

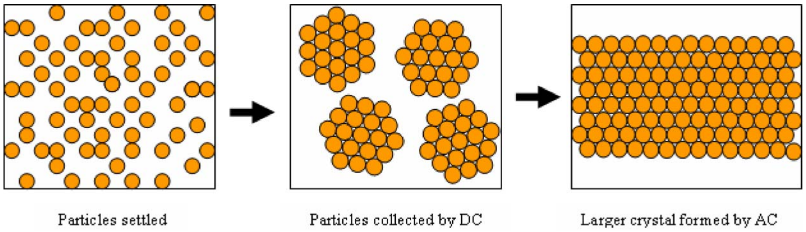

Fig. 8 Schematic illustrations of larger colloidal particle crystallization under dc followed by dc/ac electric fields

fluid flow on the crake, channel, bump surfaces, and/or sharp edges of the working electrodes, as well as the pulsing of the electric field strength in the system. Excess charges may also enhance the electrostatic repulsive forces between the particles on the working electrodes. In order to determine the actual reason(s) for the larger colloidal particle crystallization on the ground electrodes, further investigation using new techniques and approaches can be utilized.

5 Conclusions

The parallel-plate DEP tests were conducted on carboxyl functionalized PS colloidal particles (5.3 μm) to create larger 2D colloidal crystals. Test results revealed that colloidal particles could be easily formed into closely packed larger colloidal crystals on the ground electrodes for various dc and/or ac voltages. As is known, the DEP technique is a simple, inexpensive, and more rapid assembly technique compared with other methods. Therefore, this technique can have great potential for the photonic crystal fabrication, as well as many other biological, organic, and inorganic particle manipulations in the future.

Acknowledgment

The authors wish to acknowledge AFOSR (Contract No. F49620-01-1-0545) and ONR (Contract No. N00014-00-1-0333) for their financial support.

References

[1] Yablonovitch, E., 2001, "Photonic Crystals: Semiconductors of Light," Sci. Am., **285**(6), pp. 47–55.
[2] Johnson, S. G., and Joannopoulos, J. D., 2002, *Photonic Crystals: The Road From Theory to Practice*, 1st ed., Kluwer, Dordrecht.
[3] Park, S. H., and Xai, Y., 1999, "Assembly of Mesoscale Particles Over Large Areas and Its Application in Fabricating Tunable Optical Filters," Langmuir, **15**, pp. 266–273.
[4] Kitaev, V., and Ozon, G. A., 2003, "Self-Assembled Surface Patterns of Binary Colloidal Crystals," Adv. Mater. (Weinheim, Ger.), **15**, pp. 75–78.
[5] Lumsdon, S. O., Kaler, E. W., and Volve, O. D., 2004, "Two-Dimensional Crystallization of Microspheres by a Coplanar AC Electric Field," Langmuir, **20**, pp. 2108–2116.
[6] Trau, M., Sankaran, S., Saville, D. A., and Aksua, I., 1995, "Electric-Field-Induced Patterning of Colloidal Dispersions," Nature (London), **374**, pp. 437–439.
[7] Mclachlan, M. A., Johnson, P. N., De La Rue, R., and McComb, D. W., 2004, "Thin Film Photonic Crystals: Synthesis and Characterization," J. Mater. Chem., **14**, pp. 144–150.
[8] Hamagami, J. H., Hasegawa, K., and Kanamura, K., 2004, "Assembly of Monodispersed Silica Spheres by Micro-Electrophoretic Deposition Process," J. Ceram. Soc. Jpn., **12**, pp. 169–172.
[9] Ahn, J. S., Hammond, P. T., Rubner, M. F., and Lee, I., 2005, "Self-Assembled Particle Monolayers on Polyelectrolyte Multiplayer: Particle Size Effects on the Formation, Structure and Optical Properties," Colloids Surf., A, **259**, pp. 45–51.
[10] Dziomkina, N. V., Hempenius, M. A., and Vancso, G. J., 2005, "Symmetry Control of Polymer Colloidal Monolayers and Crystals by Electrophoretic Deposition Onto Patterned Surfaces," Adv. Mater. (Weinheim, Ger.), **17**(2), pp. 237–240.
[11] Mekis, A., Chen, J. C., Kurland, I., Fan, S., Villeneuve, P. R., and Joannopoulos, J. D., 1996, "High Transmission Through Sharp Bends in Photonic Crystal Waveguides," Phys. Rev. Lett., **77**(18), pp. 3787–3790.
[12] John, S., 1987, "Strong Localization of Photons in Certain Disordered Dielectric Superlattices," Phys. Rev. Lett., **58**, pp. 2486–2489.
[13] Pohl, H. A., 1978, *Dielectrophoresis*, Cambridge University Press, Cambridge.
[14] Morgan, H., and Green, N. G., 2003, *AC Electrokinetics: Colloids and Nanoparticles*, Research Studies, Baldock, UK.
[15] Kawabata, T., and Washizu, M., 2001, "Dielectrophoretic Detection of Molecular Bindings," IEEE Trans. Ind. Appl., **37**(6), pp. 1625–1633.
[16] Kawabata, T., and Washizu, M., 1999, "Separation of Biomolecules Using Dielectrophoretic Chromatography," Trans. Inst. Electr. Eng. Jpn., Sect. E, **119-E**(10), pp. 454–459.
[17] Suzuki, M., Yasukawa, T., Mase, Y., Oyamatsu, D., Shiku, H., and Matsue, T., 2004, "Dielectrophoretic Micropatterning With Microparticle Monolayers Covalently Linked to Glass Surfaces," Langmuir, **20**(25), pp. 11005–11011.
[18] Lumsdon, S. O., Williams, J. P., Kaler, E. W., and Volve, O. D., 2003, "Dielectrophoretic Assembly of Oriented and Switchable Two-Dimensional Photonic Crystals," Appl. Phys. Lett., **82**, p. 949.
[19] Abe, M., Orita, M., Yamazaki, H., Tsukamoto, S., Teshima, Y., Sakai, T., Ohkubo, T., Momozawa, N., and Sakai, H., 2004, "Three-Dimensional Arrangement of Polystyrene Latex Particles With a Hyperbolic Quadruple Electrode System," Langmuir, **20**, pp. 5046–5051.
[20] Asmatulu, R., Kim, S., Bright, R., Yu, P., Papadimitrakopoulos, F., and Marcus, H., 2006, "Fabrication and Defect Designs on DNA Linked 2D Colloidal Photonic Crystals Using a Nd:YAG Pulsed Laser," Mater. Res. Soc. Symp. Proc., **901E**, pp. Ra21–02.1-6.
[21] Geiss, E. P., 2003, "Fabrication and Defect Design in Two-Dimensional Colloidal Photonic Crystals," Ph.D. thesis, University of Connecticut, Storrs, CT.
[22] Yu, P., 2005, "Controlled Defect Insertion in 2-D Photonic Crystals Using a Nd:YAG Laser Harmonic at 532 nm," MS thesis, University of Connecticut, Storrs, CT.
[23] Alvarado-Rodriguez, I., 2003, "Fabrication of Two-Dimensional Photonic Crystal Single-Defect Cavities and Their Characterization by Elastic Scattering," Ph.D. thesis, University of California, Los Angeles, CA.
[24] Blaaderen, A. V., and Wiltzius, P., 2004, "Growing Large, Well-Oriented Colloidal Crystals," Adv. Mater. (Weinheim, Ger.), **10**, pp. 833–835.
[25] Gupta, M. C., and Ballato, J., 2007, *The Handbooks of Photonics*, CRC, Boca Raton, FL.
[26] Morgan, H., Izquierdo, A. G., Bakewell, D., Green, N., and Ramos, A., 2001, "The Dielectrophoretic and Traveling Wave Forces Generated by Interdigitated Electrode Arrays: Analytical Solution Using Fourier Series," J. Phys. D, **34**, pp. 1553–1561.
[27] Green, N., Ramos, A., Gonzales, A., Morgan, H., and Castellanos, A., 2002, "Fluid Flow Induced by Nonuniform ac Electric Fields in Electrolytes on Microelectrodes. III. Observation of Streamlines and Numerical Simulation," Phys. Rev. E, **66**, p. 026305.
[28] Green, N. G., Ramos, A., and Morgan, H., 2002, "Numerical Solution of the Dielectrophoretic and Traveling Wave Forces for Interdigitated Electrode Arrays Using the Finite Element Method," J. Electrost., **56**, pp. 235–254.
[29] Ramos, A., Gonzales, A., Castellanos, A., Green, N., and Morgan, H., 2003, "Pumping of Liquids With ac Voltage Applied to Asymmetric Pairs of Microelectrodes," Phys. Rev. E, **67**, p. 056302.
[30] Bhatt, K. H., Grego, S., and Velev, O. D., 2005, "An AC Electrokinetic Technique for Collection and Concentration of Particles and Cells on Patterned Electrodes," Langmuir, **21**(14), pp. 6603–6612.
[31] Adamson, A. W., and Gast, A. P., 1997, *Physical Chemistry of Surfaces*, 6th ed., Wiley, New York.
[32] Ramos, A., Morgan, H., Green, N. G., and Castellanos, A., 1999, "AC Electric-Field Induced Fluid Flow in Microelectrodes," J. Colloid Interface Sci., **217**, pp. 420–422.
[33] James, C. D., Okandan, M., Galambos, P., Mani, S. S., Bennett, D., Khusid, B., and Acrivos, A., 2006, "Surface Micromachined Dielectrophoretic Gates for the Front-End Device of a Biodetection System," ASME J. Fluids Eng., **128**(1), pp. 14–19.
[34] Hughes, M. P., 2000, "AC Electrokinetics: Applications for Nanotechnology," Nanotechnology, **11**, pp. 124–132.

Comparison of Turbulence Modeling Strategies for Indoor Flows

Ammar M. Abdilghanie

Lance R. Collins

David A. Caughey[1]
e-mail: dac5@cornell.edu

Sibley School of Mechanical & Aerospace Engineering,
Cornell University,
Ithaca, NY 14853-7501

Turbulence modeling techniques are compared for the simulation of low speed indoor air flow in a simple room. The effect of inlet turbulence intensity on the flow field is investigated using the constant coefficient large eddy simulation (LES) model with uniform mean inlet conditions at several levels of inlet turbulence intensities. The results show significant differences between the simulations with laminar inflow conditions and those in which turbulence was introduced at the inlet. For simulations with turbulent inlet conditions, it is noticed that the jet transitions to a state of fully developed turbulence wherein the dynamics of the flow become nearly insensitive to any further increase in the level of inlet turbulence. For laminar flow conditions, it is seen that the jet slowly spreads and mixes with the quiescent room air. As a result, the jet reaches a fully developed turbulent state further away from the inlet relative to the simulations with inlet turbulence. The effect of using experimental inlet profiles is also investigated. It is seen that, close to the inlet, the flow is sensitive to the inflow details, whereas further away from the inlet, these effects become less pronounced. The results from the constant coefficient and the dynamic LES models are compared. The most noticeable differences in the flow occur at the locations where the subgrid-scale's contribution to the turbulent kinetic energy is highest. Finally, the results from the dynamic LES and the k-ϵ models are compared. It is found that there are significant differences between the two models for the zero inlet turbulence limit where the flow is most probably transitional in nature and turbulence has not yet reached a fully developed state. It is seen that in the laminar inflow case the k-ϵ model predicts a fully turbulent jet very close to the inlet and thus fails to capture the slow development of the jet found in LES. Accordingly, the k-ϵ model results are nearly insensitive to the level of inlet turbulence especially far from the origin of the flow. It is also seen that for cases with nonzero inlet turbulence level, the k-ϵ model predicts the general features of the mean flow reasonably well; however, the k-ϵ model overpredicts the jet spreading rate and the turbulent kinetic energy close to the inlet. Furthermore, the k-ϵ model under predicts the turbulence level near the corner of the ceiling as it fails to capture the complicated mean velocity and turbulent kinetic energy, most likely because of the highly intermittent flow pattern found there in LES. [DOI: 10.1115/1.3112386]

1 Introduction

The vast majority of ventilation systems are designed assuming the pollutants and the ventilating air are well mixed within a room, regardless of its size. In many instances, this is far from reality. There are numerous cases where the dispersion of pollutants does not correspond to a well-mixed condition [1]. Computational fluid dynamics (CFD) provides a practical option for predicting the airflow and pollutant distributions in buildings. CFD can be used to determine the best locations of air supply diffusers and return outlets and the flow rate needed to create an acceptable indoor air quality.

The Reynolds number for the flow inside a built environment is most likely high; hence the CFD model must account for turbulence. Turbulence modeling can be done at a variety of levels, depending on accuracy requirements, the computational facilities, and the wall-clock time available for the calculation. Direct numerical simulation (DNS) is a model-free approach that involves obtaining the three-dimensional solution of the Navier–Stokes (NS) equations with full resolution of all of the spatial and temporal scales of the turbulent motion. With DNS, the complete flow field throughout the domain is determined with no modeling assumptions, and thus it offers the most accurate characterization of the turbulence possible. The principal drawback of DNS is that its computational cost increases in proportion to the cube of the Reynolds number [2]. This limits its use mainly to fundamental scientific investigations of turbulence, and makes it impractical for CFD of the sort required for the present application.

At the other extreme in terms of computational cost is the Reynolds-averaged Navier–Stokes (RANS) modeling. With RANS, modeled equations for the mean velocity of a statistically stationary turbulent flow are solved. The higher-order Reynolds stresses are usually obtained from a turbulent viscosity model, which is algebraically related to other turbulence quantities such as the turbulent kinetic energy k and energy dissipation rate ϵ for which modeled transport equations are solved. Because RANS is not concerned with solving for the fluctuating velocity and pressure fields, the computational cost is much lower (by orders of magnitude) than the equivalent DNS. However, the accuracy of RANS predictions is limited by the fidelity of the closure models used to represent the effects of the turbulent fluctuations. Despite decades of research, there remain fundamental limitations to what can be expected from a RANS simulation [3].

Large eddy simulation (LES) has emerged as an important intermediate approach, whereby one solves for the instantaneous filtered velocity of the largest energy-containing eddies of the turbulent motion and models the effect of the subgrid-scale motions

---

[1] Corresponding author. Present address: Department of Mechanical & Aerospace Engineering, Cornell University, 248 Upson Hall, Ithaca, NY 14853-7501.

Contributed by the Fluids Engineering Division of ASME for publication in the JOURNAL OF FLUIDS ENGINEERING DIVISION. Manuscript received June 14, 2008; final manuscript received March 8, 2009; published online April 15, 2009. Review conducted by Paul Durbin.

on the resolved scales. As LES directly solves for the large-scale turbulence, it yields more accurate results than RANS, yet has a much lower computational cost than DNS, in which all of the scales of the turbulence must be fully resolved. With the rapid growth in computer speed and memory over the past 30 years, LES has moved from being a research tool to a valuable tool for studying flows in realistic geometries.

The development of LES for turbulent flows has been an active area of research, and there have been several important advances in LES since the pioneering work of Smagorinsky [4], Lilly [5], Deardorff [6], Schumann [7], and others. Advances have been made in (i) modeling the unresolved processes; (ii) accurate numerical methods on structured and unstructured grids; (iii) detailed comparison of LES calculations with DNS and experimental data in canonical flows; (iv) extensions to include additional phenomena, e.g., turbulent combustion; and (v) computational power, which has increased by more than four orders of magnitude since the 1970s [8]. Various subgrid-scale (SS) models have been developed, beginning with the early work that relied on an eddy viscosity model with a constant coefficient C_s, which is a function of the flow regime [4–6]. The dynamic model was first introduced by Germano et al. [9], with important modifications and extensions provided by Lilly [10] and Meneveau et al. [11]. The dynamic model provides a method for estimating the Smagorinsky coefficient locally. It has proven quite successful, and the same procedure has been applied in several other contexts [2]. One requirement for truly accurate LES is that the grid adequately resolve the largest energy-containing eddies so that the subgrid model is subdominant to the resolved scales. This implies either having some a priori knowledge of the length scales of the turbulence so that the grid can be designed accordingly or having an adaptive approach that refines the grid where needed.

In the field of indoor air flow simulation, several researchers have studied the performance of the k-ϵ-model [12,13]. The authors demonstrated that the model can successfully predict the mean velocities. Chen [14] compared the performance of four different k-ϵ and Reynolds stress models (RSMs) for four common problems in air flows: natural convection, forced convection, mixed convection, and impinging jet flows. The study showed that all four models predicted the mean velocities reasonably well; however, they failed to accurately predict the turbulence levels. While RANS models are strictly applicable to fully developed turbulent flows [15], it is not uncommon in indoor air flows, especially at low ventilation rates, to have laminar, transitional, and slowly developing turbulent flows co-existing [15,16].

LES has been successfully applied to airflow simulations [17–19]. Davison and Nielson [17] compared the performance of the standard Smagorinisky and dynamic models for a simply ventilated room. It was found that the dynamic model agrees better with the experimental data. Jiang et al. [19] used LES to study air flows in and around buildings. They compared the Smagorinsky SS model, the filtered dynamic (FD) model by Zhang and Chen [20], and the stimulated small-scale subgrid-scale (SSS) model by Shah and Ferziger [21]. They concluded that the simple SS model gives less accurate results in regions where the flow is not fully developed, as compared with the FD and the SSS models. The SS model was found to work fairly well for the outdoor flows, where conditions are fully turbulent. Since the FD and the SSS models are computationally more intensive, the SS model was recommended for outdoor flows and the SSS and FD models were recommended for indoor flows. This represented an optimum solution to ensure accurate representation of upstream conditions.

Recently, Zhai et al. [22] and Zhang et al. [23] compared eight different RANS and LES models for simulation of representative indoor air flows such as forced and mixed convection in ventilated spaces and natural convection in a tall cavity. They concluded that the v2f-dav model by Davidson et al. [24] and LES are the most suitable models in predicting air velocity, temperature, and turbulent quantities for low Rayleigh number natural convection flows. In forced convection with low turbulence levels, the renormalization group (RNG) k-ϵ model by Yakhot and Orszag [25], the low Reynolds number k-ϵ model due to Launder and Sharma LRN-LS [26], the v2f-dav, and LES all performed very well. The v2f model by Durbin [27] was found to be very promising but the numerical algorithm has to be constructed so as to avoid some inherent numerical problems. The RSMs were shown to be able to capture more flow details than eddy viscosity based models; however, they require more computational time. The authors concluded that LES provided more detailed and possibly more accurate predictions for indoor air flows and that it is a very important tool for understanding the dynamics of indoor airflow.

In the current investigation, we use LES to model the air flow inside an experimental flow chamber located in the Indoor-Flow-Laboratory (IFL) at Syracuse University. The hydrodynamic conditions within the facility are typical of displacement ventilation systems, where the supply air displaces the room air with presumed minimal mixing so as to achieve a high air change efficiency [1].

Consistent with the incremental procedure for simulation of displacement ventilation systems laid out by Chen and Srebric [28] and Chen and Zhai [29], we have neglected thermal convection effects and geometrical complexities at this stage. The main objective here was limited to modeling and understanding the basic flow behavior inside the IFL, with an eye toward incorporating more comprehensive physics and more geometrical details in future investigations.

The sensitivity of the flow field to the inlet turbulence levels and the details of the flow at the inlet are investigated. The performance of the Smagorinsky LES model with constant coefficient and the dynamic model in predicting the air flow are systematically studied and analyzed. Finally, light is shed on the performance of the k-ϵ model in predicting the mean flow and the turbulent kinetic energy throughout the flow field at varying inlet turbulence levels.

2 Turbulence Models

2.1 RANS Equations. The ensemble average of the constant density NS equations takes the form [30]

$$\frac{\partial \rho}{\partial t} + \frac{\partial \rho \bar{u}_i}{\partial x_i} = 0 \tag{1}$$

$$\frac{\partial \rho \bar{u}_i}{\partial t} + \frac{\partial}{\partial x_j}(\rho \bar{u}_i \bar{u}_j) = -\frac{\partial \bar{p}}{\partial x_i} + \frac{\partial}{\partial x_j}\left[\mu\left(\frac{\partial \bar{u}_i}{\partial x_j} + \frac{\partial \bar{u}_j}{\partial x_i} - \frac{2}{3}\frac{\partial \bar{u}_l}{\partial x_l}\delta_{ij}\right)\right] + \frac{\partial}{\partial x_j}(-\rho\overline{u_i' u_j'}) \tag{2}$$

where ρ is the density, p is the pressure, μ is the dynamic viscosity, $\bar{u}_i$ is the velocity component in the x_i direction, and the overbar indicates an averaged quantity. The symbol δ_{ij} denotes the Kronecker delta, and the Einstein summation convention is used. The Reynolds-averaged approach to turbulence modeling requires that the Reynolds stress term $-\rho\overline{u_i' u_j'}$ be appropriately modeled. In the k-ϵ model, the Boussinesq approximation is used to relate the Reynolds stresses to the mean velocity gradients through

$$-\rho\overline{u_i' u_j'} = \mu_t\left(\frac{\partial \bar{u}_i}{\partial x_j} + \frac{\partial \bar{u}_j}{\partial x_i}\right) - \frac{2}{3}\left(\rho k + \mu_t \frac{\partial \bar{u}_k}{\partial x_k}\right)\delta_{ij} \tag{3}$$

where the turbulent (or eddy) viscosity μ_t must be specified in order for the above system of equations to be closed.

2.1.1 The Standard k-ϵ Model. The simplest complete models of turbulence are two-equation models in which the solution of two separate transport equations allows the turbulent velocity and length scales to be independently determined. According to Ref. [30], the standard k-ϵ model in FLUENT falls within this class of turbulence models that has become the workhorse of practical engineering flow calculations in the time since it was proposed by Launder and Spalding [31]. The turbulence kinetic energy k and its rate of dissipation ϵ are obtained from the following transport equations:

$$\frac{\partial \rho k}{\partial t} + \frac{\partial}{\partial x_i}(\rho k \bar{u}_i) = \frac{\partial}{\partial x_j}\left[\left(\mu + \frac{\mu_t}{\sigma_k}\right)\frac{\partial k}{\partial x_j}\right] + G_k - \rho\epsilon \tag{4}$$

$$\frac{\partial \rho \epsilon}{\partial t} + \frac{\partial}{\partial x_i}(\rho \epsilon \bar{u}_i) = \frac{\partial}{\partial x_j}\left[\left(\mu + \frac{\mu_t}{\sigma_\epsilon}\right)\frac{\partial \epsilon}{\partial x_j}\right] + C_{1\epsilon}\frac{\epsilon}{k}G_k - C_{2\epsilon}\rho\frac{\epsilon^2}{k} \tag{5}$$

where G_k represents the generation of turbulence kinetic energy due to the mean velocity gradients, and $C_{1\epsilon}$, and $C_{2\epsilon}$ are the model constants. The details of how these terms are calculated in FLUENT can be found in Ref. [30] and are omitted here for the sake of brevity. In these equations, σ_k and σ_ϵ are the turbulent Prandtl numbers for k and ϵ, respectively. The turbulent viscosity μ_t is computed by combining k and ϵ as follows:

$$\mu_t = \rho C_\mu \frac{k^2}{\epsilon} \tag{6}$$

The model constants $C_{1\epsilon}$, $C_{2\epsilon}$, C_μ, σ_k, and σ_ϵ have the following default values: $C_{1\epsilon}=1.44$, $C_{2\epsilon}=1.92$, $C_\mu=0.09$, $\sigma_k=1.0$, and $\sigma_\epsilon=1.3$.

2.1.2 A Two-Layer Model for the Enhanced Wall Treatment. The two-layer approach is an integral part of the enhanced wall treatment and is used to specify both ϵ and the turbulent viscosity in the near-wall cells [30]. In this approach, the whole domain is subdivided into a viscosity-affected region and a fully turbulent region. The demarcation between the two regions is determined by a wall-distance-based, turbulent Reynolds number Re_y. In the fully turbulent region ($\mathrm{Re}_y > \mathrm{Re}_y^*$), the k-ϵ model described above is employed. In the viscosity-affected near-wall region ($\mathrm{Re}_y < \mathrm{Re}_y^*$), the one-equation model of Wolfshtein [32] is employed. Here the default value of $\mathrm{Re}_y^*=200$ is used. In the enhanced wall treatment approach, the turbulent viscosity is smoothly blended with the high-Reynolds-number μ_t definition from the outer region. The main purpose of the blending function is to allow convergence even when the k-ϵ solution in the outer layer does not match the two-layer formulation [30]. In the enhanced wall function approach, FLUENT blends the linear (laminar) and the logarithmic (turbulent) laws-of-the-wall for the mean velocity using a function suggested by Kader [33] to form a single law-of-the-wall for the entire wall region. The resulting law-of-the-wall has the correct asymptotic behavior in the viscous sublayer and the log-law region and also represents the velocity profile in the wall buffer region reasonably well [30]. The k equation is solved in the whole domain including the wall-adjacent cells. The boundary condition for k imposed at the wall is

$$\frac{\partial k}{\partial n} = 0 \tag{7}$$

where n is the local coordinate normal to the wall. As we will illustrate, the dynamics of the flow are dominated by the shear layers and hence we expect the flow to be relatively insensitive to the boundary conditions applied at the walls.

2.2 LES Equations. By filtering the constant density NS equations, one obtains [30]

$$\frac{\partial \rho}{\partial t} + \frac{\partial \rho \tilde{u}_i}{\partial x_i} = 0 \tag{8}$$

$$\frac{\partial \rho \tilde{u}_i}{\partial t} + \frac{\partial}{\partial x_j}(\rho \tilde{u}_i \tilde{u}_j) = \frac{\partial}{\partial x_j}\left(\frac{\partial \sigma_{ij}}{\partial x_j}\right) - \frac{\partial \tilde{p}}{\partial x_i} - \frac{\tau_{ij}}{\partial x_j} \tag{9}$$

where the tilde indicates a filtered quantity,

$$\sigma_{ij} = \mu\left(\frac{\partial \tilde{u}_i}{\partial x_j} + \frac{\partial \tilde{u}_j}{\partial x_i}\right) - \frac{2}{3}\mu\frac{\partial \tilde{u}_l}{\partial x_l}\delta_{ij} \tag{10}$$

that represents the contributions of the filtered velocity to the viscous stress tensor, and τ_{ij} is the subgrid-scale stress defined by

$$\tau_{ij} \equiv \rho\widetilde{u_i u_j} - \rho\tilde{u}_i\tilde{u}_j \tag{11}$$

The subgrid stresses are modeled using the Boussinesq approximation as in the RANS models:

$$\tau_{ij} - \tfrac{1}{3}\tau_{kk}\delta_{ij} = -2\mu_t\tilde{S}_{ij} \tag{12}$$

where $\tilde{S}_{ij}$ is the rate-of-strain tensor for the filtered velocity, defined by

$$\tilde{S}_{ij} \equiv \frac{1}{2}\left(\frac{\partial \tilde{u}_i}{\partial x_j} + \frac{\partial \tilde{u}_j}{\partial x_i}\right) \tag{13}$$

and μ_t is the subgrid-scale turbulent (or eddy) viscosity.

2.2.1 Smagorinsky-–Lilly Model. In the Smagorinsky model, the eddy viscosity is modeled by

$$\mu_t = \rho L_s^2 |\tilde{S}| \tag{14}$$

where L_s is the mixing length for the subgrid scales and $|\tilde{S}| \equiv \sqrt{2\tilde{S}_{ij}\tilde{S}_{ij}}$. In FLUENT, L_s is computed using

$$L_s = \min(\kappa d, C_s V^{1/3}) \tag{15}$$

where $\kappa(=0.41)$ is the von Karman constant, d is the distance to the closest wall, and V is the volume of the computational cell. A value of 0.1 for C_s has been found satisfactory for a wide range of flows and was thus used in the current investigation.

2.2.2 Dynamic Smagorinsky–Lilly Model. Germano et al. [9] and subsequently Lilly [10] conceived a procedure by which the Smagorinsky model constant C_s is dynamically computed based on the information provided by the resolved scales of motion. They realized that the LES equations are solved for the filtered velocity field, although this filtering is not always explicitly performed. Using single- and double-filtered residual stress tensors, Germano [34] derived a closed expression for a tensor referred to as the *resolved stress* tensor, in terms of the grid-filtered velocity field. The resolved stress tensor can be loosely interpreted as the contribution to the residual stress from the largest unresolved scales [2]. If a Smagorinsky type model for the deviatoric part of this tensor is constructed, then an adjustable coefficient C_s can be locally matched to provide the best estimate for the deviatoric part of the resolved stress tensor. As it is impossible to match the five independent components of the deviatoric tensor, Lilly [10] derived a specification of C_s that minimizes the mean-square error. In the implementation of the dynamic LES model in FLUENT, C_s is clipped at zero and 0.23 by default to eliminate backscatter and to avoid numerical instabilities [30].

3 Numerical Solution Details

The commercial CFD code FLUENT was used to simulate the flow. The temporally second-order accurate, unsteady solver based on the noniterative time advancement algorithm was used with the incompressible pressure-based segregated solver, using the pressure-implicit with splitting of operator pressure-velocity coupling scheme. The central differencing scheme is an ideal choice for LES because of its low numerical diffusion; however, it can result in unphysical oscillations in the solution. This situation is worsened if combined with the low subgrid-scale turbulent diffusivity used in LES. The bounded central differencing scheme is a composite normalized variable diagram scheme that consists of pure central differencing, a blended scheme of the central differencing and the second-order upwind scheme, and the first-order upwind scheme, which is used only when the convection bound-

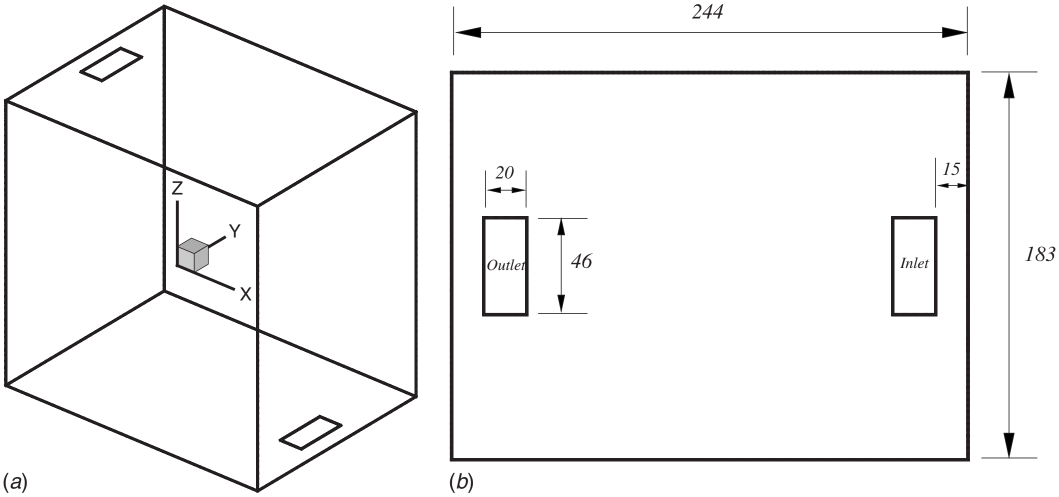

Fig. 1 (*a*) Geometry of Indoor Flowfield Laboratory Chamber; dimensions are 244×183×244 cm^3. (*b*) Top view; dimensions are in cm.

edness criterion is violated [30]. Provided that the numerical solution converges, this approach leads to pure second-order differencing [30]. The bounded central difference scheme was used for discretization of both the pressure and momentum equations, and default tolerances were used (a residual tolerance of 0.0001 and relaxation factors of 1 for the pressure and momentum equations). Air with constant density and viscosity at standard sea level conditions was used. The time step was set so that the resulting maximum Courant number would be no larger than 0.5. The boundary conditions used in the first stage of this investigation were simple plug/uniform flow velocity profile at the inlet, with uniform turbulence intensities of 0%, 5%, and 13%, a uniform turbulence length scale equal to 7% of the inlet hydraulic diameter, a pressure outlet for the outflow, and solid wall boundary conditions everywhere else. Simulations of the flow were continued up to the time when the flow was approximately statistically stationary. In the second stage of the study, the inlet velocity and turbulence profiles obtained from experiments conducted in the IFL at Syracuse University [35] were used in the simulations.

3.1 Description of the Geometry.

The IFL chamber consists of a $2.44\times 1.83\times 2.44\ \text{m}^3$ cubicle, with optical access for particle image velocimetry (PIV) measurements through the front $(1.83\times 2.44\ \text{m}^2)$ wall. The origin of the coordinate system is located at the center of the cubicle, with positive z pointing vertically upward and positive x pointing toward the front wall (see Fig. 1). The chamber half-height L is used to nondimensionalize the vertical distance. The chamber is designed to represent a typical indoor-flow environment for a single occupancy cubicle. An isometric view of the chamber is shown in Fig. 1(*a*) and a top view is shown in Fig. 1(*b*). The cubicle is ventilated by a low speed, closed-loop system that is designed to allow an occupant's thermal plume to be a significant factor in driving the flow. There is a $0.2\times 0.46\ \text{m}^2$ inlet on the floor, near the front wall, and an identically sized outlet in the ceiling near the rear wall. The average inlet and outlet flow velocity is 0.2 m/s.

3.2 Description of the Computational Grid.

An initial grid containing $48\times 32\times 48$ cells was developed using FLUENT's Gambit mesh generator to represent the chamber. The accuracy of the resulting solution was checked by grid refinement and comparison of the resulting solution with the original solution on the coarser grid. The process was repeated until an accurate solution was obtained. Based on the initial results from the coarse grid, the grid was locally refined in those regions exhibiting steep gradients of the solution variables such as the inlet, the shear layers around the inflow plume, the ceiling, and the outlet. First, a vertical column including the inlet and three cells on each side of it was refined once (by halving the mesh dimensions in each coordinate direction), and another volume around the outlet, extending three cells on each side of it and four cells below it was refined (again, by halving the mesh dimensions in each coordinate direction). Finally, a volume covering the entire ceiling area and extending four cells below, it was similarly refined. The resulting grid was again used to determine the general features of the flow. Based on the results of the initial calculations on this grid, it was determined that extra refinement of the grid in the vicinity of the inlet was required to maintain adequate accuracy. Two additional steps of refinement were done. The first involved refinement of the volume covering the inlet area and four cells away from it on all sides, and extending 18 cells above the inlet. The second refinement covered the area of the inlet and two cells away from it on all sides, and extended nine cells above the inlet. The resulting grid, referred to here as the *baseline grid*, is shown in Figs. 2(*a*) and 2(*b*) where (a) shows a side view of the vertical plane passing through the center of the inlet and (b) shows a top view of the floor and the inlet area. The baseline grid calculations were performed on a Linux cluster using ten processors. The wall-clock time per time step was about 10 s corresponding to 800 s of (wall-clock) compute time per physical second (since the time step on this grid is $\Delta t=0.0125$ s). It was found that the wall-clock time for calculations with the dynamic subgrid-scale model is nearly the same as that for the constant coefficient Smagorinsky model. To test grid convergence, one case (13% inlet turbulence intensity) was solved on *a refined grid* that contained twice the number of grid cells in each direction. The time step used on the refined grid was $\Delta t=0.006\,25$ s, so the solution for a fixed time interval was approximately 16 times more computationally expensive than the solution on the baseline grid. The computations on the refined grid were performed on a newer Linux cluster utilizing Infiniband as an interconnect, which was found to significantly decrease the wall-clock time. Using 20 cores on five nodes (each having two dual core processors) reduced the wall-clock time to about 1 s per time step.

3.3 Simulation of Inlet Turbulence.

Simulation of inlet turbulence for fully developed turbulent flows can, in principle, be achieved by adding small perturbations to a laminar flow and by having a long enough computational domain in the streamwise direction to allow the turbulence to develop. In order to reduce the development region, a more viable approach is to introduce an upstream domain and to solve for the flow assuming periodicity in the streamwise direction [36]. The result of this calculation is then used as an inflow boundary condition for the main simulation.

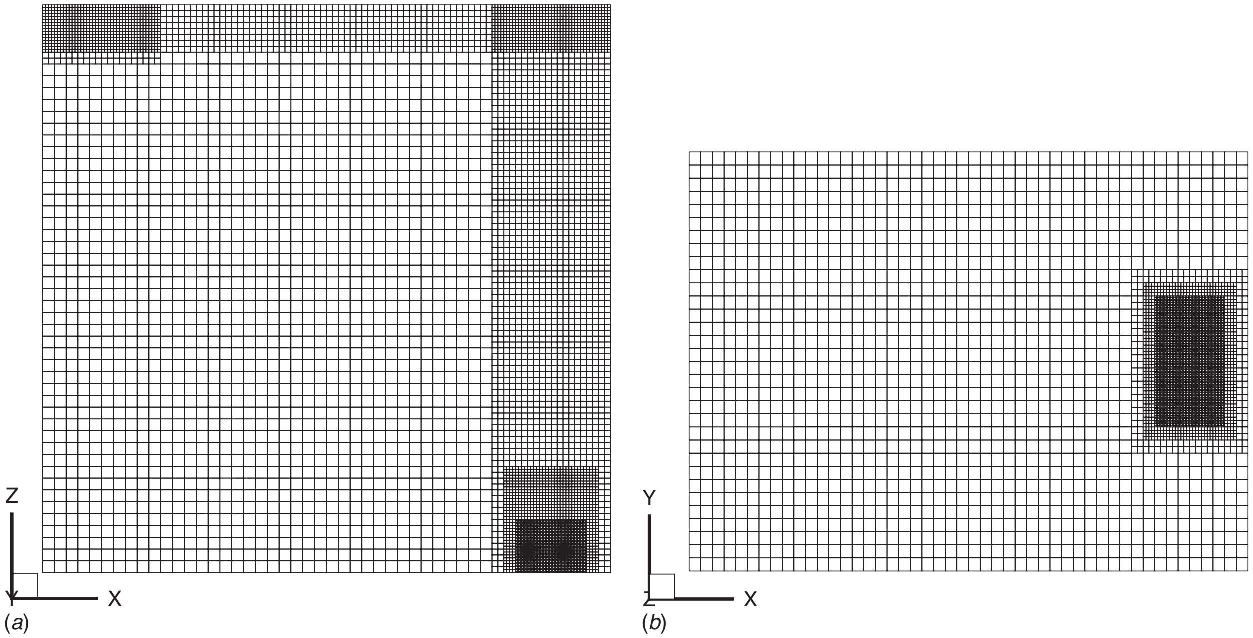

Fig. 2 Computational grid for the Indoor Flowfield Laboratory Chamber: (*a*) side (*x*-*z* plane) and (*b*) top (*x*-*y* plane) views of the baseline grid

This approach, while accurate, is too expensive to be used in engineering applications. A more practical approach is to superimpose random noise perturbations on mean velocity profiles obtained from a separate RANS simulations [37]. This approach can lead to stability problems due to the unphysical randomness of the perturbations that depend on the time step [38]. A similar approach is to use random perturbations to generate inlet turbulence with predefined characteristics. Using this technique, Lee et al. [39] built a realistic turbulence spectrum using Fourier modes with random phase shifts. This method can, however, result in an artificial transition region between the prescribed turbulent field and the solution of NS equations inside the domain [40]. FLUENT supports two techniques for generating time-dependent inlet conditions for LES. The first technique is the random flow generation (RFG) technique developed by Smirnov et al. [40]. This technique generates a divergence-free, inhomogeneous, and anisotropic flow field with predefined correlation coefficients. This method requires the specification of the anisotropic velocity correlation tensor, length, and time scales of the turbulence that may be obtained from a RANS simulation or high-resolution experimental data. The spatial and temporal variations of the resulting velocity field follow a Gaussian spectrum with the specified length and time scales. Smirnov et al. [40] successfully applied this technique to the simulation of ship wakes. The ship hull part of the domain was simulated using a RANS calculation. The resulting anisotropic field was then used as an inflow plane to the wake part of the domain, which was simulated with LES. The length and time scales required by the RFG were deduced from the length scales predicted by the RANS. The RFG is a more realistic representation of the turbulence than a simple Gaussian distribution of velocity as it guarantees that the resulting velocity field satisfies the continuity and anisotropy constraints. The RFG, however, does not guarantee that the resulting field satisfies the momentum equations and is thus an approximate method [40]. The second technique for inlet turbulence generation in FLUENT is the vortex method developed by Mathey et al. [41]. With this approach, a perturbation is added to the specified mean velocity profile via a fluctuating vorticity field (two-dimensional in the plane normal to the mean-flow direction). The use of this method requires the specification of the mean turbulent kinetic energy and dissipation rate profiles at the inlet of the computational domain [30]. The accuracy of this method has been investigated using several test cases [38] such as turbulent channel and pipe flows and the flow over periodic hills. The flow over periodic hills represents a case where the dynamics of the flow are controlled to a great extent by the level of upstream turbulence. Mathey et al. [41] compared two approaches for specifying the inlet turbulence with a reference simulation in which periodic boundary conditions were used. In the first test simulation, the vortex method was used to generate the inlet boundary conditions and in the second test simulation random noise was used. They found that the random noise simulation overestimated the re-attachment length by 50% and underestimated the spreading rate of the shear layer. They also found that the random noise underestimated the turbulence level inside the shear layers by one order of magnitude. They explained these results by the low level of kinetic energy in the random noise simulation due to the damping of the nonphysical random fluctuations at the inlet. This demonstrated the importance of the upstream history of the turbulence on the subsequent production mechanisms and thus the sensitivity of the turbulence to the accuracy of the inlet boundary conditions [38]. We therefore selected FLUENT's built-in vortex method to generate the time-dependent inlet conditions.

4 Results and Discussion

We begin by showing a comparison of solutions on the refined and the baseline grids to demonstrate that the solution on the baseline grid is spatially converged. On this basis, the baseline grid is used for all the subsequent computations. The effect of the turbulence level at the inlet is studied assuming a uniform mean velocity profile and three levels of isotropic turbulence at the inlet. Then, the 13% inlet turbulence case with uniform mean profiles is compared with the case using the measured inlet velocities and turbulence intensities to determine the significance of the detailed profiles at the inlet. We also compare the performance of different modeling approaches: the constant coefficient Smagorinsky subgrid-scale model and the dynamic model for the 13% case with uniform inlet profiles, and the constant coefficient model with the k-ϵ model at 0% and 13% inlet turbulence intensity.

4.1 Grid Convergence Study. The grid resolution for LES should be sufficient to resolve the bulk of the turbulent kinetic

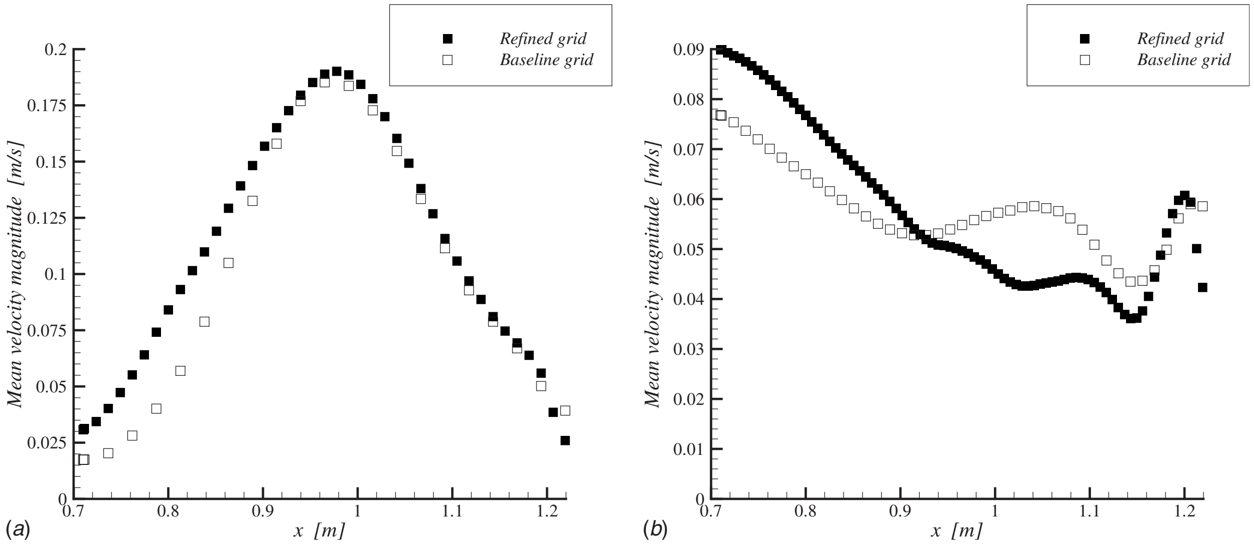

Fig. 3 Comparison of mean velocity magnitude on the baseline and the refined grids at (*a*) $z/L=-0.2$ and (*b*) $z/L=0.9375$

energy. If this is achieved, LES should be at most weakly dependent on the particular subgrid-scale model used in the computations. In FLUENT, the mixing length for the subgrid scales L_s and the subgrid-scale eddy viscosity $\nu_t=\mu_t/\rho$ are used to construct an estimate for the subgrid-scale turbulent kinetic energy k_s defined as

$$k_s=\frac{\nu_t^2}{L_s^2} \tag{16}$$

which is referred to by FLUENT as the "subtest kinetic energy." Figures 3 and 4 compare the mean and root mean square (rms) of the velocity magnitude obtained from the solutions on the baseline and the refined grids. It is seen that the shapes of the profiles agree reasonably well and that the deviations are generally small, reaching a maximum of about 30%. It is also seen that the deviations at the stations closest to the inlet (Fig. 3(*a*) and 4(*a*) at $z/L=-0.2$) occur predominantly in the shear layers. Figure 5 also compares the turbulent kinetic energy obtained from the solutions on the two grids including the subgrid-scale contributions. It is clear that on the refined grid the subtest kinetic energy is less than 5% of the total turbulent kinetic energy, except very near the inlet, so the solution on this grid is judged to be well resolved. The subtest kinetic energy on the baseline grid is somewhat larger, but still small enough relative to the total turbulent kinetic energy that we judge the solution on the baseline grid to be adequately resolved for the subsequent computations. This conclusion is supported by the earlier comparison of the mean and rms profiles shown in Figs. 3 and 4.

4.2 Effect of Inlet Turbulence Level Using Plug-Flow Inlet Conditions. Figures 6(*a*) and 6(*b*) show the contour plots of the instantaneous and mean velocity magnitudes, respectively, along the vertical *x*-*z* plane passing through the middle of the inlet for the 0% inlet turbulence intensity case. It is clear that the jet in this case is very confined and that there is little mixing with the room air. The jet flows straight up toward the ceiling, bends 90 deg, and flows along the ceiling until it reaches the exit. Other than this basic flow pattern, there are no significant organized motions or

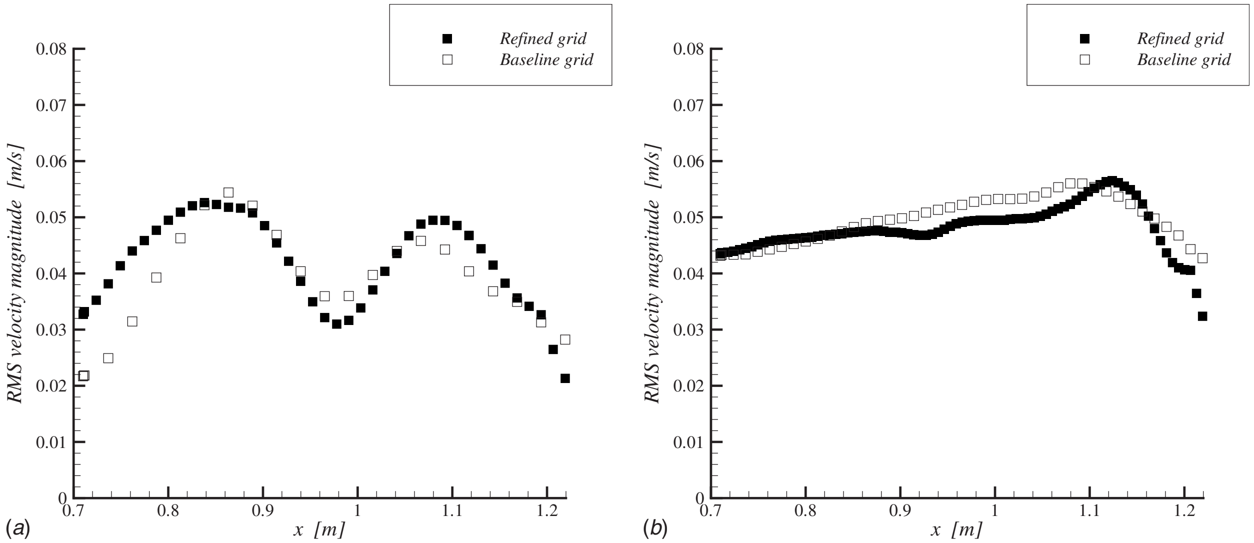

Fig. 4 Comparison of the rms of the velocity magnitude on the baseline and the refined grids at (*a*) $z/L=-0.2$ and (*b*) $z/L=0.9375$

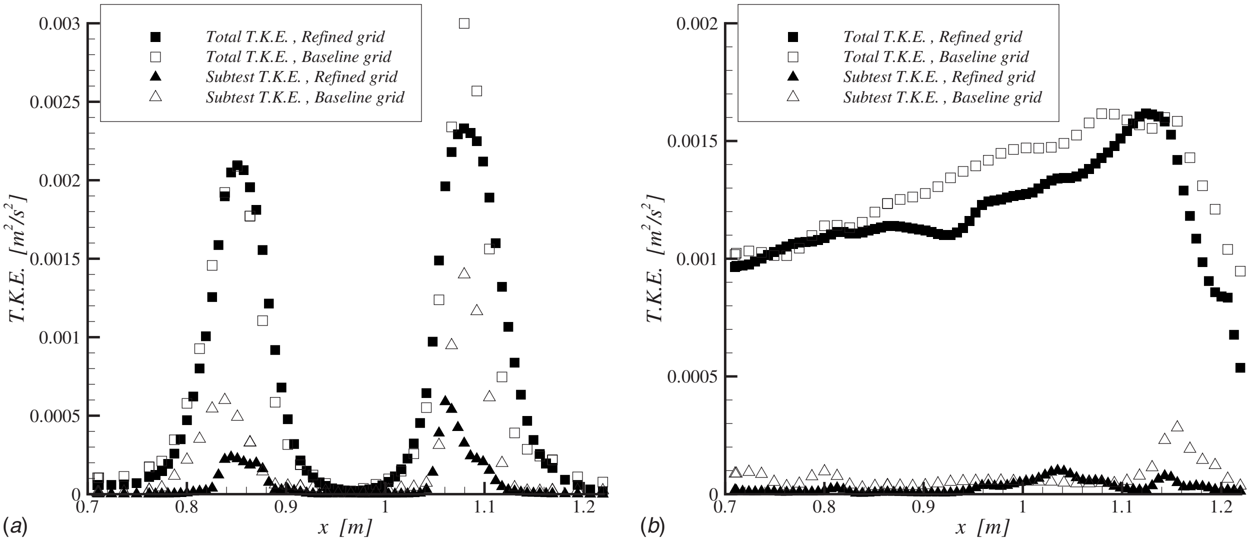

Fig. 5 Comparison of turbulent kinetic energy on the baseline and the refined grids at (*a*) $z/L=-0.8$ and (*b*) $z/L=0.9375$

circulation patterns in the room. The figures for the instantaneous and mean velocities are also reasonably similar, especially near the inlet, suggesting that the levels of turbulence are quite low. Near the ceiling, however, the jet has spread enough to interact with the front wall, generating turbulence there and in the ceiling's boundary layer. A complicated unsteady flow pattern, dominated by eddying motions, is observed in the ceiling's stagnation layer.

Figures 7 and 8 show the corresponding contour plots for the cases of 5% and 13% inlet turbulence intensity. It is seen in both cases that the jet spreads and mixes with the room air more rapidly and starting closer to the inlet than in the laminar inflow case. The mean flow, however, is still generally confined to a vertical column around the inlet and a horizontal slab along the ceiling, with only weak circulation elsewhere in the room. The reason for the more rapid mixing and spreading of the jet, and the increased levels of turbulence relative to the laminar inflow case is that the inlet jet, seeded with turbulence, undergoes a more rapid transition to a turbulent jet than the laminar inflow case. Figures 7 and 8 show significant similarity between the 5% and 13% turbulence intensity cases in both the mean and the instantaneous flow velocity magnitudes. It is also noted that the instantaneous contours in both cases are characterized by the intermittent breaking-off of blobs of high velocity fluid from the jet core that increase the local levels of turbulence as they sweep through the domain.

The above observations can be seen more quantitatively by looking at profiles of the mean velocity magnitude and the rms of the velocity fluctuations for the different levels of the inlet turbulence intensity. Figures 9 and 10 compare the profiles of the mean velocity magnitude at stations located at $z/L=-0.4$, $z/L=0.0$, and $z/L=0.75$, plotted along the horizontal lines extending from $x=0.71$ m all the way to the front wall, along the center of the inlet ($y=0$). As can be seen, the mean velocity profiles in the 5% and 13% cases are quite similar, exhibiting nearly the same spreading rate. This is consistent with the notion that, beyond a threshold level of the inlet turbulence intensity, the subsequent development of the jet is only weakly dependent on the inlet conditions. It is also noted that the profiles of the 5% and 13% cases exhibit significant asymmetry due to the front wall. The laminar inflow case, in contrast, has nearly symmetric profiles up until $z/L=0.75$, where the jet has spread enough to interact with the wall, causing an asymmetry of the profile to develop.

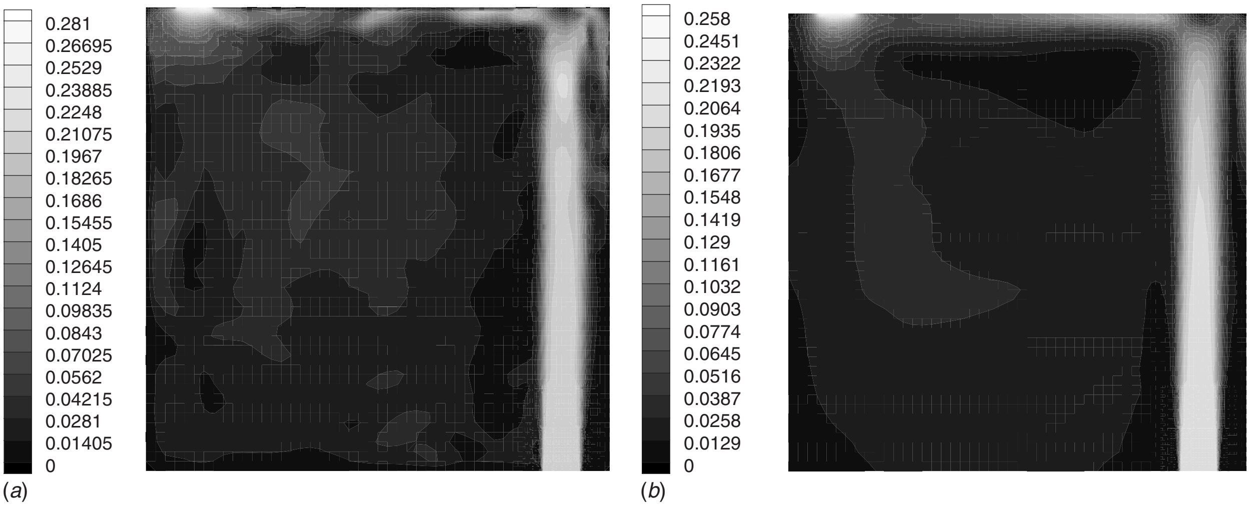

Fig. 6 (*a*) Instantaneous and (*b*) mean velocity contours on center plane; 0% inlet turbulence (units are in m/s)

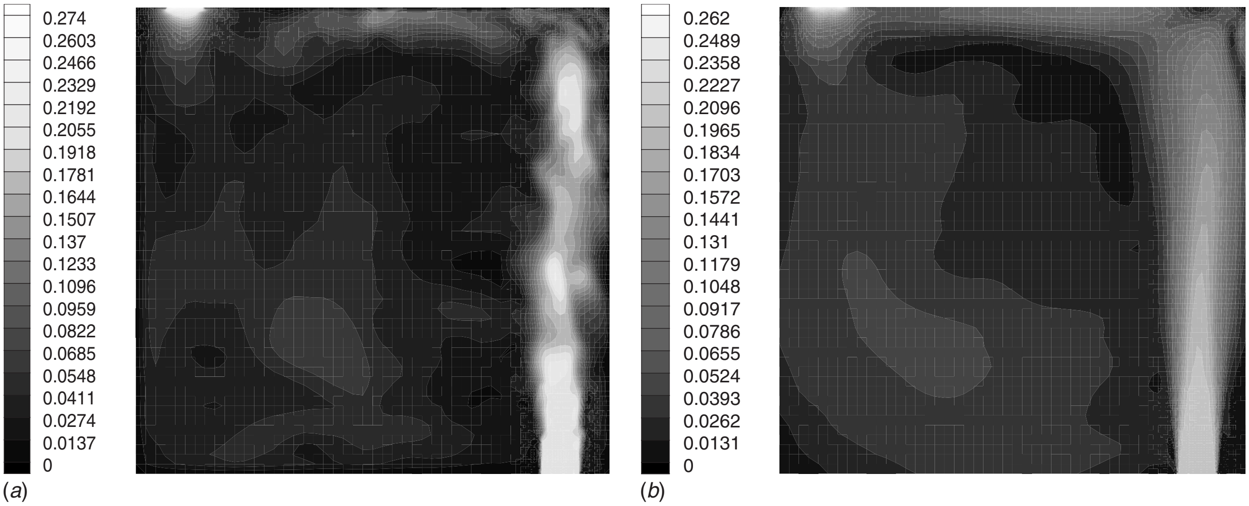

Fig. 7 (*a*) Instantaneous and (*b*) mean velocity contours on center plane; 5% inlet turbulence (units are in m/s)

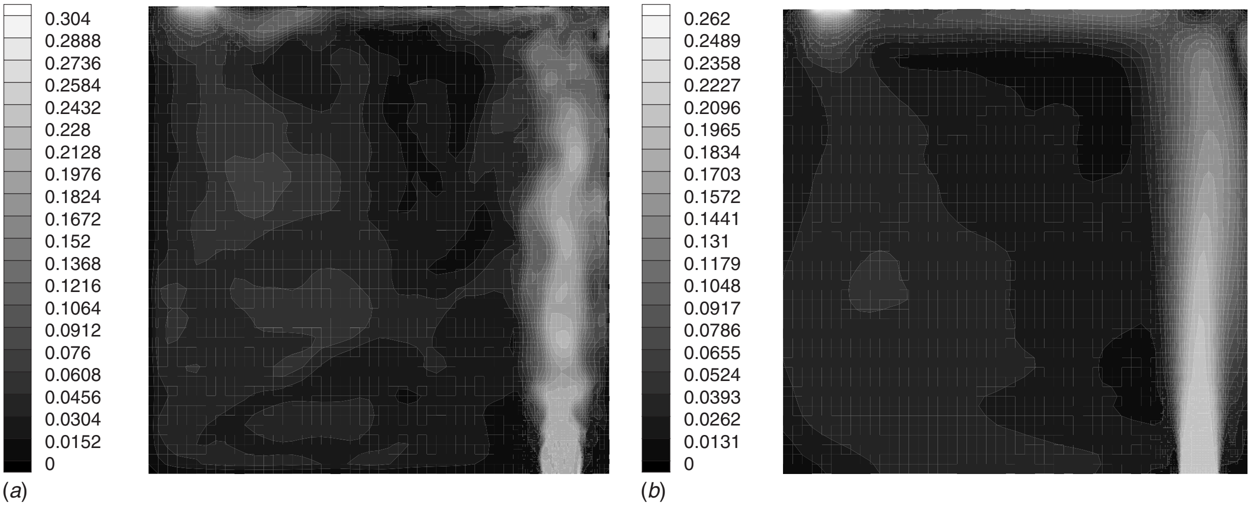

Fig. 8 (*a*) Instantaneous and (*b*) mean velocity contours on center plane; 13% inlet turbulence (units are in m/s)

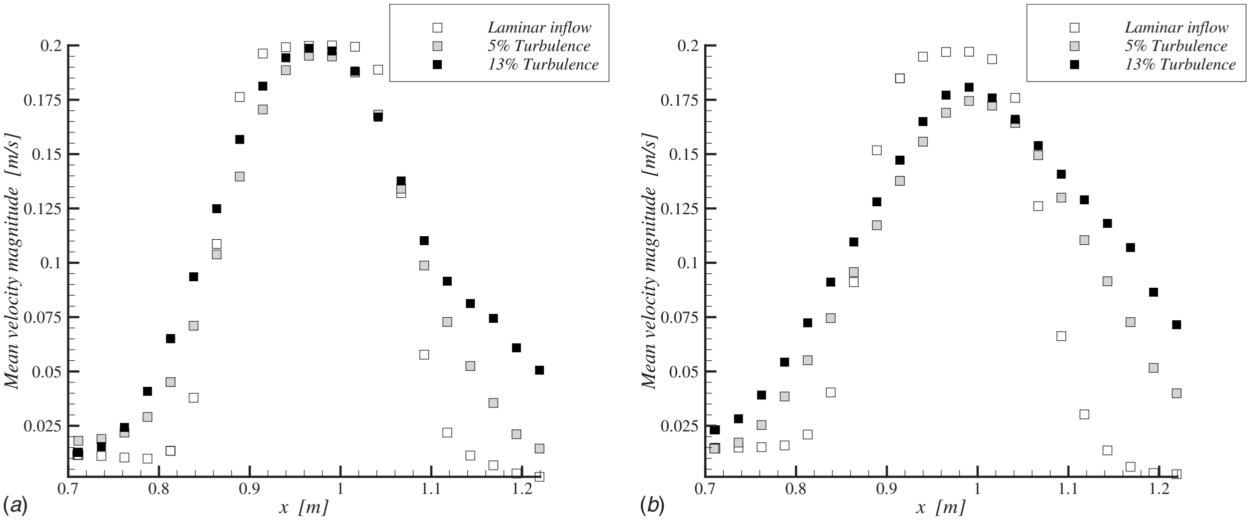

Fig. 9 Comparison of the mean velocity magnitude for three levels of inlet turbulence intensity at (*a*) $z/L=-0.4$ and (*b*) $z/L=0.0$; baseline grid

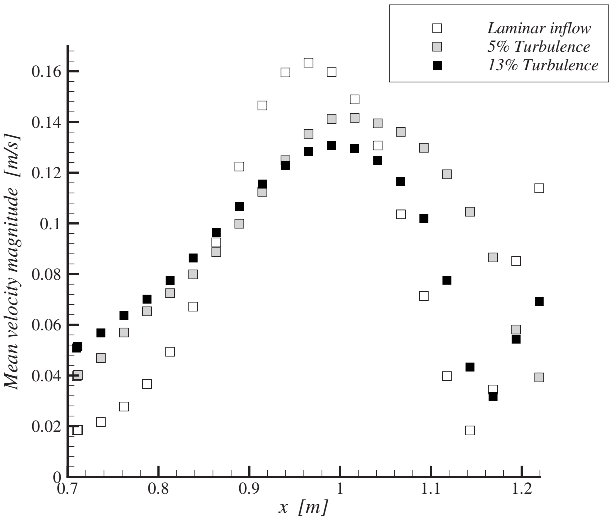

Fig. 10 Comparison of the mean velocity magnitude for three levels of inlet turbulence intensity at $z/L=0.75$; baseline grid

Profiles of the velocity rms are shown in Figs. 11 and 12. Once again the 5% and 13% cases show quite similar profiles throughout the computational domain. The behavior of the laminar inflow case needs some elaboration. At the $z/L=-0.4$ and $z/L=0.0$ stations, the level of turbulence is significantly less than for the 5% and 13% cases because of the laminar state of the entering jet. However, near the ceiling, the shear layers have grown enough to begin to interact with the front wall and turbulence is generated there and also in the ceiling's boundary layer. The contours in Fig. 6 show the generation of a blob of high velocity fluid near the ceiling, which can contribute to the high levels of turbulence near the ceiling. Accordingly, the rms levels of the velocity fluctuations in the laminar inflow case are seen to be higher than the rms levels for the 5% and 13% cases near the ceiling (see Figs. 11 and 12).

The significant differences between the simulation results for the 0% and both the 5% and 13% cases cannot be captured by the standard k-ϵ model, which is designed primarily for fully developed turbulent flows. This very fact led Loomans [42], who investigated the effect of inlet turbulence intensity level on the flow field of a displacement ventilation system in a full-scale room using the standard k-ϵ model, to conclude that the level of inlet

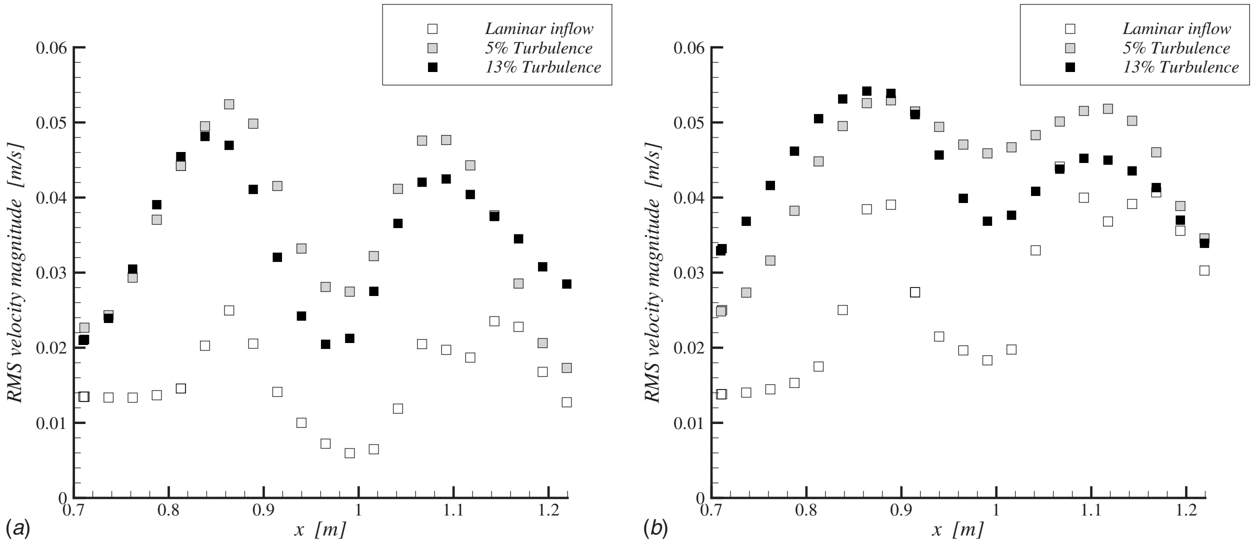

Fig. 11 Comparison of the rms velocity magnitude for three levels of inlet turbulence intensity at (*a*) $z/L=-0.4$ and (*b*) $z/L=0.0$; baseline grid

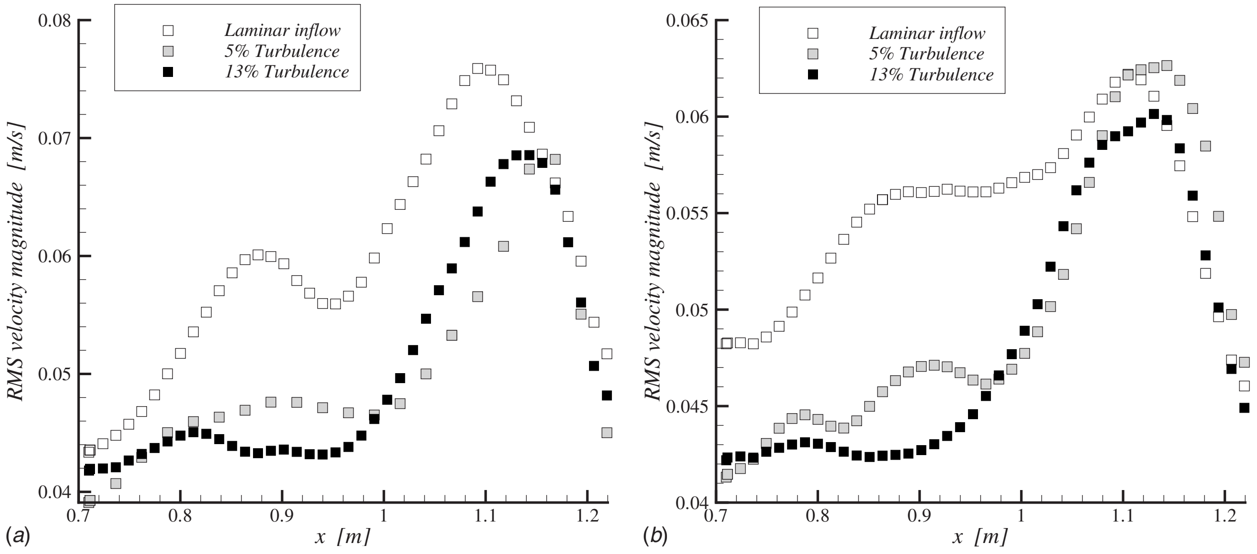

Fig. 12 Comparison of the rms velocity magnitude for three levels of inlet turbulence intensity at (*a*) $z/L=0.875$ and (*b*) $z/L=0.9375$; baseline grid

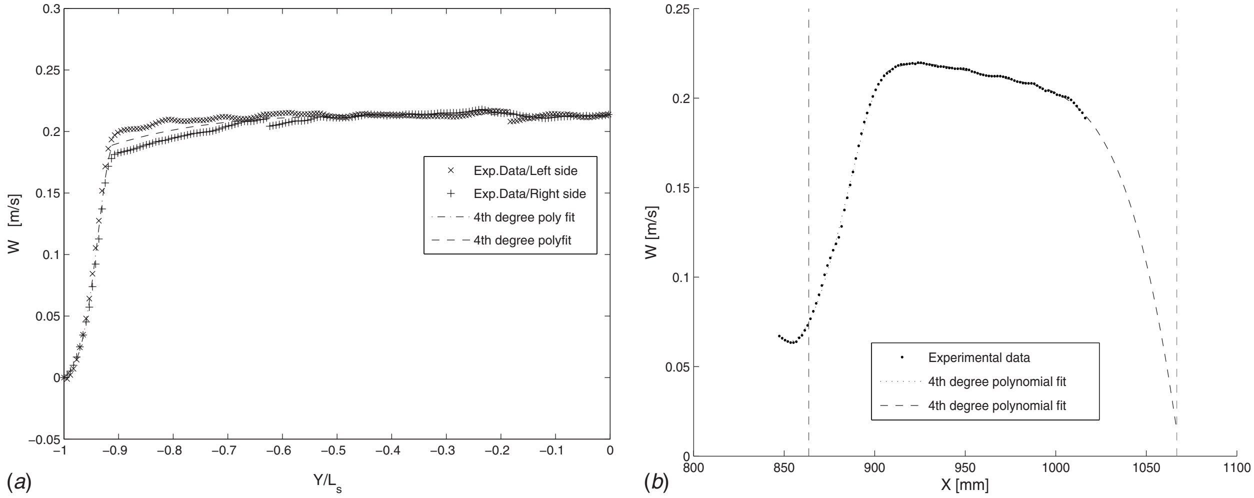

Fig. 13 Experimental data and curve fits along the (*a*) long and (*b*) short sides of the inlet. In (*a*), L_s is the half-length of the inlet section.

turbulence has a negligible effect on the flow field especially far from the inlet. As we will demonstrate, the standard k-ϵ model is insensitive to the level of inlet turbulence intensity and accordingly cannot be used to accurately predict the flow behavior for situations wherein the flow is most probably transitional in nature. It is also noted that the levels of inlet turbulence intensities investigated by Loomans were 10% and 35% and accordingly the flow was most probably fully developed even for the lower value. Using the k-ϵ model for the simulation of a jet in a two-dimensional cavity with inlet turbulence intensities of 4–37.4%, Joubert et al. [43] also concluded that the effect of the inlet turbulence intensity on the flow field was negligible.

The LES results for the 5% and 13% cases are consistent with the study of Jiang [44] who used LES and the standard k-ϵ model to investigate the effects of inlet boundary conditions on the flow field in a full-scale room. At the highest studied ventilation rate of 19.5 air change per hour (ACH), corresponding to an inlet mean velocity of 1.43 m/s and a Reynolds number of 4895, Jiang investigated three cases: (1) uniform inlet velocity profile and uniform turbulence intensity of 10%, (2) profiled velocity and turbulent kinetic energy from hot wire measurements, and (3) experimental velocity profile and uniform inlet turbulence intensity of 10%. In LES, the turbulence at the inlet was generated using a random number generator technique. The author concluded that the effect of inlet conditions on the flow field is confined to the vicinity of the inlet and negligible elsewhere in the flow field. Although the average level of inlet turbulence intensity in case (2) could not be inferred, the high ventilation rate/Reynolds number used in this study indicate that the flow was fully developed in nature. Our LES simulation with laminar inflow conditions shed some light on the potentially significant differences between simulations at low levels of inlet turbulence and those with high enough levels of inlet turbulence to cause the flow to rapidly reach a fully developed state. The existence of a threshold inlet turbulence level, above which the flow becomes independent of the inlet turbulence level, is a hypothesis that requires further investigation.

4.3 Effects of Realistic Inlet Flow Conditions. Here we consider the importance of the detailed mean and turbulence profiles at the inlet on the flow inside the room. We replace the idealized inlet velocity profile used in Sec. 4.2 by the experimentally measured inlet conditions. The first stage of utilizing the PIV experimental data obtained at Syracuse University [45] in our simulations involved interpretation of the data, which contained artifacts from the measurement technique and experimental noise. In addition, data could not be obtained for that part of the inlet closest to the front wall, due to distortions and reflections from the glass wall; consequently, assumptions had to be made about the profiles of the measured quantities. The experimental data consist of the mean values of the three components of velocity and the rms of their fluctuations. The mean velocity components in the plane of the inlet, i.e., the U and V components, were deemed small enough to neglect, whereas the vertical component W of the velocity was fitted to a smooth polynomial. The variations parallel to the long side of the inlet were not as significant as those across the short side, and a fit of the averaged experimental data on both sides was used. Figure 13(*a*) shows two fourth-order polynomials (one covering most of the profile and one representing the shear layer portion). In the direction of the short side, the interpretation of the data was complicated by the fact that part of the inlet was not covered by the measurement window; hence this part of the data was missing. We extrapolated the missing data using two, fourth-order, polynomials that represent the profile, including the missing segment, as shown in Fig. 13(*b*). The turbulent kinetic energy and the root mean square of the fluctuating velocities were assumed symmetric across the short side of the duct, with negligible variation in the direction of the long side, as shown in Fig. 14 (which shows only half of the profile since it is assumed symmetric).

FLUENT calculations with these fitted inlet profiles were run and compared with the 13% case with uniform profiles. Figures 15 and 16 show comparisons of the mean velocity at four vertical stations. Note that the significant differences at the lowest station ($z/L=-0.8$) become weaker with increasing distance from the inlet. The maximum deviation between the two cases occurs in the shear layers, where the deviation of the measured inlet turbulent kinetic energy from the spatially averaged value is greatest. This suggests that there is some memory of the inlet conditions throughout the flow.

Similar behavior of the rms of the velocity is shown in Figs. 17 and 18, where close to the inlet (at the $z/L=-0.8$ and $z/L=-0.4$ stations) the profiles are significantly different, whereas close to the ceiling, the two cases predict similar levels of turbulence (notice the offset of the origin of the vertical axis in Fig. 18 amplifies the small differences between the profiles). So in general the flow field exhibits sensitivity to the inlet flow conditions primarily near the inlet. As the flow evolves spatially, the effect of the inlet conditions becomes less pronounced. This conclusion is in agreement with Jiang's [44] conclusions from his LES and k-ϵ model calculations for similar comparisons. Joubert et al. [43] also reported that using a parabolic inlet velocity profile as opposed to a

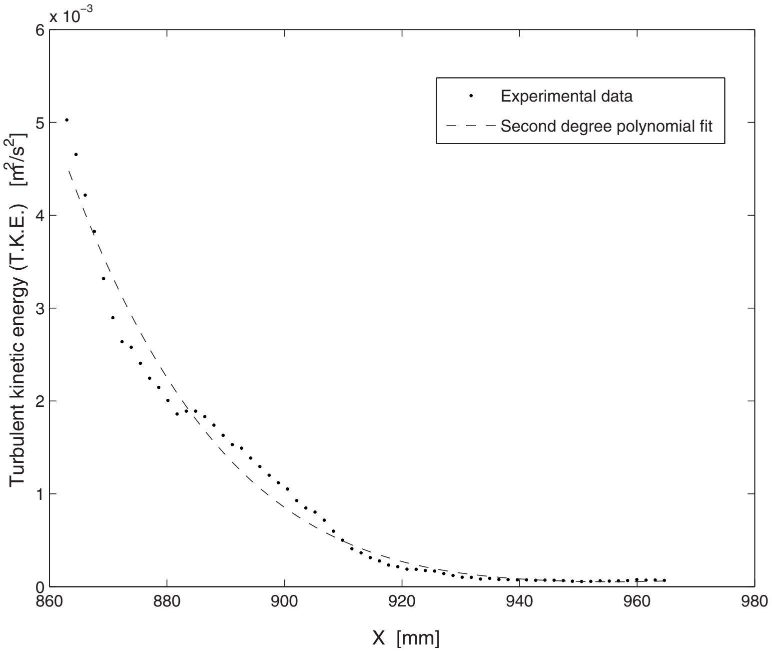

Fig. 14 Fitted profile of the turbulent kinetic energy

uniform profile does not affect the mean velocity in the two-dimensional cavity flow that they analyzed with the k-ϵ model; however, they found significant differences in the predicted levels of turbulence in the cavity, which they explained on the basis of the contribution of the shearing already present in the inflow in the parabolic profile case. It should be noted that the wall jet studied in their two-dimensional simulation is fundamentally different from the present configuration. The close proximity of the jet to the top boundary may have caused the greater sensitivity. They also noted that the width of the slot has an important effect on the turbulence level within the cavity.

4.4 Comparison of the Constant Coefficient and Dynamic Smagorinsky LES Models.

The success of a subgrid-scale model can be characterized by how well it predicts the large-scale statistics of a given turbulent flow. It is to be expected that the results should be relatively insensitive to the subgrid-scale model if the large-scale, energy-containing, turbulent motions are sufficiently resolved. The dynamic model adjusts the coefficient C_s locally in space and time based on the resolved scales. In this way, the model responds to changes in the large-scale turbulent motions, and thus it tends to be self-correcting in the sense that it adjusts the eddy viscosity coefficient based on the energy in the resolved scales. In this section, a comparison is made between the results obtained with the constant coefficient Smagorinsky subgrid-scale model and the dynamic model for the case of 13% inlet turbulence intensity, with uniform mean inlet profiles. Figures 19–22 compare the mean and the rms of the velocity magnitudes obtained from the constant coefficient and the dynamic model in both the

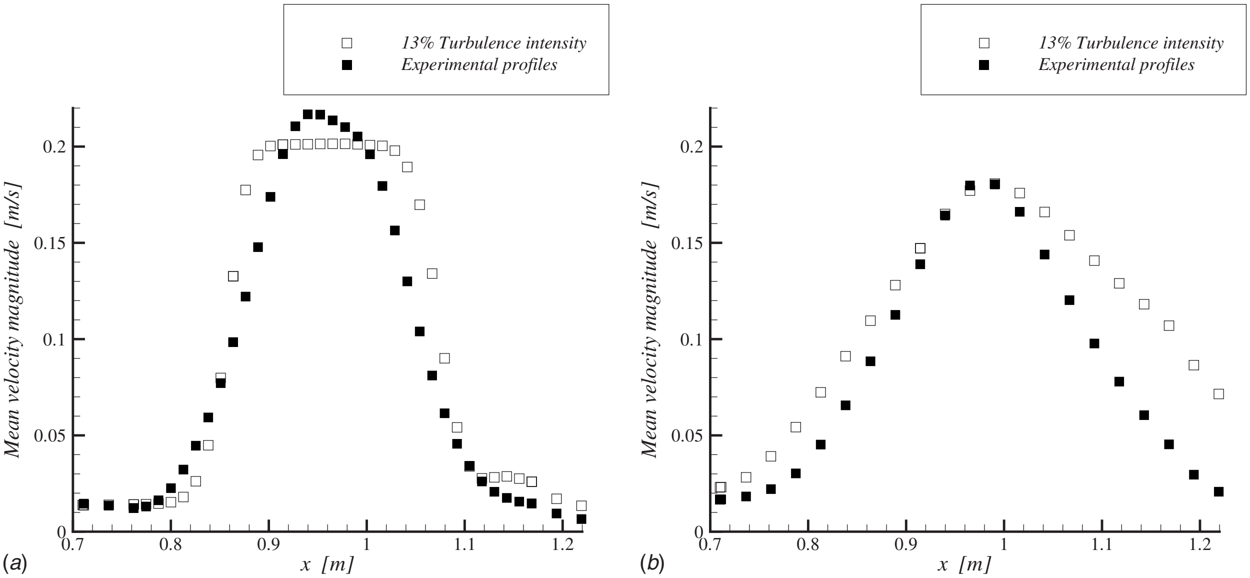

Fig. 15 Mean velocity magnitude at (*a*) $z/L=-0.8$ and (*b*) $z/L=0.0$; comparison of results with plug flow and experimentally determined inlet conditions

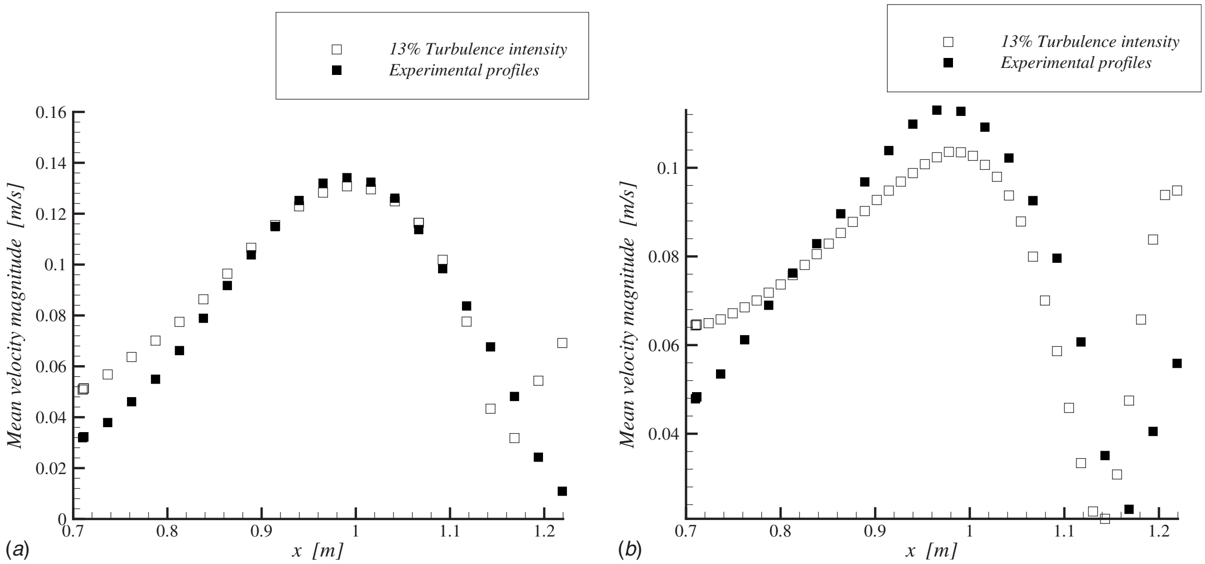

Fig. 16 Mean velocity magnitude at (*a*) $z/L=0.75$ and (*b*) $z/L=0.875$; comparison of results with plug flow and experimentally determined inlet conditions

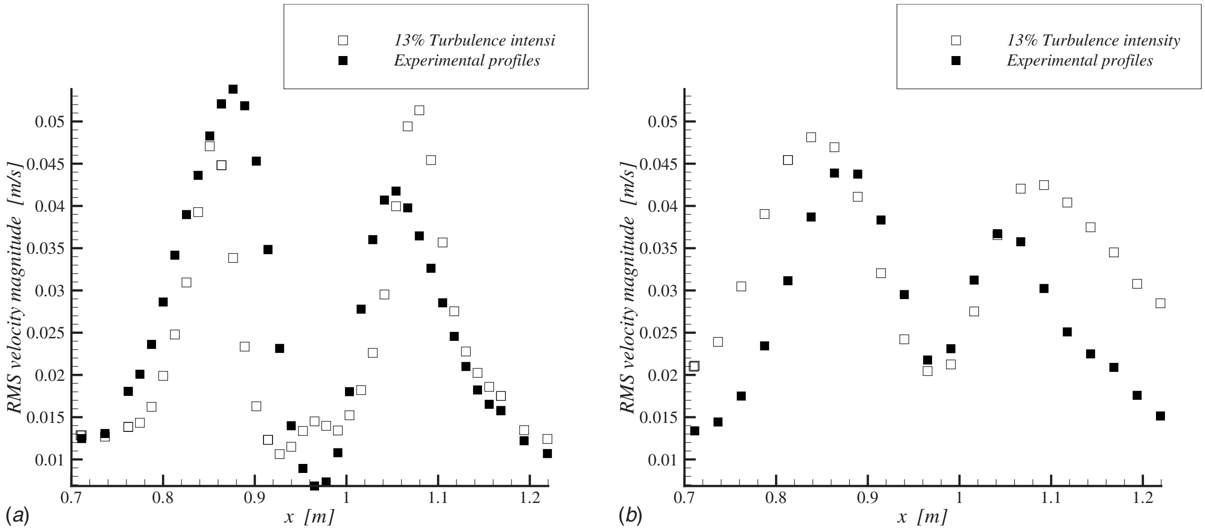

Fig. 17 rms velocity magnitude at (*a*) $z/L=-0.8$ and (*b*) $z/L=-0.4$; comparison of results with plug flow and experimentally determined inlet conditions.

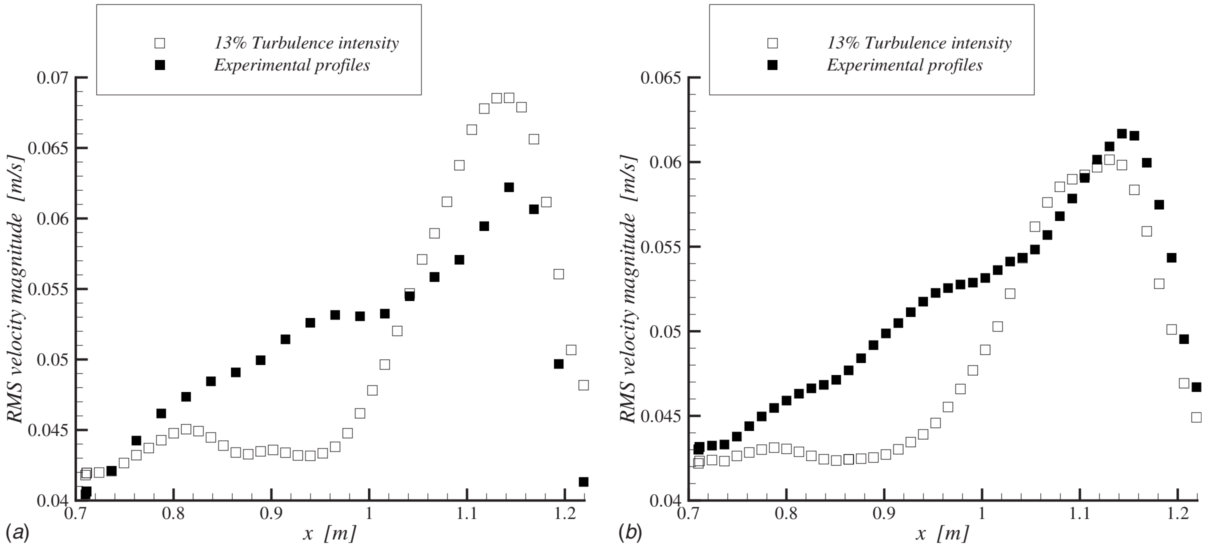

Fig. 18 rms velocity magnitude at (*a*) $z/L=0.875$ and (*b*) $z/L=0.9375$; comparison of results with plug flow and experimentally determined inlet conditions

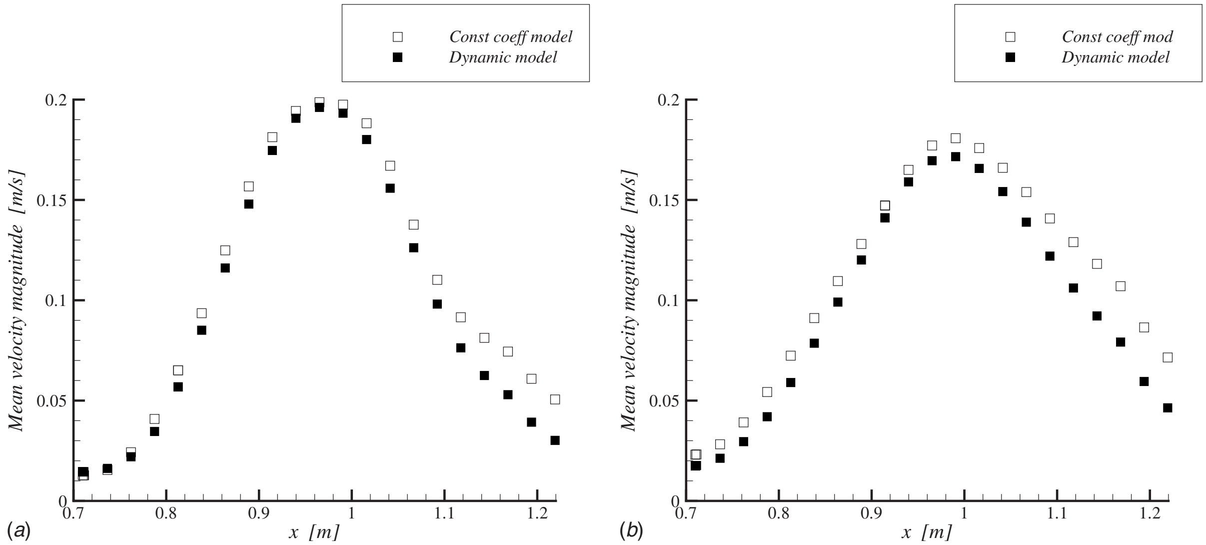

Fig. 19 Mean velocity magnitude at (*a*) *z*/*L*=−0.4 and (*b*) *z*/*L*=0.0; comparison of results using constant-coefficient and dynamic Smagorinsky models

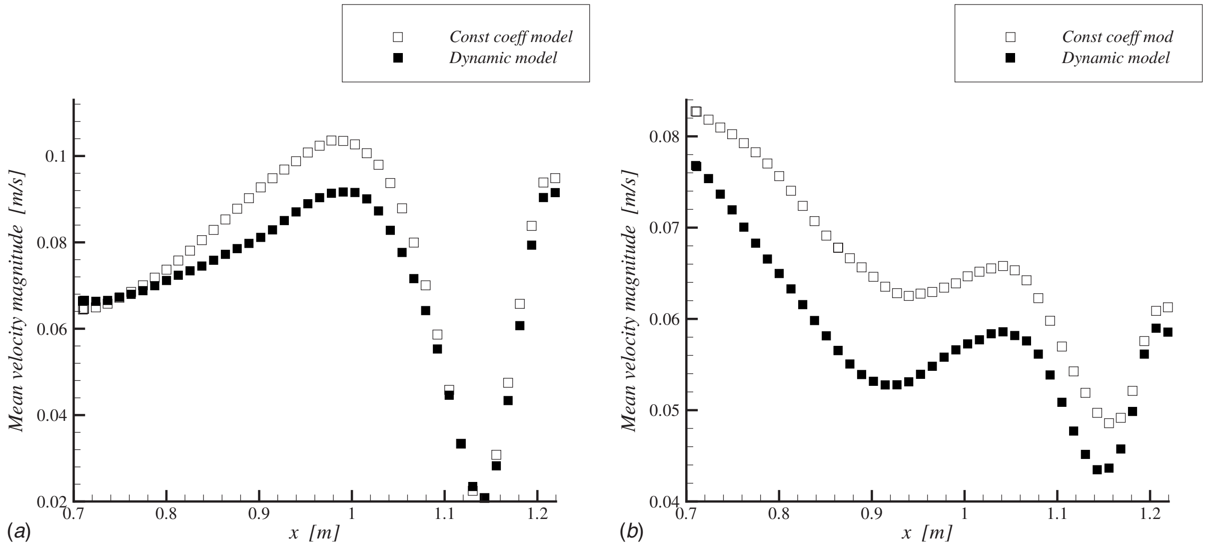

Fig. 20 Mean velocity magnitude at (*a*) *z*/*L*=0.875 and (*b*) *z*/*L*=0.9375; comparison of results using constant-coefficient and dynamic Smagorinsky models

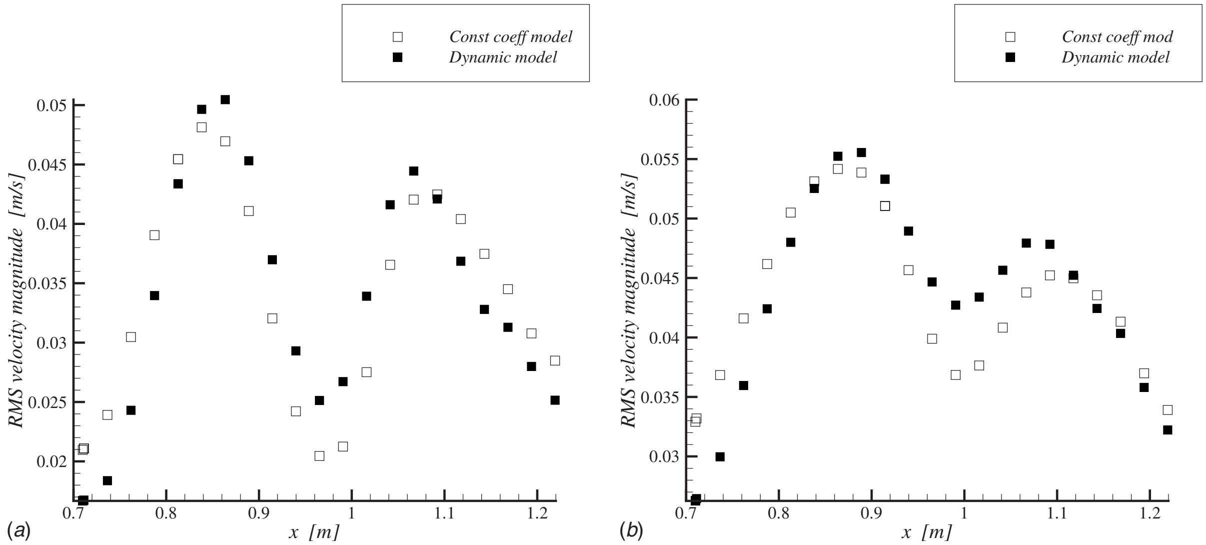

Fig. 21 rms velocity magnitude at (*a*) *z*/*L*=−0.4 and (*b*) *z*/*L*=0.0; comparison of results using constant-coefficient and dynamic Smagorinsky models

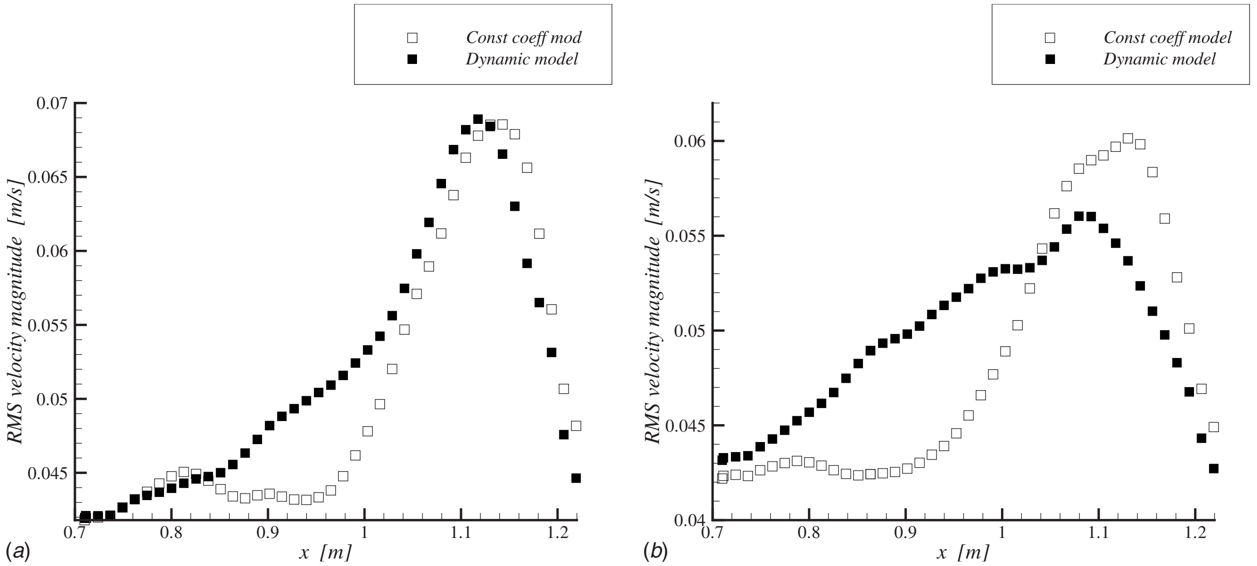

Fig. 22 rms velocity magnitude at (*a*) $z/L=0.875$ and (*b*) $z/L=0.9375$; comparison of results using constant-coefficient and dynamic Smagorinsky models

near- and the far-field of the jet. Maximum deviations of about 20–30% in the mean velocity magnitude occur near the inlet (where the largest dissipation rates are concentrated), at the $z/L=-0.4$ and $z/L=0.0$ stations (notice the origin offset in the plots near the ceiling, Figs. 20 and 22). Further from the inlet, as the jet loses its strength, maximum deviations of about 10–15% are seen at the $z/L=0.875$ and $z/L=0.9375$ stations (see Figs. 19 and 20). Similar behavior of the rms of the velocity magnitude is observed in Figs. 21 and 22, where at the $z/L=-0.4$ and $z/L=0.0$ stations, the maximum deviations are about 20%, whereas at the $z/L=0.875$ and $z/L=0.9375$ stations, the deviations are about 10–15%. The differences described above are expected, as it was shown that the subgrid-scale contribution to the total turbulent kinetic energy is largest near the inlet and smallest near the ceiling (see Fig. 5(*a*) and 5(*b*)). These results demonstrate that the constant coefficient model agrees reasonably well with the dynamic model, at least for the low-order statistics of the flow. This weak dependence on the subgrid-scale model reflects the fact that the large energy-containing scales of motion are well resolved.

4.5 k-ϵ Model Predictions at Low Inlet Turbulence Levels. As already alluded to in Sec. 4.2, significant flow field differences can potentially exist between the LES and the standard k-ϵ model predictions when the flow is slowly developing in space or time. In this section, we have systematically studied these model differences for the two extreme levels of inlet turbulence, i.e., 0% and 13%. For the 0% inlet turbulence case, LES predicts that the flow develops slowly in space and, accordingly, the flow field is a mixed laminar and turbulent state. For the 13% case, the jet rapidly transitions to a fully developed turbulent state close to the inlet. Figures 23 and 24 compare the mean velocity magnitude and turbulent kinetic energy from two simulations using the standard k-ϵ model with 0% and 13% inlet turbulent levels, respectively. It is seen that the solution is nearly insensitive to the level

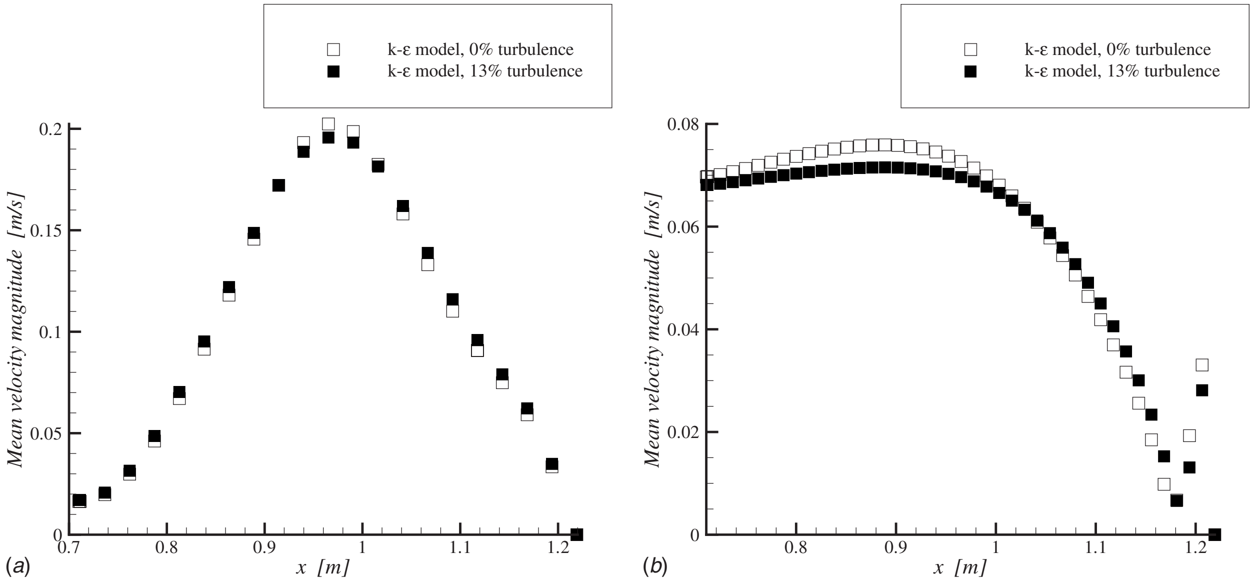

Fig. 23 Mean velocity magnitude from k-ϵ model at (*a*) $z/L=-0.6$ and (*b*) $z/L=0.875$

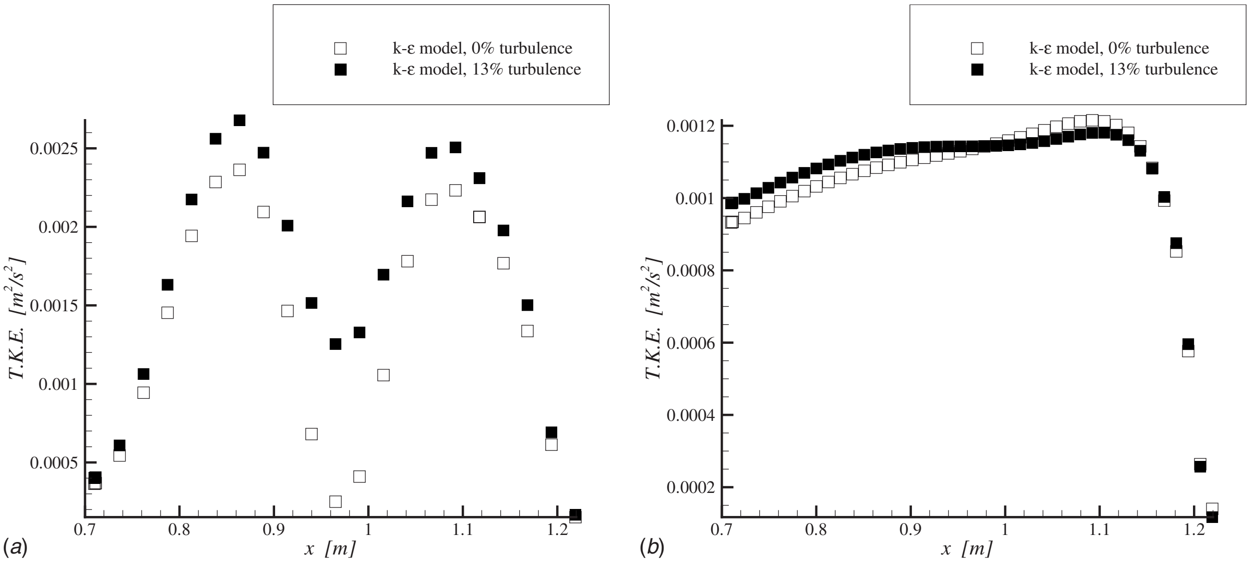

Fig. 24 Turbulent kinetic energy from k-ϵ model at (*a*) $z/L=-0.6$ and (*b*) $z/L=0.875$

of inlet turbulence especially far from the inlet. The slow development of the jet predicted by LES in the 0% case is not observed with the k-ϵ model. To emphasize this point, we compare the solution from the k-ϵ and LES, using the constant coefficient model, at 0% and 13% inlet turbulent levels. Figure 25 shows the comparison for the mean velocity magnitude profile very close to the inlet ($z/L=-0.8$) at 0% and 13% inlet turbulent intensities. At 0% turbulence intensity, LES is predicting a flat velocity profile with a sharp gradient separating the potential core from the quiescent fluid outside. The k-ϵ model, in contrast, predicts a much more diffuse profile with curved shape similar to the profile for a fully developed free jet. The two model predictions are in better agreement at the 13% turbulence intensity, as the turbulence is more nearly fully developed leading both models to predict a smoother profile. The inability of the k-ϵ model to predict the slow development of the jet at 0% inlet turbulence intensity leads to an overprediction of the spreading rate. As discussed in Ref. [2], a well-known deficiency of the k-ϵ model is that it significantly overpredicts the rate of spreading for the round jet. Although these differences could be reduced by adjusting the value of $C_{\epsilon 1}$ or $C_{\epsilon 2}$, we did not feel that this would be justified. Figure 26 shows the mean velocity profile at a location well removed from the inlet ($z/L=0.75$). The agreement between the LES and k-ϵ predictions is better at the 13% inlet turbulence intensity level. Nevertheless, it is clear that the k-ϵ model fails to capture the correct qualitative behavior near the upper right corner ($x \sim 1.22$ m), as it shows a nearly stagnant region, whereas the LES model predicts that there are small patches of intermittent activity in the corner. Figure 27 shows a comparison of the resolved turbulent kinetic energy from the LES model to the turbulent kinetic energy from the k-ϵ model at 0% and 13% inlet turbulent intensities. In the laminar inflow case, it is clear that LES is predicting the correct physical behavior of the jet close to the inlet where there is no active mechanism for turbulence generation yet at $z/L=-0.8$ as the shear layer thickness is close to zero and the jet

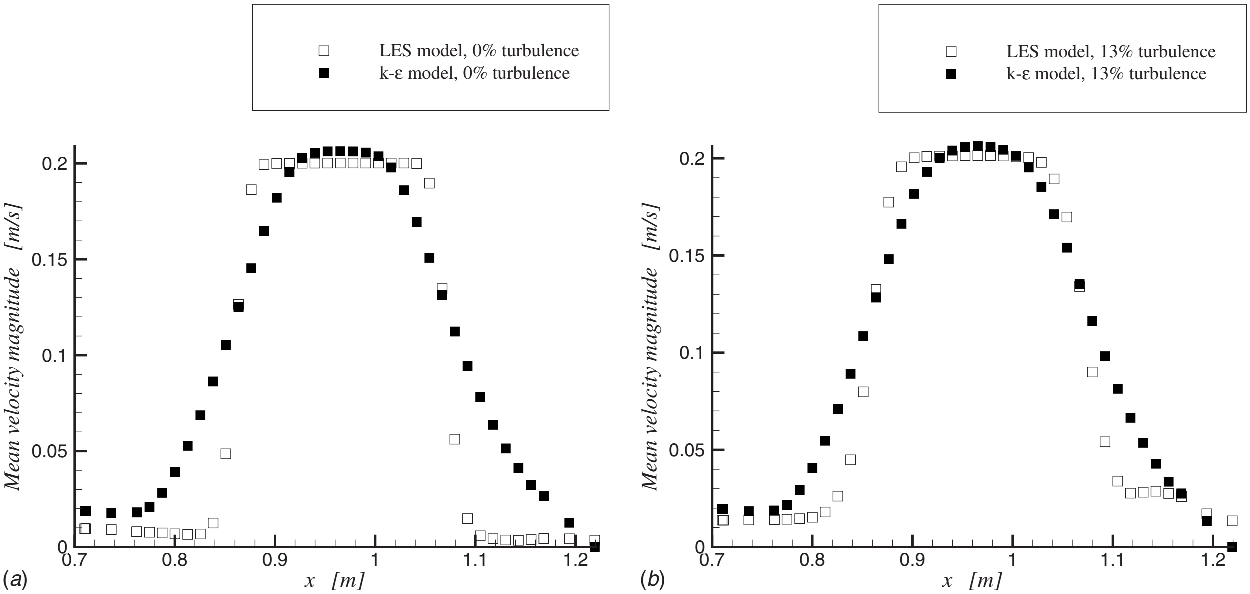

Fig. 25 Mean velocity magnitude from k-ϵ and LES models at $z/L=-0.8$: (*a*) 0% and (*b*) 13% inlet turbulence intensities

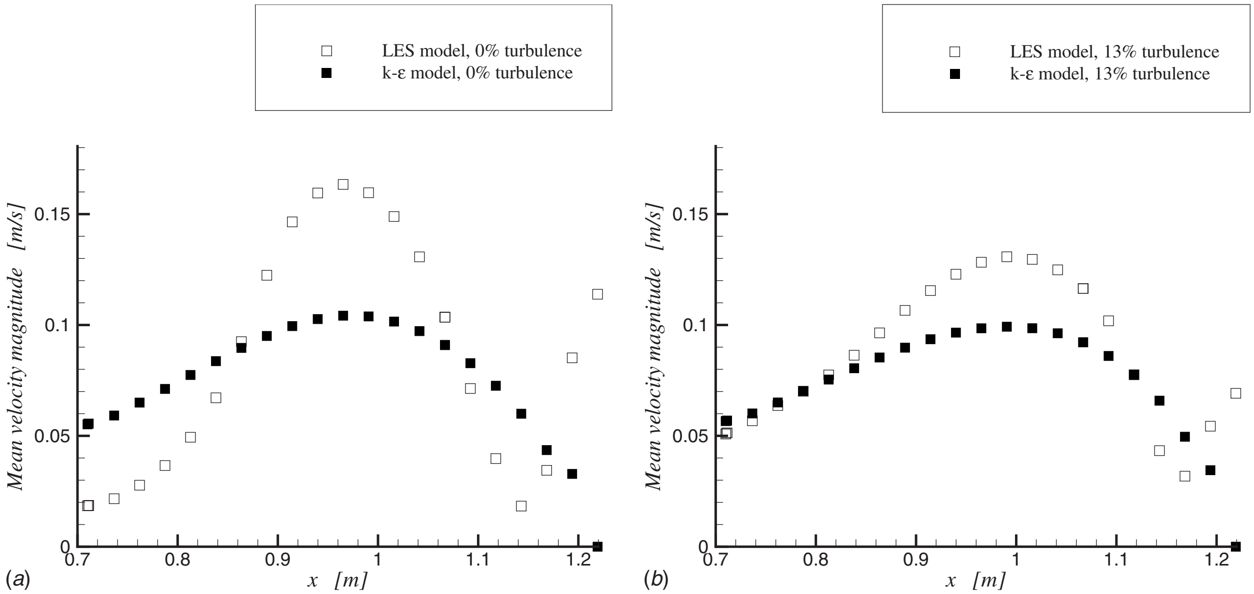

Fig. 26 Mean velocity magnitude from k-ϵ and LES models at $z/L=0.75$: (*a*) 0% and (*b*) 13% inlet turbulence intensities

inflow is laminar. The k-ϵ model on the other hand is predicting unrealistically high levels of turbulence near the inlet. In the 13% turbulence intensity case, although the k-ϵ model qualitatively captures the double-peaked profile, it still significantly overpredicts the turbulent kinetic energy relative to the LES model. Figure 28 presents similar comparisons at a location close to the ceiling ($z/L=0.75$). As noted above, LES predicts a complicated patch of activity close to the upper right corner dominated by vortical flow. The k-ϵ model, in contrast, merely predicts a decaying jet and accordingly fails to predict the turbulent patch in the corner, which is consistent with the underprediction of the level of turbulence observed in Fig. 28.

5 Conclusions

The ventilation flow inside a simple cubicle was investigated using LES with both a constant coefficient and dynamic model, and the k-ϵ model. The effect of inlet turbulence intensity has been investigated using idealized uniform mean inlet conditions with 0%, 5%, and 13% inlet turbulence intensities. It is seen that the 5% and 13% cases exhibit much faster spreading and mixing with the room air than the laminar inflow case and that the statistics predicted in these two cases are close to each other, especially far from the inlet. We conjecture that beyond a threshold level of inlet turbulence intensity, the jet develops nearly independently of the inlet turbulence intensity. This is consistent with the findings of Jiang [44], Loomans [42], and Joubert et al. [43] who likewise found little sensitivity to the inlet turbulence levels. However, the laminar inlet flow case yielded significant deviations of the mean flow and turbulence levels from the simulations with higher levels of inlet turbulence. The results of flow simulations with experimentally measured profiles for the inlet conditions are compared with those for the 13% case with uniform mean inlet profiles. It is seen that near the inlet the flow is sensitive to the inlet flow details, but these effects become less pronounced, although non-negligible, further away from the inlet. The results of simulations using the constant coefficient Smagorinsky and the dynamic LES

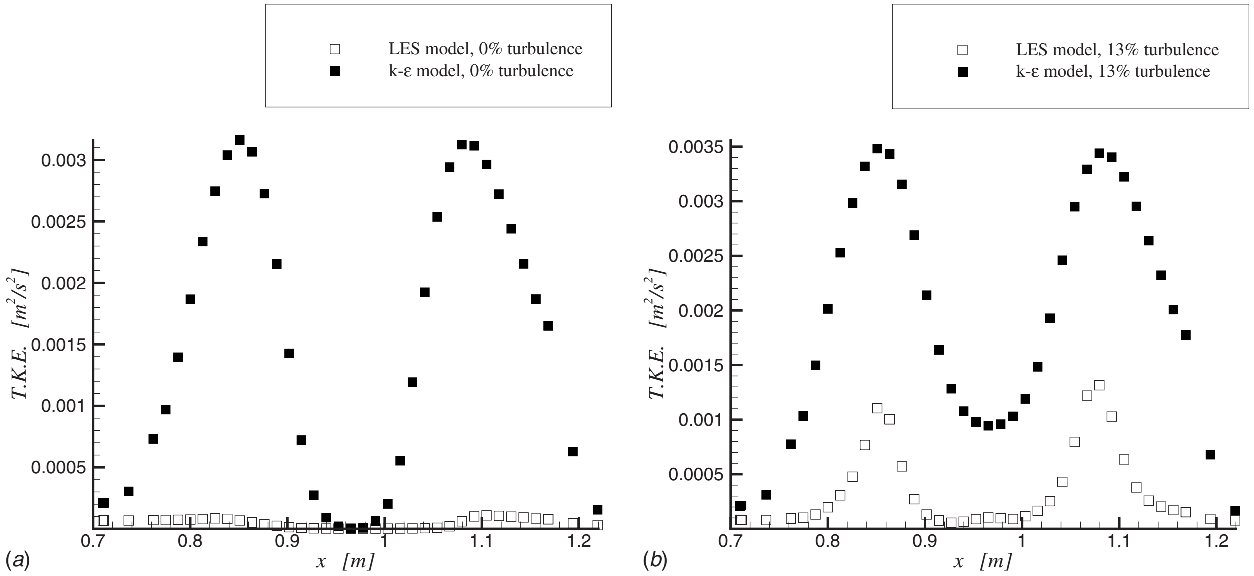

Fig. 27 Turbulent kinetic energy from k-ϵ and LES models at $z/L=-0.8$: (*a*) 0% and (*b*) 13% inlet turbulence intensities

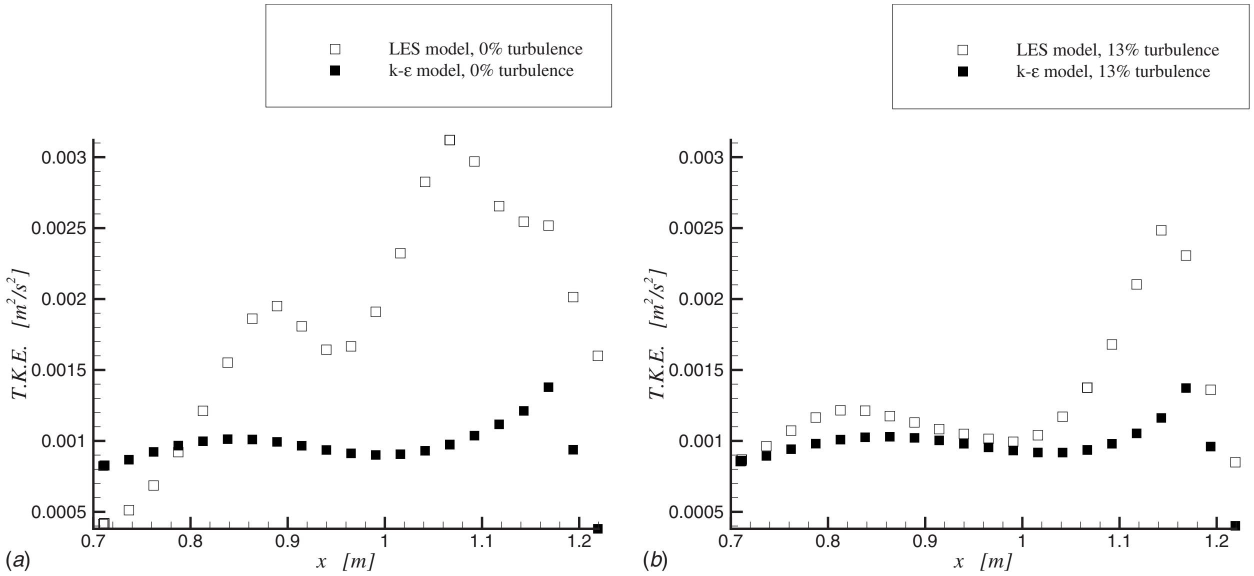

Fig. 28 Turbulent kinetic energy from k-ϵ and LES models at $z/L=0.75$: (*a*) 0% and (*b*) 13% inlet turbulence intensities

models agree reasonably well especially far from the inlet where most of the turbulent kinetic energy is resolved. The most significant differences are seen near the inlet, where the subgrid-scales' contribution to the total turbulent kinetic energy is as high as 30% of the total turbulent kinetic energy. The k-ϵ model simulations are compared at 0% and 13% inlet turbulence intensities. It is seen that the k-ϵ model is nearly insensitive to the level of inlet turbulence especially far from the inlet. Finally, the results of simulations using the k-ϵ and LES models with 0% and 13% inlet turbulence intensities are compared. It is seen that the k-ϵ model predictions for the 0% case are significantly different than the LES predictions, as the k-ϵ model fails to capture the slow spatial development of the jet into a fully turbulent state. At the 13% turbulence level, it is seen that the k-ϵ model predicts the general features of the mean velocity reasonably well. Even for this case, the k-ϵ overpredicts the spreading rate of the jet relative to the LES model and fails to capture the complicated unsteady flow pattern near the ceiling leading to significant overprediction of the turbulent kinetic near the inlet and underprediction of it near the ceiling.

Acknowledgment

This work was supported in part by the Environmental Protection Agency, through the Syracuse University NY STAR Center for Environmental Quality Systems/EPA Indoor Environmental Research Program Collaboration.

References

[1] Spengler, J. J., Samuel, J. M., and McCarthy, J. F., 2001, *Indoor Air Quality Handbook*, McGraw-Hill, New York.

[2] Pope, S. B., 2000, *Turbulent Flows*, Cambridge University Press, Cambridge.

[3] Wilcox, D. C., 2004, *Turbulence Modeling for CFD*, DCW Industries, Inc., La Canada, CA.

[4] Smagorinsky, J., 1963, "General Circulation Experiments With the Primitive Equations: I. The Basic Equations," Mon. Weather Rev., **91**, pp. 99–164.

[5] Lilly, D. K., 1967, "The Representation of Small-Scale Turbulence in Numerical Simulation Experiments," Proceedings of the IBM Scientific Computing Symposium on Environmental Sciences, IBM Form 320-1951, pp. 195–210.

[6] Deardorff, J. W., 1974, "Three-Dimensional Numerical Study of the Height and Mean Structure of a Heated Planetary Boundary Layer," Boundary-Layer Meteorol., **7**, pp. 81–106.

[7] Schumann, U., 1975, "Subgrid-Scale Model for Finite Difference Simulations of Turbulent Flows in Plane Channels and Annuli," J. Comput. Phys., **18**, pp. 376–404.

[8] Pope, S. B., 2004, "Ten Questions Concerning the Large-Eddy Simulation of Turbulent Flows," New J. Phys., **6**(35), pp. 1–24.

[9] Germano, M., Piomelli, U., Moin, P., and Cabot, W. H., 1991, "A Dynamic Subgrid-Scale Eddy Viscosity Model," Phys. Fluids A, **3**, pp. 1760–1765.

[10] Lilly, D. K., 1992, "A Proposed Modification of the Germano Subgrid-Scale Closure Method," Phys. Fluids A, **4**, pp. 633–635.

[11] Meneveau, C., Lund, T. S., and Cabot, W. H., 1996, "A Lagrangian Dynamic Subgrid-Scale Model of Turbulence," J. Fluid Mech., **319**, pp. 353–385.

[12] Nielson, P. V., Restive, A., and Whitelaw, J. H., 1978, "The Velocity Characteristics of Ventilated Room," ASME J. Fluids Eng., **100**(9), pp. 291–298.

[13] Murakami, S., Kato, S., and Suyama, Y., 1992, "Three Dimensional Numerical Simulation of Turbulent Airflow in a Ventilated Room by Means of a Two-Equation Model," ASHRAE Trans., **98**(1), pp. 82–97.

[14] Chen, Q., 1995, "Comparison of Different k-ϵ Models for Indoor Airflow Computations," Numer. Heat Transfer, Part B, **28**, pp. 353–369.

[15] Nielson, P. V., 1998, "Selection of Turbulence Models for Prediction of Room Airflow," ASHRAE Trans., **104**, pp. 1119–1127.

[16] Chen, Q., and Jiang, Z., 1992, "Significant Questions in Predicting Room Air Motion," ASHRAE Trans., **98**(1), pp. 929–939.

[17] Davidson, L., and Nielson, P. V., 1996, "Large Eddy Simulations of the Flow in Three-Dimensional Ventilated Room," Proceedings of the Fifth International Conference on Air Distribution in Rooms, Yokohama, Japan, pp. 161–168.

[18] Zhang, W., and Chen, Q., 2000, "Large Eddy Simulation of Indoor Airflow With a Filtered Dynamic Subgrid Scale Model," Int. J. Heat Mass Transfer, **43**, pp. 3219–3231.

[19] Jiang, Y., and Chen, Q., 2003, "Using Large Eddy Simulation to Study Airflows in and Around Buildings," ASHRAE Trans., **109**(2), pp. 517–526.

[20] Zhang, W., and Chen, Q., 2000, "Large Eddy Simulation of Natural and Mixed Convection Airflow Indoors With Two Simple Filtered Dynamic Subgrid Scale Models," Numer. Heat Transfer, Part A, **37**(5), pp. 447–463.

[21] Shah, K. B., and Ferziger, J. H., 1995, "A New Non-Eddy Viscosity Sub-Grid-Scale Model and Its Application to Channel Flow," *Annual Research Briefs*, Center for Turbulence Research, Stanford, CA.

[22] Zhai, Z., Zhang, Z., Zhang, W., and Chen, Q., 2007, "Evaluation of Various Turbulence Models in Predicting Airflow and Turbulence in Enclosed Environments by CFD—Part 1: Summary of Prevalent Turbulence Models," HVAC&R Res., **13**(6), pp. 853–870.

[23] Zhang, Z., Zhang, W., Zhai, Z., and Chen, Q., 2007, "Evaluation of Various Turbulence Models in Predicting Airflow and Turbulence in Enclosed Environments by CFD—Part 2: Comparison With Experimental Data From the Literature," HVAC&R Res., **13**(6), pp. 871–886.

[24] Davidson, L., Nielsen, P., and Sveningsson, A., 2003, "Modification of the v2f Model for Computing the Flow in a 3D Wall Jet," *Turbulence Heat and Mass Transfer*, K. Hanjalic, Y. Nagano, and M. J. Tummers, eds., Begell House, Inc., New York, Wallingford, UK, Vol. 213, pp. 65–72.

[25] Yakhot, V., and Orszag, S. A., 1986, "Renormalization Group Analysis of Turbulence," J. Sci. Comput., **1**, pp. 3–51.

[26] Launder, B. E., and Sharma, B. I., 1974, "Application of the Energy Dissipation Model of Turbulence to Calculation of Flow Near a Spinning Disk," Lett. Heat Mass Transfer, **1**, pp. 131–138.

[27] Durbin, P. A., 1995, "Separated Flow Computations With the k-ϵ-$v2$ Model," AIAA J., **33**, pp. 659–664.

[28] Chen, Q., and Srebric, J., 2002, "A Procedure for Verification, Validation, and Reporting of Indoor Environment CFD Analyses," HVAC&R Res., **8**(2), pp. 201–216.

[29] Chen, Q., and Zhai, Z., 2004, "The Use of CFD Tools for Indoor Environmental Design," *Advanced Building Simulation*, A. Malkawi and G. Augenbroe, eds., Spon, New York, pp. 119–140.

[30] Fluent Inc., 2006, FLUENT User's Guide, NH, Lebanon.
[31] Launder, B. E., and Spalding, D. B., 1972, *Lectures in Mathematical Models of Turbulence*, Academic, New York.
[32] Wolfshtein, M., 1969, "The Velocity and Temperature Distribution of One-Dimensional Flow With Turbulence Augmentation and Pressure Gradient," Int. J. Heat Mass Transfer, **12**, pp. 301–318.
[33] Kader, B., 1981, "Temperature and Concentration Profiles in Fully Turbulent Boundary Layers," Int. J. Heat Mass Transfer, **24**(9), pp. 1541–1544.
[34] Germano, M., 1992, "Turbulence: The Filtering Approach," J. Fluid Mech., **286**, pp. 229–255.
[35] Marr, D., 2007, "Velocity Measurements in the Breathing Zone of a Moving Thermal Manikin Within the Indoor Environment," Ph.D. thesis, Syracuse University, Syracuse.
[36] Friedrich, R., and Arnal, M., 1990, "Analysing Turbulent Backward-Facing Step Flow With the Lowpass-Filtered Navier–Stokes Equations," J. Wind. Eng. Ind. Aerodyn., **35**, pp. 101–128.
[37] Le, H., Moin, P., and Kim, J., 1997, "Direct Numerical Simulation of Turbulent Flow Over a Backward-Facing Step," J. Fluid Mech., **330**, pp. 349–374.
[38] Mathey, F., Cokljat, D., Bertoglio, J. P., and Sergent, E., 2006, "Assessment of the Vortex Method for Larged Eddy Simulation Inlet Conditions," Prog. Comput. Fluid Dyn., **6**, pp. 58–67.
[39] Lee, S., Lele, S., and Moin, P., 1992, "Simulation of Spatially Evolving Turbulence and the Applicability of Taylor's Hypothesis in Compressible Flow," Phys. Fluids A, **4**, pp. 1521–1530.
[40] Smirnov, A., Shi, S., and Celik, I., 2001, "Random Flow Generation Technique for Large Eddy Simulation and Particle Dynamics Modeling," ASME J. Fluids Eng., **123**, pp. 359–371.
[41] Mathey, F., Cokljat, D., Bertoglio, J. P., and Sergent, E., 2003, "Specification of LES Inlet Boundary Condition Using Vortex Method," *Fourth International Symposium on Turbulence, Heat and Mass Transfer*, K. Hanjalić, Y. Nagano, and M. Tummers, eds., Begell House, Inc., Antalya, Turkey.
[42] Loomans, M., 1998, "The Measurement and Simulation of Indoor Air Flow," Ph.D. thesis, Eindhoven University of Technology, Eindhoven, The Netherlands.
[43] Joubert, P., Sandu, A., Beghein, C., and Allard, F., 1996, "Numerical Study of the Influence of Inlet Boundary Conditions on the Air Movement in a Ventilated Enclosure," Proceedings of the Roomvent, Yokohama, Japan, Vol. 1, pp. 235–242.
[44] Jiang, J., 2007, "Experimental and Numerical Study of Air Flows in a Full-Scale Room," Ph.D. thesis, University of Illinois at Urbana-Champaign, Urbana.
[45] Marr, D., 2007, private communication.

H. Zidouh

L. Labraga[1]
e-mail: llabraga@univ-valenciennes.fr

M. William-Louis

Université Lille Nord de France,
F-59000 Lille, France;
UVHC, LME,
59313 Valenciennes, France

Unsteady Wall Shear Stress in Transient Flow Using Electrochemical Method

Experimental measurements of the wall shear stress combined with those of the velocity profiles via the electrochemical technique and ultrasonic pulsed Doppler velocimetry are used to analyze the flow behavior in transient flows caused by a downstream short pipe valve closure. The Reynolds number of the steady flow based on the pipe diameter is $Re = 148,600$. The results show that the quasisteady approach of representing unsteady friction is valid during the initial phase for relatively large decelerations. For higher decelerations, the unsteady wall shear stress is consistently higher than the quasisteady values obtained from the velocity profiles. Attention has been focused on the friction acceleration model. The results obtained from this study show the ability of the electrochemical method in determining the local unsteady wall shear stress even in severe decelerating transient flows. [DOI: 10.1115/1.3112387]

1 Introduction

Transient flows associated with the water hammer phenomenon are commonly encountered in both natural and engineering systems. Examples include water supply and distribution system, oil transportation systems, and human arterial network. The dramatic changes in velocity and pressure arising from these transient events can cause pipe breakages, flooding, and other damage hazards.

In engineering analysis of such flows, it is assumed that phenomenological expressions relating the wall shear stress to cross sectional averaged velocity in steady-state flows remain valid under unsteady conditions. In other words, a new Reynolds number is computed each time the velocity is altered and the wall shear stress is then adjusted to the value corresponding to stationary flow at the new Reynolds number. For example, the form of the Darcy–Weisbach equation used in water hammer models is

$$\tau_w(t) = \frac{\rho\lambda(t)|V(t)|V(t)}{2} \tag{1}$$

where λ is the friction factor. The application of such a simplified wall shear stress model is satisfactory only for very slow transients, in which the shape of the instantaneous velocity profiles does not differ markedly from the corresponding steady-state ones. During fast transients or high frequency periodic flows, on the other hand, velocity profiles change, in particular, and more complex patterns, featuring greater gradients, hence, greater shear stresses, than the corresponding steady flow values.

A simple modification of Eq. (1) involves the introduction of an unsteady component $\tau_{wu}(t)$ such that

$$\tau_w(t) = \tau_{qs}(t) + \tau_{wu}(t) \tag{2}$$

where $\tau_{wu}(t)$ is zero for steady flows, small for slow transients, and significant for fast transient flows. Daily et al. [1] conducted laboratory experiments and found $\tau_{wu}(t)$ to be positive for accelerating flows and negative for decelerating flows. They argued that during acceleration, the central portion of the stream moved somehow “bodily” so that the velocity profile steepened, giving higher shear. The relation postulated by Daily et al. [1] can be reformulated as follows:

$$\tau_w = \tau_{qs} + \frac{k\rho D}{8}\frac{dV}{dt} \tag{3}$$

where k, an empirical parameter, needs be determined either from experiments or analysis. Daily et al. [1] showed that $k=0.01$ for accelerating flows and $k=0.62$ for decelerating flows. The research of Shuy [2] led to $k=-0.0825$ for accelerating flows and $k=-0.13$ for decelerating flows. This illustrates that empirical constant k is flow case dependent. To explain these conflicting results, Vardy and Brown [3] argued that the different behaviors observed by the authors may be attributed to different time-scales. The most successful formulation of this approach is the expression proposed by Brunone et al. [4] as follows:

$$\tau_w = \tau_{qs} + k_3\frac{\rho R}{2}\left(\frac{\partial V}{\partial t} - a\frac{\partial V}{\partial x}\right) \tag{4}$$

where the unsteady friction term depends on both instantaneous local acceleration and instantaneous convective acceleration. The measurement of the unsteady wall shear stress so far was conducted in previous studies by measuring the wall drag force [2] or by determining the transient friction coefficient from the instantaneous mean flow velocity [5,6]. Whereas the above mentioned approaches are acceptable for flows accelerating or decelerating slowly at a uniform rate, they are questionable during fast transients. Moreover, the studies so far performed about transient flows are limited to quite narrow accelerations and deceleration ranges, and the results obtained by these studies are very different from one another.

From this brief review, it is shown that a critical lack of characterizing turbulent transient flow is a more precise knowledge of the local unsteady wall shear. It is shown that no conclusive result was obtained because of the scarcity of experimental data available. A nonintrusive, local, and quantitative method is actually greatly required to determine the important unsteady phenomena involved under transient conditions. The primary aim of this work was to examine the possibility of measuring the local unsteady wall shear stress within a decelerating turbulent flow in a short circular pipe. This is made possible by the use of the electrochemical method combined with the ultrasound velocimetry. Although the pipe was rather short, it was able to provide fast tran-

---

[1] Corresponding author.

Contributed by the Fluids Engineering Division of ASME for publication in the JOURNAL OF FLUIDS ENGINEERING. Manuscript received August 18, 2008; final manuscript received February 24, 2009; published online April 15, 2009. Assoc. Editor: Hassan Peerhossaini.

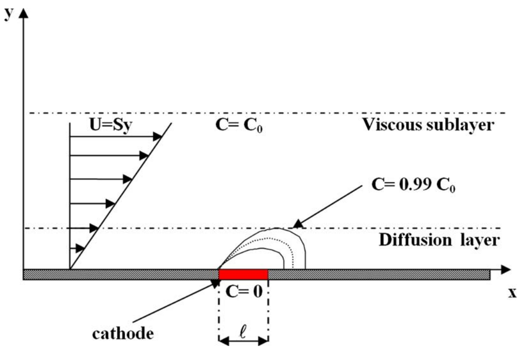

Fig. 1 Concentration fields and velocity profile over a single probe

sient flows characterized by very high decelerations and complex shapes of instantaneous velocity profiles featuring annular effects leading to local flow reversal.

2 Theory

Shear stress is determined experimentally using an electrochemical method based on the reduction in the ferricyanide ion on an electrode surface. A thorough review of this technique is provided by Hanratty and Campbell [7]. This method is based on the determination of the limiting diffusion current at the surface of an electrode under conditions for which the chemical reaction rate is fast enough so that the concentration of the reacting ions is zero at the surface of the working electrode. If the length of this electrode is very small in the flow direction, the concentration boundary layer on the electrode is thin; thus the flow velocity varies linearly throughout the thickness of this boundary layer.

A diagram of a single electrochemical probe is given in Fig. 1. The current I flowing to the test electrode of area A is related to the mass transfer coefficient K by

$$K = \frac{I}{A n_e F C_0} \tag{5}$$

where n_e is the number of electrons involved in the reaction, F is the Faraday constant, and C_0 is the bulk concentration of active species. If the dimensionless velocity gradient at the wall $S^+ = S\ell^2/D$ (where ℓ is electrode length and D is diffusion coefficient) is high enough, it is then possible to neglect the longitudinal diffusion, and a solution of the steady-state mass balance equation gives

$$K^+ = \frac{K\ell}{D} = c(S^+)^{1/3} \tag{6}$$

The integration of the mass transfer equation by several authors gives a theoretical value for the coefficient c in the case of a rectangular probe, $c=0.807$.

When flush mounted mass transfer probes are used to measure wall shear rate of unsteady flows, featuring low velocity amplitude variations, a pseudo-steady-state assumption can be made and the one-third-power law can be used to compute the instantaneous wall shear rate [8]. However, in many cases, the concentration boundary layer inertia cannot be neglected and the quasi-steady-state assumption is not valid. Most studies of the dynamic behavior of electrochemical probes assume that the amplitude of the shear rate fluctuations is small compared with the time averaged shear rate. With this assumption, the mass balance equation can be linearized and solved analytically [9] and numerically [10,11]. Then, the transfer function between the mass flux and the wall shear rate at different frequencies can be deduced. The difficulty of this approach is that the linearization assumption is not always valid. For example, in flows involving large amplitude oscillations, high frequency velocity variations, or reverse flows, the above approach cannot apply.

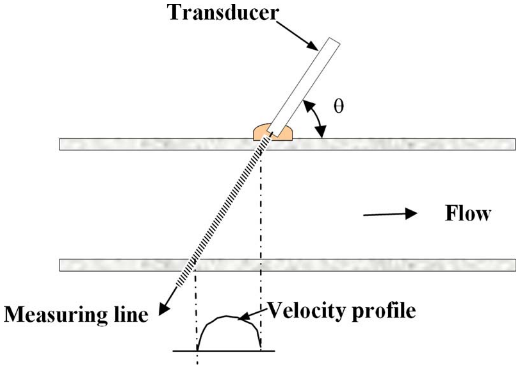

Fig. 2 Pulsed ultrasonic Doppler velocimetry technique: measurement setup

Sobolik et al. [12] introduced a technique based on the correction of the wall shear rate obtained from the Levêque solution by adding a term estimated from the known solution of the unsteady diffusion at the beginning of the potential transient process. They established that the corrected wall shear rate $S_c(t)$ is

$$S_c(t) = S_q(t) + \frac{2}{3} t_0 \left(\frac{\partial S_q(t)}{\partial t} \right) \tag{7}$$

where $t_0 = 0.486\ell^{2/3} D^{-1/3} S_q^{-2/3}$ and $S_q(t) = D/\ell^2 (K^+(t)/0.807)^3$.

This method is limited both to rather moderate frequencies and nonreverse unsteady flows. In the presence of large unsteady or reverse flows, the inverse method [13–15] seems to be more appropriate to calculate the wall shear rate from the mass transfer signal measured. This technique consists in solving the direct convection-diffusion equation and in estimating sequentially the unknown wall shear rate by minimizing the difference between measured and simulated mean concentration gradients on the probe surface. In this study both the inverse method and that suggested by Sobolik et al. [12] were applied for the determination of the "true" wall shear rate of the transient turbulent flow in a pipe.

The ultrasonic pulsed Doppler velocimetry [16–18] was used for velocity profile measurements. Figure 2 shows a common configuration of the ultrasound beam and flow. This method is based on detecting and processing the backscattered echoes originating from moving targets suspended in the flowing liquid that is to be investigated. This technique provides measurements of local one-dimensional velocity and related distance from the transducer, leading to the construction of an almost instantaneous velocity profile along the acoustic beam. Information on the position from which the ultrasound is reflected is extracted from the time delay T_D between the start of the pulse burst and its reception as $Y = aT_D/2$.

If the particle is moving at an angle θ regarding the axis of the ultrasonic beam, its velocity u is measured by computing the variation of its depth between two emissions separated by the time interval between two pulses as

$$u = \frac{f_D}{2f \cos \theta} a \tag{8}$$

where f is the emitting frequency, and f_D is the Doppler frequency shift that is due to the particle motion. According to the Nyquist theorem, a maximum detectable Doppler frequency exists for each pulse repetition frequency (f_{prf}), over which measurements are affected by aliasing

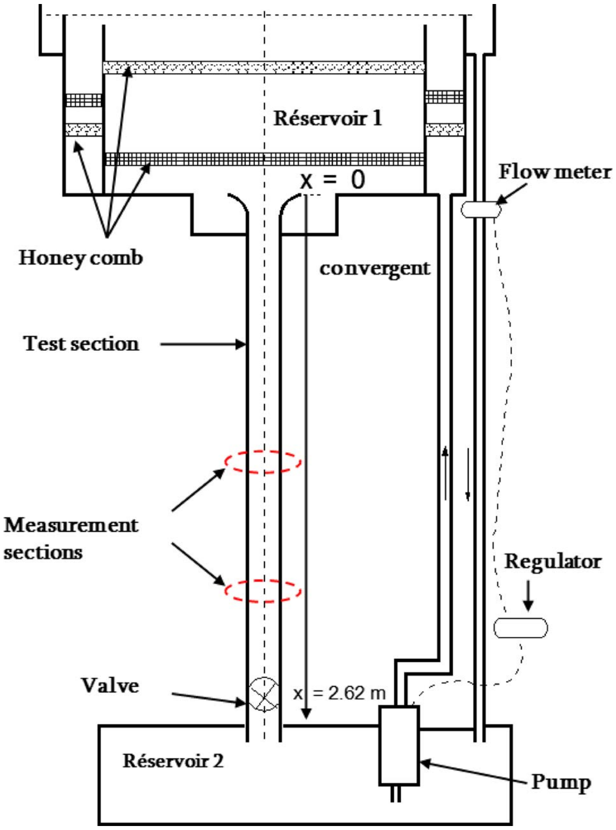

Fig. 3 Experimental setup

$$f_{D\,\max} < f_{\text{prf}}/2 \tag{9}$$

Equation (9) leads to a maximum detectable velocity for each pulse repetition frequency

$$u_{\max} = \frac{a}{4T_{\text{prf}} f \cos\theta} \tag{10}$$

In addition to the velocity, the maximum measurement depth is determined by the repetition frequency of the pulses according to the relationship $Y_{\max}=a/(2f_{\text{prf}})$. This depth can be reduced in order to increase the spatial resolution.

3 Material and Method

Experiments were conducted in a vertical water channel (Fig. 3). The main component is the $L=2.62$ m long polypropylene pipe with a 61.4 mm internal diameter and an $e=6.8$ mm wall thickness. The pipe is connected to a supply and recycling system. A constant level tank is used to keep upstream pressures constant throughout measurements. A butterfly valve at the end of the pipe is used to create controlled opening and closing actions by adjusting the discharge into the free surface tank. More details of the experimental apparatus are reported in Ref. [19]. The working fluid is either water seeded with copolyamide particles for the velocity profile measurement or an electrochemical solution for the wall shear stress measurement.

Pressure, velocity, and wall shear stress are measured at a distance of 3.27 m from the free surface.

The electrolytic solution is a mixture of potassium ferricyanide (10 mol/m^3), potassium ferrocyanide (10 mol/m^3), and potassium sulfate. The potassium sulfate acts as a low resistance vehicle for current flows and ensures that the transfer at the cathodic surface is controlled by diffusion only.

Table 1 Physical properties of the electrochemical solution at 25°C

Density, ρ (kg/m^3)	1024
Kinematic viscosity, ν (m^2 s^{-1})	1.025×10^{-6}
Diffusivity, D (m^2 s^{-1})	7.45×10^{-10}

The chemical reaction at the electrodes is described as

$$\text{Fe(CN)}_6^{3-} + e^- \rightleftarrows \text{Fe(CN)}_6^{4-}$$

The conversions of ferrycyanide and ferrocyanide that take place between the cathode and the anode maintain a constant concentration of both chemicals. The electric current I flowing between the electrodes is related to the transfer coefficient according to Eq. (5).

Two kinds of probes were used: single circular probe and sandwich rectangular probes. The latter is used to sense reversal flows. The test electrodes were constructed by inserting circular platinum wires or platinum sheet through the wall and gluing them in place. The protruding metal was smoothed flush with the pipe wall. The platinum wire was 0.4 mm in diameter. The sandwich probe was made with two platinum sheet strips. The probe is 0.5 mm long, 0.1 mm wide, and with a 0.008 mm gap. The platinum sheets and the cellophane tape are glued together and inserted into a Perspex block. The block is then mounted flush inside a Plexiglas module inserted in the pipe between two collars. The polarizations curves, not reported here, show that the electrode is polarized by an applied voltage of −200 to −600 mV over a Reynolds-number range of about 35,000–100,000. An operating voltage of −400 mV was selected.

The active surface of the electrochemical probes is determined with the Cotrell method. This technique is based on the study of the transient response of the probes to a voltage step from 0 to the diffusional plateau potential [20]; before the stationary regime is obtained, the current decreases following the Cotrell asymptote. During this period of time, the evolution of the electrical intensity as a function of $t^{-1/2}$ is linear. The slope permits to deduce the active electrode area and therefore the value of the effective diameter of the probe.

All the experiments were carried out at 25°C. Under these conditions the physical properties of the electrochemical solution take the values given in Table 1. According to these values, the Schmidt number is 1375.

Two pressure transducers of stainless diaphragm type with a recording range of 0–70 m of water, an accuracy of 0.5%, and of the full-range scale are mounted at the $L/2$ and $3L/4$ sections along the pipeline.

The ultrasound Doppler velocimeter was a DOP2000 from Signal Processing SA with a 4 MHz ultrasound transducer. The transversal dimension of the sampling volume is determined by the ultrasonic field geometry. The longitudinal dimension, however, depends on the burst length and on the bandwidth of the receiving unit. The minimum value of the sampling time is about 4 ms. The ultrasonic field continuity between the probe and the pipe was maintained with a coupling gel. The basic characteristics of the ultrasound Doppler velocimetry used in this study are presented in Table 2.

Table 2 Ultrasound Doppler velocimeter specification

Emitting frequency, f_e (MHz)	4
Emitting PRF, f (kHz)	10
Radius of the transducer's piezo (mm)	5
The angle of incidence, θ (deg)	68
Longitudinal resolution (mm)	0.69

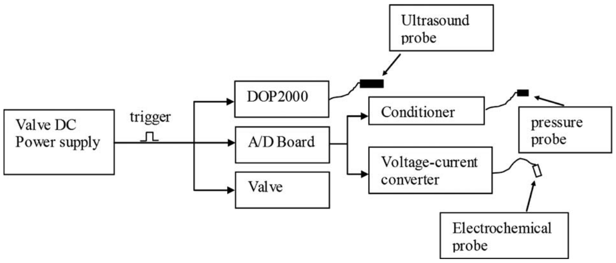

Fig. 4 Synoptic of the acquisition system

Simultaneous pressure and wall shear stress data acquisition is realized with a sample and hold device. Digitizing is done by a 12 bit A/D converter. The reference time is based on the electromechanical valve closure. The starting time $t=0$ is set by switching off a dc power supply that simultaneously triggers the valve closure and acquisition of the wall shear stress (or velocity profiles) and the pressure signals.

The sampling frequency of pressure and electrochemical signals was 10 kHz during 250 ms. The relatively high sampling rate is needed for the electrochemical signal dynamic response to be accurately corrected. When the measurement is finished, data are read by a PC high-speed data bus for final processing and storage. The detailed synoptic of the acquisition system is presented in Fig. 4.

4 Results and Discussion

Before undertaking unsteady flow measurements, a preliminary set of steady-state measurements was carried out for different Reynolds numbers. The velocity measurements were taken at a distance of 1.945 m from the inlet of the tube. The velocity profiles provided by the ultrasonic pulsed Doppler velocimetry (UDV) technique were corrected in order to remove bias errors due to the crossing of media with different acoustic properties, ultrasonic field shapes, intensity spatial variability, and finite dimension of sampling volume especially in areas close to the wall. The correction procedure suggested by Wunderlich and Brunn [21] was applied to the data. The averaged velocity profiles were obtained from instantaneous measurements, during 100 s of acquisition. Numerous experiments including velocity profiles, pressure, and wall shear stress in unsteady flow conditions caused by a fast valve closure were conducted. However, due to the lack of space, only a few representative results are reported hereby.

The experiment is being carried out in two phases. First, the instantaneous velocity profiles and pressure were simultaneously collected in seeded water. The time origin corresponds to the start of the maneuver initiated by the electromechanical valve signal. Second, since wall shear stress data required specific electrochemical solution, they were acquired later on in the same time base; thanks to the electromechanical valve signal that triggers the data acquisition system therefore allowing perfectly repeatable tests.

Figure 5 shows the response of a pressure transducer and six

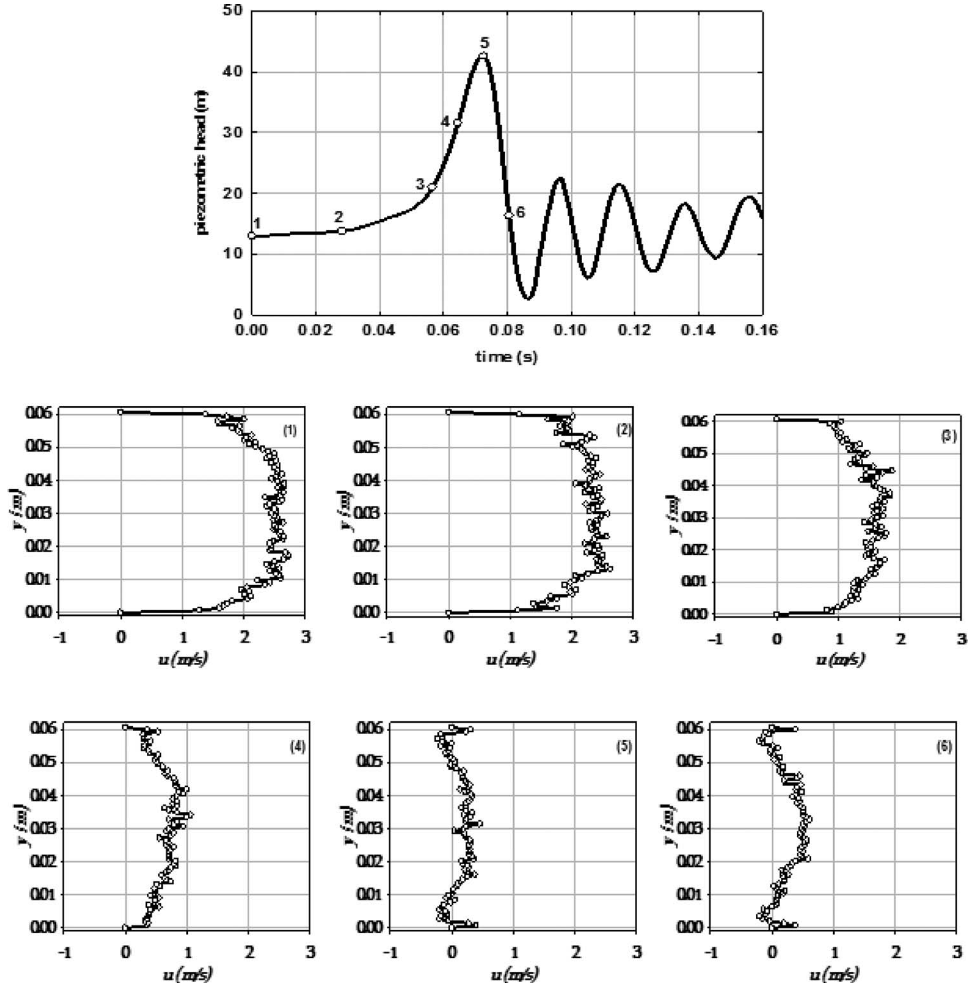

Fig. 5 Experimental results showing pressure time history and associated velocity profiles

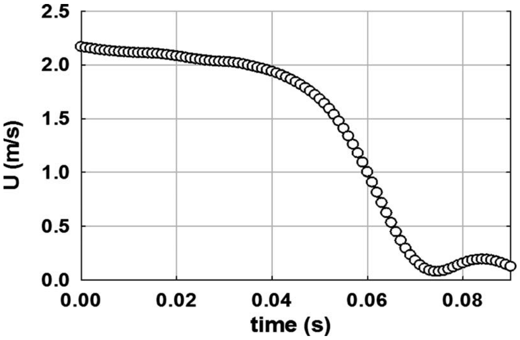

Fig. 6 Mean velocity during deceleration

corresponding velocity profiles during the transient events. A rapid decay of pressure peaks after the end of a complete valve closure is observed. The transient event associated with Fig. 5 has the following characteristics: The initial mean flow velocity is 2.42 m/s, and the valve is operated from a fully open to a fully closed position in about 70 ms. The time history of the pressure and the velocities are measured at a distance of 0.675 m upstream from the valve. The time origin, $t=0$, corresponds to the start of the maneuver of the valve. The points labeled with small numbers on the time history in the upper plot label the instants corresponding to the displayed velocity profiles. The pressure wave celerity was calculated from the recorded data based on the analysis in the time and frequency domains of the pressure waveform. The mean value of this quantity amounted to about $a=500$ m/s. This mean pressure wave speed is also calculated from the following analytical solution:

$$a = \frac{\sqrt{K_w/\rho_p}}{\sqrt{1+(1-\nu_p{}^2)\frac{K_w}{E}\frac{D}{e}}} \qquad (11)$$

where K_w, ν_p, ρ_p, E, and e are bulk modulus, Poisson's coefficient, mass density, Young's modulus, and pipe-wall thickness, respectively. Equation (11) gives a pressure wave celerity value of 496 m/s, in good agreement with the experimental findings. The velocities were obtained by time-averaging 50 velocity profiles.

The velocity profiles confirm the complex features of the flow field as it was suggested by Brunone et al. [4]. During transient flow the instantaneous velocity profiles deviate significantly from the corresponding steady-state as it is shown in Fig. 5 ((4)). A reverse flow occurs within a near wall annulus corresponding to $0.1 < y/R < 0.2$ (Fig. 5, (5) and (6)) and may be interpreted by the so called annular effect that is different from that usually found in previous studies, characterized by negative shear stresses at the wall. For this particular event, it can be found that the mean velocity is approximately null while the velocity gradient near the wall is substantial. In other words, under such a condition, even with a significant wall shear stress, steady or quasisteady criteria would give a null friction term.

The time dependence of the sectional mean velocity is shown in Fig. 6. The mean velocity exhibits several phases. It decreases slowly from 0 s to 0.04 s and undergoes a steep decrease in the time range from 0.05 s to 0.07 s. The minimum mean velocity corresponding to the highest pressure peak results from the reflected wave from the valve. A slight increase in the instantaneous mean velocity occurring at about 0.085 s is strictly linked to the minimum pressure value.

The instantaneous acceleration is shown in Fig. 7. The acceleration is negative throughout the transient event except in the $0.075 < t < 0.085$ time range corresponding to a steep decrease in the pressure. The present values of the acceleration range from 0 ms^{-2} to -100 ms^{-2}, much higher values indeed if compared with those found in literature [2,4,6].

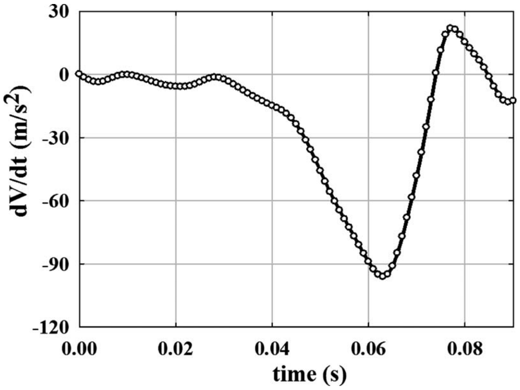

Fig. 7 Instantaneous deceleration

Preliminary measurements of the wall shear stress performed with a split probe have shown that no reverse flow occurs after a fast valve closing within the measurement section. This result was made possible, thanks to the electrochemical method, and could not be found easily from the velocity profiles provided by UDV technique.

The unsteady wall shear stress derived from the Levêque solution is compared with that corrected with the inverse method and the method of Sobolik et al. [12] (Fig. 8). The wall shear stress is normalized with that obtained at $t=0$ at the beginning of the transient flow. It is clear from Fig. 8 that the probe inertia correction is necessary, especially in the part of the transient event where the shear rate variation is significant. Figure 8 shows that the method of Sobolik et al. [12] gives nearly the same instantaneous wall shear rate. This result is not so surprising because large Peclet numbers are observed during the transient flow. Moreover, no reverse flow occurs during the valve closure. For this particular unsteady flow, the method of Sobolik et al. [12] is quite suitable as compared with the inverse method, because no additional parameters are required and no initial guess of the wall shear stress is needed.

Figure 9 shows the measured wall shear stress via the electrochemical technique. About 40 tests were performed for the measurement of the transient wall shear stress. The wall shear stress is normalized with that obtained at $t=0$ at the beginning of the transient event, therefore removing uncertainties due to the difficulty to estimate the actual probe surface. In the same figure, the absolute pressure and the normalized wall shear stress predicted by using a quasisteady assumption are displayed. Here we define the quasisteady friction coefficient λ_q using the instantaneous Reynolds number as follows:

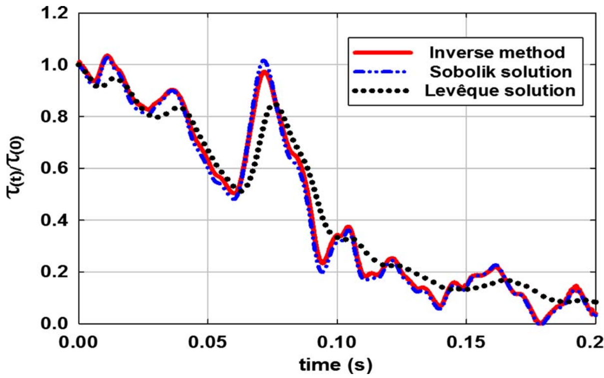

Fig. 8 Comparison between wall shear stress obtained with different methods

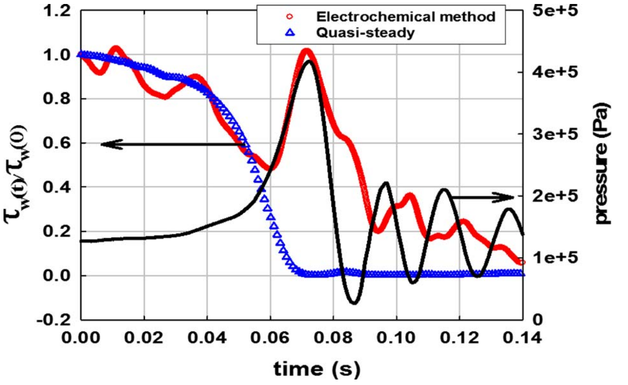

Fig. 9 Wall shear stress and pressure distributions during deceleration

$$\lambda q = \begin{cases} \dfrac{64}{R_e} & \text{(laminar)} \\ \dfrac{0.316}{R_e^{0.25}} & \text{(turbulent)} \end{cases} \qquad (12)$$

The results show that the wall shear stress measured from the electrochemical signals oscillates around that predicted by a quasisteady model for the time range between $t=0$ s, corresponding to the start of the valve closure, up to $t=0.055$ s. The ability of the electrochemical method to sense the local instantaneous flow unsteadiness is clearly shown in Fig. 9. Indeed, the wall shear stress exhibits a wavy behavior probably due to the pressure wave originating from the valve closure. As for the quasisteady model, it tends to smoothen out the actual wall shear stress fluctuations.

Shuy [2] found that the unsteady wall shear stress is higher than the quasisteady values (computed from the Karman–Nikuradse equation based on instantaneous velocity), for a value of the acceleration parameter $\phi=2D/\lambda_s V^2|dV/dt|$ up to 2. The values of the acceleration parameter of the present study range within $0 \leq \phi \leq 100$ for $t<0.05$ s. For this severe decelerating flow, the present results show that the unsteady wall shear stress may be either greater or lower than that obtained from a quasisteady approach, following the local fluctuating acceleration with a phase shift, as it is shown below.

For $0.06\text{ s}<t<0.07$ s, the quasisteady assumption is no longer valid to determine the wall shear stress. The effective wall velocity gradient is considerably higher than the one resulting from the pseudosteady approach. The unsteady wall shear stress inferred from the electrochemical probe increases up to a maximum value corresponding to that of the pressure. It is shown that the maximum unsteady wall shear stress value reaches the steady one at the end of this phase.

For $t>0.07$ s, the unsteady wall shear stress tends asymptotically toward zero with large oscillations resulting from all reflected pressure waves.

Figure 10 gives a synthesis of the results of both unsteady wall shear stress component and acceleration (τ_{wu}). According to Eq. (3), it is expected that the changes in the unsteady wall shear stress component τ_{wu} correspond closely to those of the acceleration. It is shown that the sudden change in the core of the pipe first affects the acceleration before unsteady wall shear stress is changed. The change in flow rate is then transferred toward the wall by viscous shear. As a result, changes in the velocity field of the fluid adjacent to the pipe wall, and in resulting wall shear stresses, lag behind flow rate changes in the core of the pipe [22]. This should explain the discrepancies in phase shift between experimental and numerical head traces obtained in some previous studies with the friction model based on instantaneous local acceleration for later time of the transient flows.

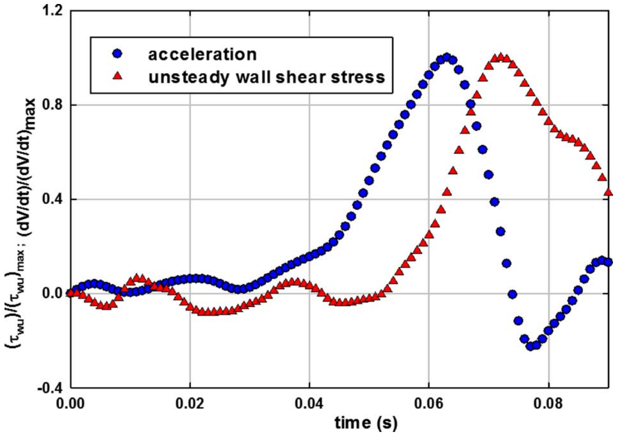

Fig. 10 Unsteady wall shear stress component and acceleration

Axworthy et al. [23] suggested that the unsteady friction formulas based on instantaneous accelerations such as Eq. (3) are applicable to transient flow problems in which the wave passage time-scale ($L/a=0.0052$ s in the present study) is significantly shorter than the vorticity diffusion time-scale ($\sqrt{2}D/2u_\tau=0.46$ s in the present study). According to Axworthy et al. [23], the changes in wall shear stress in the conditions mentioned above should correspond closely to the acceleration. In the light of the present study, it can be stated that the time-scale arguments do not allow any definitive conclusion to be made to clarify the applicability of the instantaneous-acceleration approach in both attenuation and phase shift of the transient wall shear rate.

Shuy [2] rewrote Eq. (3) in the following dimensionless form:

$$\frac{\tau_w}{\tau_{ws}} = 1 + \frac{k}{2}\phi \qquad (13)$$

It seems interesting to check the validity of Eq. (13) using the present data. Figure 11 shows the dependence of the ratio between unsteady and steady wall shear stresses on the acceleration parameter ϕ.

For $|\phi|<40$, corresponding to the beginning of the transient, the ratio between unsteady and steady wall shear stresses scatters about a mean value of 1, confirming a quasi-steady-state behavior observed in Fig. 9. Over the range of $40<|\phi|<150$ the data take a nearly constant value and show clearly that the unsteady wall shear stress is lower than the pseudosteady one.

For $|\phi|>150$ the data are remarkably aligned and correspond to an unsteady wall shear stress that is higher than the quasisteady one. The highest acceleration parameter (-400) is reached at $t \cong 0.06$ s just before the complete valve closure. The acceleration parameter of the present study takes very high values because of

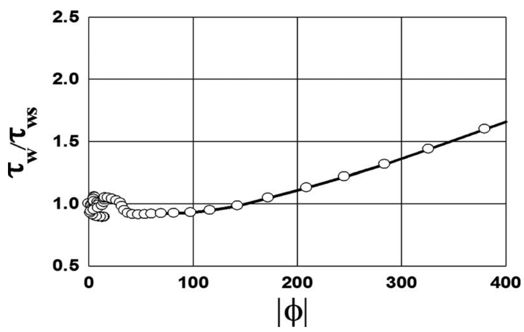

Fig. 11 Dependence of the ratio between unsteady and steady wall shear stresses on the acceleration parameter

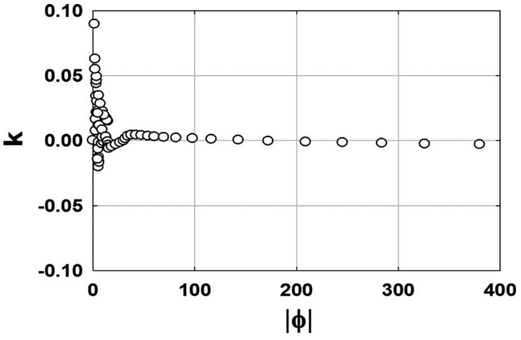

Fig. 12 Dependence of *k* on the acceleration parameter

the short length of the pipe and the relatively high Reynolds number. The electrochemical technique is actually the only method able to measure with a fine time resolution the unsteady wall shear stress in these severe experimental conditions, not found in literature.

The computed values of the empirical coefficient k, obtained from Eq. (13), are displayed against φ in Fig. 12. The values of k are consistent with the distribution of the ratio between unsteady and steady wall shear stresses analyzed above. The present results show that the values of k are rather low compared with those found in literature. Moreover, k is variable in time and therefore depends on the acceleration parameter as it was already suggested by Axworthy et al. [23].

Further experiments are performed in order to check the validity of the well known model of Brunone [4] (Eq. (4)), the most widely used due to its ability to produce reasonable agreement with experimental pressure history.

5 Conclusion

The electrochemical technique is combined with ultrasonic pulsed Doppler velocimetry for measurements of the unsteady transient wall shear stress and velocity profiles. Acquired unsteady wall shear stress by using the electrochemical method provides complementary and additional near wall information to the velocity profiles and demonstrates the complex nature of the near wall flow field.

The conclusions are summarized as follows.

(1) The dynamic response of the electrochemical probes is being corrected by using the inverse method and the method of Sobolik et al. [12]. Both methods provide remarkable similar results despite complex flow conditions characterized by very high decelerations.
(2) The velocity profiles measured with ultrasonic pulsed Doppler velocimetry clearly show, during transient events, regions of reverse flow occurring at a finite distance from the wall and associated with high values of the velocity gradient at the wall.
(3) The quasisteady approach for predicting the wall shear stress is valid on average for a wide ranging acceleration parameter, much more higher than that found in the previous studies.
(4) The unsteady wall shear stress component lags behind the instantaneous acceleration, suggesting that the average velocity field responds more quickly to changes in the flow at the core of the pipe.

For more meaningful progress in the numerical modeling of unsteady flows, much more series of experimental tests must be first carried out, using a reliable technique for the measurement of the wall shear stress. In the light of this study, the electrochemical method seems to be the most appropriate technique that could contribute to a better understanding of transient flow dynamics and energy dissipation. Further experimental measurements should be performed in a longer pipe allowing both short and long time-scales to take advantage of this powerful method.

Nomenclature

a = sound velocity (m/s)
A = active surface of the probe (m^2)
C = bulk concentration ($\mathrm{mol/m}^3$)
d = pipe diameter (m)
D = diffusion coefficient (m^2/s)
F = Faraday number
f = frequency (Hz)
F_{prf} = pulse repetition frequency (Hz)
I = limiting diffusion current (A)
k = empirical coefficient of unsteady friction
K = transfer coefficient (m/s)
ℓ = probe width (m)
n_e = number of electrons exchanged in a reaction
p = fluid pressure (m)
R = pipe radius (m)
Re = Reynolds number: Vd/ν
S = velocity gradient at the wall (1/s)
t = time (s)
T_{prf} = $1/f_{\mathrm{PRF}}$ (s)
V = mean axial velocity (m/s)

Special Characters

λ = friction factor
ν = kinematic viscosity (m^2/s)
ρ = fluid density ($\mathrm{kg/m}^3$)
τ_w = wall shear stress (Pa)
τ_{ws} = quasisteady wall shear stress (Pa)
τ_{wu} = unsteady wall shear stress (Pa)

References

[1] Daily, J. W., Hankey, W. L., Olive, R. W., and Jordan, J. M., 1956, "Resistance Coefficient for Accelerated and Decelerated Flows Through Smooth Tubes and Orifices," Trans. ASME, **78**, pp. 1071–1077.
[2] Shuy, E. B., 1996, "Wall Shear Stress in Accelerating and Decelerating Turbulent Pipe Flows," J. Hydraul. Res., **34**(2), pp. 173–183.
[3] Vardy, A., and Brown, J. M. B., 1997, "Discussion on Wall Shear Stress in Accelerating and Decelerating Pipe Flows," J. Hydraul. Res., **35**(1), pp. 137–139.
[4] Brunone, B., Golia, U. M., and Greco, M., 1991, " Some Remarks on the Momentum Equation for Transients," *International Meeting on Hydraulic Transients With Column Separation, Ninth Round Table*, IAHR, Valencia, Spain, pp. 201–209.
[5] Carstens, M. R., and Roller, J. E., 1959, "Boundary-Shear Stress in Unsteady Turbulent Pipe Flow," ASCE J. Hydr. Div., **85**(HY2), pp. 67–81.
[6] Kurokawa, J., and Morikawa, M., 1986, "Accelerated and Decelerated Flows in a Circular Pipe (1st. Report, Velocity Profiles and Friction Coefficient)," Bull. JSME, **29**(249), pp. 758–765.
[7] Hanratty, T. J., and Campbell, J. A., 1983, "Measurement of Wall Shear Stress," *Fluid Mechanics Measurements*, R. J. Goldstein, ed., Hemisphere, Washington, DC, pp. 559–615.
[8] Reiss, L. P., and Hanratty, T. J., 1963, "An Experimental Study of the Unsteady Nature of the Viscous Sub-Layer," AIChE J., **9**, pp. 154–160.
[9] Mitchell, J. E., and Hanratty, T. J., 1966, "A Study of Turbulence at a Wall Using an Electrochemical Wall Shear Stress Meter," J. Fluid Mech., **26**, pp. 199–221.
[10] Fortuna, G., and Hanratty, T. J., 1971, "Frequency Response of the Boundary Layer on the Wall Transfer Probes," Int. J. Heat Mass Transfer, **14**, pp. 1499–1507.
[11] Deslouis, C., Gil, O., and Tribollet, B., 1990, "Frequency Response of Electrochemical Sensors to Hydrodynamic Fluctuations," J. Fluid Mech., **215**, pp. 85–100.
[12] Sobolik, V., Wein, O., and Cermac, J., 1987, "Simultaneous Measurement of the Film Thickness and Wall Shear Stress in Wavy Flow of Non-Newtonian Liquids," Collect. Czech. Chem. Commun., **52**, pp. 913–928.
[13] Labraga, L., Bourabaa, N., and Berkah, T., 2002, "Wall Shear Stress From a Rotating Cylinder in Cross Flow Using the Electrochemical Technique," Exp. Fluids, **33**, pp. 488–496.
[14] Zhuoxiong, M., and Hanratty, T. J., 1991, "Analysis of Wall Shear Stress Probes in Large Amplitude Unsteady Flows," Int. J. Heat Mass Transfer, **34**, pp. 281–290.
[15] Rehimi, F., Aloui, F., Ben Nasrallah, S., Doubliez, L., and Legrand, J., 2006,

"Inverse Method for Electrodiffusional Diagnostic of Flows," Int. J. Heat Mass Transfer, **49**, pp. 1242–1254.

[16] Takeda, Y., 1995, "Velocity Profile Measurements by Ultrasonic Doppler Method," Exp. Therm. Fluid Sci., **10**, pp. 444–453.

[17] Berni, A., 2005, "Unsteady Velocity Profiles and Energy Dissipation in Turbulent Pipe Flow," Ph.D. thesis, Dipartimento di Ingegneria Civile ed Ambientale, Perugia, Italy.

[18] Nowak, M., 2002, "Wall Shear Stress Measurement in a Turbulent Pipe Flow Using Ultrasound Doppler Velocimetry," Exp. Fluids, **33**, pp. 249–255.

[19] Zidouh, H., 2007,"Etude expérimentale du frottement pariétal instationnaire," Ph.D. thesis, Université de Valenciennes et du Hainaut-Cambrésis, France.

[20] Sobolik, V., Tihon, J., Wein, O., and Wichterle, K., 1998, "Calibration of Electrodiffusion Friction Probes Using a Voltage-Step Transient," J. Appl. Electrochem., **28**, pp. 329–335.

[21] Wunderlich, T., and Brunn, P. O., 2000, "A Wall Layer Correction for Ultrasound Measurements in Tube Flow: Comparison Between Theory and Experiments," Flow Meas. Instrum., **11**, pp. 63–69.

[22] Washington, P. A., 1997, "Discussion on 'Wall Shear Stress in Accelerating and Decelerating Turbulent Pipe Flows'," J. Hydraul. Res., **35**(1), pp. 140–142.

[23] Axworthy, D. H., Ghidaoui, M. S., and McInnis, D. A., 2000, "Extended Thermodynamics Derivation of Energy Dissipation in Unsteady Pipe Flow," J. Hydraul. Eng., **126**(4), pp. 276–287.

Inviscid Flow Past Two Cylinders

R. S. Alassar

M. A. El-Gebeily

Department of Mathematics and Statistics,
King Fahd University of Petroleum & Minerals,
Dhahran 31261, Saudi Arabia

A simple solution of the problem of inviscid flow past two circular cylinders is presented. The two cylinders may be of different diameters and located at any distance from each other. The solutions of the two main cases, namely, when the flow is perpendicular to the center-to-center line and when the flow is parallel to it (tandem cylinders), lead to a solution of the problem when the flow is in an arbitrary direction. [DOI: 10.1115/1.3114678]

1 Introduction

The study of the flow past two circular cylinders is important due to the related scientific applications. One can find numerous papers written on the solution of the flow past a single sphere or a single cylinder. A review of the flow past spheres can be found in Ref. [1], past cylinders in Ref. [2], and past oblate and prolate spheroids in Refs. [3,4]. The potential flow past a single spheroid, as a generalization of a sphere, was treated by Alassar and Badr [5]. Exact and closed form solutions in terms of the potential and stream functions were obtained. There is, however, far less work conducted on the effect of the existence of one body onto another. While we are not aware of any simple closed form solution to the potential flow past two interacting spheres, some typical studies that deal with the problem are those by Hicks [6], Basset [7], Herman [8], Lamb [9], Rouse [10], Bentwich [11], and Sun and Chwang [12]. The mutual force between two pulsating spherical bubbles far apart was studied by Bjerknes [13]. Lagally [14,15] considered the problem of the potential flow induced by two stationary circular cylinders in a uniform stream. The method of obtaining a complicated solution was based on conformal mappings. The work of Lagally [14,15] was extended by Wang [16] to the unsteady problem of two circular cylinders expanding and translating arbitrarily in a still fluid. Crowdy et al. [17] published a follow-up to Wang's paper describing the inviscid flow solution for two arbitrary shaped cylinders. Crowdy [18] also found a solution for uniform flow past multiple cylinders, again using conformal mapping techniques.

In this paper, we show that a simple solution of the problem of inviscid flow past two circular cylinders can be obtained by hosting the problem in bipolar coordinates. The inviscid flow solution provides a good approximation for high Reynolds number flows. There are two interesting arrangements of the cylinders, namely, tandem when the flow is parallel to the center-to-center line and side-by-side when the flow is perpendicular to the center-to-center line. The two cylinders may be of different diameters and located at any distance from each other.

2 The Inviscid Flow Problem

The bipolar cylindrical coordinate system (θ,ξ,z) is a three-dimensional orthogonal coordinate system that results from projecting the two-dimensional bipolar coordinate system (θ,ξ), in the perpendicular z-direction. The two-dimensional version is composed of Apollonian circles, which are two sets of circles where every circle in the first set intersects every circle in the second set orthogonally (Fig. 1). The transformation equations of the bipolar cylindrical coordinates are

$$x=\frac{a\sinh\xi}{\cosh\xi-\cos\theta},\quad y=\frac{a\sin\theta}{\cosh\xi-\cos\theta},\quad \text{and}\quad z=z \tag{1}$$

with scale factors given by

$$h_\theta=\frac{a}{\cosh\xi-\cos\theta},\quad h_\xi=\frac{a}{\cosh\xi-\cos\theta},\quad \text{and}\quad h_z=1 \tag{2}$$

Eliminating ξ from Eq. (1), we get $x^2+(y-a\cot\theta)^2=a^2\csc^2\theta$, which defines the first coordinate surfaces (θ=constant, $0\leq\theta\leq 2\pi$) as circular cylinders centered at $(0,a\cot\theta)$ and of radius $|a\csc\theta|$. Eliminating θ, on the other hand, we get the equation $(x-a\coth\xi)^2+y^2=a^2\csc h^2\xi$, which defines the second coordinate surfaces (ξ=constant, $-\infty<\xi<\infty$) as circular cylinders centered at $(a\coth\xi,0)$ and of radius $|a\csc h\xi|$. As $\xi\rightarrow\mp\infty$, the circles degenerate into the two focal points $(\mp a,0)$, the cylinders to lines. The third coordinate surfaces are obviously the planes (z=constant).

The problem considered here is that of two cylinders, possibly of different diameters, placed in a frictionless incompressible fluid of infinite extent. The fluid far away from the two cylinders moves with a velocity U_x or U_y. It can be shown that specifying the radius of each of the two cylinders and the center-to-center distance fixes a particular bipolar coordinate system in the sense that ξ_1 (first circle), ξ_2 (second circle), and a are uniquely determined.

We introduce the stream function ψ using the following traditional definition:

$$h_\xi h_z w_\theta=+\frac{\partial\psi}{\partial\xi},\quad h_\theta h_z w_\xi=-\frac{\partial\psi}{\partial\theta} \tag{3}$$

where w_θ and w_ξ are the velocity components in the directions of θ and ξ, respectively. This definition identically satisfies the continuity equation. The condition of vanishing vorticity can be written as

$$\frac{\partial}{\partial\theta}\left(\frac{h_\xi}{h_\theta h_z}\frac{\partial\psi}{\partial\theta}\right)+\frac{\partial}{\partial\xi}\left(\frac{h_\theta}{h_\xi h_z}\frac{\partial\psi}{\partial\xi}\right)=0 \tag{4}$$

3 Flow Perpendicular to the Center-to-Center Line

Consider the case when the freestream flow is perpendicular to the center-to-center line. The boundary conditions to be satisfied are the impermeability of the surfaces of the cylinders and the freestream conditions. The freestream boundary conditions can be obtained by defining two unit vectors on the directions θ and ξ, then taking the projection of the freestream velocity onto these orthogonal directions. One can show that these conditions can be written in terms of the stream function as

$$\frac{\partial\psi}{\partial\xi}\rightarrow\frac{aU_y(\cosh\xi\cos\theta-1)}{(\cosh\xi-\cos\theta)^2}\quad\text{and}\quad\frac{\partial\psi}{\partial\theta}\rightarrow\frac{aU_y\sinh\xi\sin\theta}{(\cosh\xi-\cos\theta)^2} \tag{5}$$

or simply,

$$\psi\rightarrow-\frac{aU_y\sinh\xi}{\cosh\xi-\cos\theta}\quad\text{as}\quad(\theta,\xi)\rightarrow(0,0) \tag{6}$$

The complete boundary conditions in terms of the velocity and the stream function are shown in Figs. 2(*a*) and 2(*b*), respectively. Due to symmetry, only the upper half plane is considered. It is interesting to observe that the freestream conditions are expressed in bipolar coordinates at a single point, namely, $(\theta,\xi)\rightarrow(0,0)$. This is exactly the major difficulty in hosting the problem in bipolar coordinates. The single point written in bipolar coordinates

---

Contributed by the Fluids Engineering Division of ASME for publication in the JOURNAL OF FLUIDS ENGINEERING. Manuscript received April 2, 2008: final manuscript received March 11, 2009; published online April 16, 2009. Review conducted by Dimitris Drikakis.

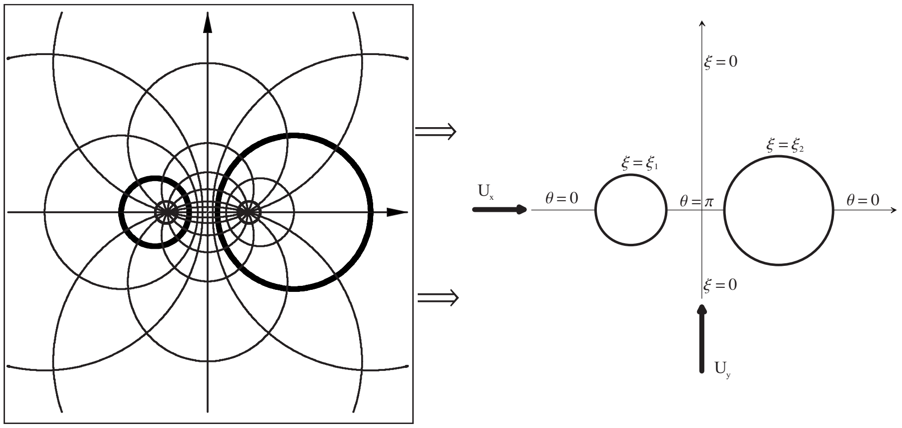

Fig. 1 The problem configuration

carefully as $(\theta,\xi)\rightarrow(0,0)$ is the huge circle with infinite radius that engulfs the whole domain.

The present problem is not separable due to boundary conditions. Our idea is to solve a perturbed separable problem and then mend the solution with a nonseparable part to satisfy the freestream conditions. We define the two functions as follows:

$$\Phi(\theta,\xi) = \sum_{n=1}^{\infty} c_n \cos n\theta \sinh n(\xi - \xi_1) \tag{7}$$

$$\Omega(\theta,\xi) = \sum_{n=1}^{\infty} d_n \cos n\theta \sinh n(\xi - \xi_2) \tag{8}$$

These two functions are harmonic and, respectively, satisfy the bottom and the top boundaries in Fig. 2(*b*). Furthermore, they both satisfy the right and left boundaries except at the point $(\theta,\xi)\rightarrow(0,0)$. We use the top boundary to get the coefficients c_n by setting $\partial\Phi/\partial\theta|_{\xi=\xi_2}$ equal to the similarly defined derivative boundary condition at the far field (Eq. (5)). Thus,

$$\left.\frac{\partial\Phi}{\partial\theta}\right|_{\xi=\xi_2} = \sum_{n=1}^{\infty} - nc_n \sin n\theta \sinh n(\xi_2 - \xi_1) = \frac{aU_y \sinh \xi_2 \sin \theta}{(\cosh \xi_2 - \cos \theta)^2} \tag{9}$$

The fact that Φ does not vanish as $(\theta,\xi)\rightarrow(0,0)$ can be dealt with by adding to it the constant term $\Sigma_{n=1}^{\infty} c_n \sinh n(\xi_1)$ so that

$$\Phi(\theta,\xi) = \sum_{n=1}^{\infty} c_n \cos n\theta \sinh n(\xi - \xi_1) + \sum_{n=1}^{\infty} c_n \sinh n(\xi_1) \tag{10}$$

Similarly, at ξ_1 we set

$$\left.\frac{\partial\Omega}{\partial\theta}\right|_{\xi=\xi_1} = \sum_{n=1}^{\infty} - nd_n \sin n\theta \sinh n(\xi_1 - \xi_2) = \frac{aU_y \sinh \xi_1 \sin \theta}{(\cosh \xi_1 - \cos \theta)^2} \tag{11}$$

and

$$\Omega(\theta,\xi) = \sum_{n=1}^{\infty} d_n \cos n\theta \sinh n(\xi - \xi_2) + \sum_{n=1}^{\infty} d_n \sinh n(\xi_2) \tag{12}$$

Using the orthogonality properties of trigonometric functions, the coefficients c_n and d_n can be determined as

$$\begin{aligned} c_n &= - \frac{aU_y \sinh \xi_2}{n\pi \sinh n(\xi_2 - \xi_1)} \int_0^{2\pi} \frac{\sin \theta \sin n\theta}{(\cosh \xi_2 - \cos \theta)^2} d\theta \\ &= - \frac{2aU_y \; e^{-n\xi_2}}{\sinh n(\xi_2 - \xi_1)} \end{aligned} \tag{13}$$

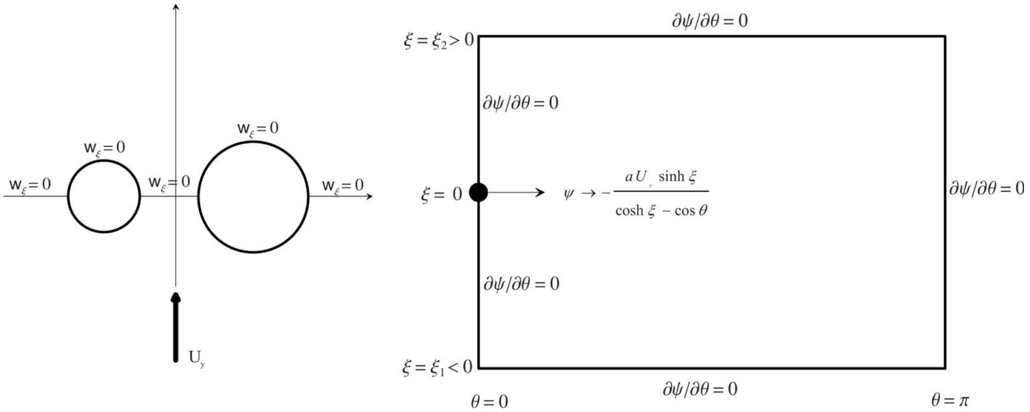

(*a*) (*b*)

Fig. 2 Boundary conditions

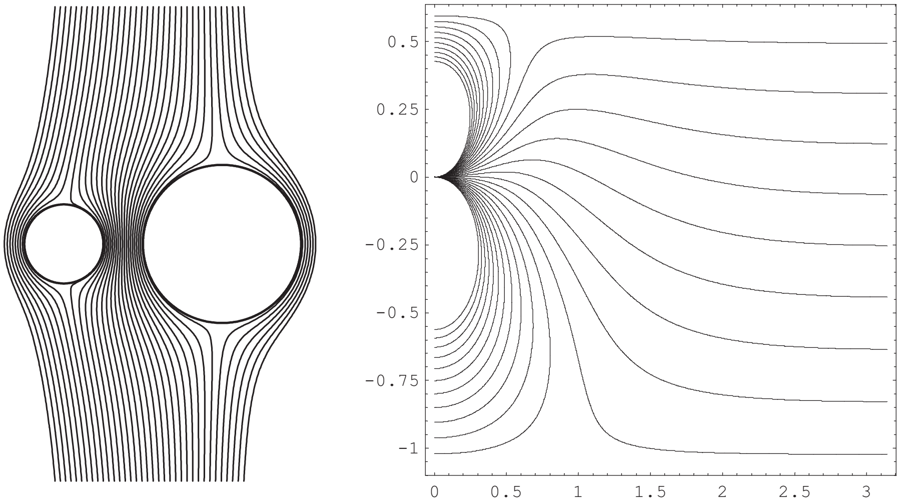

Fig. 3 Streamline patterns for the case $r_1=1$, $r_2=2$, and $H=4$

$$\begin{aligned} d_n &= -\frac{aU_y \sinh \xi_1}{n\pi \sinh n(\xi_1-\xi_2)}\int_0^{2\pi}\frac{\sin\theta \sin n\theta}{(\cosh \xi_1-\cos\theta)^2}d\theta \\ &= +\frac{2aU_y\ e^{+n\xi_1}}{\sinh n(\xi_1-\xi_2)} \end{aligned} \tag{14}$$

Now the function $\psi_y=-(aU_y \sinh \xi)/(\cosh \xi-\cos\theta)-\Phi-\Omega$ has all the required properties in the sense that it is harmonic and satisfies all boundary conditions including the freestream. The solution of the problem may be written compactly as

$$\begin{aligned} \frac{\psi_y(\theta,\xi)}{2aU_y} &= -\frac{\sinh \xi}{2(\cosh \xi-\cos\theta)} \\ &\quad + \sum_{n=1}^{\infty}\frac{\cos n\theta[e^{-n\xi_2}\sinh n(\xi-\xi_1)+e^{+n\xi_1}\sinh n(\xi-\xi_2)]}{\sinh n(\xi_2-\xi_1)} \\ &\quad + \sum_{n=1}^{\infty}\frac{\sinh n(\xi_2+\xi_1)}{\sinh n(\xi_2-\xi_1)} \end{aligned} \tag{15}$$

Typical streamline patterns are shown in Fig. 3 for both the transformed and actual physical domains. The case shown in Fig. 3 is for $r_1=1$, $r_2=2$, and $H=4$ where H is the center-to-center distance. The streamlines are orthogonal to the boundaries $\theta=0$ and $\theta=\pi$. The two lines (originally the cylinders) $\xi=\xi_1$ and $\xi=\xi_2$ are streamlines themselves. The point $(\theta,\xi)\rightarrow(0,0)$ works like a black hole where all streamlines are sucked into.

Once the flow field has been determined, the distribution of the pressure P along the surfaces of the cylinders can be obtained from the equation of conservation of momentum. The θ-component of the momentum equation can be written as

$$\frac{\partial P}{\partial\theta} = -\rho w_\theta \frac{\partial w_\theta}{\partial\theta} \tag{16}$$

where ρ is the fluid density. We define the dimensionless pressure $P^*(\eta,\xi)$ as

$$P^*(\eta,\xi)=\frac{P(\eta)-P(0)}{\rho U_y^2} = -\frac{1}{U_y^2}\int_0^{\eta} w_\theta\frac{\partial w_\theta}{\partial\theta}d\theta \tag{17}$$

which measures the scaled pressure at any location relative to that at $\theta=0$. $P^*(\eta,\xi)$ may be evaluated on the surface of either cylinder. Figure 4 shows the distribution of $P^*(\omega,\xi_2)$ for the case $r_1=1$, $r_2=1$. Since the bipolar coordinate variable θ is neither fixed nor uniformly distributed over the surface of the cylinder, we use the uniform angle ω, which is used in the normal polar cylindrical coordinates system. A polar plot of the pressure is also provided in Fig. 4(*b*).

As the distance between the two cylinders increases, the effect of the existence of one cylinder on the other becomes negligible. Consider, for example, two cylinders having the same diameters $(|\xi_1|=|\xi_2|)$. Equation (15) reduces to

$$\frac{\psi_y(\theta,\xi)}{2aU_y} = -\frac{\sinh \xi}{2(\cosh \xi-\cos\theta)} + \sum_{n=1}^{\infty}\frac{e^{-n\xi_2}\sinh n\xi \cos n\theta}{\sinh n\xi_2} \tag{18}$$

As $H\rightarrow\infty$, $\xi_2\rightarrow\infty$. Using Eq. (18) to calculate $P^*(\eta,\infty)$ (i.e., the dimensionless pressure around the right cylinder when the two cylinders are far apart), one finds that

$$P^*(\eta,\infty) = -\frac{1}{U_y^2}\int_0^{\eta}\left(w_\theta\frac{\partial w_\theta}{\partial\theta}\right)_{\xi_2\rightarrow\infty}d\theta = 1-\cos 2\eta \tag{19}$$

This result is identical to that obtained from analyzing the inviscid flow past a single cylinder using cylindrical coordinates. Figure 4 shows that as the distance between the two cylinders becomes large, the negative pressure gradient created by the existence of the other cylinder at $\theta=\pi$ disappears and the pressure approaches that for a single cylinder given by Eq. (19).

To have an idea of the truncation error involved in the series solution, we estimate the error that results from considering N terms of the series in Eq. (18). It can be shown that the error decays exponentially and has the following bound:

$$\left|\sum_{n=N+1}^{\infty}\frac{e^{-n\xi_2}\sinh n\xi \cos n\theta}{\sinh n\xi_2}\right| \le \frac{e^{(N+1)(|\xi|-2\xi_2)}}{1-e^{|\xi|-2\xi_2}} \tag{20}$$

4 Flow Parallel to the Center-to-Center Line (Tandem Cylinders)

The freestream boundary conditions (Fig. 5) in bipolar coordinates can be written in terms of the stream function as

$$\frac{\partial\psi}{\partial\xi}\rightarrow -\frac{aU_x \sinh \xi \sin\theta}{(\cosh \xi-\cos\theta)^2} \quad \text{and} \quad \frac{\partial\psi}{\partial\theta}\rightarrow -\frac{aU_x(1-\cosh \xi \cos\theta)}{(\cosh \xi-\cos\theta)^2} \tag{21}$$

or simply,

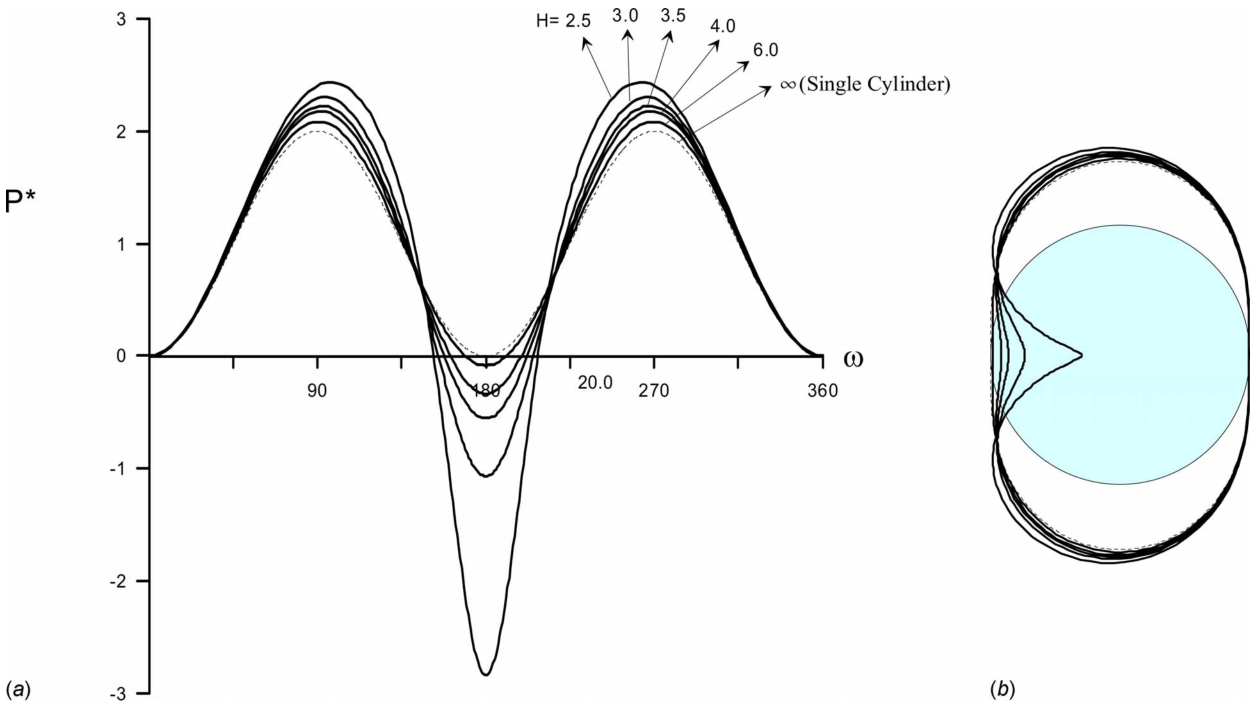

Fig. 4 The pressure distribution around the right cylinder for the case $r_1=1$, $r_2=1$

$$\psi \to +\frac{aU_x \sin\theta}{\cosh\xi - \cos\theta} \quad \text{as} \quad (\theta,\xi)\to(0,0) \tag{22}$$

The following solution, which we denote by $\psi_x(\theta,\xi)$, is harmonic and satisfies all boundary conditions including the freestream:

$$\psi_x(\theta,\xi) = +\frac{aU_x \sin\theta}{\cosh\xi - \cos\theta} - \sum_{n=1}^{\infty} f_n \sin n\theta \sinh n(\xi-\xi_1) - \sum_{n=1}^{\infty} g_n \sin n\theta \sinh n(\xi-\xi_2) \tag{23}$$

The solution is obtained in a similar way to the previous case. It is noted here that the two sums in the solution vanish as $(\theta,\xi)\to(0,0)$ and no adjusting constant terms are needed.

The coefficients f_n and g_n are given by

$$f_n = -\frac{aU_x}{n\pi \sinh n(\xi_2-\xi_1)}\int_0^{2\pi} \frac{\cos n\theta(1-\cos\theta\cosh\xi_2)}{(\cosh\xi_2-\cos\theta)^2}d\theta = +\frac{2aU_x e^{-n\xi_2}}{\sinh n(\xi_2-\xi_1)} \tag{24}$$

$$g_n = -\frac{aU_x}{n\pi \sinh n(\xi_1-\xi_2)}\int_0^{2\pi} \frac{\cos n\theta(1-\cos\theta\cosh\xi_1)}{(\cosh\xi_1-\cos\theta)^2}d\theta = +\frac{2aU_x e^{+n\xi_1}}{\sinh n(\xi_1-\xi_2)} \tag{25}$$

The solution can now be written as

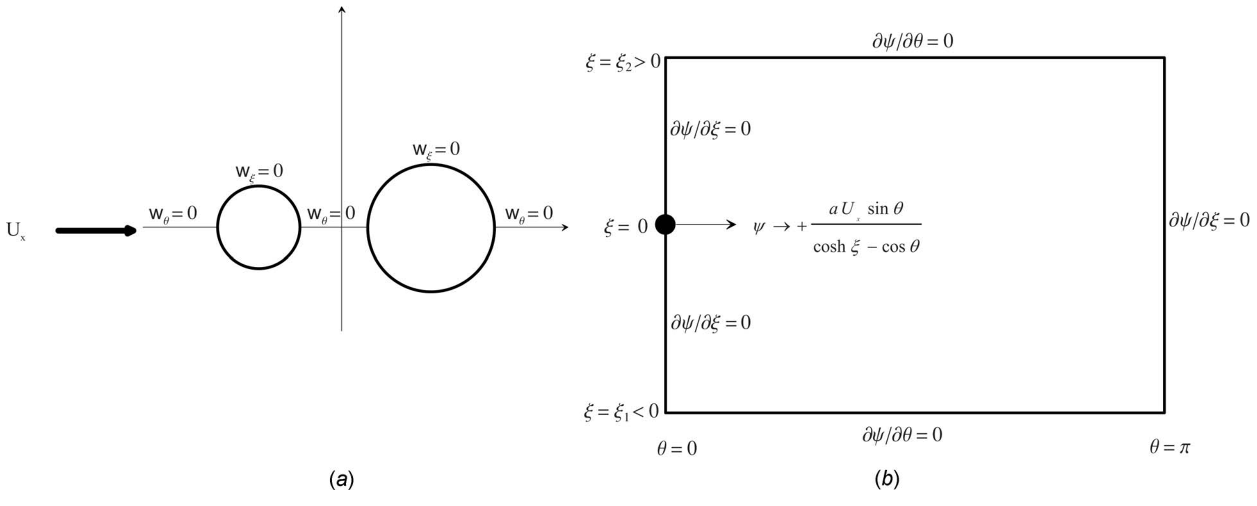

Fig. 5 Boundary conditions for tandem cylinders

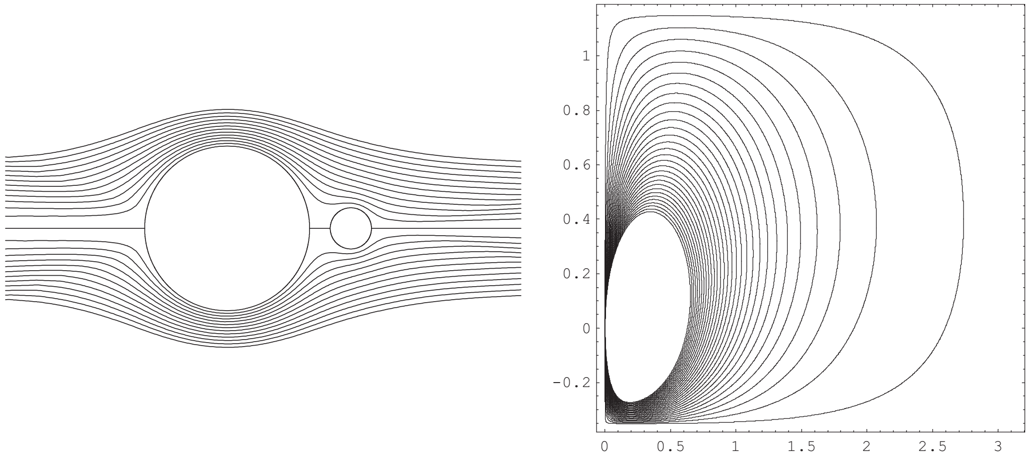

Fig. 6 Streamline patterns for the case $r_1=4$, $r_2=1$, and $H=6$

$$\frac{\psi_x(\theta,\xi)}{2aU_x} = +\frac{\sin\theta}{2(\cosh\xi-\cos\theta)} - \sum_{n=1}^{\infty}\frac{\sin n\theta[e^{-n\xi_2}\sinh n(\xi-\xi_1) - e^{+n\xi_1}\sinh n(\xi-\xi_2)]}{\sinh n(\xi_2-\xi_1)} \tag{26}$$

Typical streamlines are given in Fig. 6 for the case $r_1=4$, $r_2=1$, and $H=6$. Figure 7 shows the distribution of $P^*(\omega,\xi_2)$ for the case $r_2=1$, $H=6$ for different sizes of the left cylinder.

5 Flow in an Arbitrary Direction

Consider a freestream with velocity U_o, which makes angle δ with the positive x-axis. The only boundary conditions to be satisfied here are the impermeability conditions on the surfaces of the cylinders and the freestream. No conditions are set at $\theta=0$ or at $\theta=\pi$. We, then, must consider the whole plane as there is no symmetry involved in this case.

The far field boundary conditions can be written in terms of the stream function as

$$\frac{\partial\psi}{\partial\theta} \to -\frac{aU_o\cos\delta(1-\cosh\xi\cos\theta)}{(\cosh\xi-\cos\theta)^2} + \frac{aU_o\sin\delta\sinh\xi\sin\theta}{(\cosh\xi-\cos\theta)^2}$$

$$\frac{\partial\psi}{\partial\xi} \to -\frac{aU_o\cos\delta\sinh\xi\sin\theta}{(\cosh\xi-\cos\theta)^2} + \frac{aU_o\sin\delta(\cosh\xi\cos\theta-1)}{(\cosh\xi-\cos\theta)^2} \tag{27}$$

Or simply,

$$\psi \to +\frac{aU_o\cos\delta\sin\theta}{\cosh\xi-\cos\theta} - \frac{aU_o\sin\delta\sinh\xi}{\cosh\xi-\cos\theta} \quad \text{as} \quad (\theta,\xi)\to(0,0) \tag{28}$$

It is easy now to see that the solution $\psi(\theta,\xi)$ can be written as

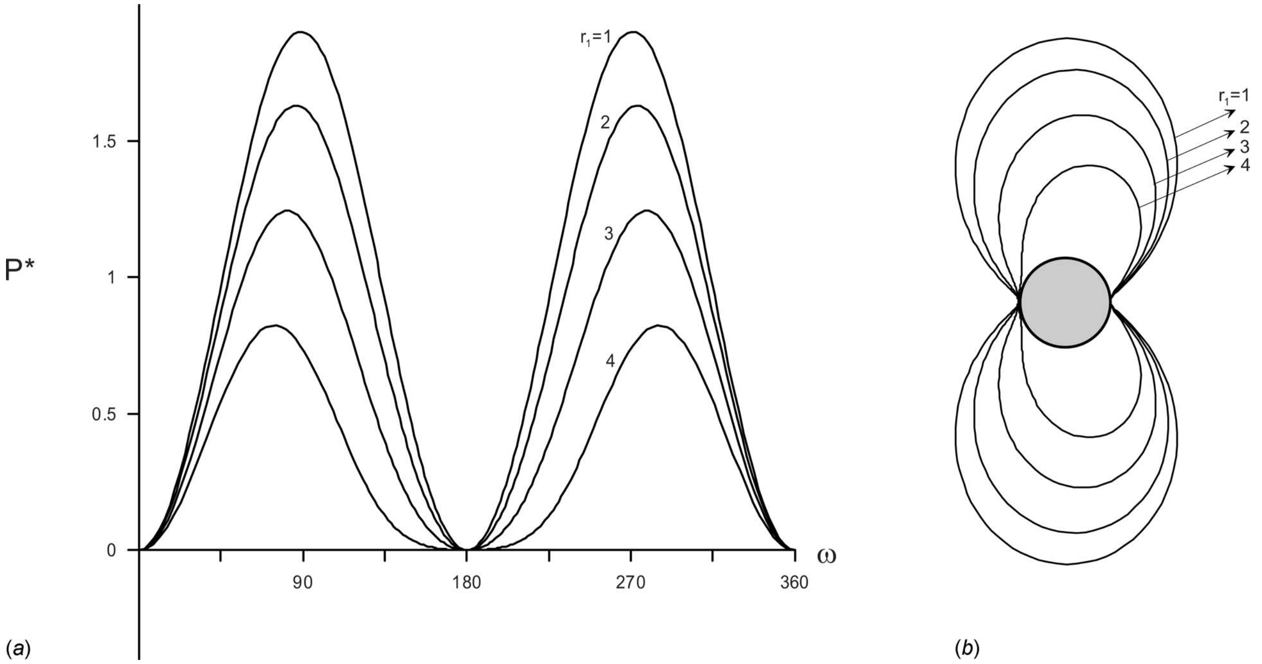

Fig. 7 The pressure distribution around the right cylinder for the case $r_2=1$, $H=6$

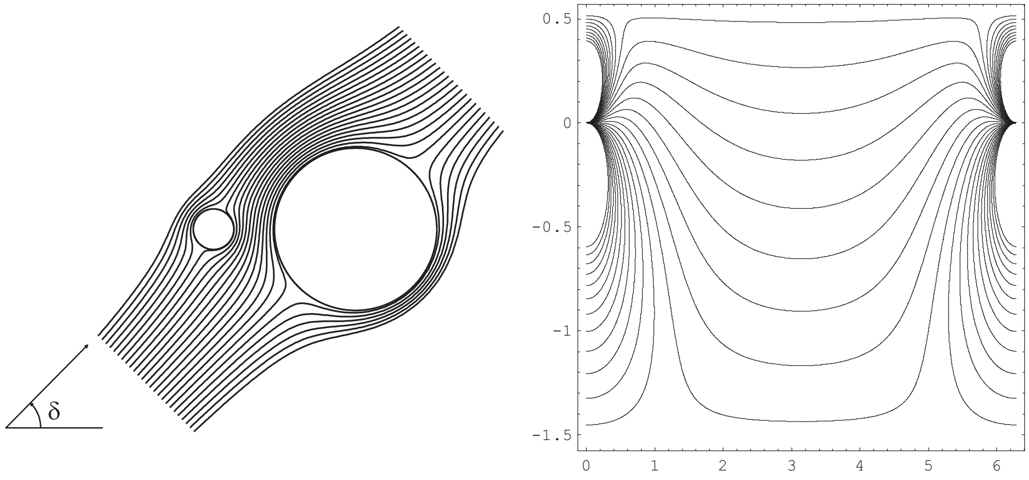

Fig. 8 Streamline patterns for the case $r_1=1$, $r_2=4$, $H=7$, and $\delta=\pi/4$

$$\psi(\theta,\xi)=\psi_y(\theta,\xi)+\psi_x(\theta,\xi) \tag{29}$$

where the velocities U_y and U_x are to be replaced, respectively, by U_o sin δ and U_o cos δ in the expressions of $\psi_y(\theta,\xi)$ and $\psi_x(\theta,\xi)$. The function ψ is harmonic and satisfies all boundary conditions. Figure 8 shows a typical solution for the case $r_1=1$, $r_2=4$, $H=7$, and $\delta=\pi/4$.

Acknowledgment

The authors would like to thank King Fahd University of Petroleum & Minerals (KFUPM) for supporting this research under Grant No. MS/Inviscid/375. R.S.A. is grateful to Professor M. Amara and the Applied Mathematics Laboratory at the Pau University in France for such a pleasant visit that made this research possible.

References

[1] Alassar, R. S., Badr, H. M., and Allayla, R., 2000, "Viscous Flow Over a Sphere With Fluctuations in the Free-Stream Velocity," Comput. Mech., **26**(5), pp. 409–418.
[2] Badr, H. M., 1994, "Oscillating Inviscid Flow Over Elliptic Cylinders With Flat Plates and Circular Cylinders as Special Cases," Ocean Eng., **21**(1), pp. 105–113.
[3] Alassar, R. S., and Badr, H. M., 1999, "Oscillating Flow Over Oblate Spheroids," Acta Mech., **137**(3–4), pp. 237–254.
[4] Alassar, R. S., and Badr, H. M., 1999, "Oscillating Viscous Flow Over Prolate Spheroids," Trans. Can. Soc. Mech. Eng., **23**(1A), pp. 83–93.
[5] Alassar, R. S., and Badr, H. M., 1997, "Analytical Solution of Oscillating Inviscid Flow Over Oblate Spheroids With Spheres and Flat Disks as Special Cases," Ocean Eng., **24**(3), pp. 217–225.
[6] Hicks, W. M., 1880, "On the Motion of Two Spheres in a Fluid," Philos. Trans. R. Soc. London, **171**, pp. 455–492.
[7] Basset, A. B., 1886, "On the Motion of Two Spheres in a Liquid, and Allied Problems," Proc. London Math. Soc., **s1–18**, pp. 369–378.
[8] Herman, R. A., 1887, "On the Motion of Two Spheres in Fluid and Allied Problems," Q. J. Math., **22**, pp. 204–231.
[9] Lamb, H., 1932, *Hydrodynamics*, 6th ed., Cambridge University Press, Cambridge, UK, Chap. 6.
[10] Rouse, H., 1976, *Advanced Mechanics of Fluids*, Krieger Publishing Company, Malabar, FL, Chap. 3.
[11] Bentwich, M., 1978, "Exact Solution for 2-Sphere Problem in Axisymmetrical Potential Flow," ASME Trans. J. Appl. Mech., **45**, pp. 463–468.
[12] Sun, R., and Chwang, A. T., 2001, "Hydrodynamic Interaction Between a Slightly Distorted Sphere and a Fixed Sphere," Theor. Comput. Fluid Dyn., **15**, pp. 11–22.
[13] Bjerknes, V. F. K., 1906, *Fields of Force*, Columbia University Press, New York.
[14] Lagally, M., 1929, "The Frictionless Current in the Outer Areas of Double Circuits," Z. Angew. Math. Mech., **9**, pp. 299–305.
[15] Lagally M., 1931, "The Frictionless Flow in the Region Around Two Circles," N.A.C.A. Technical Memorandum No. 626.
[16] Wang, Q. X., 2004, "Interaction of Two Circular Cylinders in Inviscid Flow," Phys. Fluids, **16**(12), pp. 4412–4425.
[17] Crowdy, D. G., Surana, A., and Yick, K.-Y., 2007, "The Irrotational Motion Generated by Two Planar Stirrers in Inviscid Fluid," Phys. Fluids, **19**, p. 018103.
[18] Crowdy, D. G., 2006, "Analytical Solution for Uniform Potential Flow Past Multiple Cylinders," Eur. J. Mech. B/Fluids, **25**, pp. 459–470.